Etudes expérimentales et numériques de la dynamique des vagues et leurs implications pour les échanges océan - atmosphère.

Luc Lenain

NNT : 2017SACLN033

Thèse de doctorat de l'Université Paris-Saclay préparée à l'École Normale Supérieure de Cachan (École Normale Supérieure Paris-Saclay)

Ecole doctorale n°573
Ecole Doctorale Interfaces
Spécialité de doctorat : Physique

par

M. Luc Lenain

Études expérimentales et numériques de la dynamique des vagues et leurs implications pour les échanges océan - atmosphère

Thèse présentée et soutenue à Cachan, le 11 Septembre 2017.

Composition du Jury :

Mme	Daniele Hauser	Directrice de Recherche CNRS, LATMOS	(Présidente du jury)
M.	Bertrand Chapron	Directeur de Recherche IFREMER	(Rapporteur)
M.	Olivier Kimmoun	Maître de conférence Université Aix-Marseille	(Rapporteur)
M.	Jacques Piazzola	Professeur Université de Toulon	(Examinateur)
M.	Florian de Vuyst	Professeur Université Tech. de Compiègne	(Directeur de thèse)
M.	Frédéric Dias	Professeur UCD	(Co-directeur de thèse)
M.	Ken Melville	Professeur Scripps Institution of Oceanography	(Co-directeur de thèse)

A mes parents, Jacqueline et Jean-Luc Lenain,
my wife Melissa, and my two wonderful children, Zoé and Tiago.

Acknowledgments

I would like to begin with expressing my gratitude to my advisors, Florian de Vuyst, Frederic Dias, and Ken Melville for their guidance and support during the past few years. I would also like to thank the members of the jury, Bertrand Chapron, Olivier Kimmoun, Danièle Hauser, and Jacques Piazzola for providing helpful comments and suggestions on my work.

The work presented here was largely based on field experiments conducted in southern California. None of these measurements would have been possible without the incredible support, expertise and energy of the Air-Sea Interaction Laboratory (Scripps Institution of Oceanography) present and past members: Nick Statom, Ben Reineman, Peter Sutherland, Leonel Romero, Ralph "RJ" Jiorle, Luc Deike, Laurent Grare, Nick Pizzo among others. I am particularly grateful to Luc Deike for his support with Gerris and fruitful discussions on the work presented here. Laurent Grare provided invaluable help in the interpretation of some of the results presented in this work. Nick Statom's skills and dedication lead to the collection of data sets of incredible quality.

I am particularly grateful to Ken Melville, who encouraged me to pursue this PhD while working full-time in his group. His trust and confidence in my abilities lead to accomplish much more than I had ever anticipated. It has truly been a pleasure to have the chance to work and learn from him for the past 12 years.

None of this would have been possible without the unconditional support of my family, in particular my wife Melissa and two children Zoé and Tiago. They have been an exceptional source of support and motivation throughout this process. Their love and support have been tremendous and I thank them for that.

This research was conducted under grants to Ken Melville from the Office of Naval Research (ONR) and the National Science Foundation (NSF).

Résumé en Français

Presque 71 % de la planète Terre est recouverte d'eau. À l'interface air-mer, se trouve un lieu d'échanges de propriétés (chaleur, quantité de mouvement, humidité, gaz,...) entre l'océan et l'atmosphère. Nous trouvons sous cette interface, la couche mélangée océanique qui sépare l'atmosphère des couches profondes de l'océan. Les processus qui se produisent près de la surface ont un effet important sur les échanges et transports entre l'ocean et l'atmosphère. Ces processus sont présentés de manière conceptuelle dans la figure 1.1. Les vagues, par leurs effets sur les flux entre l'océan et l'atmosphère, ont des effets directs ou indirects sur les circulations de l'océan et de l'atmosphère, et donc le climat, régulant les cycles géophysiques de la planète. Les vagues influencent la variabilité des propriétés de la couche de surface océanique d'une part, et les interactions entre les processus, (en particulier) à petite échelle, et les phénomènes à grande échelle (circulation des oceans, courants etc...)

Pour améliorer notre compréhension du couplage entre l'atmosphère et l'océan, et les paramétrages du flux de masse à cette interface (gaz, aérosols, par exemple), du flux de moment (pour la génération de vagues et de courants marins) et du flux d'énergie (flux de chaleur et énergie cinétique pour les courants et le processus de mélange près de la surface) dans les modèles couplés océan-atmosphère, les vagues doivent être prises en compte. La physique du couplage dépend de la cinématique et de la dynamique du champ de vagues, y compris les processus de génération de vagues liées au vent, les interactions non-linéaires, ondes-ondes et la dissipation des vagues, cette dernière étant normalement considérée comme dominée par le déferlement. Nous présentons ici une série d'études expérimentales et numériques, démontrant l'importance du champ de vagues sur les interactions océan-atmosphère.

Aprés une introduction sur les interactions océan-atmosphère et états de mer, notre exposé s'articule autour de quatre parties. Dans la première partie, les propriétés spectrales de la distribution directionelle du champs de vagues basées sur des mesures lidar de la topographie de la surface de l'océan sont présentées. L'objectif y est de démontrer la validité d'un modèle existant de génération de vagues (Phillips, 1985) et d'y étendre le paramétrage des modèles de vagues. L'analyse se concentre principalement sur les propriétés directionelles du champs de vagues, et ses caractéristiques spectrales. Dans la deuxième partie, une autre composante essentielle aux échanges océan-atmosphère est présentée : la génération d'aérosols marins, et en particulier l'effet des vagues, traditionellement ignoré, sur la paramétrage de la distribution de taille d'aérosols marins

et leurs concentrations. Dans la troisième section, un outil numérique, Gerris, est utilisé pour caractériser l'effet du déferlement de vagues sur le mélange océanique près de la surface de l'eau. Enfin dans la dernière partie, le potentiel de l'utilisation de plateformes de mesure autonomes pour l'étude des processus océan-atmosphère dans les ouragans est demontrée, car elles permettent d'obtenir des mesures à la fois atmospheriques, océanographiquse et de champs directionel de vagues dans des conditions extrêmes (tempête cyclonique de catégorie 3). Les principaux résultats de chaque section sont presentés ci-dessous.

Dans la première partie (correspondant au deuxième chapitre du manuscrit), les propriétés spectrales de la distribution directionelle du champs de vagues sont présentées, en mettant l'accent sur la transition entre la zone dite d'équilibre et celle de saturation (Phillips, 1985), en utilisant des mesures lidar de la topographie de la surface de l'océan, faites depuis un avion de recherche pendant la campagne de mesures SOCAL2013 au large des côtes du sud de la Californie. R/P FLIP, une plateforme de recherche océanologique basée au Scripps Institution of Oceanography à San Diego, était ancrée au centre de la zone d'opération, et était instrumentée pour mesurer les caractéristiques de la couche limite atmosphérique. La vitesse du vent a variée de 1-2 m/s jusqu'à 11 m/s et la hauteur significative des vagues H_s de 0.8 à 2.5 m pendant les 10 jours de campagne de mesures. Les spectres directionels de vagues en nombre d'onde montrent très clairement une distribution bimodale, pour des nombres d'ondes nettement plus élevés que ce qui avait été déja publié dans le passé. L'évolution spectrale de la zone d'équilibre et celle de la zone de saturation est présentée dans le contexte des travaux de Phillips (1985). Il y décrit un modèle de génération des vagues, sur une partie du spectre de vagues dite zone d'équilibre, ou le flux d'énergie non-linéaire liés aux interactions vague-vague, le forçage du vent et la dissipation d'énergie, cette dernière étant principalement liée au déferlement de vagues, sont en *équilibre*, *proportionels*, et *d'amplitude comparable*. Son modèle prédit une pente de $-5/2$ pour le régime d'équilibre du spectre omnidirectionel de vagues en nombre d'ondes. Au-delà de cette zone, à plus haut nombre d'onde, des mesures temporelles et spatiales en mer ont demontrées l'existence d'une transition vers un autre régime, dit de saturation, ou le terme non-linéaire d'interaction vague-vague devient très faible, et l'équilibre est cette fois entre le forçage du vent et la dissipation (produite principalement par le déferlement de vagues).

À notre connaissance, il s'agit des premières mesures de spectres directionels en nombre d'onde sur une gamme aussi importante de nombre d'onde, montrant une séparation

de presque π pour les deux lobes de la distribution directionelle du spectre pour les plus hauts nombres d'ondes, autour de $k/k_p \approx 100 - 200$. Ici k_p représente le nombre d'onde au pic du spectre des vagues. Ces résultats demontrent que des vagues de directions opposées peuvent coexister sans pour autant qu'elles soient produites par deux tempêtes differentes, ou par des vents de directions opposées. L'existence de ce type de système de vagues est très importante, car il peut s'agir d'un phénomène à l'origine des bruits microsismiques dans l'océan (Longuet-Higgins, 1950; Farrell and Munk, 2010; Ardhuin et al., 2015).

Le spectre omnidirectionel de vagues présente une loi de puissance de $-5/2$ pour la zone d'équilibre, et -3 pour la zone de saturation. La transition entre ces deux régimes est très bien définie et nous obtenons un bon accord avec le modèle de Phillips (1985), avec un nombre d'onde à la transition proportionel à $(u_*^2/g)^{-1}$, u_* représentant la vitesse de friction dans l'air. Le regroupement des spectres dans les régimes d'équilibre et de saturation lorsqu'ils sont tracés en fonction du nombre d'onde non-dimensionalisé ku_*^2/g est remarquable. Ce nombre d'onde est également très efficace pour regrouper la séparation non-dimensionalisée azimutale des lobes trouvée dans les distributions directionelles de vagues.

Ce jeu de données nous a également permis de tester et améliorer la formulation empirique du nombre d'onde à la transition équilibre-saturation, k_n, définie par Romero and Melville (2010a,b) qui le spécifie comme étant proportionel à une des caractéristique spectrale du flux d'énergie non-linéaire. Le nombre d'onde k_n depend de l'âge des vagues, mais également de la vitesse de friction non-dimensionalisée $u_*/\sqrt{gH_s}$, cette dernière étant mieux adaptée pour représenter l'évolution du spectre à la transition entre les zones d'équilibre et de saturation.

Dans le troisième chapitre, nous concentrons nos efforts sur les aérosols marins, un autre processus influençant le couplage entre l'océan et l'atmosphère. Ces aerosols sont produits lors du déferlement de vagues et représentent une large portion des aérosols présents dans l'atmosphère au-dessus des océans.

Des mesures d'aérosols collectées pendant deux campagnes océanographiques, la première au large des côtes de la Californie du Nord en Juin 2010, "the phase-resolved High-Resolution Air-Sea Interaction Experiment (HIRES)", et la seconde, "GOTEX2004", qui a eu lieu au Mexique en 2004, au large du Golfe de Tehuantepec, sont analysées. En utilisant un avion de recherche (CIRPAS Twin Otter et NCAR C130 respectivement), nous avons obtenu pendant ces campagnes des distributions de diamètre d'aérosols pour

des altitudes allant de 30 à 800 m au-dessus de la surface de l'eau, pour une gamme de conditions météorologiques variant de 10 à 18 m/s pour le vent à 10 m (U_{10}) et une hauteur significative de vagues H_s variant de 2 à 4.5 m. Des aérosols marins de large diamètres, $D > 40\mu m$, ont été trouvés à des altitudes élevées, atteignant le haut de de la couche limite atmosphérique marine (MABL), démontrant que les mécanismes de transport et de génération des aérosols marins de grandes tailles sont encore très mal compris (Veron, 2015), malgré leur importance pour les échanges de flux de chaleur, d'humidité et le transport de composés carbonés provenant des océans vers l'atmosphère (Quinn et al., 2015).

Par ailleurs, malgré la démonstration du rôle du déferlement de vagues dans le couplage de l'océan et l'atmosphère, les fonctions (souvent empiriques) d'estimation de la production d'aérosols marins ne sont traditionnellement parametrées que par la vitesse du vent. Il est clair que cette approche est incomplète car le vent **et** l'état de mer doivent être pris en compte. Dans ce chapitre, nous présentons un paramétrage du volume total d'aérosols marins mesurés à 30m d'altitude qui inclut ces deux effets. L'amélioration des résultats avec l'ajout de l'état de mer est évidente, en comparaison des résultats obtenus quand seul le vent est pris en compte.

Dans le quatrième chapitre, nous présentons les résultats de simulations numériques de déferlement de vagues en utilisant un canal à vagues idealisé, et un code numérique, Gerris, qui permet de résoudre les équations aux dérivées partielles de Navier-Stokes, pour décrire les écoulements biphasiques d'un système de fluides air-eau. Notre approche est de reproduire, ou tout au moins tenter de reproduire, les résultats de travaux en laboratoire de Rapp and Melville (1990), en générant un déferlement pour une gamme de caractéristiques de vagues, en variant leur fréquence centrale, f_c, et leur pente moyenne S. Des particules Lagrangiennes, initialement à la surface dans la zone de déferlement sont suivies en temps et espace, pour caractériser le taux d'approfondissement après l'impact. Nous obtenons des résultats comparables à ceux de Rapp and Melville (1990), qui avaient à cet effet utilisé de l'encre dans leurs expériences en laboratoire. On constate des différences, très certainement causées par des artéfacts numériques. Nous montrons ici que la portion d'eau se trouvant initialement à la surface à proximité d'un déferlement de vague peut atteindre des profondeurs équivalentes à une ou deux fois la hauteur de la vague qui déferle. Ce résultat peut être extrapolé aux conditions rencontrées en mer lors de tempête, en utilisant la hauteur de vague significative H_s. Celle-ci ne représente que la hauteur "moyenne" des vagues sur une période donnée. Il n'est pas rare de trouver des

vagues de hauteur équivalente à $1.5-2\times H_s$ sur cette même période. Dans le chapitre 2 et 3, nous avons montré que H_s pouvait atteindre presque 5m dans des tempêtes au large de la Californie. Dans d'autres parties du monde (Mer du Nord, océans autrales, Atlantique nord ou dans des ouragans, par exemple), la hauteur significative des vagues atteint souvent des valeurs qui dépassent 10m. Nos résultats numériques impliquent donc que dans ces conditions, de l'eau initialement à la surface peut se trouver transportée rapidement jusqu'a des profondeurs de 20 à 40 m, uniquement sous l'effet des vagues, et ce faisant en produisant également du mélange dans la couche limite océanique.

Nous avons également montré que les distributions de taille d'aérosols produites lors du déferlement de vagues dans les simulations numériques du canal à vague idealisé sont en accord avec les lois de puissance obtenues lors d'experiences en laboratoire (Veron et al., 2012; Towle, 2014) et numériques (Wang et al., 2016), même si nos résultats sont limités par l'aspect 2D des simulations. Pour permettre la comparaison avec des études en laboratoire, des simulations à haute résolution, en 3D, sont nécessaires.

Dans le dernier chapitre, nous présentons le rôle à venir des plateformes de mesures autonomes pour améliorer notre compréhension du couplage entre l'océan et l'atmosphère dans des conditions extrêmes, telles que des ouragans ou des cyclones tropicaux. Le 31 décembre 2012, une de ces plateformes autonomes, un "Wave Glider", en route vers l'Australie depuis l'île d'Hawaii (Projet PacX) est passé à 46 km de l'oeil d'un cyclone de categorie 3, le cyclone Freda, en mesurant des vents de près de 37 m/s pour une hauteur de vague significative H_s de presque 10 m. Le Wave Glider était équipé pour des mesures océanographiques, atmosphériques et conditions de surface : pression atmosphérique, vitesse du vent, température de l'air et de l'eau, salinité, concentration d'oxygène dans l'eau, fluorescence (Chlorophyll-a et turbidité), et le spectre directionel de vagues. Ce dernier est calculé via le déplacement de la partie de la plateforme qui flotte à la surface, mesuré par un capteur GPS.

Nous trouvons ici une évolution unimodale (houle) à bimodale (houle + vagues de vent) du spectre directionel avant le croisement avec le cyclone, évoluant ensuite vers une distribution unimodale une fois que la tempête s'est eloignée. Les spectres frequentiels des vagues obtenus par le Wave Glider montrent une loi de puissance en f^{-4}, en accord avec les travaux de Donelan et al. (1985) et Young (2006).

La dérive de Stokes est estimée à partie du spectre directionel de vagues. Le nombre de turbulence de Langmuir, La_t, l'échelle de profondeur de Stokes, et la dérive de Stokes à proximité du cyclone Freda sont en accord avec les simulations LES de Sullivan et al.

(2012) de l'ouragan Frances. Le terme La_t, mesuré à la surface, varie de 0.28 à 0.6, avec les valeurs les plus basses, pour $La_t < 0.4$, en amont de la tempête et dans son sillage, après le passage de l'oeil du cyclone. La distribution spatiale de la dérive de Stokes centrée sur la position du cyclone Freda est comparable aux résultats numériques de Sullivan et al. (2012), avec une amplitude maximale près de l'oeil du cyclone et à sa droite. Dans cette section, nous evoquons également de la contribution de la turbulence de Langmuir dans le mélange de la couche limite océanique.

Même si l'approfondissement de la couche melangée océanique dans les cyclones reste principalement produite par les courants inertiels formés à l'arrière de ces systèmes, correspondant au mécanisme par lequel de l'eau froide, provenant des profondeurs des océans, vient se mélanger avec les eaux de surface, ce processus n'explique pas le transport vertical de chlorophyll-a mesuré à l'avant du cyclone Freda. Plusieurs mécanismes potentiels a l'origine de ce phénomène sont présentés dans ce chapitre.

Pour conclure, nous présentons dans cet exposé les avantages d'une approche pluridisciplinaire, combinant études numériques et experimentales, différentes technologies de capteurs, plateformes de mesures (navire de recherche, avions, plateforme et vehicules autonomes ...) pour améliorer notre compréhension des processus physiques qui influencent les interactions entre l'océan et l'atmosphère. Le développement de plateformes de mesure autonomes, en conjonction avec la miniaturisation des capteurs et autres instrumentation, ont revolutionné nos capacité de mesures, à l'exemple de celles realisées au cœur du cyclone Freda. Ce type de mesure dans de telles conditions était encore considéré comme impossible il n'y a de cela pas si longtemps.

Ces 50 dernières années, de très importants progrès ont étés réalisés dans notre compréhension des processus d'interaction océan-atmosphère, par exemple sur la génération des vagues présentée dans l'introduction. Cependant la communauté scientifique cherche encore a acquérir des connaissances dans certains aspects fondamentaux du couplage air-mer, dans le but d'améliorer la compréhension de la dynamique du flux de moment, de chaleur et les échanges de gaz entre l'atmosphère et l'océan. Les vagues ont des effets directs ou indirects sur les circulations de l'océan et de l'atmosphère, influencant le climat à l'échelle globale. Elles sont également la source principale du bruit de fond sismique, qui agit directement sur la croûte terrestre, un élement essentiel de la dynamique sédimentaire marine. Par quels mécanismes les vagues déferlantes injectent-elles du flux de moment dans la couche océanique? Quel est le rôle de la circulation océanique (et de la turbulence dans la couche mélangée) sur la génération de champ de vagues et de leur déferlement?

Quel est l'impact du champs de vagues sur les instabilités à des fronts océaniques? Comment paramétrer ces phénomènes dans les modèles de circulation océaniques? Toutes ces questions restent ouvertes. Il est clair qu'une approche pluridisciplinaire telle que celle décrite dans cet exposé peut aider à résoudre ces problèmes.

Contents

List of Figures

Chapter 1

Introduction and Background

Contents

Close to 71 percent of the Earth's surface is covered by water. The ocean and atmosphere are continuously interacting, controlling both weather and climate through processes occurring at the interface between the two, the ocean surface. A shallow layer of water, the mixed layer, sits right below the surface, separating the atmosphere from the deeper ocean. Processes taking place in the vicinity of the surface plays a critical role in the transport processes between the atmosphere and the oceans. Some of these processes are presented conceptually in figure 1.1. Fluxes of energy, momentum, mass, moisture, heat and gases are critical components of the Earth's climate system, regulating geophysical cycles on Earth. Wind forcing drives waves and currents and heat exchange between the atmosphere and ocean while large-scale (mesoscale) atmospheric and oceanic circulation continuously interacts with smaller scales features (submesoscale) such as fronts (see e.g. figure 1.3 depicting enhanced breaking at the boundary of a small scale ocean front) or eddies.

The physical understanding of the processes occurring at the air-sea interface has a direct impact on global scale and climate modelling as those effects have to be properly parameterized. For example, it is now well accepted in the scientific community that a primary cause of climate and environmental change is the anthropogenic addition of greenhouse gases to the atmosphere which lead to increased atmospheric temperatures, melting glaciers and rising ocean temperatures, in turn producing sea level rise, and changes to terrestrial and oceanic ecosystems. Carbon dioxide (CO2) is one of those

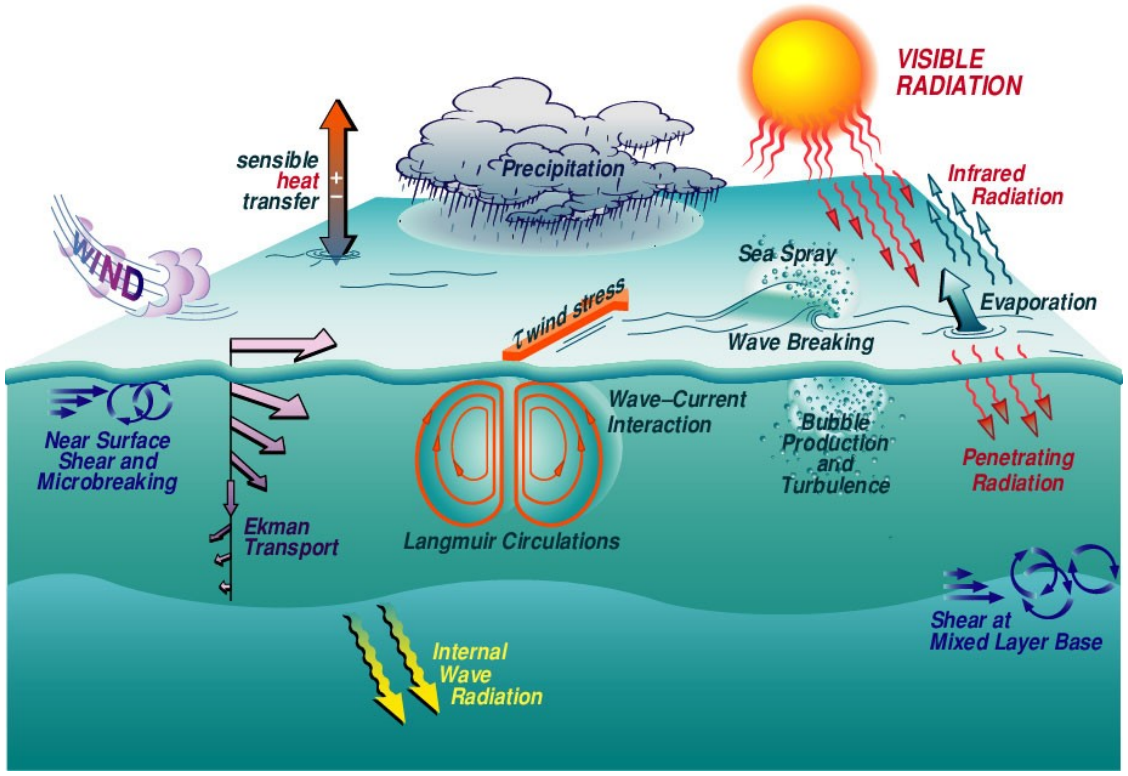

Figure 1.1: Processes of air-sea interactions (taken from the Coupled Boundary Layers, Air-Sea Interaction Experiment in Low to Moderate Winds (Edson et al., 2007)).

prominent greenhouse gas. The Intergovernmental Panel on Climate Change (IPCC) has estimated that approximately 40% of anthropogenic CO2 fluxes to the atmosphere in the 1990s were accumulating in the atmosphere, while the remainder was taken up by the terrestrial biosphere and the ocean in approximately equal proportions (Forster et al., 2007). While the accumulation in the atmosphere can be measured with some reasonable level of accuracy, The largest errors are found in characterizing the uptake by the terrestrial biosphere and ocean ($\approx$ 50% and 20%, respectively). Also note that both the terrestrial biosphere and ocean can be both sources and sinks of CO2 with the net transfers being the small difference, of the order of 1% (O(1%)) , between two large numbers. Of the three reservoirs for carbon, the atmosphere, the ocean and the terrestrial reservoir, the ocean is by far the largest, being approximately fourty times that of the atmosphere and ten times that of the land (Emerson and Hedges, 2008).

While this is the case, models of greenhouse gases fluxes between the atmosphere and the ocean, an essential component of climate change research, remain very simplistic, mostly lacking critical improved observations and parameterization of the processes

Figure 1.2: Instrumented Wave Glider (Liquid Robotics) during the Langmuir Cell DRI experiment in March 2017 off the coast of Southern California. Wind speed at that time was about 16 m/s with a significant wave height of 3.4m. Note the range of scales of breaking waves, and sprays and aerosols being sheered off the breakers (photo by Laurent Grare, SIO).

occurring at the ocean surface. To improve these models we need to better understand the fluxes of mass (gases and spray/aerosols), momentum and energy that occur throughout the marine atmospheric boundary layer and the the role that surface processes play in the coupling between the air and the ocean below.

1.1 Air-Sea Interaction and Surface Wave Processes

Over the last several decades, there has been growing recognition from both oceanographic and atmospheric sciences communities that surface waves play a crucial role in the processes by which the ocean and atmosphere interact. To better understand the coupling between the atmosphere and the ocean, and in turn to improve our understanding of air-sea fluxes of mass (e.g. gases, aerosols), momentum (e.g. generation of waves and currents) and energy (e.g. heat and kinetic energy for currents and mixing) in coupled ocean-atmosphere models, surface-wave processes must be taken into account.

For example, air-sea fluxes of momentum, represented by the drag coefficient C_d

have traditionally been correlated just with the wind speed at 10 meters, U_{10}, and the stability of the atmosphere above (described in the next section), but such correlations can only capture the physics when the surface wave field is "fully developed", and the wave variables are a function only of the atmospheric forcing (wind speed and stability). Otherwise, explicit measures of the state of development of the wave field need to be considered. These include the wave age, the ratio of the phase speed at the peak of the wave spectrum to U_{10} (or to u_* the friction velocity in the air, a more fundamental measure of the wind forcing), and an independent measure of the wave slope.

The physics of the coupling depends on the kinematics and dynamics of the wave field, including processes of wind-wave growth, nonlinear wave-wave interactions, wave-current interactions and wave dissipation, with the last generally considered dominated by breaking waves.

The theoretical foundations of wave generation by wind were established in the 1950s (Miles, 1957; Phillips, 1957), and nonlinear wave-wave interactions in the 1960s (Phillips, 1960; Hasselmann, 1962). Phillips (1957) focused on the turbulent pressure fluctuations over the waves. The Miles (1957) approach considered the interaction of the wave induced perturbations by the free surface, leaving turbulence only to support the wind velocity profile. However, it was not until 1985 that Phillips (1985) presented a rational statistical and dynamical framework for the inclusion of breaking in wind-wave models. Up until that time, models of wave dissipation in numerical wind-wave models had been heuristic and empirical.

The basic equation driving wind wave simulation is the "radiative transfer equation", usually written as

$$\frac{dN(\mathbf{x},\mathbf{k},t)}{dt} = \frac{S}{\sigma} = \frac{S_{in} + S_{nl} + S_{ds}}{\sigma}, \tag{1.1}$$

where

$$N = \frac{F(\mathbf{x},\mathbf{k},t)}{\sigma}, \tag{1.2}$$

$$\omega = \sigma + \mathbf{k}.\mathbf{U}, \tag{1.3}$$

$$\frac{\partial \mathbf{k}}{\partial t} + \nabla\omega = 0, \tag{1.4}$$

$$\sigma^2 = gk \tanh kh. \tag{1.5}$$

$\mathbf{x}$ is the horizontal position, $\mathbf{k}$ is the wavenumber, t is time, N is the wave action spectral density, g is gravity, $\sigma(k,h)$ is the intrinsic frequency, h is the water depth, $k = |\mathbf{k}|$, $\mathbf{k} \equiv (k,\theta)$, and $\mathbf{U}$ is the horizontal surface current (Komen et al., 1996, Section 1.2.8

through 1.2.10). S_{in}, S_{nl} and S_{ds} are the energy density "source terms" representing wave growth due to wind, nonlinear wave-wave interactions and dissipation, respectively.

The term F is the spectral density defined by

$$\left\langle \eta^2 \right\rangle \equiv \iint F(k,\theta) k dk d\theta, \tag{1.6}$$

where η is the sea surface displacement. Combination of the theoretical approach of the Miles critical layer theory with experimental measurements collected during field efforts in the early 1970's resulted in parameterizations of the wind-input source function that provide good results in operational wave models (Cavaleri et al., 2007).

Equation (1.1) can be expanded to

$$\frac{\partial N}{\partial t} + \nabla_x . \Big(\big(\mathbf{c_g} + \mathbf{U} \big) N \Big) - \nabla_k . \left(\nabla_x \omega \, N \right) = \frac{S}{\sigma}, \tag{1.7}$$

where $\mathbf{c}_g$ is the group velocity.

Following Komen et al. (1996), the general relationship to the characterize the evolution of the wave action density N can then be written as

$$\left(\frac{\partial}{\partial t} + \big(\mathbf{c_g} + \mathbf{U} \big) \frac{\partial}{\partial \mathbf{x}} - \left(\nabla_x \omega \right) . \frac{\partial}{\partial \mathbf{k}} \right) N = \frac{S}{\sigma}. \tag{1.8}$$

Note that the left hand side of the equation describes the propagation of the wave field in a non homogeneous medium. Assuming that the water depth is large enough, the current gradients are negligible, and $\mathbf{U}/\mathbf{c_g} \ll 1$, equation (1.8) reduces to the well-known energy balance equation written as

$$\left(\frac{\partial}{\partial t} + \mathbf{c_g} . \frac{\partial}{\partial \mathbf{x}} \right) F(\mathbf{x}, \mathbf{k}, t) = S_{in} + S_{nl} + S_{ds}. \tag{1.9}$$

To start resolving equation (1.9), Phillips (1985) suggests the development of an equilibrium model, such that

$$\frac{dN}{dt} = \frac{S_{in} + S_{ds} + S_{nl}}{\sigma} = 0 \tag{1.10}$$

for the spectrum built around the assumption that the nonlinear energy flux, wind forcing and energy dissipation from breaking waves are in *balance*, *proportional*, and of *similar magnitude*, i.e., $S_{ds} \propto S_{in} \propto S_{nl}$.

From there, Phillips introduces a statistical spectral description of breaking kinematics, $\Lambda(\mathbf{c}) d\mathbf{c}$, the mean length of breaking crests in the velocity range $(\mathbf{c}, \mathbf{c} + d\mathbf{c})$, which led to the prediction that $\Lambda(c) \propto c^{-6}$ in the equilibrium range defined above.

Figure 1.3: Enhanced breaking at the boundary of a front during the HIRES experiment in June 2010. Note the spatial variability in whitecap coverage density (see Romero et al. (2017) for details).

Note that the wave spectral energy dissipation due to breaking in equation (1.9) is related to the fifth moment of $\Lambda(\mathbf{c})$ by

$$\rho_w g S_{ds}(\mathbf{c}) d\mathbf{c} = \rho_w b g^{-1} \mathbf{c}^5 \Lambda(\mathbf{c}) d\mathbf{c}, \tag{1.11}$$

such that

$$S_{ds}(\mathbf{c}) = b g^{-2} \mathbf{c}^5 \Lambda(\mathbf{c}) d\mathbf{c}, \tag{1.12}$$

where b is the dimensionless breaking parameter (an implicit function of $\mathbf{c}$ or $\mathbf{k}$), which is a measure of the strength of breaking and $\mathbf{c}$ is the phase velocity of the breaking wave. The fourth moment of $\Lambda(\mathbf{c})$ gives the momentum flux lost from the wave field by breaking that is available to generate currents.

Of all the terms in equation (1.9), S_{ds} remains the one for which we have the least knowledge and understanding. It is expected to be dominated by breaking over most of the wind-wave spectrum and is the topic of active research.

Parameterization of wave growth input functions are key elements in the on-going exploration of energy, momentum and mass transport between the atmosphere and ocean. Full theories incorporating air-sea interaction and wave dynamics are explored in wave boundary layer models. Traditional models rely on bulk formulation and parameterizations based on empirical descriptions of the wind and wave state (Fairall et al., 1996, 2003; Taylor and Yelland, 2001) and numerically and analytically driven models (Janssen, 1991; Kudryavtsev et al., 1999, 2014) in an attempt to incorporate the wind-wave/wave-wind feedback present at the air-sea interface. The feedback is related to the partition between wave induced and turbulent momentum fluxes, which ultimately depends on the state of the wave field driven by the wind input (i.e. wave generation), evolution (i.e. wave-wave interaction) and dissipation due to wave breaking wave.

1.2 Surface Wave Effects on Upper Ocean Dynamics

Apart from the wave action balance equation described in the prior section, the coupling between the surface waves and the ocean boundary layer is dominated by breaking waves (a process through which most of the momentum and energy is transferred from waves into the water column) and the Stokes drift, u_s, defined as the contribution from the wave field to the mean Lagrangian velocity near the surface.

The Craik-Leibovich II (CLII) theory of Langmuir circulations[1], coherent streamwise vortical structures in the ocean boundary layer and aligned with the wind, introduces a vortex force which is the vector product of the Stokes drift of the wave field and the vorticity of the Eulerian current, $F_{\mathrm{v}} = u_s \times \omega_E$ where ω_E is the vorticity of the mean Eulerian flow (Craik and Leibovich, 1976). Figure 1.4 shows an example of the surface expression of Langmuir circulations. Their surface signature is described as windrows: lines of bubbles and foam aligned in the wind direction corresponding to the convergence zones between the vortices. In these zones, bubble clouds produced by breaking waves (or by rain) are concentrated, then carried downward, enhancing gas-exchange with the atmosphere. For deep-water surface gravity waves, the stokes drift is given by

$$\mathbf{u_s}(\mathbf{k}) = \frac{1}{\rho_w} \int \int F(\mathbf{k}) \frac{\mathbf{k}}{\sigma(\mathbf{k})} . \left[\frac{2k \; cosh \; 2k(z+h)}{sinh \; 2kh} \right] d\mathbf{k} \tag{1.13}$$

where F is the directional wave energy spectrum, $\mathbf{k}$ is the horizontal wavenumber, σ

[1] also called "Langmuir turbulence"

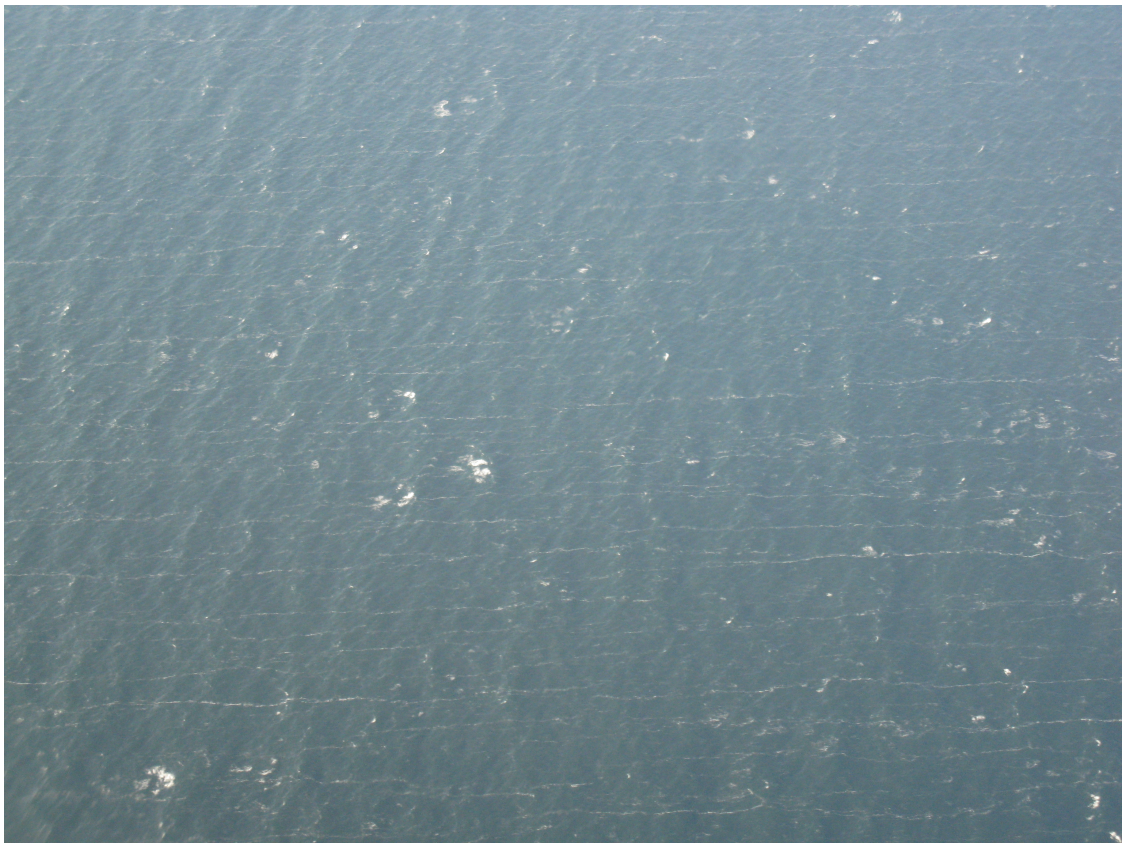

Figure 1.4: Photograph of foam streaks due to Langmuir circulations in Monterey Bay, on June 20 2010. Water depth is approximately 45m. (credit: Luc Lenain)

is the radial wave frequency and ρ_w is the density of water (Kenyon, 1969).

The Stokes drift also impacts the vertical mixing through the Stokes production of turbulent kinetic energy (TKE) (e.g. Kantha et al., 2010). Both observations and numerical simulations suggest that Langmuir Circulations (LC) can significantly enhance mixed layer deepening. Large Eddy Simulation LES studies from McWilliams et al. (1997), Skyllingstad et al. (2000), Sullivan et al. (2007) indicate that the buoyancy entrainment flux may be greatly enhanced by LC. They found that the mixed-layer depth is enhanced by the vortex force, reporting that the maximum entrainment flux was found to be two to five times larger in numerical simulations that included the vortex force. The detailed role of LC processes contributing to entrainment at the base of the mixed layer however remains an active area of research (Kukulka et al., 2010). Sullivan and McWilliams (2010) provide a very detailed review of both the numerical and experimental evidence of the effect of Stokes drift on upper ocean dynamics. The latter is discussed in Chapter

5 of this thesis, in the context of a very energetic storm, Tropical Cyclone Freda, and the LES simulation of Hurricane Frances performed by Sullivan et al. (2012). Ultimately, an accurate evaluation of the Stokes drift and related processes, and in turn the directional wave spectrum, leads to improved representation of surface physics in coupled air-sea models and general circulation models.

1.3 The Atmospheric Boundary Layer over the Ocean

The *atmospheric boundary layer* (ABL) is defined as the lowest layer of the atmosphere directly influenced by the surface of the earth (both land and ocean). The height of the ABL varies typically between 100m and 3 km and depends on the surface properties, the time of the day, the seasons and the synoptic weather conditions, typically responding to surface forcing with a timescale of one hour or less. Above this layer, we find the *Free Atmosphere* (FA). In this layer the wind is approximately geostrophic while the effects associated with the surface of the earth are negligible. The Marine Atmospheric Boundary Layer (MABL), is defined as the part of the troposphere directly influenced by the processes occurring at the ocean surface.

The idea of a boundary layer was first introduced in the early part of the 20th century by Ludwig Prandl. He focused on the flow past a rigid body, demonstrating that it could be split in multiple regions: a thin layer, connected to the solid body, containing all the viscous effect of the fluid interacting with the solid, and an outer region, above the viscous layer, considered inviscid.

The Reynolds Number, Re, is defined as the ratio between inertial and viscous forces. It is often used to describe relatively low viscosity flows (e.g. water and air). For large values of Re, the flow becomes fully turbulent. Therefore, flows over a rigid surface exhibit three distinct regions: an outer flow (assumed inviscid and turbulence free), a turbulent inner flow characterized by a high Re, and a very thin region directly at the surface known as the viscous sublayer, where Re is low and viscous effects are again relevant.

The vertical gradient of horizontal wind speed within the atmospheric boundary is traditionally described as a logarithmic profile, defined as

$$U(z) = \frac{u_*}{\kappa}\left(ln\left(\frac{z}{z_o}\right) - \psi(z, L)\right) \tag{1.14}$$

where $U(z)$ is the mean wind speed (m/s) at height z above the ground, u_* is the friction

velocity, κ is the von karman constant (approximately 0.41), z_o is the roughness length, $\psi(z, L)$ is the empirical stability function and L is the Monin-Obukhov length.

The Obukov length L, also referred to as the Monin-Obukov length, was first introduced by Obukhov to quantify the buoyancy effects on turbulent flows (Obukhov, 1971, , originally published in 1946). Obukov equated the pure shear production to the buoyant production to define L such that

$$L = \frac{u_*^3 \overline{\theta_v}}{g\kappa \overline{(w'\theta_v)}} \tag{1.15}$$

where $\overline{\theta_v}$ is the mean virtual potential temperature, $\overline{(w'\theta_v)}$ is the heat flux. The friction velocity u_* is defined as

$$u_* = (\overline{u'w'}^2 + \overline{v'w'}^2)^{1/4}, \tag{1.16}$$

where the covariances $\overline{u'w'}$ and $\overline{v'w'}$ represent the vertical momentum flux of u and v respectively. The Monin-Obukov length is a measure of the atmospheric stability: the atmosphere is considered stable if warm (less dense) air lies under a cold (denser) layer of air and stable in the opposite case. The term L is negative (positive) in stable (unstable) conditions.

Under stable stratification $z/L < 0$,

$$\psi(z/L) = 2ln\left(\frac{1+\Phi_m^{-1}}{2}\right) + ln\left(\frac{1+\Phi_m^{-2}}{2}\right) - 2tan^{-1}(\Phi_m^{-1}) + \pi/2, \tag{1.17}$$

where $\Phi_m(z/L) = (1 - c_- z/L)^{-1/4}$ and $c_- \approx 17$ (Jones and Toba, 2001).

For unstable conditions, $z/L > 0$,

$$\psi(z/L) = -c_+ \frac{z}{L}, \tag{1.18}$$

where $c_+ \approx 4.5$ (Jones and Toba, 2001).

Monin-Obukov similarity theory (MOS) states that turbulence statistics are universal functions of z/L implying that thermal and or mechanical sources of turbulent fluxes across the boundary layer can be stated purely in terms of z/L. MOS has been validated over land by several independent studies (e.g. Wyngaard and Coté, 1971). It is important to note that over the ocean, the MOS can only be applied above the direct influence of waves. This is because similarity arguments do not include wave-induced pressure and velocity perturbations (e.g. Edson et al., 1998).

1.4 Outline of the Dissertation

As shown earlier, surface waves play a crucial role in the processes through which the ocean and atmosphere interact. In this work, we generally attempt to characterize and at times quantify the influence of surface processes on the coupling between the ocean and the atmosphere.

In chapter 2, properties of the directional distributions of the surface wave field across the equilibrium-saturation ranges are investigated from airborne lidar data collected during the ONR SOCAL2013 experiment, conducted off the coast of Southern California in November 2013. During the field effort, detailed characterization of the marine atmospheric boundary layer was performed from R/P FLIP, moored at the center of the aircraft operational domain. The wind speed ranged from approximately 1-2 m/s to up to 11 m/s while the significant wave height varied from 0.8 to 2.5m during the 10 days of data collection considered in the analysis. In those measurements, the directional wavenumber spectrum shows a clear bimodal distribution, that extends well beyond what was reported in previous studies. Evolution of the transition across equilibrium-saturation ranges over a range of wind forcing conditions is shown and presented in the context of Phillips' (1985) model of the equilibrium range of wind-generated gravity waves. Based on the properties of the non-linear energy fluxes, wind stress and waves, a parameterization of the upper wavenumber limit of the equilibrium range is presented.

In chapter 3, we focus on another surface process affecting the coupling between the ocean and the atmosphere: The generation of sea-spray aerosols. Sea-spray aerosols represent a large fraction of the aerosols present in the maritime environment. Despite evidence of the importance of surface-wave and wave-breaking related processes in coupling the ocean with the atmosphere, sea-spray source generation functions are traditionally parameterized by the ten meter wind speed (U_{10}) alone. It is clear that unless the wind and wave field are fully developed, the source function will be a function of both wind and wave parameters. Breaking waves are also known to generate sea spray aerosol even in the absence of wind (e.g. surfzone), so it is not unexpected to be a combination of the two, wave and winds, in the deep ocean.

In this chapter, we analyzed aerosol data collected duting air-sea interaction experiment, the phased-resolved High-Resolution Air-Sea Interaction experiment (HIRES), conducted off the coast of Northern California in June 2010. Detailed measurements of aerosol number concentration in the Marine Atmospheric Boundary Layer (MABL), at altitudes ranging from as low as 30m and up to 800m above mean sea level (AMSL) over

a broad range of environmental conditions (significant wave height, H_s, of 2 to 4.5m, and U_{10} from 10 to 18 m/s) collected from an instrumented research aircraft, are presented. Aerosol number densities and volume are computed over a range of particle diameters from 0.1 to 200 μm, while the sea-surface conditions, including H_s, moments of the breaker length distribution, $\Lambda(c)$, and wave breaking dissipation, were measured by a suite of electro-optical sensors that included the NASA Airborne Topographic Mapper (ATM). The sea-state dependence of the aerosol concentration in the MABL is evident, stressing the need to incorporate wave parameters in the spray source generation functions that are traditionally parameterized by surface winds alone.

Another approach to improve our understanding of the role played by surface waves in the coupling between the ocean and the atmosphere is to use numerical models. Here we present Direct Numerical Simulations (DNS) of deep-water breaking waves generated in a numerical wave tank. Numerical simulations of a two-phase air-water flow have been implemented using the Open Source solver Gerris solving the full 2D Navier Stokes equations. Following the laboratory experiments of Rapp and Melville (1990), and Drazen and Melville (2009), we focused on the vertical mixing associated with a single breaking event by seeding the numerical domain with particles, in an attempt to reproduce the dye experiments of Rapp and Melville (1990). The aerosol size distribution produced by mechanically generated breaking waves is also discussed in the context of the laboratory studies of Veron et al. (2012) and Towle (2014). Challenges and limitations of this numerical code are discussed.

Finally, in chapter 5, we investigate the use of novel unmanned, autonomous surface vehicles to help us elucidate and improve our understanding of the coupling between the ocean and atmosphere in energetic storms, i.e. hurricanes and tropical cyclones. On December 31, 2012, an instrumented autonomous surface vehicle (Liquid Robotics Wave Glider) transiting across the Pacific from Hawaii to Australia as part of the PacX project came very close (46km) to the center of a category 3 tropical cyclone, TC Freda, experiencing winds of up to 37 m/s and significant wave heights close to 10m. The Wave Glider was instrumented for surface-ocean-lower-atmosphere (SOLA) measurements including atmospheric pressure, surface winds and temperature, sea surface temperature, salinity, dissolved oxygen, fluorescence (Chlorophyll-a and turbidity), and surface-wave directional spectra. Such measurements in close proximity to a tropical cyclone are rare. We present in this section novel observations of the ocean's response in three quadrants of TC Freda collected from the instrumented glider. Evolution of the wind, the directional wave field, the sea surface temperature and the Stokes drift profile (calculated from the

wave directional spectrum) as Freda passed near the vehicle are examined. Results are discussed in the context of the recent coupled wind-wave modeling and LES modeling of the marine boundary layer in hurricane Frances (Sullivan et al., 2012). Processes by which cold nutrient-rich waters are entrained and mixed from below into the mixed layer as the TC passes near the Wave Glider are presented and discussed. The results of this encounter of an autonomous surface vehicle with TC Freda demonstrate the usefulness of ASVs for regular TC (hurricane) monitoring to complement remote sensing and "hurricane hunter" aircraft missions.

CHAPTER 2

Measurements of the Directional Spectrum across the Equilibrium-Saturation Ranges of Wind-generated Surface Waves

Contents

2.1 Introduction

Until recently, most of the observational literature on surface waves was driven by studies based on time series of wave measurements at a point (or at a relatively slowly-moving mooring) combined with directional information from the dynamics of the moving (pitch-roll) buoy or measurement platform. The directional and frequency response of these systems is limited and not capable of the resolution required to fully test modern theories of directional surface-wave spectra. Additionally, Doppler shift induced by longer dominant waves can distort the high frequency portion of wave frequency spectra (Kitaigordskii et al., 1975; Banner, 1990).

It is only in the last two decades that observations of bimodal directional spectra at wavenumbers and frequencies higher than the spectral peak have been available to test numerical predictions (Banner and Young, 1994; Dysthe et al., 2003; Romero and Melville, 2010b; Romero et al., 2012). However, these observations are typically limited to wavenumbers and frequencies that are just a few multiples of the peak values (Hwang et al., 2000a,b; Romero and Melville, 2010a); most recently up to 25 times the peak wavenumber (Leckler et al., 2015). Directional observations at higher wavenumbers, those approaching wavelengths at the lower end of the gravity-wave range, are especially limited, but are important as the spectrum transitions into the shorter wavelengths that are of direct relevance for many aspects of air-sea interaction and the interpretation of many remote sensing techniques. Recent improvements in image processing techniques have lead to significant progress in our ability to better understand the spatio-temporal properties of short gravity waves, through stereo imagery (Leckler et al., 2015; Yurovskaya et al., 2013) or polarimetric techniques (Zappa et al., 2008), but these studies are generally limited to wavelengths shorter than a few meters, due to the small field of view generally considered. Also they are potentially affected by wave reflections from the platform or ship from which the measurements are collected.

Here we focus on directional wavenumber measurements of the surface-wave field extending from kilometer down to submeter scales using airborne topographic lidar. In recent years, the development of scanning lidars along with high-precision GPS and inertial motion units (GPS/IMU) has permitted airborne measurements of the sea surface elevation with swath widths of order 100 to 1000 m under the aircraft track (Hwang et al., 2000a; Romero and Melville, 2010a; Reineman et al., 2009; Melville et al., 2016), significantly improving our understanding of the physical regimes occurring over a broader range of wave scales.

The omnidirectional wavenumber spectrum $\Phi(k)$, where k is the wavenumber, computed by integrating azimuthally a directional wavenumber spectrum, $\phi(k,\theta)$, is traditionally described by a peak wavenumber, followed by a region approximately proportional to $k^{-5/2}$, or its frequency equivalent [1], ω^{-4}, where ω is the radial frequency, referred to as the *equilibrium* range. This region of the wave spectrum has been extensively studied, both through analytical, spatial and temporal observations (Donelan et al., 1985; Battjes et al., 1987; Hwang et al., 2000a; Romero and Melville, 2010a; Melville et al., 2016, among others) and numerical investigation (Pushkarev et al., 2003; Romero and Melville, 2010b, among others) of the wave field, more specifically of wind waves. Kitaigorodskii (1983), largely based on the pioneering work of Phillips (1958) and Kitaigorodskii (1962), suggested that the spectral form of the equilibrium range of the wind-wave spectrum was the direct consequence of a Kolmogoroff-type energy cascade from low to high frequency, combined with the existence of gravitational instabilities (breaking waves). Zakharov and Filonenko (1967) found a similar spectral shape by deriving a "wave turbulence" Kolmogoroff-type solution based on resonant interactions between weakly nonlinear surface gravity waves. In 1985, Phillips proposed a model of the equilibrium range, built around the assumption that the nonlinear energy flux, wind forcing and energy dissipation from breaking waves are in *balance*, *proportional*, and of *similar magnitude* (Phillips, 1985). His model also predicts a $k^{-5/2}$ spectral shape for the equilibrium range. It should also be noted that empirical parameterizations of this spectral region are also available (Toba, 1973; Resio et al., 2004).

Beyond the equilibrium range, spatial and temporal observations of wind waves as well as numerical studies show a power law transition from a $k^{-5/2}$ to a k^{-3} slope (Forristall, 1981; Banner, 1990; Romero and Melville, 2010a,b; Romero et al., 2012), corresponding to another regime, the *saturation* range. Here, the primary balance is between the wind input and the dissipation from breaking waves. Observational evidences of the transition between the equilibrium and saturation ranges are very limited, as a broadband wavenumber spectrum is needed to fully resolve both regimes.

In the present study, we investigate the properties of directional wavenumber spectra of surface gravity waves, including the transition from equilibrium to saturation ranges, collected in November 2013 off the coast of California from an airborne scanning lidar installed on a research aircraft. The experiment, instrumentation, environmental conditions and processing techniques are presented in section 2. Section 3 describes the directional properties of the wave field, including bi-modality, the transition from the equilibrium to

[1] based on the deep water dispersion relationship

the saturation ranges, and provides some insight on the contribution of the equilibrium range to the mean square slope, $\langle s^2 \rangle$, in the context of the seminal work of Cox and Munk (1954). Results are summarized in section 4.

2.2 Experiment

Data were collected during the SOCAL2013 experiment, an Office of Naval Research (ONR) funded project specifically designed to collect spatio-temporal, phased-resolved measurements of wind and waves over a broad range of environmental conditions. The experiment was located between San Clemente and San Nicholas Islands (33^o13.202′N, 118^o58.767′W) where R/P FLIP was moored, from November 7 to 22, 2013. R/P FLIP was instrumented with a suite of sensors described below to characterize the atmospheric, surface and subsurface conditions at the experiment site. A total of 7 research flights are considered in the analysis, corresponding to 19.2 hrs on station.

2.2.1 Sea Surface Topography

Spatio-temporal measurements of the sea surface topography and surface kinematics were collected from a Partenavia P68 aircraft instrumented with the Modular Aerial Sensing System (MASS), an instrument package developed at Scripps Institution of Oceanography (SIO) (Melville et al., 2016).

At the heart of the system, and of specific interest for this study, a Q680i waveform scanning lidar (Riegl, Austria) is used to make spatio-temporal measurements of the sea surface. The sensor has a maximum pulse repetition rate of 400 kHz, a maximum ±30° cross-heading raster scan rate of 200Hz, and has been used at altitudes up to 1500 m with good returns for surface-wave measurements. The theoretical swath width over water is typically proportional to the altitude of the aircraft[2], and its effective width is also dependent on the wind speed and sea state. More details are available in Melville et al. (2016) and Reineman et al. (2009), the latter presenting detailed performance analysis from an earlier version of the MASS.

The MASS is also equipped with a 14-bit, 640x512 QWIP FLIR SC6000 infrared camera operating up to a 126 Hz frame rate in the 8.0-9.2 μm band, to measure the ocean surface temperature field including modulations and gradients due to fronts, surface signatures of Langmuir circulation and wave breaking (Sutherland and Melville 2013). A

[2]The swath width is close to the aircraft altitude.

hyperspectral camera (SPECIM AisaEagle, Finland) operating in the 400-990 nm range (visible to near-IR) and a JaiPulnix (San Jose, CA USA) AB-800CL (3296px x 2472px) color (24 bit) video camera that operates at a frame rate up to 17 Hz are used to provide visible imagery of the kinematics of whitecaps (Melville and Matusov, 2002; Kleiss and Melville, 2010, 2011; Sutherland and Melville, 2013).

All data collected are carefully georeferenced from the aircraft to an earth coordinate frame using a Novatel SPAN-LN200; a very accurate GPS-IMU system combining GPS technology with an IMU using fiber-optic gyros and solid-state accelerometers to provide position and attitude data at up to 200 Hz. After differential GPS processing, using Waypoint Inertial Explorer software (Novatel Inc.), the stated accuracy for the instrument position is 0.01 m horizontal and 0.015 m (vertical), with attitude accuracies of 0.005°, 0.005°, and 0.008° for roll, pitch, and heading, respectively. A calibration-validation flight is conducted prior to and after each campaign to minimize boresight errors due to the misalignment between the GPS-IMU system and the lidar (Melville et al., 2016). Once calibrated, we typically find absolute vertical errors for the topographic product of 2 to 4 cm (per ping), estimated at 2.3 cm in the present study from the calibration flight conducted prior to and after the experiment.

2.2.2 Environmental Conditions

A suite of atmospheric sensors was installed on R/P FLIP's port boom to characterize the marine atmospheric boundary layer variables used in the analysis. Wind speed and direction were measured using an array of five sonic anemometers (four CSAT3 and one Gill R3-50) mounted on a vertical telescopic mast that was deployed from the end of the port boom of FLIP, ranging from approximately 15 down to 2.65 m above mean sea level (AMSL). The altitude above mean sea level varied during the course of the experiment, depending on environmental conditions (Grare et al., 2016) but were typically in the range of 2.6 to 4 m AMSL, for the lowest sensor, the Gill R3-50. The friction velocity in the air, u_*, is given by

$$u_* = (\overline{u'w'}^2 + \overline{v'w'}^2)^{1/4} \tag{2.1}$$

where the covariances $\overline{u'w'}$ and $\overline{v'w'}$ are computed over 30-min records from the average cospectra for (u', w') and (v', w').

The Gill sonic anemometer was preferred over the Campbell model to compute the friction velocity, following the recommendations of Grare et al. (2016) who demonstrated the better performances of this unit in varying wind directions. Nevertheless, we found

that during the research flights, all five sensors show consistent atmospheric friction velocity values, within 5−10%, implying that the measurements were collected in a constant stress layer. The wind speed at 10-m height, U_{10}, was extrapolated from the data collected at the closest measurement height, approximately 8.5m AMSL, assuming a constant flux layer with a logarithmic wind profile.

Figure 2.1(a) shows the time series of wind speed U_{10} in m/s and corresponding wind direction for the duration of the R/P FLIP deployment. Figure 2.1(d) shows the friction velocity u_* also in m/s for the same period of time. Note the gray areas corresponding to the times when the aircraft was collecting data in close proximity (i.e. <10km) to R/P FLIP. The wind speed, particularly variable over the duration of the experiment, ranged from approximately 1-2 m/s to up to 11 m/s. In addition, an array of five nadir-looking laser wave gauges (MDL ILM500), located on the three booms of FLIP, was used to sample the directional frequency spectrum of the sea surface elevation. All wave time series were corrected for FLIP's motion using a state of the art GPS-IMU: a Novatel SPAN-CPT mounted on the port boom. Figure 2.1(b) shows the spectrogram of the sea surface displacement computed for one of the wave gauges installed on the port boom. A series of short local wind events can be clearly seen, with peak energy slowly moving toward the lower frequency as the waves grow. The significant wave height, H_s, is shown in figure 2.1(c), ranging from 0.8 to up to 2.5m on November 16, 2013. The amplitude of the swell component in the spectra was found to be typically 1 to 2 orders of magnitude lower than the wind component. In the few cases considered in the analysis where the spectral amplitude of the swell component was larger than that of the wind, the swell and wind seas were approximately aligned.

2.2.3 Spectral Analysis

Surface elevation data collected from the MASS lidar were carefully georeferenced from aircraft to an earth-coordinate 3D point cloud. Ten-kilometer long swaths of data centered on R/P FLIP were gridded and interpolated on a regular grid, with the horizontal spatial resolution a function of the flight altitude: $dx = dy = 0.1m$ for aircraft altitude lower than 200m AMSL (typical swath width 50-150m), and $dx = dy = 1m$ for higher altitude (typical swath width of 200-800m). The data collected at the edge of the swath were discarded due to high dropout rates (<10-15% returns). Two-dimensional Fast Fourier Transforms were computed over 5km segments with 50% overlap. All segments were first detrended, tapered with a two-dimensional Hanning window and padded with ze-

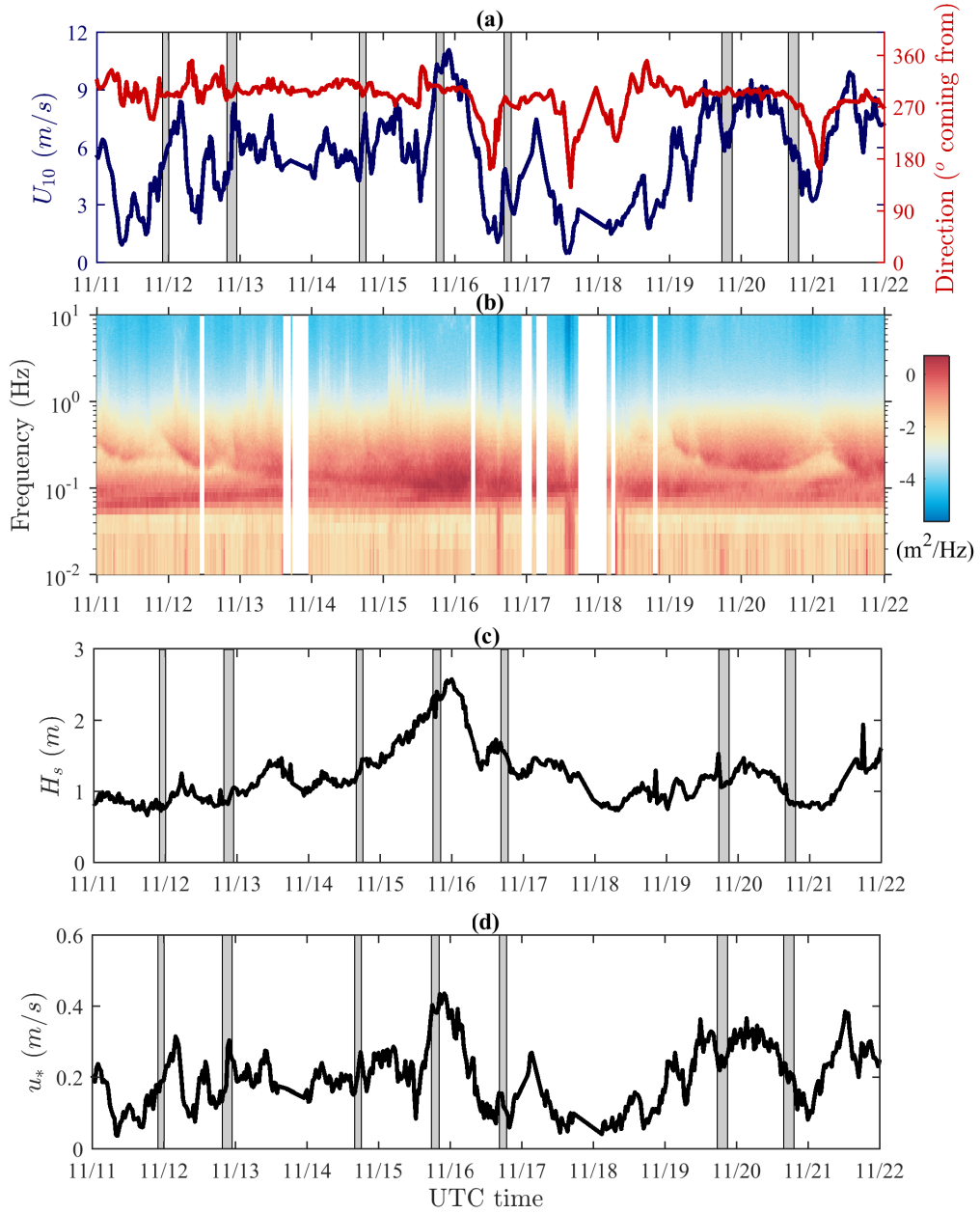

Figure 2.1: Environmental conditions collected from R/P FLIP during the SOCAL2013 Experiment: (a) U_{10} (dark blue line), wind direction (red line), (b) spectrogram of the surface displacement, (c) significant wave height H_s and (d) atmospheric friction velocity u_*. All data points are 30-min averages. The thick gray vertical lines represent the periods of time when the aircraft was on station.

ros (25%). To correct for the Doppler shift induced by the relative motion between the phase speed of the wave and the aircraft velocity, each spectrum was corrected iteratively following the method developed by Walsh et al. (1985). The change in wavenumber component in the along track direction is taken as

$$\delta k_x = \frac{\omega}{v_a} \tag{2.2}$$

where $\omega(k)$ (rad/s) is the radial wave frequency, computed from a deep-water dispersion relationship, and v_a (m/s) is the aircraft velocity in the along-track-direction.

2.2.4 Wind-Wave Modelling

Identifying the upper wavenumber limit of the equilibrium range (Phillips, 1985) is of obvious importance for wave modelling. Romero and Melville (2010b) and Romero et al. (2012) empirically defined this upper limit as a function of the zero-up crossing, k_u, of the azimuth-integrated non-linear energy fluxes based on the requirements of Phillips 1985's equilibrium model. In particular, Phillips requirement that all three "source" terms be proportional excludes zero crossings if any one term is sign-definite, as is dissipation. The present data set offers an unique opportunity to test this assumption, as the measured directional wavenumber spectrum extends from the equilibrium into the saturation range. Here, the non-linear wave-wave interaction source function, S_{nl}, is computed from the measured wave directional spectrum $\phi(k, \theta)$ using the so-called exact Webb-Resio-Tracy (WRT) method by Tracy and Resio (1982), based on the work by Webb (1978). We used the implementation from van Vledder (2006) used in WAVEWATCH III. Note that an αk^{-4} spectral tail (α a constant) was added to the directional spectrum for wavenumber, k, larger than k_m, the wavenumber corresponding to the measured noise floor, following the methodology described in Romero et al. (2012).

2.3 Results

2.3.1 Bimodal Structure of the Directional Wave Spectrum

An example of a directional spectrum $\phi(k, \theta)$ from a flight conducted on November 15, 2013, is shown in Figure 2.2. These data down to wavelengths of approximately 50 cm were acquired at a flight altitude of approximately 200m. For clarity, two versions of the same directional spectrum are shown (a) in linear wavenumber scale, only extending to 2

rad/m to highlight the bimodal distribution and (b) a logarithmic wavenumber scale plot showing the full wavenumber range of the measured spectrum, extending over almost 3 decades, up to 12 rad/m . The wind speed, U_{10}, collected from R/P FLIP was equal to 10.2 m/s at the time of the measurements.

The bimodal distribution of the directional wave spectrum for wavenumbers larger than the spectral peak has been measured in a number of past studies (Hwang et al., 2000b; Long and Resio, 2007; Romero and Melville, 2010a; Young, 2010). Romero and Melville (2010a) found the bimodal distribution to extend out to 4-5 times the peak wavenumber k_p, but were limited by the horizontal sampling resolution of the lidar they used. Similar results from a stereo imaging system installed on the Katsiveli platform (Black Sea coast of Crimea) were found recently by Leckler et al. (2015) where measurements of the bimodal distribution extended up to $k/k_p \approx 25$. In the present study, we find bimodal distributions extending up to $k/k_p \approx 100$, as shown in Figure 2.3, where the directional spectrum $\phi(k,\theta)$ is plotted against normalized azimuthal direction $\theta - \theta_p$, where θ_p is the peak direction. Here $k_p = 0.024\ rad/m$,while the bimodal peaks reach approximately $\pm\ 90^o$ at a wavenumber of approximately 3-4 rad/m and remain weakly bimodal for higher wavenumbers. To our knowledge, these are the first directional wave spectrum measurements over such a broad range of scales. We define the half azimuthal separation between the two lobes as

$$\theta_{lobe}(k) = \frac{|\theta_1 - \theta_2|}{2}, \tag{2.3}$$

where $\theta_1(k)$ and $\theta_2(k)$ are the azimuthal angles corresponding to the two maxima of the bimodal distribution.

Figure 2.4 shows the azimuthal separation $\theta_{lobe}(k)$ colorcoded for wave age, equal to c_p/u_*, where c_p is the peak phase velocity, as a function of k/k_p and the non-dimensional wavenumber $\hat{k} = ku_*^2/g$, following Phillips (1985) scaling of the upper limit of the equilibrium range (top and bottom panels respectively). Also shown are the measurements by Hwang et al. (2000b) (black triangle). Data from the GOTEX experiment (see Romero and Melville, 2010a, for details) are also plotted as solid lines with open circles.

While we find a lot of scatter in figure 2.4(a), the collapse of the data in (b) is remarkable. Here we fit the data over that range to the functional form

$$\theta_{lobe} = \theta_o + \gamma log(\hat{k}) \tag{2.4}$$

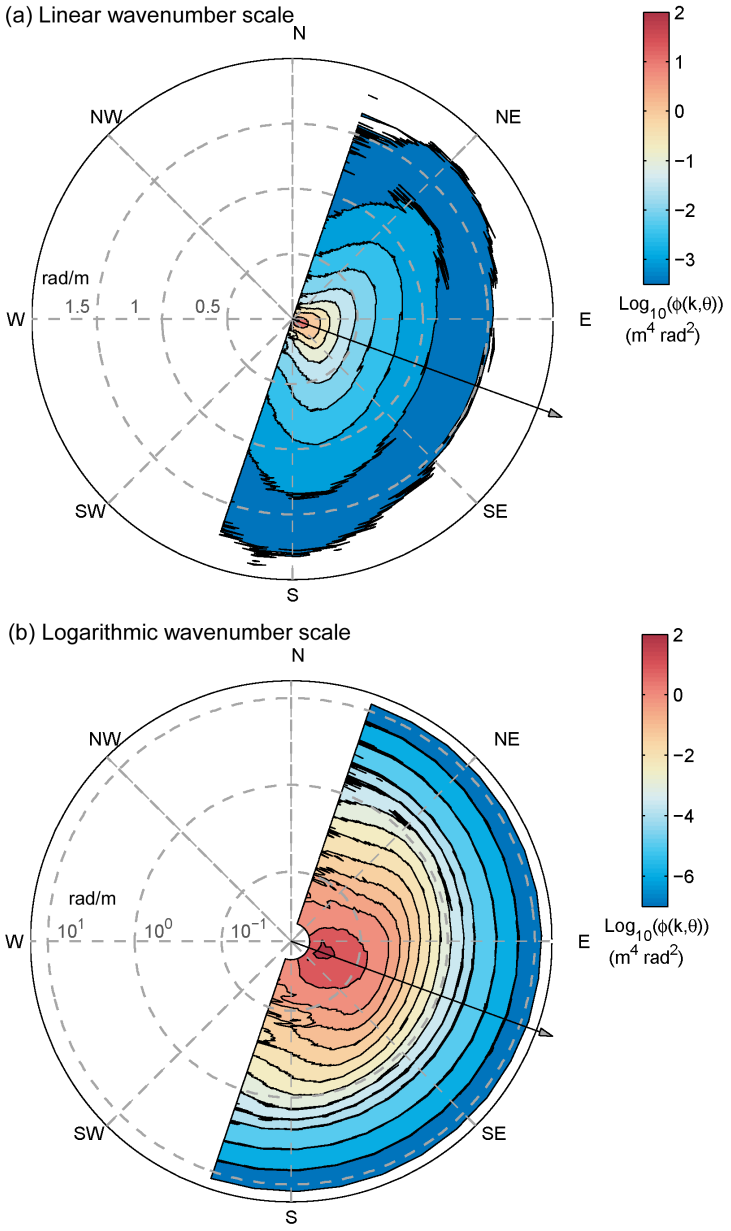

Figure 2.2: Sample directional wavenumber spectrum $\phi(k,\theta)$ collected on November 15 2013 during the SOCAL2013 experiment,(a) using a linear scale for the wavenumber k (rad/m), and (b) in logscale. Note the clear bimodal distribution, particularly evident in (a). The arrow represents the direction the waves at the peak wavenumber are *propagating*. The average wind speed U_{10}, collected on R/P FLIP, was equal to 10.2 m/s at the time of the flight. Note that for clarity, only a portion of the data, up to 1.5-2 rad/m, are shown in (a).

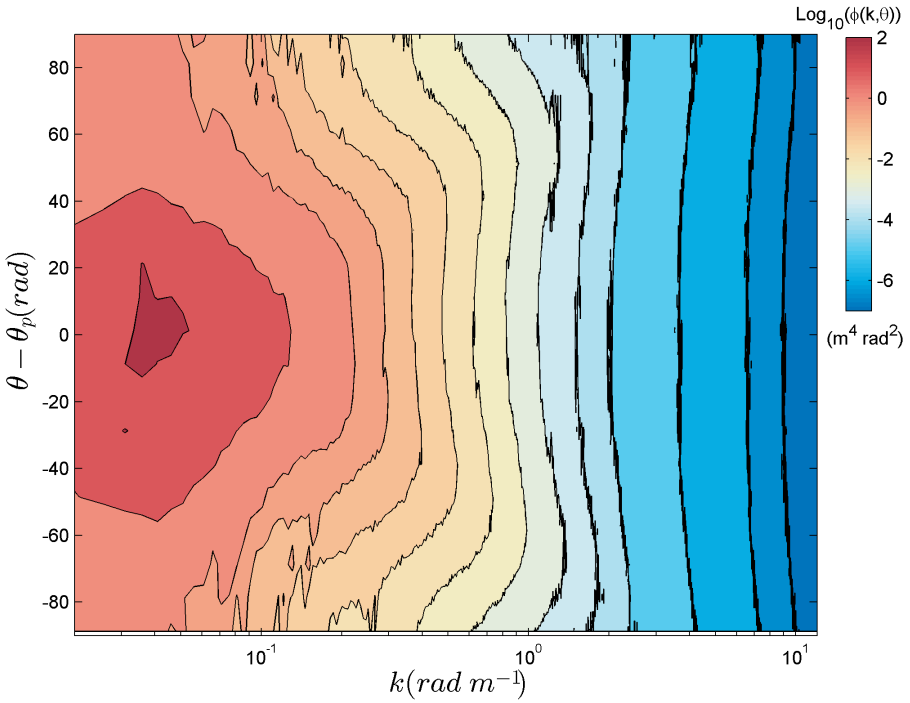

Figure 2.3: The same directional wavenumber spectrum $\phi(k,\theta)$ shown in figure 2.2 collected on November 15 2013 during the SOCAL2013 experiment, plotted against k and relative azimuthal direction $\theta - \theta_p$. Note the clear bimodal distribution extending up to the larger values of k. An isotropic spectrum would be depicted as a vertical contour line.

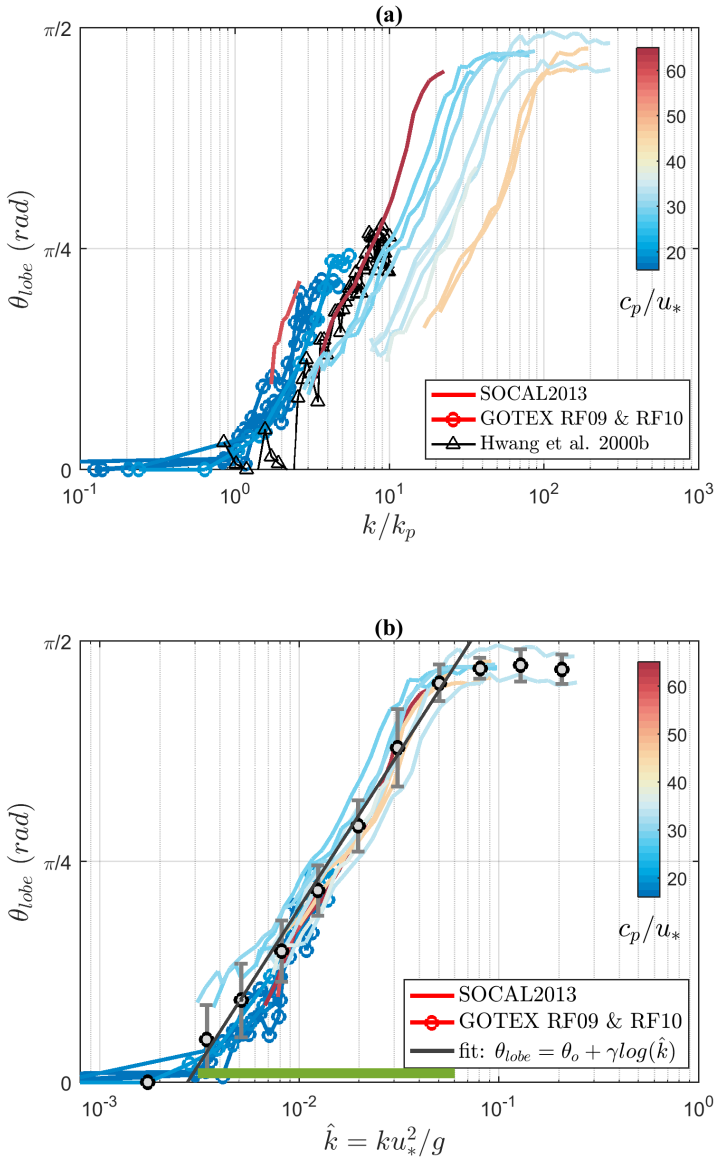

Figure 2.4: Bin averaged lobe separation θ_{lobe} plotted against (a) normalized wavenumber k/k_p and (b) non dimensional ku_*^2/g, colorcoded for wave age c_p/u_* for the SOCAL2013 (solid line) and GOTEX (solid line with circle) experiments. RF09 and RF10 represent two of the research flights conducted during GOTEX (Romero and Melville, 2010a). The black open triangle corresponds to the measurements by Hwang et al. (2000b). A power fit is also shown in (b), along with bin-averaged values of the lobe separation computed over the SOCAL2013 and GOTEX data sets (black circles) and corresponding error bars (one standard deviation). We find $r^2 = 0.96$ for the fit with $\theta_0 = 2.835$ and $\gamma = 0.48$. The range of validity of the fit is represented as a green horizontal bar.

$k\ (rad/m)$	0.01	0.05	0.1	0.5	1	10
$d\theta\ (rad)$	6.2	1.24	0.62	0.124	0.062	0.0062

Table 2.1: Directional resolution for selected wavenumbers.

with $\theta_0 = 2.835$ and $\gamma = 0.48$ ($r^2 = 0.96$), valid over the range $3\times10^{-3} < \hat{k} < 6\times10^{-2}$. The directional resolution of the bifurcation from a unimodal to a bimodal distribution in the neighborhood of $\hat{k} = 3 \times 10^{-3}$ and to $\theta_{lobe} = \pi/2$ in the neighborhood of $\hat{k} = 6 \times 10^{-2}$ is not sufficient to posit a functional form resolving these areas.

The lack of collapse of the azimuthal separation plotted against k/k_p is likely associated with other processes involved in the evolution of the longer wavelength portion of the spectrum (e.g. non-linear wave-wave interactions) and measurement errors in estimating k_p.[3]

Also recall that the cross-track swath width is much shorter than the along-track, effectively reducing the azimuthal directional resolution $d\theta$ we can achieve for the longer waves of our spectra. Following Romero and Melville (2010a), we compute $d\theta$ as

$$d\theta = \frac{dk_2}{k}, \tag{2.5}$$

where dk_2 is the spectral resolution in the cross-track direction. Values of $d\theta$ for representative wavenumbers are shown in table 2.1. The lack of sufficient directional resolution for the lowest wavenumbers, i.e. $\hat{k} < 2 - 4 \times 10^{-3}$ makes the identification of a bimodal distribution for this range of wavenumbers particularly difficult.

Overall, we find that the half azimuthal separation extends well beyond what was reported in previous studies, reaching close to $\pi/2$ for the highest wavenumbers, right at the limit of what we can azimuthally resolve in the present data set. This effectively implies that waves propagating in opposing directions can be found at scales of wavenumbers around 10-12 rad/m, or 10-11 rad/s for linear gravity waves in the frequency domain. The existence of such wave systems has been argued to be a leading mechanism through which microseismic noise is generated (Longuet-Higgins, 1950; Ardhuin et al., 2015). Space-time measurements of the evolution of the wave field are needed to explore this topic further.

The average amplitude of the lobes relative to the spectral energy in the dominant wave direction $r_{lobe}(k)$ is defined as

[3]The horizontal offset is driven by k_p.

$$r_{lobe}(k) = \frac{\phi(k,\theta_1) + \phi(k,\theta_2)}{2\phi(k,0)}. \tag{2.6}$$

Figure 2.5(a) shows the measured $r_{lobe}(k/k_p)$ colorcoded for wave age for the SOCAL2013 (solid line) and GOTEX (solid line with circle) experiments. The black open triangle corresponds to the measurements by Hwang et al. (2000b). We find that r_{lobe} generally increases as a function of k/k_p, reaching $r_{lobe} \approx 2$, with a few cases showing an amplitude reduction after reaching the maxima.

Figure 2.5(b) shows $r_{lobe}(k)$ for the SOCAL2013 (solid line) and GOTEX (solid line with circle) experiments colorcoded for wave age, plotted against $\hat{k} = ku_*^2/g$. The set of curves we obtain are better collapsed than in Figure 2.5(a), but more work is needed to explain the remaining scatter.

2.3.2 Azimuthally Integrated Wave Spectrum Properties

Figure 2.6 shows the azimuthally integrated omnidirectional spectrum computed from the directional spectrum presented in figure 2.2. The separation at wavenumber k_n of the spectral slopes into -2.5 (equilibrium) and -3 (saturation) regions is clear with $k_n = 0.6$ rad/m in this specific example. The first region corresponds to the equilibrium range while the second is traditionally referred to as the saturation range (e.g. Banner et al., 1989; Banner, 1990; Hwang et al., 2000a,b; Romero and Melville, 2010a). Phillips (1985) proposed a model of the equilibrium range, based on the assumption of balance, proportionality and similar order of magnitude of the terms in the radiative transfer equation, namely the wave-wave interactions, wind forcing and wave-breaking dissipation. His model, and others, predicts a $k^{-5/2}$ slope for the equilibrium range of the omnidirectional spectrum, in agreement with the present measurements.

Figure 2.7 shows the frequency spectrum computed from a nadir looking lidar altimeter installed on FLIP's port boom at the same time and location the airborne lidar data shown in figure 2.6 were collected. The equilibrium and saturation ranges identified from the wavenumber spectrum are shown in red and blue, for reference, as well as the peak and transition frequencies, f_p and f_n, computed from k_p and k_n, assuming the deep-water dispersion relationship. While the transition is obvious in the wavenumber spectrum, the frequency spectrum does not exhibit any clear change of slope between the two regimes.

Temporal point measurements are more likely to be influenced by the Doppler shift caused by the orbital motions of longer waves on the shorter waves (Kitaigordskii et al., 1975; Banner, 1990). A vertical gradient of horizontal velocity close to the surface

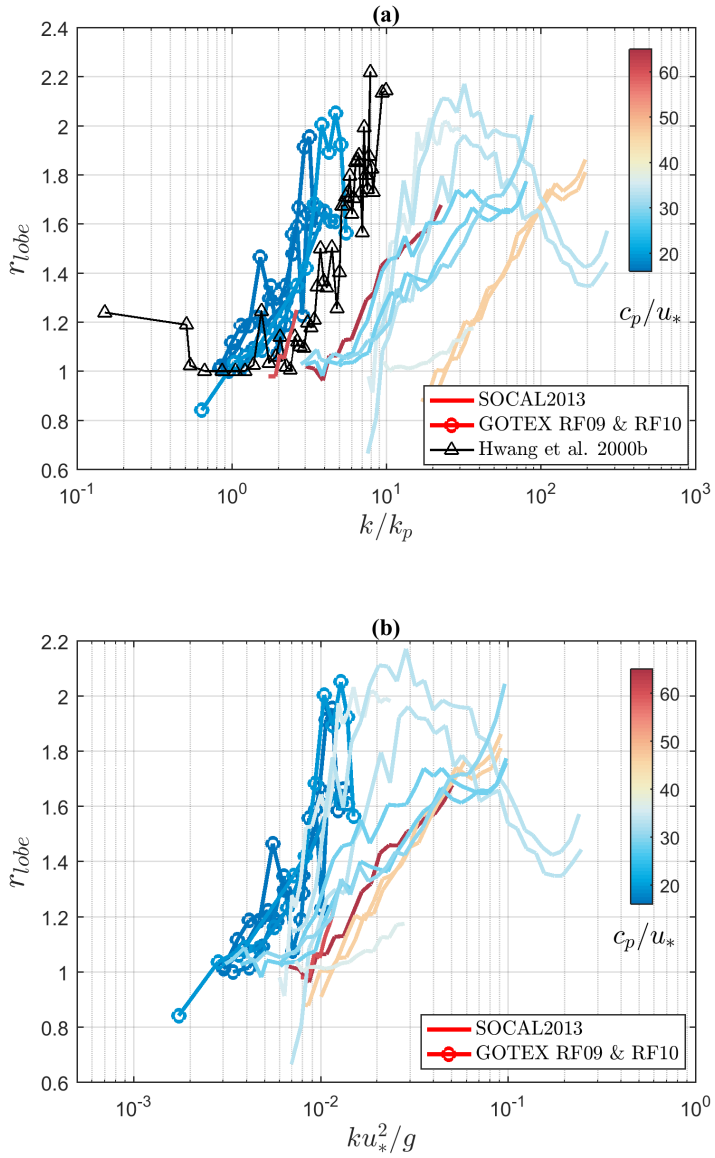

Figure 2.5: Bin averaged relative lobe amplitude r_{lobe} plotted against (a) normalized wavenumber k/k_p and (b) non dimensional ku_*^2/g, colorcoded for wave age c_p/u_* for the SOCAL2013 (solid line) and GOTEX (solid line with circle) experiments. The black open triangle corresponds to the measurements by Hwang et al. (2000b).

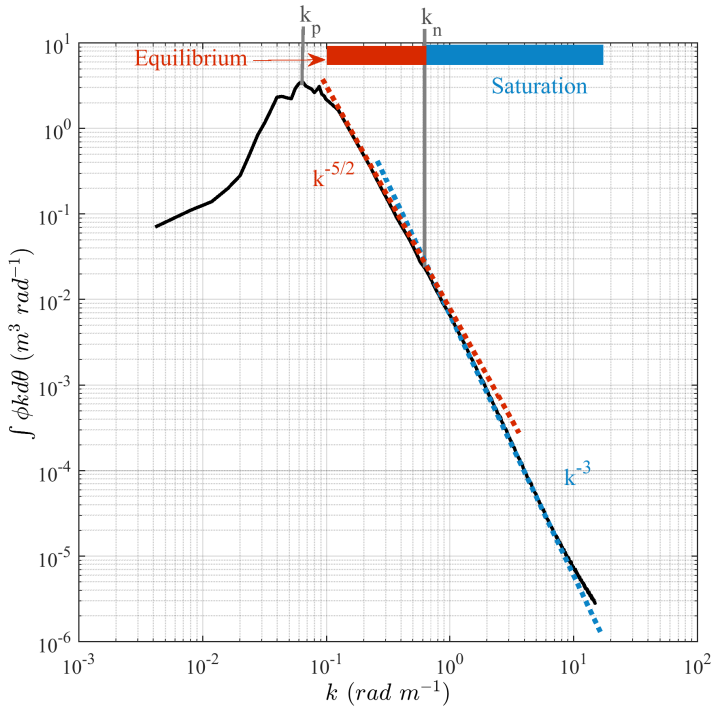

Figure 2.6: Sample omnidirectional wavenumber spectrum collected on November 15 2013 during the SOCAL2013 experiment. Note the -5/2 and -3 spectral slopes, and the three-decade bandwidth of the data.

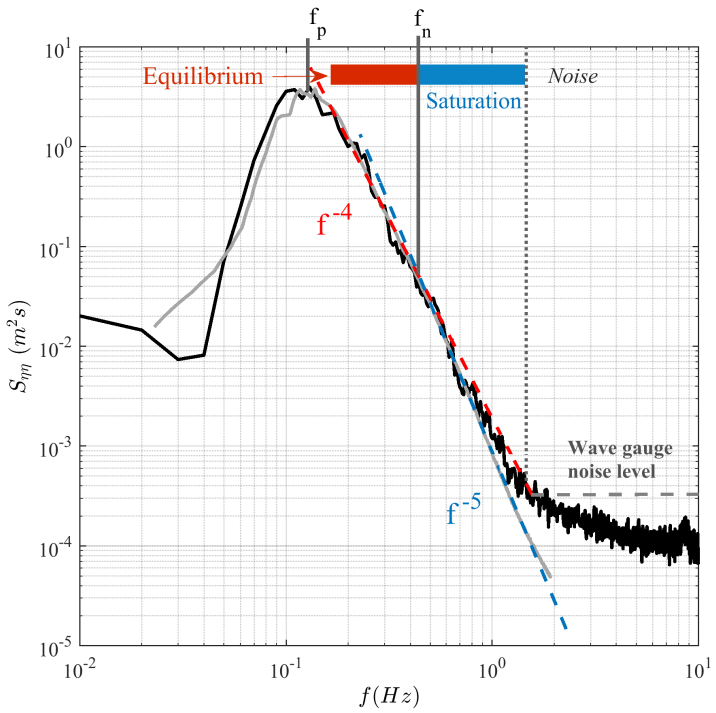

Figure 2.7: Wave frequency spectrum (black) computed from wave gauge installed on one of R/P FLIP's booms at the time when the airborne lidar data shown in figure 2.6 were collected, on November 15 2015, along with the frequency spectrum (using the linear dispersion relationship) computed from the directional wavenumber spectrum (gray) used to generate figure 2.6. Also shown are the saturation and equilibrium ranges, determined from the wavenumber spectrum. While obvious in figure 2.6, and in its frequency spectrum equivalent, the transition from a f^{-4} to f^{-5} behavior is not discernable in the frequency spectrum computed from the laser wave gauge on FLIP.

leads to Doppler effects of varying amplitude as a function of frequency (i.e. penetration depth), and therefore has the potential to change the slope of the wave frequency spectrum. Additionally, frequency spectra measured from single point wave gauges or buoys are generally noisier, making it harder to identify slope behavior. To illustrate this effect, we also show in figure 2.7 the frequency spectrum computed from the measured directional wavenumber spectrum (gray solid line) assuming the deep-water dispersion relationship, following Phillips (1985), where the frequency spectrum $S(\omega)$ is defined as

$$S(\omega) = 2g^{-1/2} \int_{-\pi}^{\pi} \left[k^{3/2} \phi(k, \theta) \right]_{k=\omega^2/g} d\theta. \tag{2.7}$$

This time the transition from a f^{-4} to f^{-5} power law is evident. This result reiterates the more fundamental nature of the spatial measurements of the wave field for elucidating the dynamics, as compared to the traditional parameterization of the wave field based on single point, temporal measurements from wave gauges or buoys.

Figure 2.8 shows wavenumber omnidirectional spectra colorcoded for $u_*/\sqrt{gH_s}$ collected during the SOCAL experiment. The term $u_*/\sqrt{gH_s}$ is a non-dimensional quantity corresponding to the atmospheric friction velocity scaled by the velocity $\sqrt{gH_s}$, the speed at impact of a particle following a ballistic trajectory from a height $H_s/2$. This quantity has been used to parameterize wave breaking dissipation (Drazen et al., 2008), whitecap coverage (Sutherland and Melville, 2013) and more recently air entrainment by breaking waves (Deike et al., 2016). This definition was preferred to the more traditionally used wave age, equal to c_p/u_*, as c_p, the peak phase velocity, is often difficult to characterize, especially in the conditions we experienced during the experiment (a mix of swell and wind waves coming from multiple directions). Also note that in fetch limited conditions, $c_p \propto \sqrt{gH_s}$.

We find that as $u_*/\sqrt{gH_s}$ increases, the transition between equilibrium and saturation ranges is reached at lower wavenumbers, as Phillips suggested for decreasing wave age (Phillips, 1985).

2.3.3 Scaling of the Saturation Spectrum by the Friction Velocity

We introduce the azimuth-integrated saturation spectrum, $B(k)$, defined as

$$B(k) = \int \phi k^4 d\theta. \tag{2.8}$$

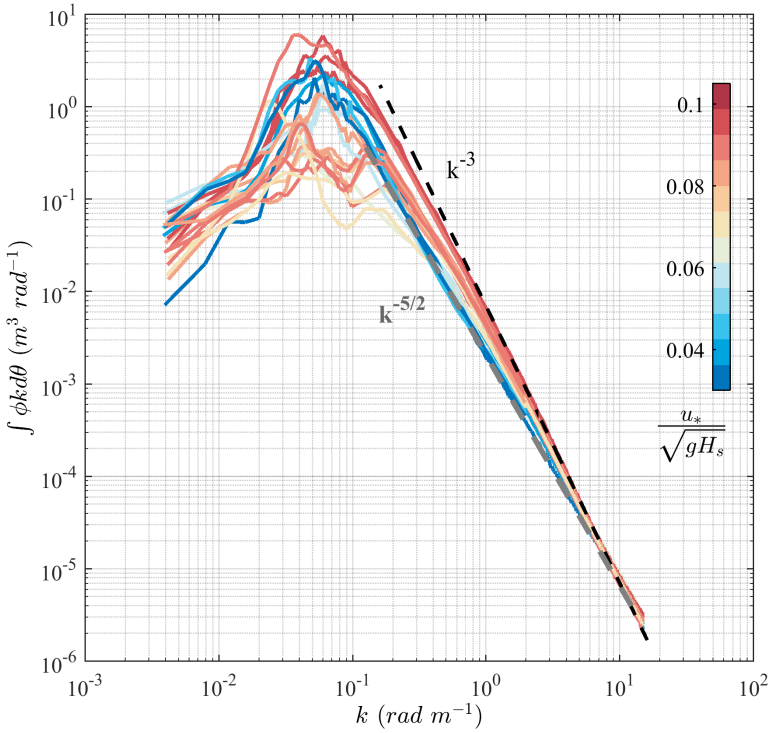

Figure 2.8: Omnidirectional spectra collected during the SOCAL2013 experiment, colorcoded for the ratio $\frac{u_*}{\sqrt{gH_s}}$.

The saturation spectra $B(k)$, colorcoded for $u_*/\sqrt{gH_s}$, computed from the directional wave spectra collected during the experiment are shown in Figure 2.9. Spectral levels in the equilibrium and saturation ranges are increasing as a function of $u_*/\sqrt{gH_s}$, converging to a constant saturation level around 7 rad/m then increasing for the highest wavenumbers, up to 12-13 rad/m. This level increase beyond 7 rad/m could be physical as other studies have predicted an increase of the saturation level for this range of wavenumbers. However, since it is also near the limit of the spatial resolution of the measurements it could also be measurement noise. A subset of these saturation spectra is shown in figure 2.10, this time colorcoded for the wind speed, U_{10}, to compare the spectral saturation levels to past studies and numerical parameterization of the *omnidirectional* saturation spectrum. Here we show results from stereo-imagery field measurements (Banner et al., 1989; Yurovskaya et al., 2013, Veron et al. 2017, manuscript in preparation), imaging slope gauge data collected in a laboratory experiment (Jähne and Riemer, 1990), an empirical formulation based on field measurements from a wave gauge array (Hwang, 2005) and numerical parameterization (Elfouhaily et al., 1997). While we find a lot of scatter between all these studies, the spectral levels found in the present study are generally within the range of other data sets. The equilibrium range levels are consistent with the Elfouhaily et al. (1997) model for the larger wind speeds and Hwang (2005) for the intermediate wind speeds (U_{10} = 5.8 m/s). The spectral levels in the saturation range are within the scatter of the other studies. Note the increase in B found for $k > 7\ rad/m$, stressing the need for field measurements of saturation spectra at higher wavenumbers.

The saturation spectra presented in figure 2.9 are shown in figure 2.11, also colorcoded for $u_*/\sqrt{gH_s}$, but this time as a function of the non-dimensional wavenumber $\hat{k}$, following Phillips (1985) scaling of the upper limit of the equilibrium range. He defines

$$k_n = rg/u_*^2, \tag{2.9}$$

where r is a constant [4]. The saturation spectra collapse for non-dimensional wavenumbers $\hat{k}$ above 2×10^{-3}, both in the equilibrium ($\hat{k}^{-1/2}$, extending to $\hat{k} \approx 10^{-2}$) and saturation ranges. The transition wavenumber, k_n, is computed for each saturation spectrum, estimating iteratively the intersect between a $k^{-1/2}$ fit in the equilibrium range and a constant saturation value at higher wavenumbers.

Figure 2.12 shows k_n plotted against $u_*/\sqrt{gH_s}$, along with a quadratic fit of the data

[4] r is assumed constant for fully developed seas in Phillips (1985)

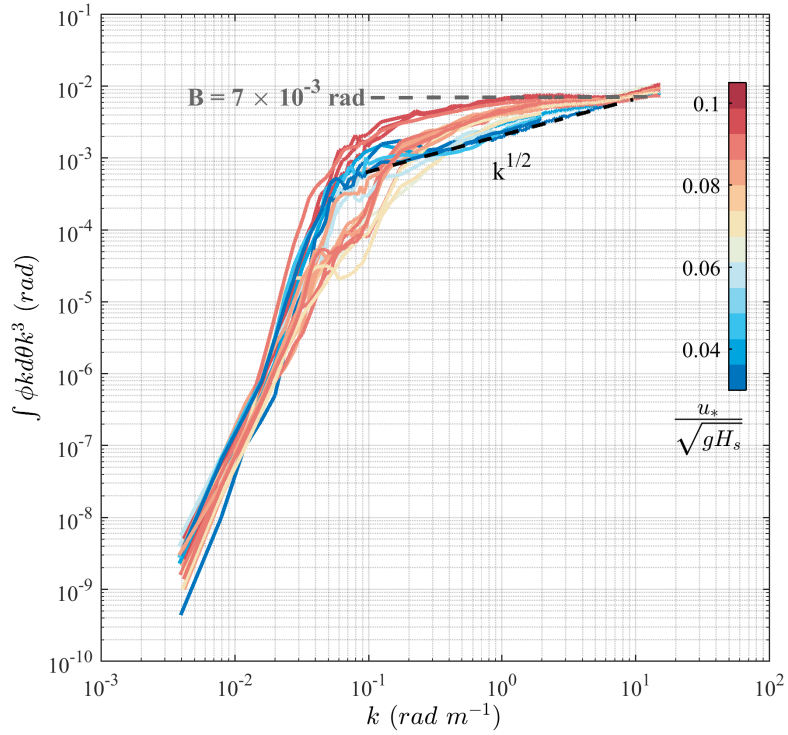

Figure 2.9: Azimuth-integrated saturation spectra $B(k) = \int \phi k^4 d\theta$, collected during the SO-CAL2013 experiment; the curves are colorcoded for the the ratio $\frac{u_*}{\sqrt{gH_s}}$.

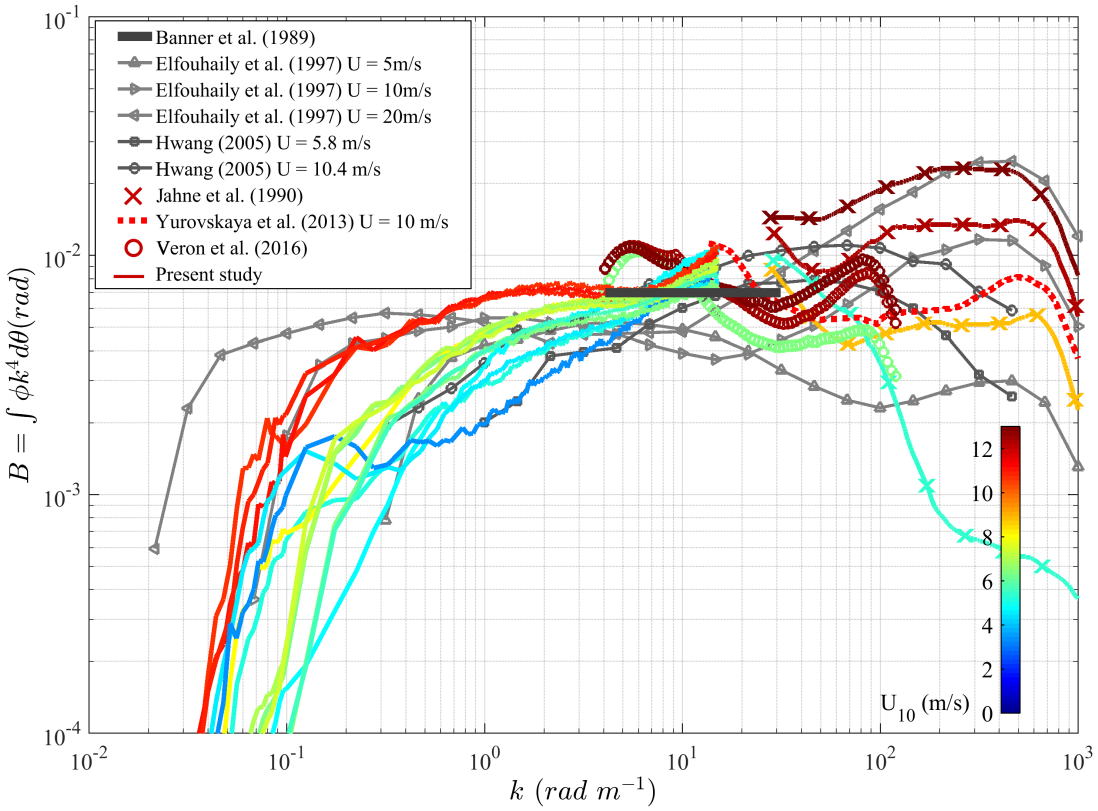

Figure 2.10: Azimuth-integrated saturation spectra $B(k) = \int \phi k^4 d\theta$, collected during the SO-CAL2013 experiment (solid lines) colorcoded for the wind speed U_{10} along with results from past observational and modelling studies.

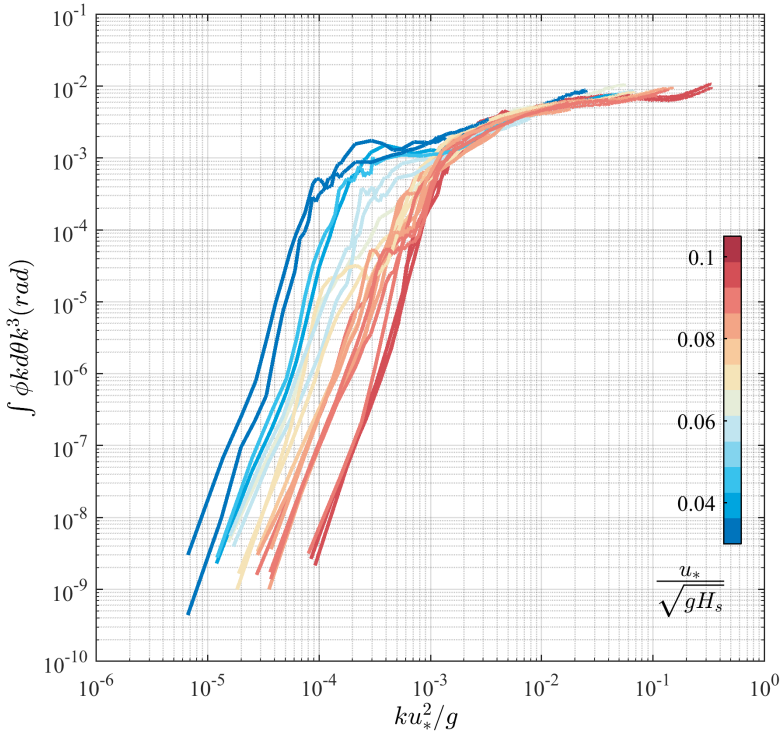

Figure 2.11: Azimuth-integrated saturation spectra $B(k) = \int \phi k^4 d\theta$ plotted against $\hat{k} = ku_*^2/g$. The curves are colorcoded for the the ratio $\frac{u_*}{\sqrt{gH_s}}$. Note the collapse of the spectra for the larger values of $\hat{k}$.

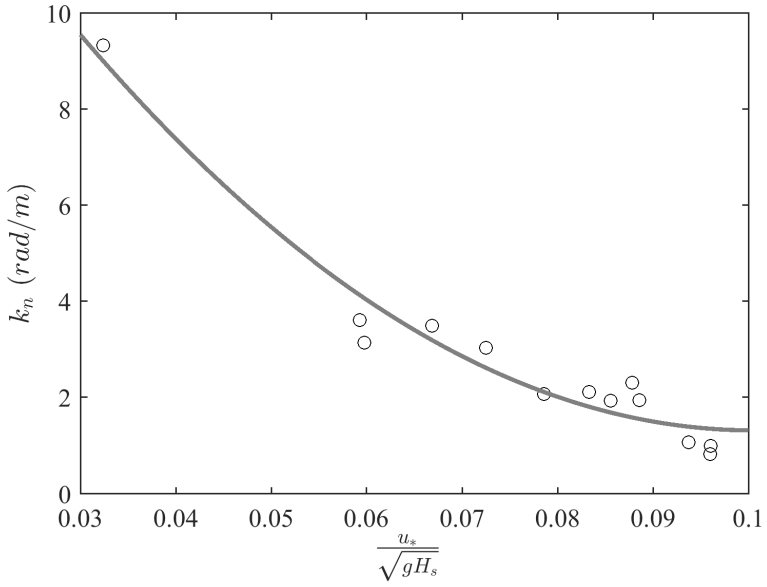

Figure 2.12: The transition wavenumber k_n plotted against $\frac{u_*}{\sqrt{gH_s}}$.

that gives

$$k_n = \Gamma_1 \left(u_* / \sqrt{gH_s}\right)^2 - \Gamma_2 \left(u_* / \sqrt{gH_s}\right) + \Gamma_3 \tag{2.10}$$

where $\Gamma_1 = 1.7 \times 10^3$, $\Gamma_2 = -3.3 \times 10^2$, and $\Gamma_3 = 18$ ($r^2 = 0.94$).

We introduce here the non-dimensional fetch χ^*, computed from the empirical formulation of Kahma and Calkoen (1992):

$$\chi^* = g\chi / u_*^2, \tag{2.11}$$

where χ is the fetch. Using the unstable stratification formulation based on the dimensionless peak frequency $\omega_p^* = 2\pi f_p u_* / g$,

$$\omega_p^* = 3.755 \left(\chi^*\right)^{-0.287}. \tag{2.12}$$

Eddy flux measurements collected on R/P FLIP (Grare et al. 2017, manuscript in preparation), showed the atmosphere to be unstable at the time and location where the data were collected.

We find r to vary between 0.01 and 0.025, a factor of 2.5, over the range of wave ages experienced during the field effort (Figure 2.13), $30 < c_p/u_* < 120$. The term r remains also approximately constant as a function of non-dimensional fetch. Since identifying

an appropriate phase speed, c_p, is challenging and typically requires strong assumptions, c_p is computed in two ways: from the in-situ lidar measurements collected on R/P FLIP based on the wind-wave frequency spectrum peak (labeled as "wind waves only") and from the peak frequency (labeled as "full spectrum").

2.3.4 Non-linear Energy Fluxes in Equilibrium and Saturation Ranges

The non-linear term S_{nl} of the radiative transport equation was computed from the measured directional wavenumber spectra assimilated into WaveWatch III using the implementation from van Vledder (2006). An example is shown in figure 2.14. The black arrow in the figure corresponds to the direction the waves are *propagating*. S_{nl} is positive over the measured range of azimuth and wavenumber, but in the peak direction of wave propagation, for $k \approx 1 - 4 \times 10^{-1}$, S_{nl} is found to be negative. Along the same direction, for lower and higher wavenumbers, the same term is positive. The evolution of S_{nl} is consistent with the work of Romero and Melville (2010a) and Romero et al. (2012), where k_n was defined as a function of the zero-up crossing k_u of the azimuth-integrated non-linear energy fluxes S_{nl}. This was motivated in part by Phillips' (1985) equilibrium argument, which by assuming that the three source terms were all proportional can not include zero crossings in the nonlinear term since the wind input, under Phillips assumptions, was positive definite [5]. The three-lobe structure found in the non-linear term S_{nl} is a direct consequence of the need to conserve both the *energy* and *action* (see Komen et al., 1996, p. 184-185 of Janssen, "The Interaction of Ocean Waves and Wind", for details). Figure 2.15 shows k_n plotted against its corresponding k_u, colorcoded for u_*. Two reference dashed lines are also shown, in blue, $k_n = 2k_u$, and in gray $k_n = k_u$. For larger values of u_*, k_n is close to twice the zero-up crossing wavenumber, decreasing to a range between 1-2 $\times k_u$ as u_* decreases below 0.3 m/s.

The dependence of the ratio k_n/k_u over wave age is shown in Figure 2.16(a). Here the wave age is computed using the peak wavenumber k_p. We find that the ratio is decreasing with wave age. A quadratic fit of the data gives:

$$\frac{k_n}{k_u} = a_1 \left(\frac{c_p}{u_*}\right)^2 + a_2 \left(\frac{c_p}{u_*}\right) + a_3, \tag{2.13}$$

where $a_1 = 1.36 \times 10^{-4}$, $a_2 = -2.89 \times 10^{-2}$, and $a_3 = 2.43$.

[5] If considering swell as well as wind waves, then the wind input term can be negative since momentum can be transferred from the waves to the wind (Hanley et al., 2010).

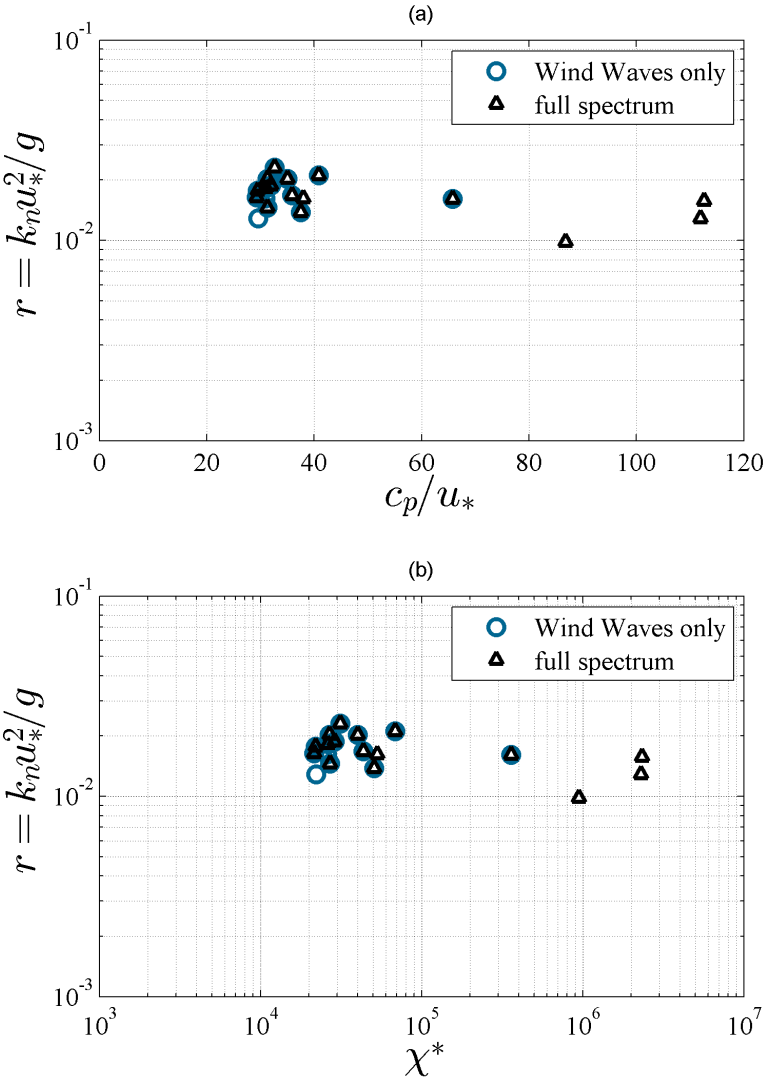

Figure 2.13: The nondimensional transition wavenumber $k_n u_*^2/g$ plotted versus wave age c_p/u_* and the non-dimensional fetch χ^*.

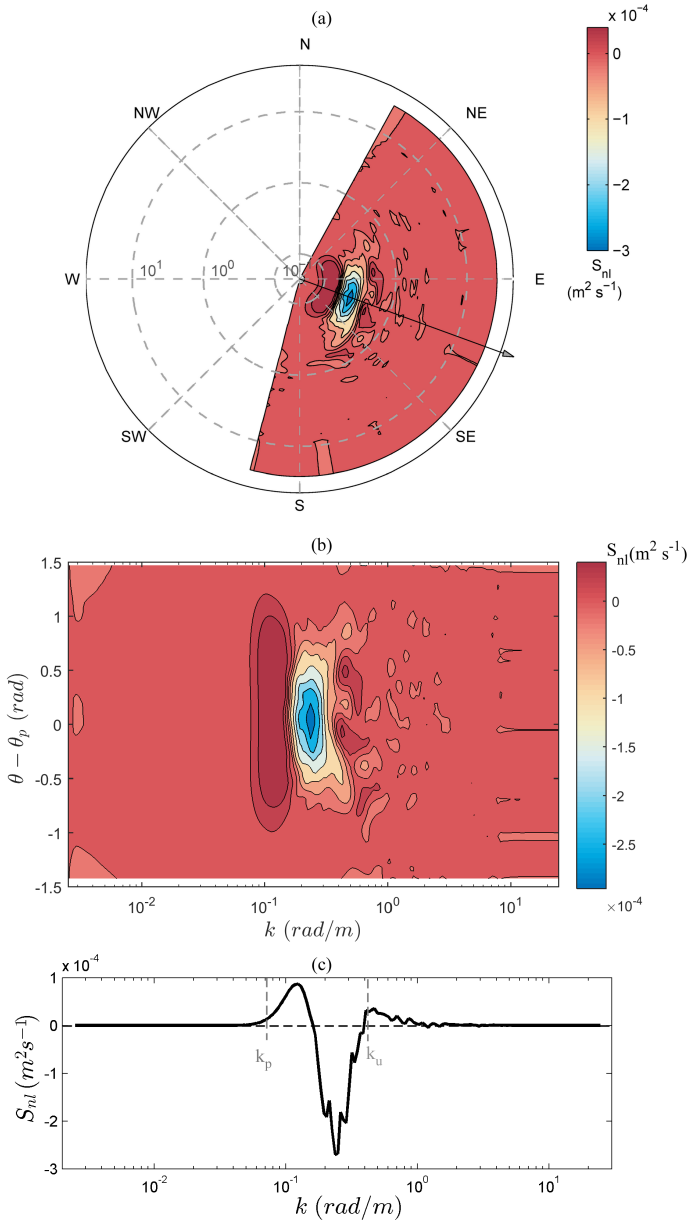

Figure 2.14: Non-linear term S_{nl} of the radiative transport equation computed from the directional wavenumber spectrum shown in figure 2.2 displayed in polar coordinates in (a) and plotted against k and $\theta - \theta_p$ in (b). (c) Cut through along the black arrow in (a), depicting the peak wave direction (going to). The zero-up crossing wavenumber k_u is highlighted in (c).

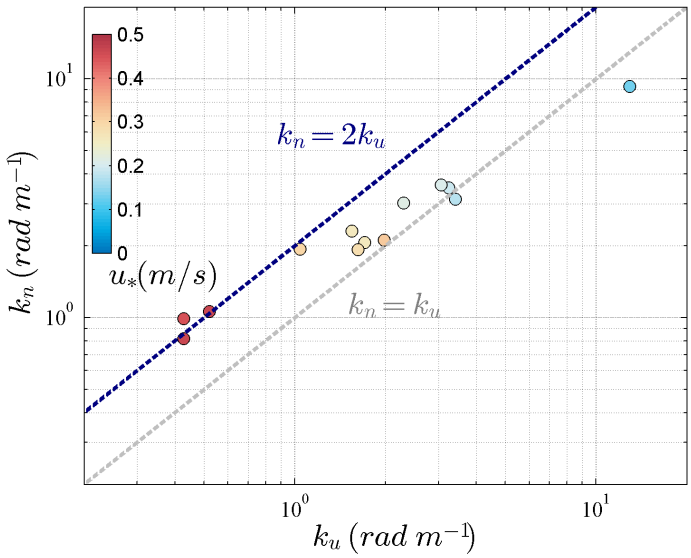

Figure 2.15: Measured upper limit of the equilibrium range k_n as a function of the zero-up crossing of the non-linear energy fluxes k_u. Each point is colorcoded for friction velocity u_*.

As mentioned in earlier sections, correctly identifying c_p is particularly challenging and might be misleading when the spectral peak wavenumber k_p is used. Figure 2.16(b) shows the dependence of the ratio k_n/k_u on the non-dimensional quantity $u_*/\sqrt{gH_s}$. We find that the ratio is increasing with $u_*/\sqrt{gH_s}$. An exponential fit[6] of the data gives:

$$\frac{k_n}{k_u} = b_1 + b_2 e^{\frac{b_3 u_*}{\sqrt{gH_s}}}, \tag{2.14}$$

where $b_1 = 9.3 \times 10^{-1}$, $b_2 = 4.0 \times 10^{-4}$, and $b_3 = 84.4$.

2.3.5 Contribution from the Equilibrium Range to the Total Mean-Square Slope

In deriving the total mean-square slope associated with the equilibrium range, Phillips (1985) showed that r, the constant used in his study to relate k_n to u_*, is defined as

$$r = \frac{\left\langle s^2 \right\rangle^2}{\beta^2} \tag{2.15}$$

[6]We found a better r^2 using an exponential growth fit as opposed to a quadratic fit, 0.84 and 0.76 respectively, which motivated its use.

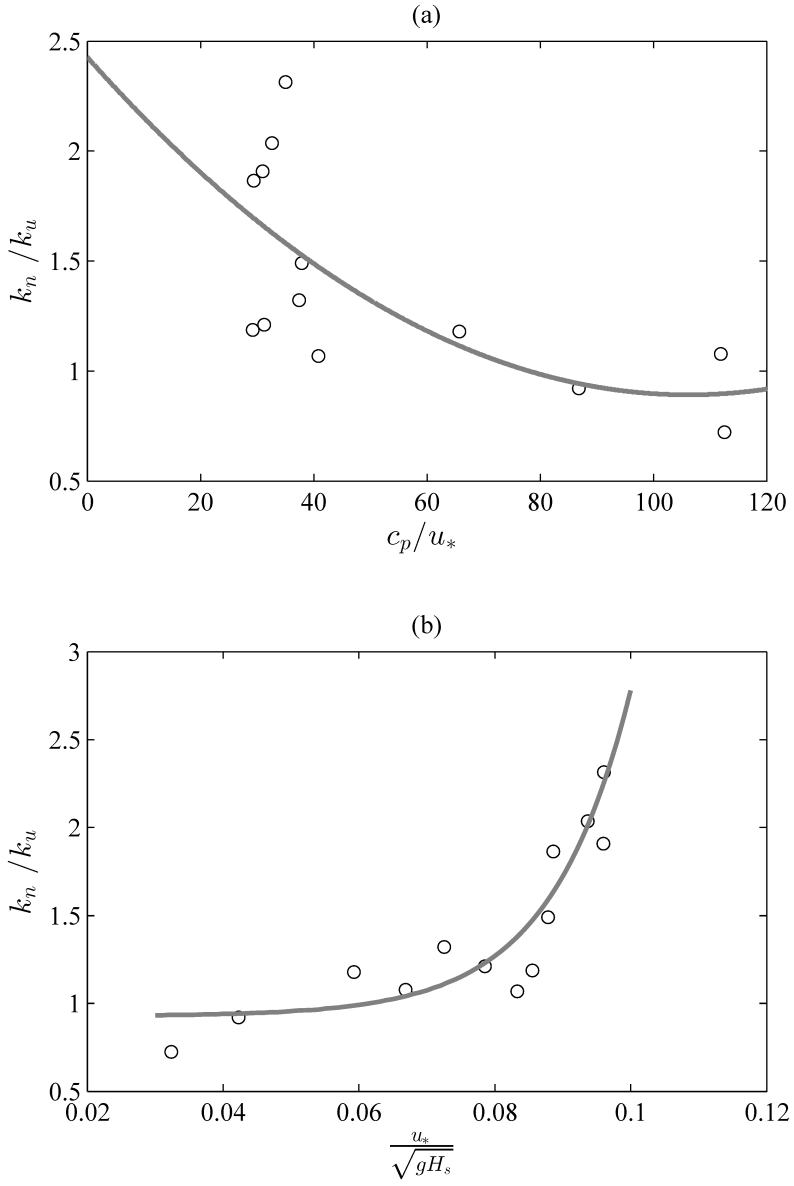

Figure 2.16: Ratio k_n/k_u plotted against (a) wave age and (b) $\frac{u_*}{\sqrt{gH_s}}$. The gray curve shows the corresponding fits (r^2= 0.45 and 0.84 for (a) and (b), respectively).

where $\left\langle s^2 \right\rangle$ is the total mean-square slope computed over the equilibrium range, from k_o to k_n, and β is Toba's constant. Here β is computed from the equilibrium range of the omnidirectional wave spectrum following Toba (1973), where the equilibrium range is defined as

$$\Phi(k) = \frac{\beta}{2} u_* g^{-1/2} k^{-5/2}. \tag{2.16}$$

Toba's constant β is calculated here as

$$\beta = \frac{2g^{1/2}}{u_*} \left\langle \Phi(k) k^{5/2} \right\rangle \tag{2.17}$$

where the mean compensated spectrum $\left\langle \Phi(k) k^{5/2} \right\rangle$ is computed over the equilibrium range, integrated from $2.25k_p$ to k_n. The low wavenumber bound was set according to Donelan et al. (1985), also used in Romero and Melville (2010a), to avoid contamination from the spectral peak.

Figure 2.17 shows r computed from equations 2.9 and 2.15. We obtain values ranging from 0.01 to 0.025 using equation 2.9 and generally lower values using equation 2.15, ranging from 0.005 to 0.015. Using the limited observational data available at the time, Phillips concluded that $r \approx 0.3$, a value much larger than what we find in the present study. This discrepancy is not unexpected, and caused by the fact that Phillips used Cox and Munk's (1956) classical result to compute the total mean-squared slope. Their estimate, derived from airborne measurements of sunglitter, does not discriminate between equilibrium and saturation ranges. The saturation range, and beyond, in the capillary range, contributes significantly to the mean-square slope, in turn, leading to significant overestimation of r in Phillips' work.

In Figure 2.18 we characterize the contribution of the equilibrium range to the total mean-square slope. The term $\left\langle s^2 \right\rangle (k)$ is computed cumulatively based on the measured directional wave spectrum, defined as

$$\left\langle s^2 \right\rangle (k) = \int_{k_o}^{k} S(m) dm \tag{2.18}$$

where

$$S(k) = \Phi(k) k^2. \tag{2.19}$$

As our reference, we use here the classical parameterization from Cox and Munk

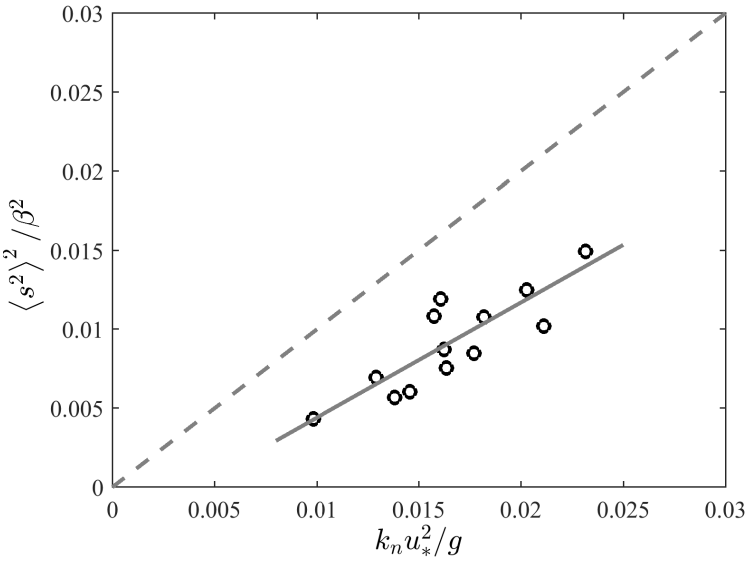

Figure 2.17: Total mean squared slope squared, computed over the equilibrium range k_o to k_n, normalized by the Toba parameter (Romero and Melville, 2010a) against normalized wavenumber $k_n u_*^2/g$, following Phillips (1985). A linear fit is shown in gray, where $\langle s^2 \rangle^2 / \beta^2 = 0.73\hat{k} - 0.0029$.

(1954), subsequently confirmed by Bréon and Henriot (2006), that

$$\langle s^2 \rangle_{ref} = s_a + s_b U_{10} \pm \varepsilon, \tag{2.20}$$

where $s_a = 4 \times 10^{-3}$, $s_b = 5.01 \times 10^{-3}$ and $\varepsilon = 0.71 \times 10^{-3}$. Note that U_{10} was estimated from satellite scatterometry in Bréon and Henriot (2006), while the wind speed in Cox and Munk (1954) was measured from an anemometer installed 12.5m above the deck of a sailboat located at the experiment site. Each curve is colorcoded for friction velocity. We find that the contribution from the equilibrium range typically corresponds to just 10 – 30% of the total mean-square slope.

2.4 Summary and Discussion

Detailed topographic measurements of surface waves, ranging from kilometer to submeter scales, collected from an airborne, scanning, high-resolution waveform lidar, combined with in-situ marine atmospheric boundary layer data recorded on R/P FLIP during the ONR SOCAL2013 experiment, has provided an opportunity to characterize the directional properties of the wave field across the equilibrium-saturation ranges of wind-

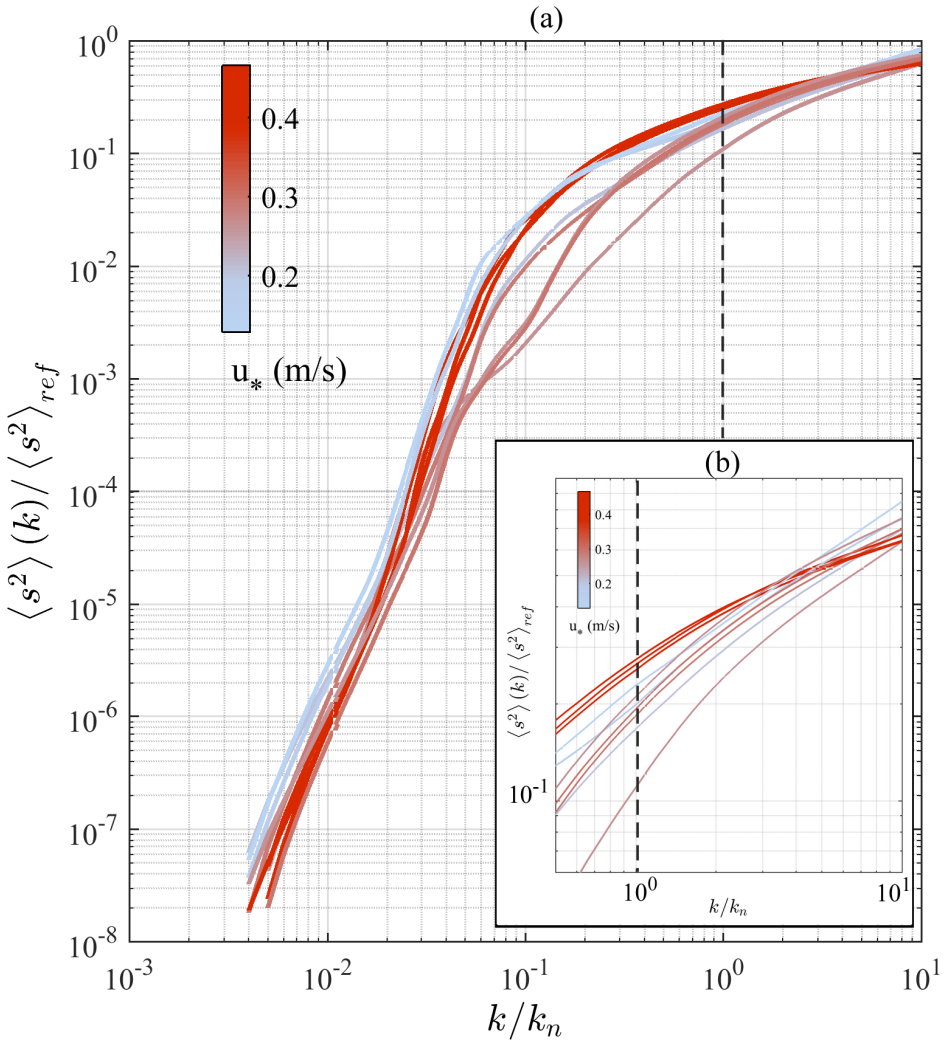

Figure 2.18: (a) Total spectral mean-square slope $\langle s^2 \rangle (k)$ computed from the omnidirectional wave spectrum, normalized by the total mean-square slope defined by Cox and Munk (1954), $\langle s^2 \rangle_{ref}$, plotted against the normalized wavenumber k/k_n. (b) shows a zoomed-in version of the same plot, focusing on the higher wavenumber portion. The normalized wavenumber reference band $k/k_n = 1$ is shown as a black dashed line.

generated surface waves and correlate them with the wind forcing. To our knowledge, this is the first study that shows directional characterization of surface waves over such a broad range of wavenumbers and environmental conditions (i.e. wind forcing).

Our measurements extends the known bimodal distribution well beyond what was reported in previous studies, with an azimuthal separation between the two lobes reaching close to π for the highest wavenumbers we could resolve, up to $k/k_p \approx 100 - 200$. Though more work is needed, in particular to resolve the 180^o ambiguity in the directional spectrum computed from the lidar topographic surface wave maps, these results show that waves propagating in opposing directions can be found at wavenumbers around 10-12 rad/m (10-11 rad/s for linear gravity waves) in waves from one storm system, rather than requiring waves from opposing storms. The existence of such wave systems is believed to be a leading mechanism through which microseismic noise is generated (Longuet-Higgins, 1950; Farrell and Munk, 2010; Ardhuin et al., 2015).

Our measurements provide no definitive mechanism which leads to such a wide bimodal spectrum; however, there are some suggestions in the literature. From the available four-wave numerical modeling (e.g. Dysthe et al., 2003; Socquet-Juglard et al., 2005) the broadest bimodal effects have been seen out to $\pm 70^o$. But it is important to remember that the standard gravity-wave modeling using four-wave resonance is just an asymptotic model and for larger times and larger slopes five- and higher wave resonances are possible. For example, in the laboratory Su et al. (1982) and Melville (1982) showed direct evidence of the growth of crescent-shaped waves which occur at larger wave slopes and are the result of five-wave interactions leading to three-dimensional instabilities that are stronger than the two-dimensional Benjamin-Feir instabilities (McLean et al., 1981). The tails of the crescent-shaped waves propagate in almost opposing transverse directions. Wave breaking can also be a source of wave components travelling in almost transverse directions as well as upstream (Rapp and Melville, 1990). In general, breaking must be considered as an omnidirectional source of high wavenumber disturbances, but as far as we are aware there has not been any modelling of these effects. Thus the source of the opposing transverse waves remains elusive, but the evidence presented here calls for more measurements and modeling of higher-order wave-wave interactions.

The omnidirectional wavenumber spectra show a consistent power law behavior, proportional to $k^{-5/2}$ in the equilibrium range, and k^{-3} in the saturation range. The transition between these two regimes is very well defined and we find good agreement with the model of Phillips (1985) that predicts that the upper limit of the wavenumber in the equilibrium range is, to within a factor of 1-2, proportional to $(u_*^2/g)^{-1}$. The collapse across

the equilibrium-saturation ranges of the omnidirectional saturation wavenumber spectra plotted against non-dimensional wavenumber $\hat{k}$ is remarkable, as shown in figure 2.11. Note that the same scaling is also very effective in collapsing the bimodal azimuthal separation found in the directional properties of the spectra.

Direct measurements of the transition across the equilibrium and saturation regimes, over a broad range of environmental conditions, offer an opportunity to test the empirical parameterization of k_n of Romero and Melville (2010a,b), defined as a function of the zero-up crossing wavenumber, k_u, of the azimuth-integrated non-linear energy fluxes S_{nl} based on Phillips' (1985) equilibrium argument. The upper limit of the equilibrium range is indeed a function of k_u, with a clear dependence on wave age and the non-dimensional atmospheric friction velocity $u_*/\sqrt{gH_s}$. This non-dimensional quantity appears to be better suited in the present data set to capture the evolution of the equilibrium-saturation ranges than is the wave age.

Now able to characterize its spectral bounds, we showed that the equilibrium range of the surface wave field contributed up to $10-30\%$ of the total Cox and Munk (1954) mean-square slope in our measurements.

This work was accepted for publication in the Journal of Physical Oceanography (AMS) on May 23 2017 (Lenain and Melville, 2017b):

Lenain, Luc, and W. Kendall Melville. "Measurements of the Directional Spectrum across the Equilibrium Saturation Ranges of Wind-Generated Surface Waves." Journal of Physical Oceanography 47.8 (2017): 2123-2138.

CHAPTER 3

Surface-Wave Effects on Sea Spray and Aerosol Processes

Contents

3.1 Introduction

Sea-spray aerosols represent a significant fraction of the aerosol particles that exist in the maritime atmosphere. Despite extensive work and remarkable progress in the last two decades, mostly motivated by cloud microphysics, atmospheric chemistry, regional and global climate modelling, and the direct and indirect radiative effects of marine aerosols, our understanding of the mechanisms through which spray is ejected from the surface and transported in the Marine Atmospheric Boundary Layer (MABL), and then higher up in the atmosphere, remains very limited. Scatter in sea spray source functions span more

than an order of magnitude (de Leeuw et al., 2011; Veron, 2015) especially for the larger particle sizes. Transport and generation mechanisms for the latter are poorly understood. In their review of sea-spray source function parameterized from laboratory and field experiments on sea spray aerosol production, de Leeuw et al. (2011) showed that there remains large uncertainties in the sea-spray source generation functions (SSSGFs). Most SSSGFs of marine aerosols are traditionally parameterized by wind speed (Smith et al., 1993; Fairall et al., 1994; Lewis and Schwartz, 2004). Hanley et al. (2010) conducted a global climatology of Wind-Wave Interaction based on a 40-yr ECMWF Re-Analysis (ERA-40) dataset. They found that there were few occurrences of wind-wave equilibrium, even in the Southern Ocean and northern latitude Trade Wind regimes. This was due in part to the presence of swell but also due to the variability of the winds. In short, one cannot assume that wave effects that might be included at equilibrium are included in general.

Few studies have investigated the use of wave-breaking characteristics as a proxy: whitecap coverage (Monahan et al., 1986; Mårtensson et al., 2003; Norris et al., 2013a), and distribution of lengths of surface breaking fronts (Mueller and Veron, 2009), based on Phillips (1985) formulation.

Recent work has explored the use of a range of wave state parameters in formulating SSSGFs. Norris et al. (2013b) and Ovadnevaite et al. (2014) use a wave Reynolds number, originally introduced by Zhao and Toba (2001) (see also Zhao et al., 2006). In most of these studies, wave measurements are limited, making the inclusion of wave parameters into the SSSGF formulation very challenging.

Though important for the global aerosol budget and biochemical aspects of ocean-atmosphere interaction processes, the mechanisms through which larger sea spray aerosols, of diameters greater than $20\mu m$, are generated and transported into the MABL remain poorly understood, leading to significant uncertainty regarding the contribution of spray-mediated fluxes to the total air-sea fluxes for such size ranges. Laboratory experiments (e.g. Fairall et al., 2009; Veron et al., 2012) have focused on the generation and dispersion mechanisms of such droplets, but field measurements in this size range are very sparse, especially at height, within the MABL. Recent LES modelling (Shpund et al., 2011, 2012, 2014) showed that large eddies play a crucial role in transporting large spray aerosols vertically, to heights of several hundreds meters above the ocean surface, significantly impacting the vertical dynamics and cloud microphysical structures in tropical cyclones (Shpund et al., 2014).

Evidence of large concentrations of marine aerosols well above the ocean surface

have been documented in severe weather environments. Following a nearly catastrophic failure of a NOAA WP3D aircraft that lost power to three of its four engines in the north Atlantic Ocean flying at approximatively 800m AMSL in a hurricane force wind region, Reid et al. (2007) concluded in their post-incident assessment that

> "sea salt aerosol particles generated in the high winds and high (up to 20 m) seas coated the aircraft and caused severe engine fouling resulting in compressor stalls."

In the present study, detailed, coincident and collocated field measurements of aerosols of diameters ranging from 0.1 to 200 μm, waves, wave kinematics, and atmospheric conditions were gathered over a range of wind speeds and wave conditions, providing a rare opportunity to investigate the relationship between aerosol concentration in the MABL and both atmospheric and sea-state conditions.

We find guidance from the scaling of breaking by Sutherland and Melville (2013), that has its roots in the inertial scaling of breaking by Drazen et al. (2008) and Romero et al. (2012). This influences the dimensional analysis that leads to the best collapse of the data from both the HiRes and GoTex experiments with a dependence on both wind and wave parameters.

In Section 2 the Hires experiment and the instrumentation are presented. In Section 3 following a brief presentation and analysis of the measurement, we present a dimensionally consistent equation for the aerosol concentration. The results are summarized in Section 4.

3.2 Experiment and Methods

The results presented here were collected from a Twin Otter research aircraft, from the Center for Remotely Piloted Aircraft Studies (CIRPAS), in June 2010 during the main field campaign of the Office of Naval Research High-Resolution Air-Sea Interaction Departmental Research Initiative (HIRES DRI), off the coast of Northern California (Grare et al., 2013).

In addition to carrying a basic navigation and meteorological system, the aircraft was outfitted with a suite of aerosol particle-size sensors, atmospheric turbulence sensors, surface-wave and surface kinematics instrumentation. The aircraft flight team is specifically trained to conduct low level flights over the ocean, down to 30m AMSL in high-wind conditions for extended periods of time. Figure 3.1 shows the environmental

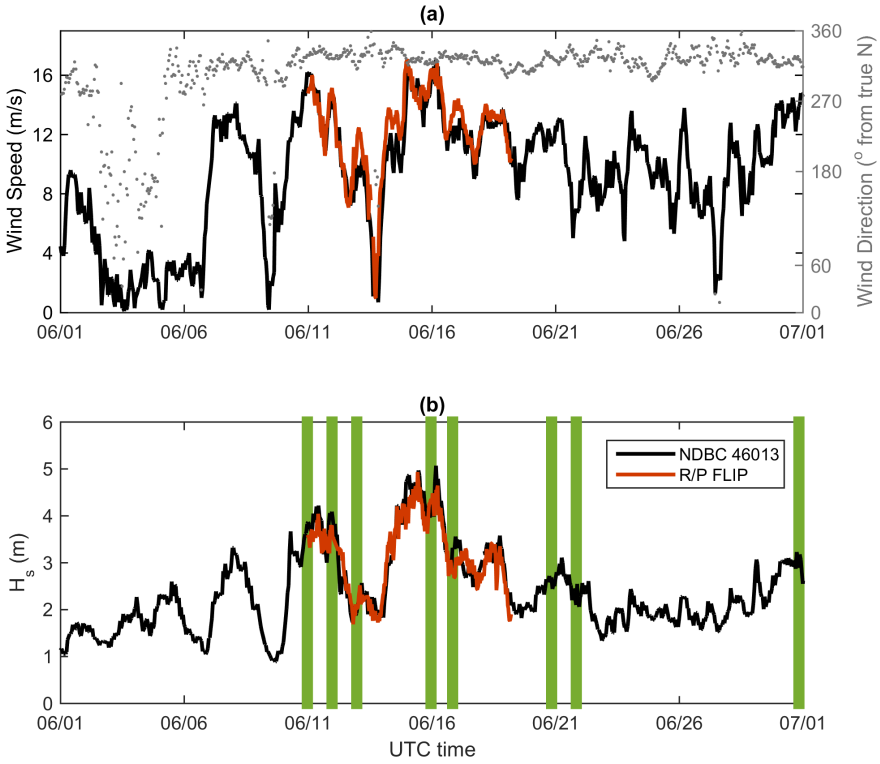

Figure 3.1: (a) Wind speed and direction and (b) significant wave height, H_s (m), for the month of June 2010 at NDBC 46013, the closest meteorological buoy to the experiment site, and the corresponding measurements from R/P FLIP (red). The time of the CIRPAS aircraft research flights considered in this study are highlighted in green.

conditions experienced during the experiment, measured from the closest meteorological buoy (NDBC 46013) and R/P FLIP which was moored 25km off the California coast (38^o 20′ N, 123^o 26′ W) for part of the experiment (see figure 3.2(g)). The flight times are highlighted in yellow, covering a broad range of environmental conditions with U_{10} ranging from 8 to 19 m/s and H_s from 2 to 4.5 m. The low-level tracks for two of the considered flights (out of a total of eight flight-days), on June 15 and June 30, 2010, are shown in figure 3.2(g). Note that low-level track data were analyzed for all eight flight-days, corresponding to a total of approximately 3 flight-hours out of the total 32 flight-hours we flew at the experiment site during the project.

3.2.1 Aerosol Instrumentation

Aerosol measurements were made using a suite of sensors installed on wing pylons to provide in-situ sampling of the particles present in the air flow. The instrument pod is shown in Figure 3.2(b). A Passive Cavity Aerosol Spectrometer Probe (PMS PCASP-100X) and a forward Scattering Scatterometer Spectrometer Probe (PMS FSSP-100) measured particle size (diameter) from 0.11 to 2.124 μm and 2.37 to 28.24 μm, respectively, over 20 size bins for each system. A Cloud Aerosol Precipitation Spectrometer (DMT CAPS) and a Cloud Imaging Probe (DMT CIP), sampled the larger aerosol particles of diameters ranging from 0.62 to 53.72 μm and 25 to 1,550 μm over 20 and 62 size bins, respectively. All instruments were calibrated prior to and after the field deployment at the CIRPAS calibration facility, accurately characterizing the lower and upper bounds of each size-range channel for all four sensors.

3.2.2 Wave and Surface Kinematics

The sea surface elevation was measured with a scanning lidar instrument, the National Aeronautics and Space Administration NASA-EG&G Airborne Topographic Mapper (NASA ATM III). Although this system is primarily used to characterize ice-sheet thickness in polar regions as part of the NASA Ice Bridge project (Krabill et al., 1995), the ATM has proven to be an excellent tool to measure directional wave fields in past experiments (Hwang et al., 2000a,b; Romero and Melville, 2010a,b; Romero et al., 2012). During the HIRES experiment, the ATM's conical scanning angle was set to 22^o with a pulse repetition rate of 5 kHz and a scanning frequency of 20 Hz. In addition, a suite of nadir-looking high-resolution visible and infrared imagers provided information about surface kinematics and wave breaking.

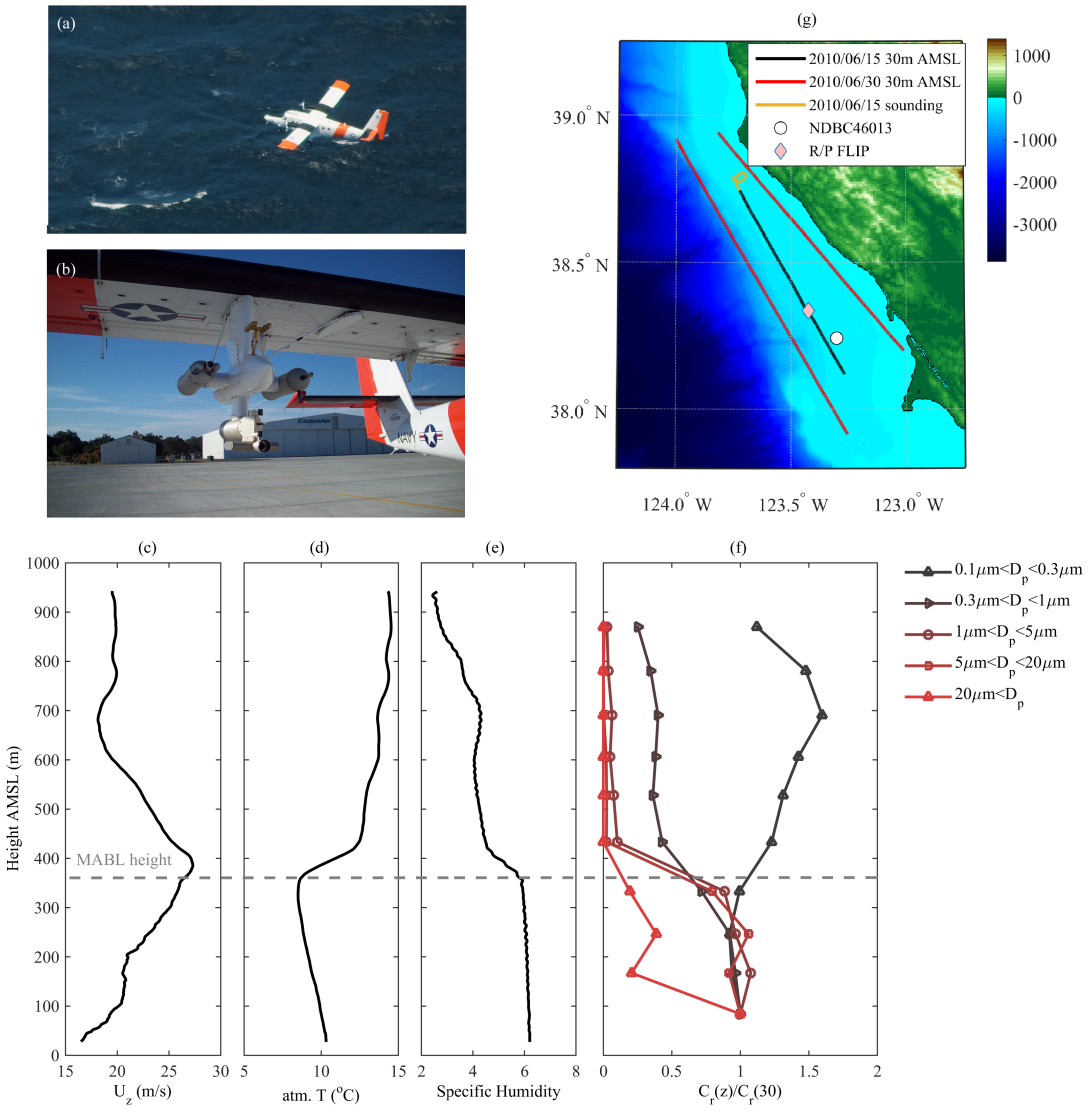

Figure 3.2: (a) CIRPAS Twin Otter flying at 30m AMSL during the ONR HIRES2010 experiment. (b) Aerosol sampling instrumentation mounted on the starboard wing of the aircraft (PCASP+CIP+CAPS+FSSP). (c-f) Vertical profiles of wind speed (m/s), atmospheric temperature (^{o}C), specific humidity, and aerosol concentration for five diameter ranges, respectively, collected on June 15 2010 during one of the "sounding" portions of the flight, depicted as an orange color track in (g). (g) Bathymetric map of the operation area showing three of the 30m AMSL flight tracks considered in the present analysis, and the location of R/P FLIP and the NDBC 46013 meteorological buoy during the experiment.

Though the ATM lidar was not designed for atmospheric measurements, careful analysis of the waveform signal collected for each laser pulse sent and received by the sensor was conducted to identify partial or spurious returns from aerosols above the ocean surface. A similar approach was tested in a laboratory setting in recent work from Toffoli et al. (2011). Note that the ATM laser wavelength is 532nm (green) and therefore can penetrate the first few meters of the water column. Similar lasers have been used for biochemical remote sensing both from aircraft and ships (e.g. Churnside et al., 1998, 2001; Brown et al., 2002; Carrera et al., 2006). Figure 3.3 shows a large breaking event captured from the ATM lidar and nadir-looking video camera, installed on the aircraft, in the vicinity of R/P FLIP during the HIRES experiment on June 15 2010 at 23:01 UTC. The wind speed U_{10} measured from FLIP was 14.8 m/s at that time. The transverse length scale for this particular breaker is large, reaching close to 85m, for a crest to trough individual wave amplitude of 7.2m implying the generation of a significant amount of aerosols during the breaking process. The data collected from the airborne system are split in two, corresponding to the columns (a) and (b) in figure 3.3, to differentiate between the data collected $forward$ and aft of the aircraft location (recall that the ATM has a circular scan pattern). This results in the lidar (as well as the camera) effectively scanning the same area at two different times, separated by a δt which depends on flight altitude, aircraft speed and the azimuthal position of the lidar beam. Here δt was approximately equal to 5 seconds for the transect shown in the figure. The two lower panels show a cross-section corresponding to the transect shown in the plan view plotted in the upper panels. Surface elevation is shown in red while returns from aerosols are shown as black dots. The active part of the breaking wave corresponds to the area where the number of aerosol returns increases. This result, though very qualitative, reinforces the need to incorporate some characteristics of the wave field in aerosol production models, especially the effects due to wave breaking. Also note the presence of lidar returns below the surface (blue dots), likely associated with the presence of a bubble plume right below the breaking wave.

In addition, a nadir-looking fixed lidar altimeter (Riegl LD90-3800VHS) provided measurements of sea surface displacement when flying at altitudes between 30 and 200 m above mean sea level, below the minimum range of the ATM. The altimeter was set to sample at 1kHz, averaged down to 100Hz to improve the signal-to-noise ratio.

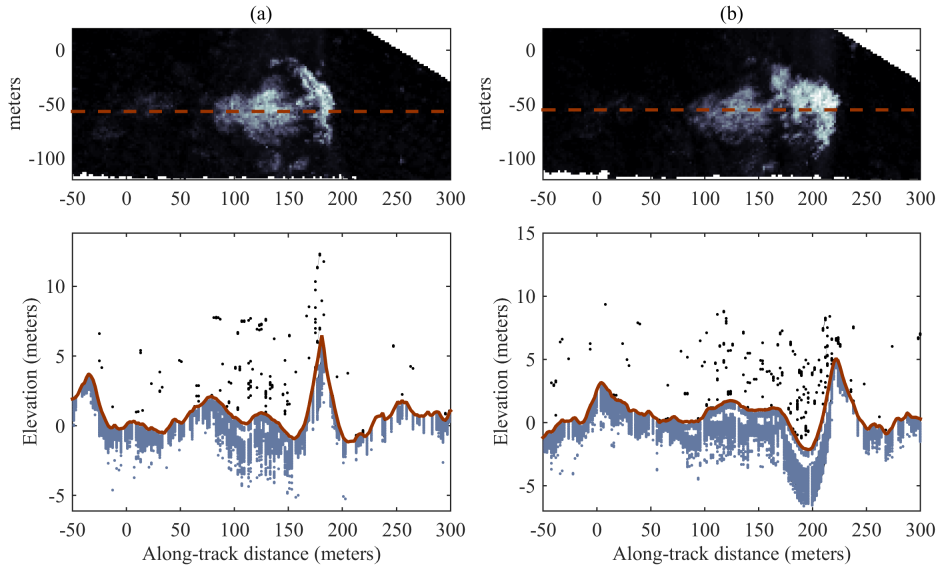

Figure 3.3: Large breaking wave event captured with the ATM lidar and collocated video camera on July 15 2010 at 23:01 UTC during the HIRES experiment. Columns (a) and (b) show the same wave at instant $t = t_o$ and $t = t_o + \delta t$ respectively, where $\delta t = 5sec$. The two bottom panels show the surface elevation (red) corresponding to the transect shown as a dashed line in the two upper panels. ATM waveform outlier returns, a proxy for the presence of larger aerosols or bubbles, are also plotted as blue (bubbles below the water surface) and black (above the water surface) dots. Note the persistent returns below the surface likely from the underlying bubble layer and plume from the breaker.

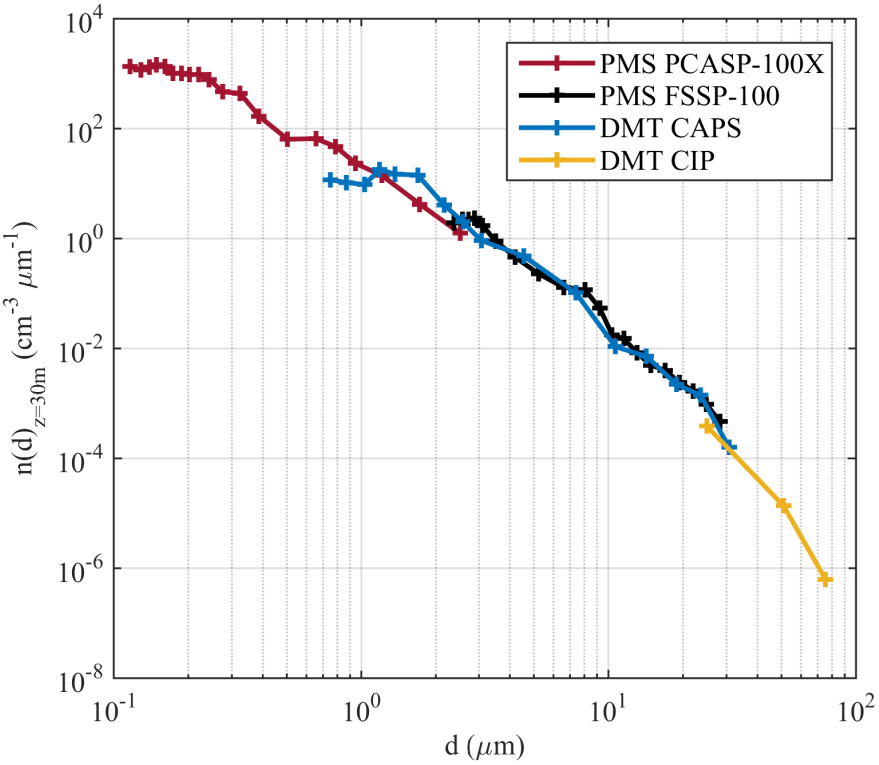

Figure 3.4: Representative example of aerosol number distributions taken on July 15 2015 2010 at 23:30 (UTC) during the HIRES experiment, showing the overlap between the four sensors: PMS PCASP-100X (red), DMP CAPS (blue), PMS FSSP-100 (black) and DMP CIP(yellow).

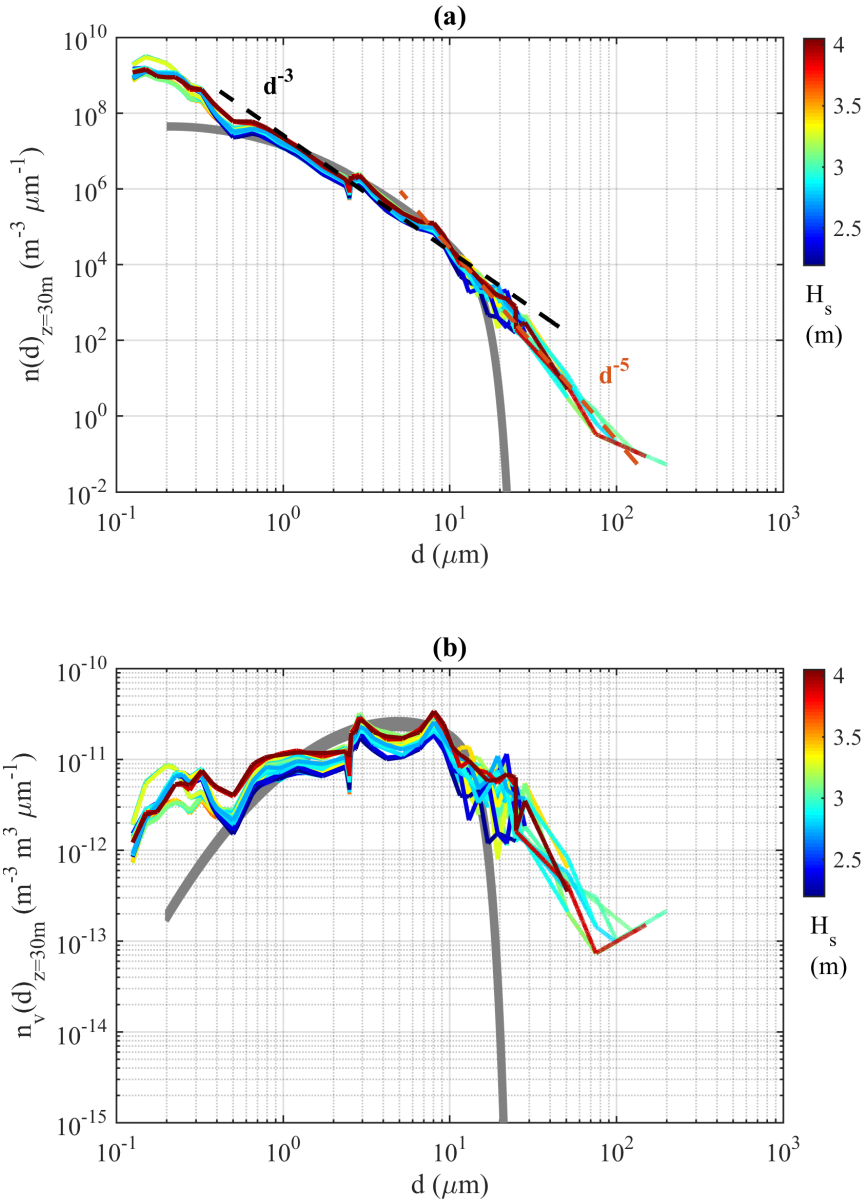

Figure 3.5: (a) Aerosol number distributions collected from the instrumentation mounted on the CIRPAS Twin Otter during the low-level flights (30m AMSL) for a wind speed $U_{10} = 15 \pm 1$ m/s. Distributions are colorcoded for H_s. Shown in gray is the predicted aerosol number distribution at the same altitude based on an empirical SSSGF described in Lewis and Schwartz (2004), assuming that the vertical transport of droplets by turbulence is balanced by gravitational settling for the same surface wind speed (Fairall et al., 2009; Veron, 2015).(b) Corresponding aerosol volume distributions.

3.3 Measurements

The flight profiles for each sortie included periods of time flying at the lowest permitted altitude, typically 30m AMSL, with its reciprocal track at 300m AMSL altitude to permit directional wave measurements and surface kinematics from the nadir-looking electro-optical system, and helical soundings at the beginning and end of each flight leg from 30 to 1000m to characterize the structure of the MABL. A representative example of (c) wind speed at z meters AMSL U_z (in m/s), (d) atmospheric temperature T (in ^oC), (e) specific humidity q (dimensionless) as a function of height $z(m)$ AMSL collected on June 15, 2010, at the northern end of an upwind flight leg is shown in figure 3.2. Figure 3.2(f) shows the measured fraction of aerosol concentration relative to the measurements at 30m AMSL for 5 ranges of diameter d, from 0.1 to 20 μm and larger sizes. The MABL extends at that time to approximately 400m AMSL (see panel (c), (d), and (e) in figure 3.2). Aerosols of diameter ranging from approximately 1 to 20 μm show an approximately constant concentration within the MABL, and rapidly drop to zero above it. The smaller particles, with diameters $d < 1\mu$m while also close to constant concentration as a function of height inside the MABL, show an increased concentration above the MABL likely associated with other sources not related to the air-sea interface. Larger aerosols ($> 20\mu m$) are present in the MABL, but their concentration rapidly decreases with increasing height.

3.3.1 Aerosol Distributions

We define the size distribution function $n(d)$ such that $n(d)\mathrm{d}d$ is the number of aerosol particles per unit volume of air having diameters in the range d to $d + \mathrm{d}d$. The total number of particles per unit volume of air is therefore

$$N = \int_0^\infty n(d)\mathrm{d}d \tag{3.1}$$

Our measurements are obviously discrete and limited to a set range of aerosol diameters; the measured number of particles in the size range d to $d + \mathrm{d}d$ is defined as $\mathrm{d}N = n(d)\mathrm{d}d$ leading to the more commonly used expression of the aerosol number distribution $\frac{\mathrm{d}N}{\mathrm{d}d}$. Surface area, volume and mass distribution of aerosols are of particular interest, as a number of aerosol properties depend on these variables. While the aerosol surface is where thermal, gas, and chemical exchanges occur, the aerosol volume density characterizes the amount of sea water and its content transferred to the atmosphere

by marine aerosols. In the present study, we focus on the relationship between sea-state conditions and size and volume distributions of marine aerosols.

Figure 3.4 shows an example of aerosol number distribution computed from the four aerosol instruments considered during a 6km segment flying at 30m altitude. Overall, we find good agreement between all sensors.

We define the aerosol volume distribution $n_v(d)$ as the volume of particles per unit volume of air having diameter in the range d to $d + \mathrm{d}d$ where

$$n_v(d) = \frac{\pi}{6} d^3 n(d) \tag{3.2}$$

such that the total volume of aerosol per volume of air [1], i.e. the total aerosol volumetric concentration V is

$$V = \frac{\pi}{6} \int_0^\infty d^3 n(d) \mathrm{d}d \tag{3.3}$$

Figure 3.5(a) shows the aerosol size distributions collected from the Twin Otter instrumentation for a selected wind speed, $U_{10} = 15 \pm 1$ m/s during all considered flights and colorcoded for H_s. H_s is computed from the surface displacement η measured by the nadir-looking laser altimeter, such that $H_s = 4\eta_{rms}$ where η_{rms} is the root-mean-square surface elevation. Note the two power laws, d^{-3} for $1\mu m < d < 10\mu m$, and rolling off to a d^{-5} power law for the aerosols of larger diameter. These measurements are compared against an empirical source concentration function to verify that the observed concentration levels are generally consistent with accepted aerosol marine source functions. Note that this approach is far from ideal, as it requires crude assumptions and simplifications of the transport mechanisms through which the aerosols are transported into the MABL. The lack of consensus and basic understanding of the physics involved in the transport mechanisms, in particular for the larger particles, is in fact the primary motivation for not computing aerosol production fluxes in the present study, by extrapolating our measurements at height to the surface. The following comparison should therefore not be taken as a detailed validation, but rather a consistency check. Here we use an empirical source concentration function at the surface defined by Lewis and Schwartz (2004) in a similar approach to the one used in Jones and Andreas (2012) as

$$n_o = \frac{dN}{dr_{80}} = \frac{7 \times 10^4 U_{10}^2}{r_{80}} exp\left(-\frac{1}{2}\left(\frac{ln(r_{80}/0.3)}{ln2.8}\right)^2\right) \tag{3.4}$$

[1] For consistency with the literature we consider here the volume of air and not the volume of the air and aerosol as the difference is negligible.

for the same range of wind speed U_{10}. Here r_{80} is the equilibrium aerosol radius at an equivalent 80% relative humidity. This radius is commonly used to characterize smaller diameter aerosols to account for the exchange of moisture between the hygroscopic drop and its surrounding. It is assumed here that the aerosols reach equilibrium by the time they are sampled, such that $d = 2 \times r_{80}$. As the measurements presented here were collected well above the source region ($z = 30m$), we need to assume a transport mechanism from the source to the measurements height. Fairall et al. (2009) suggest that the vertical transport of droplets by turbulence is balanced by the gravitational settling velocity v_d leading to

$$n(d, z) = n_o(d)\left(\frac{z}{h_o}\right)^{\frac{-\mathrm{v}_d S c_t}{\kappa u_* f_s}} \tag{3.5}$$

where h_o is the upper limit of the source region, $S c_t$ the droplet's turbulent Schmidt number and f_s a slip coefficient first introduced by Rouault et al. (1991). Here u_* is the atmospheric friction velocity, computed iteratively from the wind speed measured at the 30m flight altitude U_{30} using TOGA COARE 3.0 (Fairall et al., 2003) assuming a constant flux layer with a logarithmic wind profile:

$$U_z = \frac{u_*}{\kappa} ln\left(\frac{z}{z_o}\right), \tag{3.6}$$

where z is the measurement height above mean sea level, z_o is the roughness length. Here we use the most recent parameterization implemented in TOGA COARE 3.0, that utilizes a characteristic of the wave field, the wavelength at the peak of the wave spectrum λ_p, based on Oost et al. (2002), as described in Fairall et al. (2003):

$$z_o = \frac{50}{2\pi}\lambda_p\left(\frac{u_*}{c_p}\right)^{4.5} + \frac{0.11\nu_a}{u_*}, \tag{3.7}$$

where ν_a is the kinematic viscosity of air. Equation 3.6 is also used to compute the wind speed at 10m, U_{10}, from the measurements at the 30m flight altitude.

The velocity v_d is defined as

$$\mathrm{v}_d = \frac{\rho_w d^2 g}{18\mu} C_c \tag{3.8}$$

where ρ_w is the density of sea water, g is the gravitational acceleration and μ the viscosity of air. C_c is the so-called Cunningham factor (Cunningham, 1910), a correction factor needed to account for the reduced slippage at the particle surface for aerosol diameters

smaller than $1\mu m$. It is defined as

$$C_c = 1 + \frac{2.52\lambda}{d} \tag{3.9}$$

where λ is the mean free path of molecules of gas (in our case air).

The aerosol concentration at $z = 30m$ derived from the empirical formulation described in equations 3.4 and 3.5 are shown in gray in Figure 3.5. Here h_o was set to the significant wave height H_s and $S\,c_t$ is taken to be equivalent to that for water vapor (Rouault et al., 1991). While our measurements agree with the general shape of the distribution derived from the empirical formulation described above for $0.5 < d < 15\mu m$, significant differences are shown above and below that range. For the smaller range of aerosol diameters, $d < 0.5\mu m$, the measured concentration is higher, likely due to the presence of a non-local source of aerosols (marine or even perhaps terrestrial). The largest differences are found for droplet diameters $d > 15\mu m$. The simplified vertical transport model considered here, taken here as u_*, is not large enough to balance the droplet settling velocity for those larger droplets. The simple fact that large diameter aerosols are found well above the marine aerosol source layer implies that other transport mechanisms (e.g. initial ejection velocity from the jet drops, large eddies) needs to be considered to explain how those droplets are found at such altitudes.

3.3.2 Ocean Surface Kinematics and Breaking Statistics

Wave breaking plays a fundamental role in the generation of marine aerosols. Spume drops are ejected from breaking waves when the wind speed is high enough, the toe of plunging breakers generate spray on impact with the surface below, while bursting bubbles from the subsurface bubble plume generated during the wave breaking process produces film and jet drops (Veron, 2015; Andreas, 1995). Phillips (1985) introduced the length of breaking fronts, $\Lambda(c)$, and its moments to characterize breaking statistics. The first moment R

$$R = \int c\Lambda(c)dc. \tag{3.10}$$

represents the fraction of ocean surface turned over by breaking fronts per unit time. Phillips (1985) (see also Duncan (1981)) also defined the total energy dissipated by breaking waves (per unit area of ocean surface) as

$$F = \frac{\rho_w}{g}\int b(c)c^5\Lambda(c)dc \tag{3.11}$$

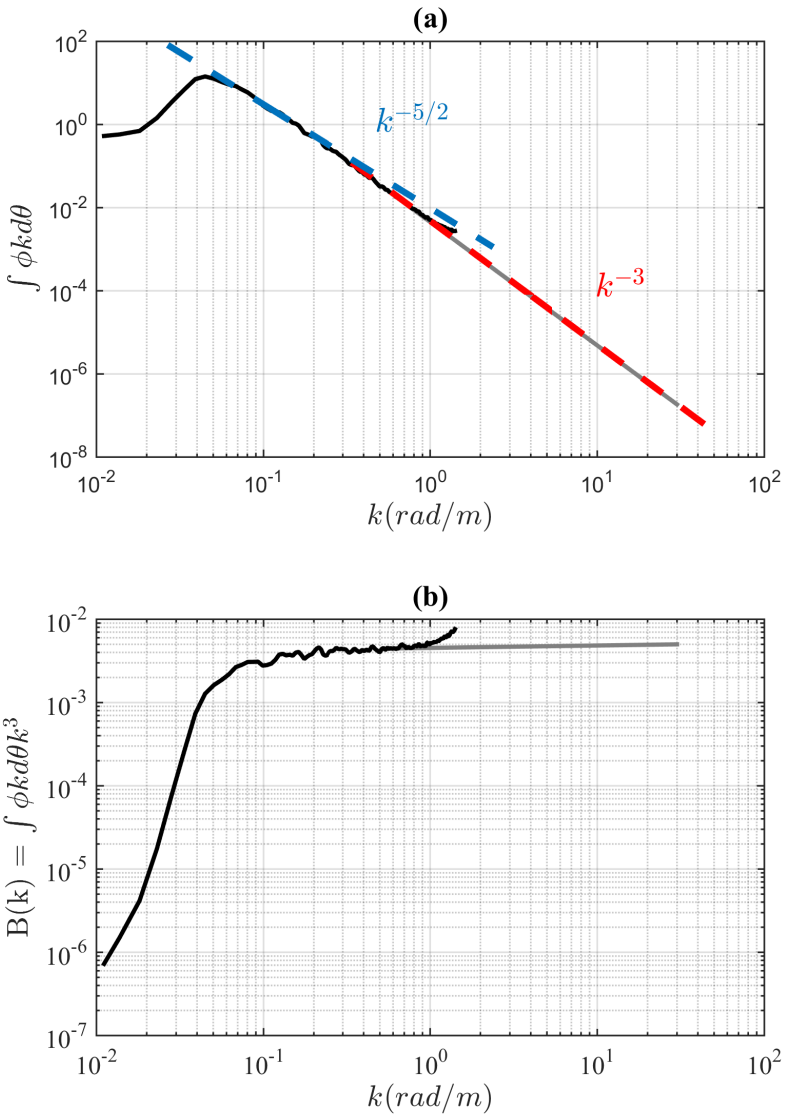

Figure 3.6: (a) Sample omnidirectional wavenumber spectrum collected on June 15 2010 during the HIRES experiment.The measured spectrum with a high wavenumber cutoff at 1.2 rad/m, is shown in black, while the spectrum, extrapolated to 30 rad/m, used in the computation of the energy dissipated by breaking waves (see equation 3.11) is shown in gray. Note the -5/2 and -3 spectral slopes. (b) Corresponding saturation spectra $B(k)$.

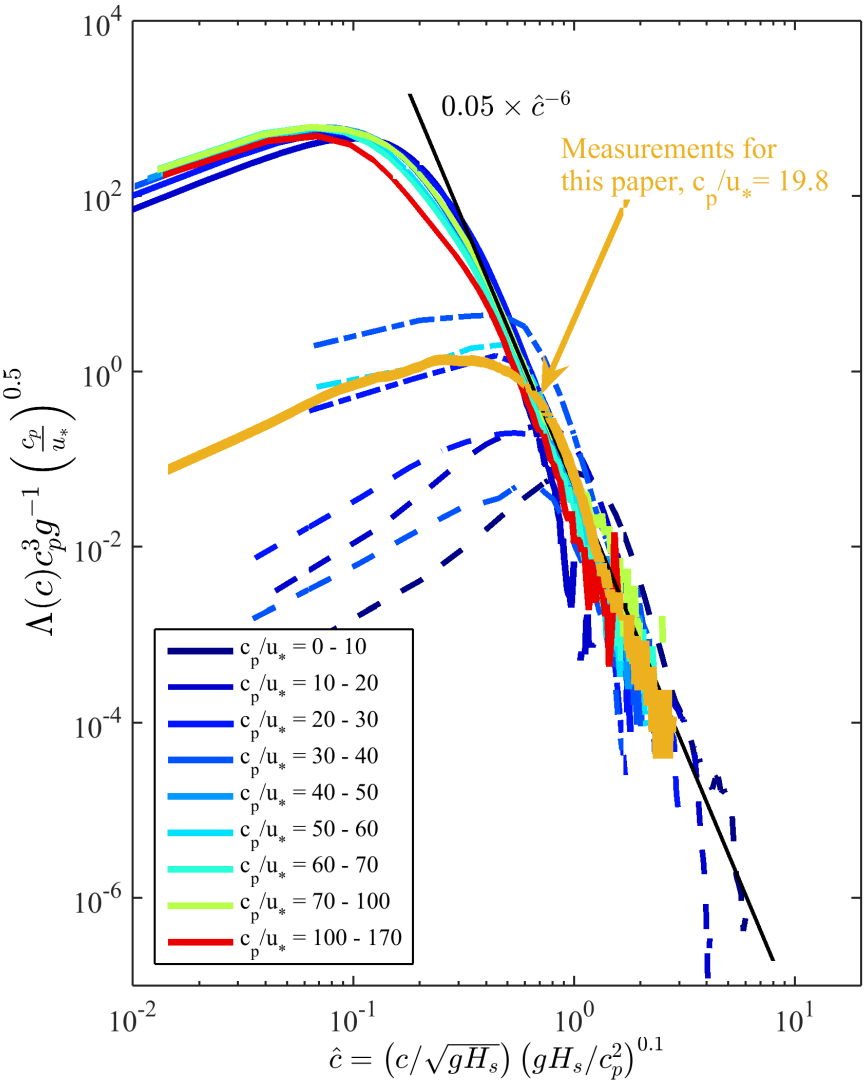

Figure 3.7: Representative example of nondimensional breaking length distribution computed from the airborne imagery collected on July 11 2015 2010 at 01:20 (UTC) during the HIRES experiment (orange solid line), overlaid on the nondimensional breaking distributions presented in Figure 4 of Sutherland and Melville (2013). Distributions have been binned by wave age with corresponding colors. Solid lines are measurements taken using stereo IR imagery, dash-dotted lines are from visible imagery, both collected from R/P FLIP, and dashed lines are from the airborne measurements of Kleiss and Melville (2010) during GOTEX.

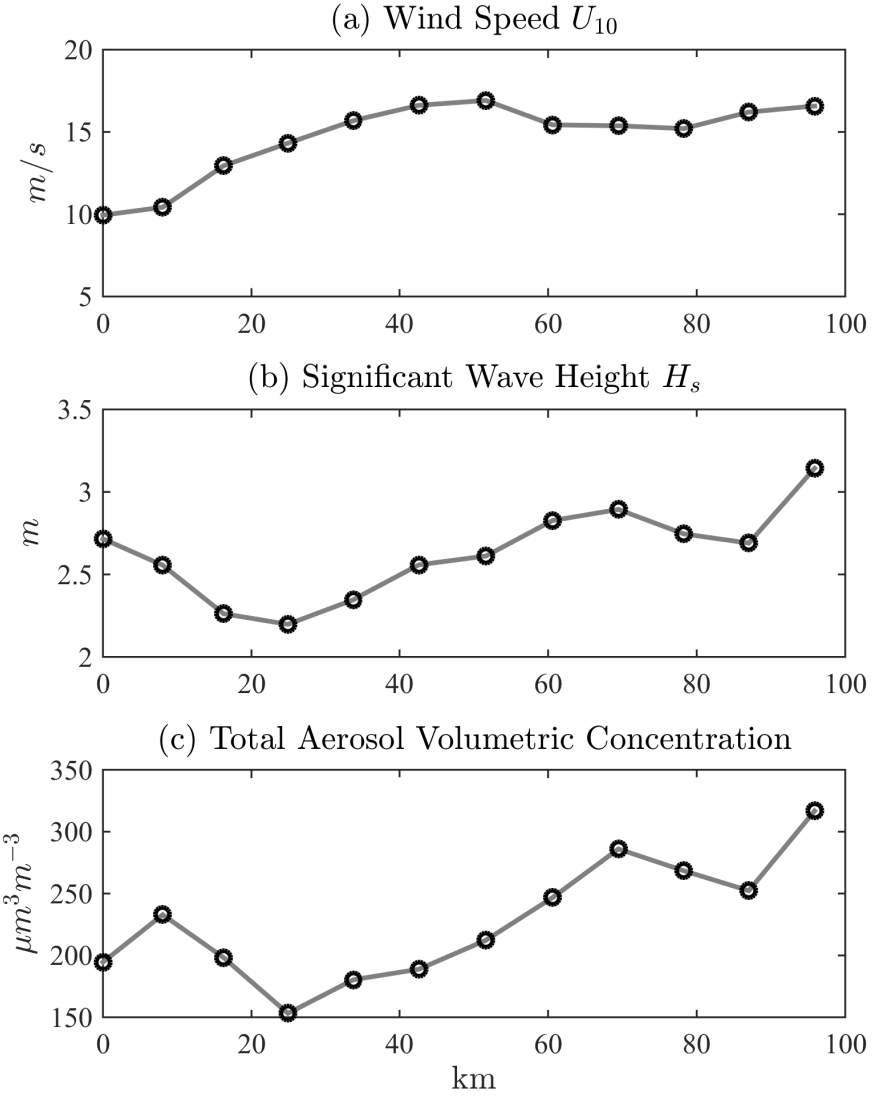

Figure 3.8: (a) Wind speed U_{10} (m/s), (b) significant wave height H_s(m) and (c) total aerosol volumetric concentration $V(\mu m^3 m^{-3})$ measured during a 95km, straight, 30m AMSL flight section on June 30 2010.

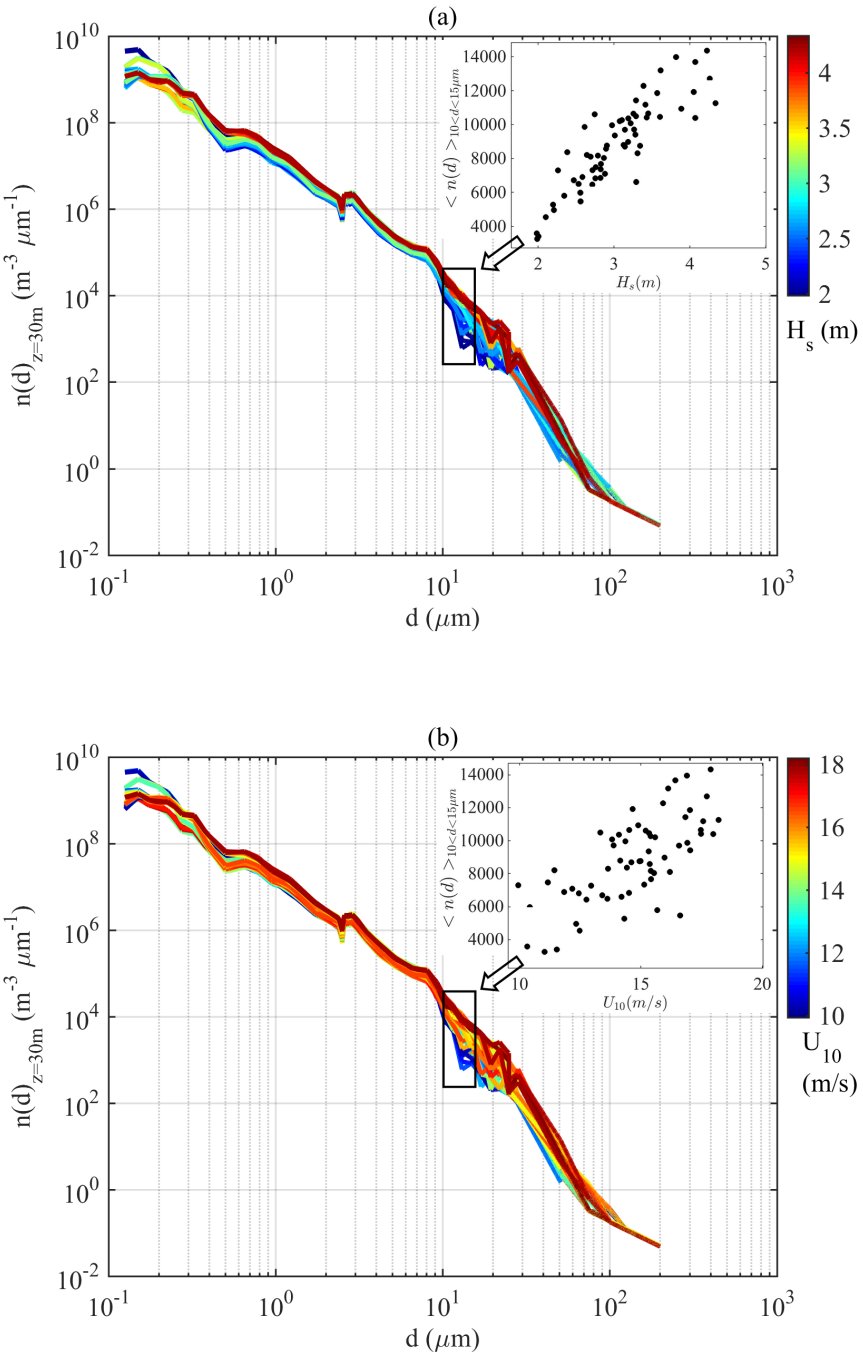

Figure 3.9: Aerosol size distributions for all HIRES2010 low-level flights (30m AMSL) color coded for (a), significant wave height H_s (m) and (b), 10m wind speed U_{10} (m/s). The inserts show the distribution level for an aerosol range diameter of 10 to 15 μm as a function of H_s (a) and U_{10} (b) illustrating the increased scatter in the aerosol size distribution levels when plotted as a function of wind speed.

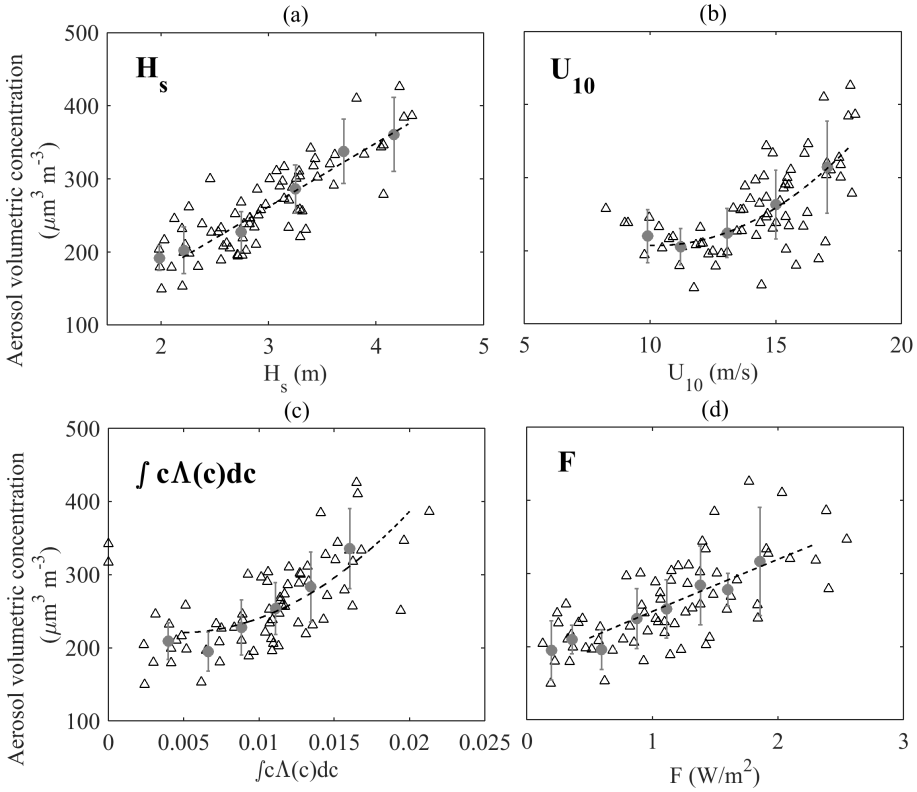

Figure 3.10: Total volume of aerosols measured during the HIRES 30m-AMSL flight sections as a function of (a) significant wave height H_s (m), (b) wind speed U_{10} (m/s), (c) first moment of the $\Lambda(c)$ distribution, and (d), computed dissipation by wave breaking F (W/m^2). The gray dots represent the corresponding bin-averaged values (with associated error bars), while the dashed line represents the fit of the data ((a) and (d) linear, (b) and (c) quadratic).

where b is the nondimensional breaking parameter. Based on the inertial scaling and laboratory data of Drazen et al. (2008) and Melville (1994) and laboratory data of Banner and Pierson (2007), Romero et al. (2012) computed a dimensionless breaking parameter that uses the azimuth-integrated surface wave saturation spectrum $B(k)$ defined as

$$B(k) = \int_{-\pi}^{\pi} \phi k d\theta k^3 \tag{3.12}$$

where $\phi(k, \theta)$ is the directional surface wave spectrum, a function of θ, the azimuthal direction (coming from) and k the surface wavenumber.

$b(k)$ is then defined as

$$b(k) = A_1(B(k)^{1/2} - B_T^{1/2})^{1/2} \tag{3.13}$$

where B_T is a threshold saturation and A_1 is a constant defined in Romero et al. (2012). This approach is supported by recent theoretical work from Pizzo and Melville (2013). Then $b(c)$ was computed from $b(k)$ assuming a linear dispersion relationship for gravity waves, $c = (g/k)^{1/2}$. Also, note that in this analysis we approximate the speed of the breaker c as the phase speed of the underlying wave[2].

Directional wavenumber spectra $\phi(k, \theta)$ are computed from the sea-surface displacement data collected with the ATM. Six-kilometer swath lengths are used for the analysis, typically 250 to 300 m wide in the cross track direction, using only the forward portion of the ellipsoidal scanning pattern[3]. Each data subset is regridded to a 2.5m horizontal spatial resolution using 2D linear interpolation, leading to an approximately 1.26 rad/m cutoff wavenumber. We found that the noise level typically started at lower wavenumbers, around 0.8-1 rad/m, the measured spectrum above this value was therefore discarded. The measured *directional* wavenumber spectra are extrapolated toward larger wavenumbers, up to 30 rad/m, using a k^{-4} power law that matches a constant saturation regime for the larger wavenumbers. This extrapolation is needed as a significant portion of the wave breaking dissipation lies in the 1 to 30 rad/m range (Romero et al., 2012; Sutherland and Melville, 2013). A sample omnidirectional and saturation spectrum is shown in figure 3.6.

The $\Lambda(c)$ distributions are computed from the non-dimensional scaling derived by Sutherland and Melville (2013), where the non-dimensional Λ distribution $\hat{\Lambda}(\hat{c})$ is given

[2]Field measurements of the speed of breaking fronts are typically found in the $[0.8 - 1]c$ range

[3]No significant differences were found between the spectra computed from the rear and forward scans computed over the same area

by

$$\hat{\Lambda}(\hat{c}) = \Lambda(c)c_p^3 g^{-1}\left(\frac{c_p}{u_*}\right)^{0.5} = 0.05 \times \hat{c}^{-6} \tag{3.14}$$

and

$$\hat{c} = \left(\frac{c}{\sqrt{gH_s}}\right)\left(\frac{gH_s}{c_p^2}\right)^{0.1}. \tag{3.15}$$

Here c_p is the phase speed of the waves at the peak frequency and H_s the significant wave height, both computed from the ATM measurements, $\sqrt{gH_s}$ is the speed at impact of a particle following a ballistic trajectory from a height $H_s/2$, c_p/u_* is the wave age and gH_s/c_p^2 is a characteristic wave steepness, also called the significant wave slope.

Measurements of the $\Lambda(c)$ distribution computed from the nadir-looking video imager installed on the aircraft for a selected number of representative portions of the flights were consistent with the scaling defined above by Sutherland and Melville (2013). A representative example is shown in figure 3.7. Based on the agreement of this scaling with the measurements, we use the formulation from Sutherland and Melville (2013) to compute the breaking distribution in the subsequent analysis. Note that the range of c was taken to be from 0.1 to 30 m/s for the wave breaking dissipation computation, and from 3 to 30 m/s for the first moment of the $\Lambda(c)$ distribution, phase speeds large enough to produce air entrainment during the breaking process (Sutherland and Melville, 2013) .

3.3.3 Dependence of Aerosol Concentration on Local Atmospheric and Sea State Conditions

The aerosol concentration measured at 30m above the mean sea level is expected to be influenced by non-local sources, but mostly for the smaller diameter particles that can travel over long distances for extended periods of time. Because of the measurement altitude considered here (30m AMSL), we can safely assume that most particle concentration measured at this height, under the considered range of conditions (2 to 4.5 m significant wave height, and 8 to 18 m/s wind speed) will be correlated with the local conditions. A simple estimate can be made based on the mean vertical Lagrangian velocity in a logarithmic boundary layer, which is $O(u_*)$, the friction velocity in the air. Now, $u_* = \sqrt{C_D}U_{10}$ where the usual notation holds. Thus the average time for a small particle to reach a height H is just H/u_*, and the horizontal distance traveled is just

$$X = \int_0^{H/u_*} U(z = u_* t)\mathrm{d}t. \tag{3.16}$$

If U_{10} is used to scale the horizontal velocity over heights of $O(10)$ m then $X \approx O(H/\sqrt{C_D})$. So for $H = 30$ m and $C_D = O(10^{-3})$, we have that the horizontal distance traveled from the surface to 30 m is of the order of one kilometer. This is the scale of the length of wave groups, the scale over which large breaking events are observed (Terrill and Melville, 1997, see also figure 3.3). Furthermore, given the potential significance of the large initial velocities associated with breaking events, it is likely that this is an overestimate for some range of particle sizes. Figure 3.8 illustrates the influence of local conditions on the aerosol volumetric concentration, where time series of wind speed U_{10}, significant wave height H_s, and total aerosol volumetric concentration V (aerosol diameters ranging from 0.1 to 200 μm) measured during a 95km, straight portion of flight (approximately 24min flight time) at 30m AMSL on June 30 2010 is shown. Each value is computed over a 6-km record of collected data. We find here that not only the total aerosol volumetric concentration generally better correlates with significant wave height and not wind speed, but the rapid response to the local changes in sea state conditions by the aerosol concentration data is remarkable, again stressing the need to incorporate local sea state information in SSSGF parameterization.

Figure 3.9 shows the aerosol number density distributions, $n(d)$, collected during all low-level flights (30m AMSL) over the range of environmental conditions experienced during the HIRES 2010 experiment. Each distribution is computed over a 6-km record of data collected from all available aerosol sensors described earlier, then interpolated over a regularly spaced range of diameters d ranging from 0.1 to 200 μm with 0.025 μm increments.

The aerosol number density distribution plotted in figure 3.9(a) is color coded for the significant wave height H_s computed from the nadir-looking lidar altimeter data over the same record length. Starting from diameters d larger than 0.3 μm, the aerosol distributions show a nicely organized dependence on the significant wave height, with levels increasing as H_s increased from 2 to almost 4.5m. In figure 3.9(b) the same distribution is shown, but this time color coded for U_{10}. In that case, the relationship between distribution levels and wind speed is much less organized. The two inserts show the distribution levels for an aerosol size range of 10 to 15 μm to illustrate the increased scatter with U_{10}.

The total aerosol volumetric concentration V measured over the 0.1 to 200μm diameter range considered here during the low altitude (30m AMSL) portions of the flights is shown in figure 3.10, as a function of the wave and MABL state parameters described in the prior section: (a) significant wave height H_s (m), (b) wind speed U_{10} (m/s), (c) first moment of the $\Lambda(c)$ distribution, and (d), computed dissipation by wave breaking F

(W/m^2). The measured aerosol volumetric concentration appears better correlated with H_s ($r^2 = 0.71$). Note that the first moment of the $\Lambda(c)$ distributions is often used to estimate active whitecap coverage, see e.g. Kleiss and Melville (2010, 2011). The first moment of the $\Lambda(c)$ distributions ($r^2 = 0.54$), the spectral estimate of the energy dissipated by wave breaking F ($r^2 = 0.49$), and the wind speed U_{10} (in figure 3.10(b), $r^2 = 0.48$) all show significantly lower correlations. This is of importance, as the wind speed has traditionally been used to parameterized sea spray source generation functions (de Leeuw et al., 2011; Veron, 2015).

3.3.4 Scaling of Aerosol Volumetric Concentration

To improve our understanding of the physical processes leading to the generation of such aerosol distributions in the MABL, and to relate them to the mechanisms through which marine aerosols may be created, we conduct a classical dimensional analysis of the dependence of $\mathcal{V}$, the total aerosol volumetric concentration, on other variables and parameters that characterize the local atmospheric and wave states. Note that $\mathcal{V}$ is the ratio of the total volume of aerosol $\mathcal{V}_p$ divided by the total volume of air, $\mathcal{V}_{air}$, and that $\mathcal{V} \equiv V$ for the measurements collected at z=30m in the present study.

$\mathcal{V}_p$ can be written as $f(H_s, u_*, \nu, \Gamma, g, \rho_a, \rho_w, k_p, \mathcal{V}_{air}, z)$ where ν is the kinematic viscosity of water, Γ is the surface tension, ρ_a and ρ_w the density of air and water, respectively, and k_p is the wavenumber at the peak of the wave spectrum. Aerated breaking is expected over the wavenumber range bounded at its lower end by k_p up to the wavenumber at the minimum phase speed in the gravity-wave range k_m defined as

$$k_m = \sqrt{\frac{\rho_w g}{\Gamma}} \tag{3.17}$$

Through dimensional analysis, we obtain

$$\mathcal{V} = \frac{\mathcal{V}_p}{\mathcal{V}_{air}} = f\left(\frac{u_* H_s}{\nu}, H_s k_p, \frac{c_p}{u_*}, \frac{\rho_a}{\rho_w}, \frac{k_m}{k_p}, B_o\right) q\left(\frac{z}{h_o}\right) \tag{3.18}$$

where $u_* H_s/\nu$ is a wave-state dependent Reynolds number, $H_s k_p$ is the significant wave slope, $\frac{c_p}{u_*}$ is the wave age computed using the wavelength at the peak of the wave spectrum, B_o is the spectral Bond number that uses the the speed attained in a ballistic trajectory from a height $H_s/2$ such that $B_o = (\rho_w - \rho_a)(gH_s)^2/g\Gamma$, and z/h_o is the ratio between the measurement height above mean sea level and the upper height of the evaporative region, set to H_s (see section 3a). The function f effectively represents the

amplitude of the volumetric concentration $\mathcal{V}$, while q captures the dependence on z. Unfortunately, we can not characterize q with the present data set, where detailed measurements are only available at one measurement height, z = 30m. Instead, we limit the scaling analysis to the amplitude term of $\mathcal{V}$, f, using V, the volumetric concentration measured at 30m such that

$$V = f\left(\frac{u_* H_s}{\nu}, H_s k_p, \frac{c_p}{u_*}, \frac{\rho_a}{\rho_w}, \frac{k_m}{k_p}, B_o\right). \tag{3.19}$$

That is, by definition $q(z/30) = 1$. We neglect here $\frac{\rho_a}{\rho_w}$, which is approximately constant during our measurements, and $\frac{k_m}{k_p}$, as $k_m >> k_p$. Since the ratio $(\rho_w - \rho_a)/g\Gamma$ was approximately constant during the experiment, and the remaining term only depends on H_s, we are left with

$$V = f\left(\left(\frac{u_* H_s}{\nu}\right)^{\alpha} \left(H_s k_p\right)^{\beta} \left(\frac{c_p}{u_*}\right)^{\gamma}\right). \tag{3.20}$$

Without loss of generality we can set $\alpha = 1$, then β and γ are iteratively varied to minimize a square difference cost function of the total aerosol volumetric concentration V. We find the best collapse for $\beta = 0.1$ and $\gamma = 3/4$ corresponding to $r^2 = 0.77$. The non-dimensional aerosol volumetric concentration for the HIRES experiment is shown in figure 3.11 as well as from the Gulf of Tehuantepec Experiment (GOTEX, Romero and Melville, 2010a; Kleiss and Melville, 2010, 2011), described in Appendix A. Aerosol number distributions, wave and atmospheric parameters were computed for Research Flight 10 of GOTEX, following the same procedures used for the HIRES experiment.

As the airborne aerosol sensors have a sample volume, the chance of undersampling, oversampling or mischaracterizing the spatial variability of the aerosol distribution increases for the larger aerosols, in particular for diameters above 20 μm. In that context, a more conservative approach consists of minimizing the same cost function described above, but this time for aerosol particles of diameter d smaller than $20\mu m$.

Taking $\alpha = 1$, we find $\beta = 0.25$ and $\gamma = 1$ corresponding to a r^2 of 0.84. Figure 3.12 shows the corresponding nondimensional volumetric concentration, and two quadratic fits computed from the HIRES data (red: y-intercept forced to zero, gray: no forcing). For aerosol diameters smaller than $20\mu m$, we find that the aerosol volumetric concentration can be parameterized by a wave Reynolds number, significant slope and wave age such that:

$$V = a\xi^2 + b\xi + c \tag{3.21}$$

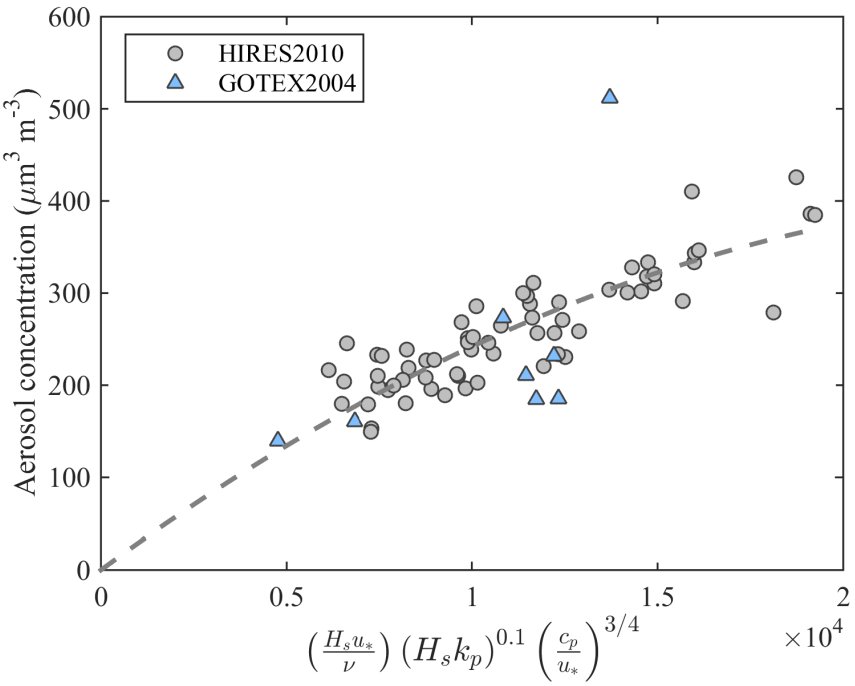

Figure 3.11: Non-dimensional total aerosol volumetric concentration for the HIRES and GOTEX2004 experiments plotted as a function of wave-state Reynolds number, significant wave slope, and wave age. The corresponding quadratic fit with the y-intercept forced to zero is shown as a dashed gray line.

where

$$\xi = \left(\frac{u_* H_s}{\nu}\right)\left(H_s k_p\right)^{0.25}\left(\frac{c_p}{u_*}\right) \tag{3.22}$$

For the quadratic fits shown in figure 3.12, we find $a = -2.0\text{x}10^{-7}$ ($-2.36\text{x}10^{-7}$), $b = 0.015$ (0.016), and $c = 14.7$ (0), with the values in the parentheses corresponding to the case with the y-intercept forced to zero.

Relating the aerosol volumetric concentration to both atmospheric and wave state variables over a wide range of environmental conditions is an important step toward better parameterization of the SSSGFs.

3.4 Section Summary

In this study, we have presented detailed measurements of aerosol number concentration in the Marine Atmospheric Boundary Layer, at altitudes ranging from as low as 30m and up to 800m AMSL over a broad range of environmental conditions (significant wave

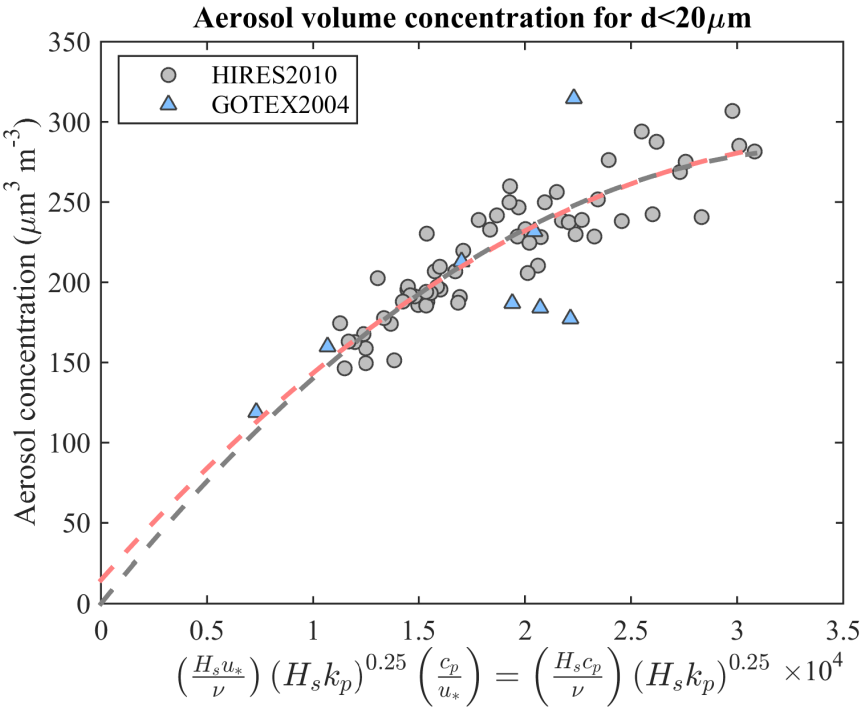

Figure 3.12: Non-dimensional aerosol volumetric concentration for the HIRES and GOTEX2004 experiments, plotted as a function of wave state Reynolds number, significant wave slope, and wave age, for aerosol diameters smaller than 20 μm. The corresponding quadratic fit with the y-intercept forced to zero is shown as a dashed gray line, while the one without forcing is shown in light red color.

height, H_s, of 2 to 4.5m and wind speed at 10m height, U_{10}, of 10 to 18 m/s) collected from instrumented research aircraft during the HIRES and GOTEX2004 experiments. The sea-state, parameterized as significant wave height, moments of the breaker distribution $\Lambda(c)$, and wave breaking dissipation F were measured by a suite of electro-optical sensors that included the NASA Airborne Topographic Mapper (ATM).

Large aerosol particles ($d > 40\mu m$) were found up to the top of the MABL. This is of importance as the role, generation and transport mechanisms of this range of aerosols are poorly understood (Veron, 2015), but are known to contribute to sensible and latent heat fluxes, and can also offer a means of transport for larger organic carbon compounds from the ocean, including the Dissolved Oxygen Component (DOC) and the Particulate Organic Component (POC)(Quinn et al., 2015).

Though much progress has been made in the past two decades, our understanding of the physical processes that occur when aerosol particles are created and ejected into the air flow, especially for the the larger particles with $d > 20\mu m$, is very limited. The scatter in SSSG estimates, especially for larger particles, is significant and has serious implications for modeling global aerosol budgets.

We presented here the sensitivity to a physically-based non-dimensional parameterization of the aerosol volumetric concentration measured at 30m AMSL during the HIRES2010 and GOTEX204 experiments. Though limited to one measurement height (30m AMSL) in the present work, this approach shows promise for including wave effects into models of marine aerosol production. More laboratory and field measurements are needed, perhaps along the lines of the Reid et al. (2001) experiment, collecting direct aerosol flux measurement in a fetch-limited environment, both in the surface aerosol source layer, perhaps from a a research vessel, buoy or platform, or unmanned surface vehicles (Lenain and Melville, 2014) and at height, from an aircraft (manned or unmanned), collocated with detailed measurements of the wave kinematics and wave breaking.

This work was published in the Journal of Physical Oceanography (American Meteorological Society) in December 2016 (Lenain and Melville, 2017a):

Lenain, Luc, and W. Kendall Melville. "Evidence of Sea-State Dependence of Aerosol Concentration in the Marine Atmospheric Boundary Layer." Journal of Physical Oceanography 47.1 (2017): 69-84.

CHAPTER 4

Numerical Simulations of Breaking Waves

Contents

4.1 Introduction

As shown in the previous section, the dynamics of breaking waves play a critical role in air-sea interaction processes. While important, the intermittency characteristic, both in time and space, of this phenomenon makes field measurements very challenging. Laboratory measurements of breaking waves permit the study of the dynamical quantities under strict control of the initial conditions. While this is a great improvement as compared to field efforts, the measurements remain limited by the sensors. Numerical simulations of breaking waves provide an independent opportunity to improve our understanding of the physics involved.

During the course of this thesis work, various numerical approaches were considered. The first one was a Lagrangian meshless method, called Smoothed Particle Hydrodynamics model (SPH), and its parallelized version, DualSPHysics, developed by Crespo et al. (2015). In this technique, the discretized Navier-Stokes equations are locally integrated

at the location of material points or particles initially seeded in the domain, according to the physical properties of surrounding particles. At each time-step new physical properties are calculated for each particle, and they are then displaced according to the updated values.

Monaghan (2012) provided an excellent review of the SPH model capabilities, initially developed in the late eighties, with renewed interest in the late 2000's once computation capability drastically improved, motivated in part by Graphics Processing Unit (GPU) computing. This method has been extensively used over the last 10 years for coastal engineering applications (e.g. Altomare et al., 2015) including sloshing and wave impact studies (e.g. Colagrossi et al., 2010; Shao et al., 2012; Rafiee et al., 2015, among others). This approach was however discarded in the present study, due to strong limitations in two-phase air-water simulations, as SPH has difficulties maintaining a homogeneous sampling of the flow, especially in the case of violent impact (e.g. generation of cavities without particles, instabilities close to the surface, particle clusters likely caused by local conservation problems).

Another approach was then considered, a two-phase flow, compressible, low-diffusive model built around a robust remapped Lagrangian solver to solve a "five-equation" gas-liquid volume averaged model (Allaire et al., 2002; Kokh and Lagoutiere, 2010). Lagrange-remap numerical schemes are a particular family of Eulerian Finite Volume Method (FVM). At each time step, the equations are solved in a Lagrangian frame with a mesh that is advected by the flow itself. The obtained so-called "Lagrange solution" is then *remapped* on the initial mesh by estimating both mass and momentum flux. The model considered here was based on the work of Bernard-Champmartin and De Vuyst (2014) who developed a remapped Lagrangian solver to solve a "three-equation" gas-liquid volume averaged model. For the capture of the interface, a challenging aspect of bifluid numerical simulations, a combination of upwinding and downwinding schemes (Després and Lagoutière, 2001; Kokh and Lagoutiere, 2010), and a variant improved anti-diffusive approach was used. The resulting interface capturing, based on the solution of a transport equation of an Eulerian Cartesian grid, provided very sharp gas-liquid moving boundaries. Arbitrary Lagrangian-Eulerian Methods (ALE) were used to simulate the displacement of a piston-type vertical paddle at one end of a numerical channel. Despite initial promising results, consistent with the dam break numerical and experiment comparisons of Bernard-Champmartin and De Vuyst (2014), the experimental model turned out to be too unstable to study breaking wave processes.

Our final approach, presented in the following section, was to turn to a volume-of-

fluid (VOF) model, GERRIS. Here, a numerical tool provides a framework to calculate the solutions of the Navier-Stokes equations in an idealized experimental setup. This section presents numerical simulation of deep water breaking wave in an idealized wave channel by solving the full Navier-Stokes equations in a two-phase flow (air and water), in two dimensions using Gerris. Here we focus on two majors experimental results:

- The work of Rapp and Melville (1990), Drazen et al. (2008) and Drazen and Melville (2009) that demonstrated the important role played by breaking waves in the mixing of the upper ocean. Through laboratory dye experiments, Rapp and Melville (1990) showed that the mixed region generated by a breaking wave rapidly deepened below the surface, then followed a $(t - t_b)^{1/4}$ power law (t is the time, and t_b the time of breaking).

- The aerosol size distribution produced by mechanically-generated breaking waves, based on the laboratory work of Veron et al. (2012), Towle (2014), and the recent LES simulations of breaking waves from Wang et al. (2016).

A description of the numerical code and a detailed presentation of the breaking wave generation procedure is follows.

4.2 Gerris Numerical Code

Gerris is an open-source numerical code, developed by Stephane Popinet (Popinet, 2003, 2009), and supported by NIWA (National Institute of Water and Atmospheric Research, New Zealand) and the Institut Jean le Rond d'Alembert. Gerris is a framework to solve partial differential equations adaptively based on quad/octree spatial discretization. It has been successfully used over a range of finite-volume discretisation techniques which allow the solution of: advection-diffusion equations, Euler, Stokes, Navier-Stokes, Saint-Venant, Poisson and Helmholtz equations and systems of conservation laws. Detailed description of the numerical methods is presented in Popinet (2003, 2009). This numerical tool has been used to simulate complex multiphase flow, such as atomization processes (Fuster et al., 2009; Agbaglah et al., 2011), capillarity wave studies (Deike et al., 2014, 2015) and more recently air-entrainment under breaking waves (Deike et al., 2016). It has been extensively validated in a number of studies, see for example Popinet (2009); Bagué et al. (2010); Fuster et al. (2013) among others.

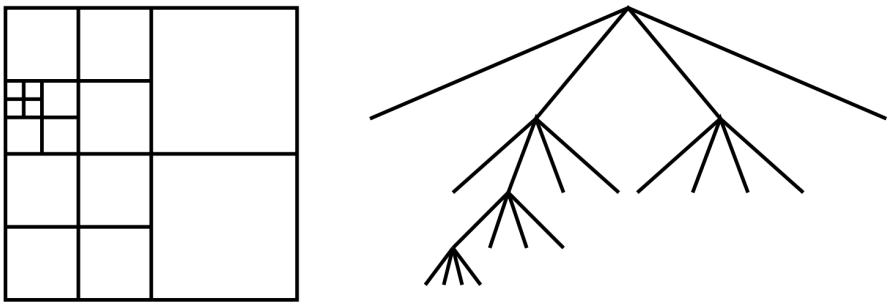

Figure 4.1: Graphical representation of Gerris quadtree discretisation (left) and corresponding logical structure (right), taken from Agbaglah et al. (2011).

Here the full Navier-Stokes equations in a two-phase, incompressible, air-water, flow are solved with constant surface tension, in 2D. The interface between air and water is reconstructed using a volume of fluid (VOF) method. The multifluid interface is traced using a function defined as the volume fraction of a given fluid in each cell of the computation domain (Popinet, 2003, 2009). The level of idealization is mainly driven by the domain dimensions (2D vs. 3D), the complexity of the physical models embedded in the equations (e.g. description of the interface for multiphase flows), the level of complexity of the boundary conditions (e.g. velocity profiles, free/no-slip conditions) and the treatment of the turbulence.

Gerris combines the use of quadtrees (octrees in 3D) for adaptive spatial discretisation with efficient parrallelisation (Agbaglah et al., 2011), making it very well suited for the proposed simulations. This approach helps mitigate computational time issues in fluid flow modelling associated with the broad range of spatial scales encountered in complex simulations. In that context, the benefits of the adaptive mesh refinement, where the spatial discretization is adjusted to follow the scale and temporal evolution of flow structures, is evident.

The Gerris code solves the incompressible, variable density, Navier-Stokes equations with surface tension such that

$$\rho\left(\frac{\partial \mathbf{u}}{\partial t} + \mathbf{u}\cdot\nabla\mathbf{u}\right) = -\nabla p + \nabla\cdot(2\mu\mathbf{D}) + \gamma\kappa\delta_s\mathbf{n}, \tag{4.1}$$

$$\frac{\partial \rho}{\partial t} + \nabla\cdot(\rho\mathbf{u}) = 0, \tag{4.2}$$

$$\nabla\cdot\mathbf{u} = 0. \tag{4.3}$$

with **u** the fluid velocity in vector form, $\rho \equiv \rho(x, y, z, t)$ the fluid density, $\mu \equiv \mu(x, y, z, t)$ the dynamic viscosity and **D** the deformation rate tensor defined as

$$\mathbf{D}_{ij} \equiv \frac{\partial_i \mathbf{u}_j + \partial_j \mathbf{u}_i}{2}. \tag{4.4}$$

The term δ_s is the Dirac distribution function for the surface tension concentrated at the interface where γ is the surface tension coefficient, κ and **n** the curvature and normal to the interface. The domain can be 2D, 3D or axisymmetric. These equations are called a "one-fluid" formulation (Tryggvason et al., 2011) where the same equations apply in the entire domain.

The volume fraction $\mathrm{T}(x, y, t)$ is used to define the density and viscosity in the domain, such that

$$\rho(\mathrm{T}) = \mathrm{T}\rho_w + (1 - \mathrm{T})\rho_a \tag{4.5}$$

and

$$\mu(\mathrm{T}) = \mathrm{T}\mu_w + (1 - \mathrm{T})\mu_a \tag{4.6}$$

with ρ_w, ρ_a, μ_w and μ_a representing respectively the density and viscosity of the two phases, water and air. Following the method described in Popinet (2009), the surface tension effects in equation 4.1 are represented explicitly in the simulations and are uniform throughout the domain.

The domain is composed of adjacent boxes, connected together. Each box is discretized using a quadtree (octree in 3D) scheme (see figure 4.1). Each cell may be the parent of either four (2D) or eight (3D) children. Spatial discretisation is done by splitting the cells into two in each directions several times. The level of refinement corresponds to the number of times this splitting is applied to reach the size of the cell. The finest refinement used in the simulation is obtained for the maximum grid level L_{max}. For reference, a maximum grid level L_{max} of 11 means that the smallest cell in the domain is 2048 times smaller than the box (2^{11}).

In the case of surface wave simulations, we choose a refinement criteria based on the flow vorticity and the interface between the liquid and the gas phases to obtain a high resolution depiction of the interface and the boundary layer where energy will be dissipated. In turn, further away from the interface, the resolution decreases since the quasi-irrotational motion can be appropriately described with a coarser mesh. For simplicity in the code, the level of neighboring cells cannot differ by more than one. The

scheme to solve the equations is second order in time and space. A classical time splitting projection method leads to the resolution of a Poisson equation. A multigrid Poisson solver is described in Popinet (2003) for the quad/octree data structure of Gerris.

4.3 Breaking Wave Generation

Breaking waves are generated using dispersive focusing, a technique initially introduced by Longuet-Higgins (1974), subsequently used in laboratory experiments to study turbulence, dissipation and air entrainment produced by deep-water breaking waves (Melville and Rapp, 1985; Dommermuth et al., 1988; Chan and Melville, 1988; Rapp and Melville, 1990; Lamarre and Melville, 1991; Loewen and Melville, 1994; Deane and Stokes, 2002; Drazen et al., 2008; Drazen and Melville, 2009).

In the laboratory, waves are generated using a computer controlled wavemaker/wave paddle apparatus installed at one end of a long channel, moving horizontally to produce surface waves. For reference, the channel used in Drazen et al. (2008)'s work, located at the Hydraulics Laboratory, Scripps Institution of Oceanography (SIO, San Diego, CA USA) is 30m long, 0.5m wide and 1m deep.

In the dispersive focusing technique, a packet of waves of varying frequency and amplitude is generated such that through constructive interference, the phases add at a pre-determined time t_b, and distance x_b, to produce a breaking event. As an example, figure 4.2 shows a sequence of images of a plunging breaker collected from a high-speed camera at the SIO hydraulics laboratory, in the same wave channel used by Drazen et al. (2008). The free surface displacement in the channel is defined as

$$\eta(x,t) = \sum_{n=1}^{N} a_n cos\left(k_n x - \omega_n t - \phi_n\right) \tag{4.7}$$

where a_n is the amplitude of the nth component, k_n is the wavenumber, $\omega_n = 2\pi f_n$ the angular frequency, ϕ_n the phase and N the total number of frequency components.

We introduce here the linear surface wave dispersion relationship, defined as

$$\omega_n = g k_n tanh(k_n H), \tag{4.8}$$

where H is the water depth and g is the gravitational constant. To focus a wave packet at a pre-determined time and location, t_b and x_b respectively, we can force the phase of each component to constructively interact such that

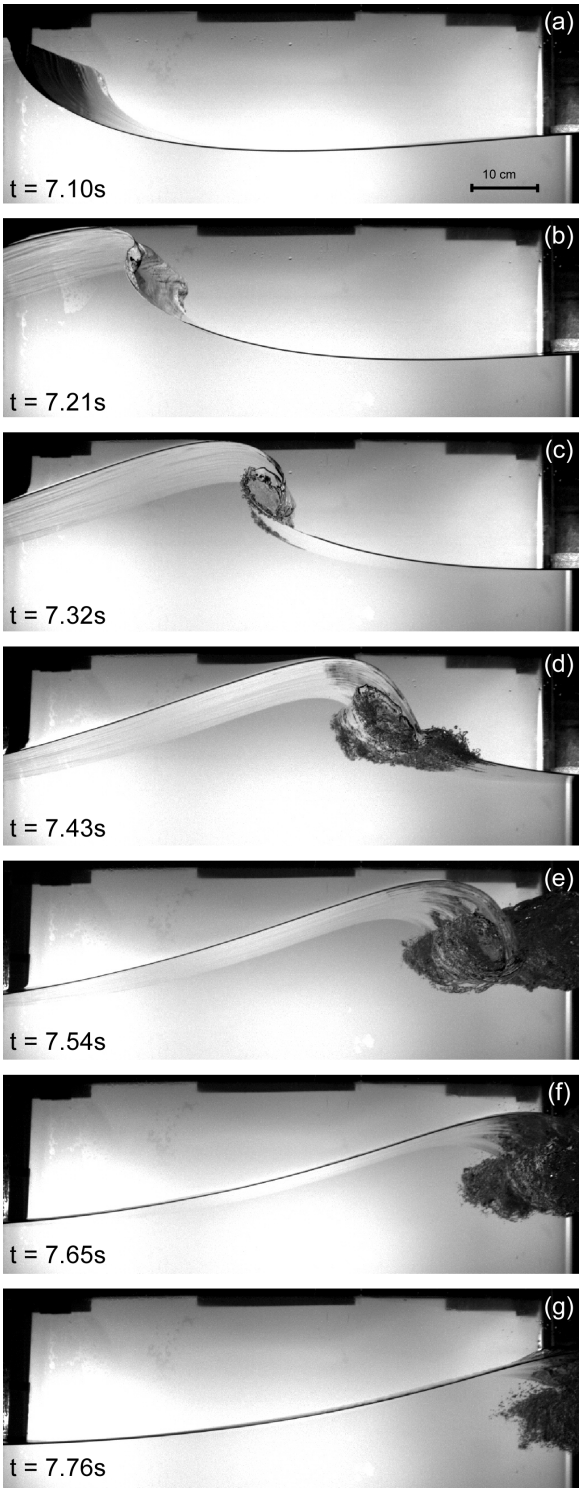

Figure 4.2: A sequence of images taken from a high-speed video of a plunging breaking wave generated at the SIO Hydraulics Laboratory Glass channel. The time is noted in each frame ($dt = 0.11s$). The wave was set to break 6m away from the paddle, with a wave packet central frequency $f_c = 0.8Hz$ and an non-dimensional bandwidth $\delta f / f_c$ of 1.

$$cos(k_n x_b - \omega_n t_b - \phi_n) = 1. \tag{4.9}$$

Substituting into equation 4.8, we obtain

$$\eta(x,t) = \sum_{n=1}^{N} a_n cos\left(k_n(x - x_b) - \omega_n(t - t_b)\right). \tag{4.10}$$

Using the same method, the velocity vector $\mathbf{u} = (u, v)$, a function of the depth z is then defined as

$$u(x,y,t) = \sum_{n=1}^{N} a_n \omega_n sin\left(k_n(x - x_b) - \omega_n(t - t_b)\right) \frac{cosh\left(k_n(z + H)\right)}{cosh\left(k_n H\right)} \tag{4.11}$$

and

$$v(x,y,t) = \sum_{n=1}^{N} -a_n \omega_n cos\left(k_n(x - x_b) - \omega_n(t - t_b)\right) \frac{sinh\left(k_n(z + H)\right)}{cosh\left(k_n H\right)} \tag{4.12}$$

At the paddle location, for $x = 0$, equation 4.10 simplifies to

$$\eta(0,t) = \sum_{n=1}^{N} a_n cos\left(-k_n x_b - \omega_n(t - t_b)\right). \tag{4.13}$$

Following Drazen et al. (2008), a_n is adjusted such that the contribution to the energy spectrum is equal for each component, by keeping $a_n k_n$ constant. Note that Rapp and Melville (1990) used instead a constant amplitude assumption. The total slope S is defined as

$$S = \sum_{n=1}^{N} a_n k_n. \tag{4.14}$$

We also introduce here the center frequency of each wave packet, f_c, and its non-dimensional bandwidth $\delta f / f_c$, used as input to the simulations.

An example of a wave packet, showing both surface displacement $\eta(x = 0, t)$ and velocity profile $\mathbf{u}(x = 0, z, t)$ is shown in figure 4.3. In this example, f_c is equal to 0.8Hz, $\delta f / f_c = 1$, $x_b = 6m$, and $N = 32$.

In the present study, numerical simulations of breaking waves are conducted for $f_c = 1.28Hz$ and $f_c = 0.88Hz$, keeping $\delta f / f_c$ constant and equal to 0.75 for all cases. The slope S is varied from as low as 0.368 and up to 0.432. Finally, the breaking location x_b

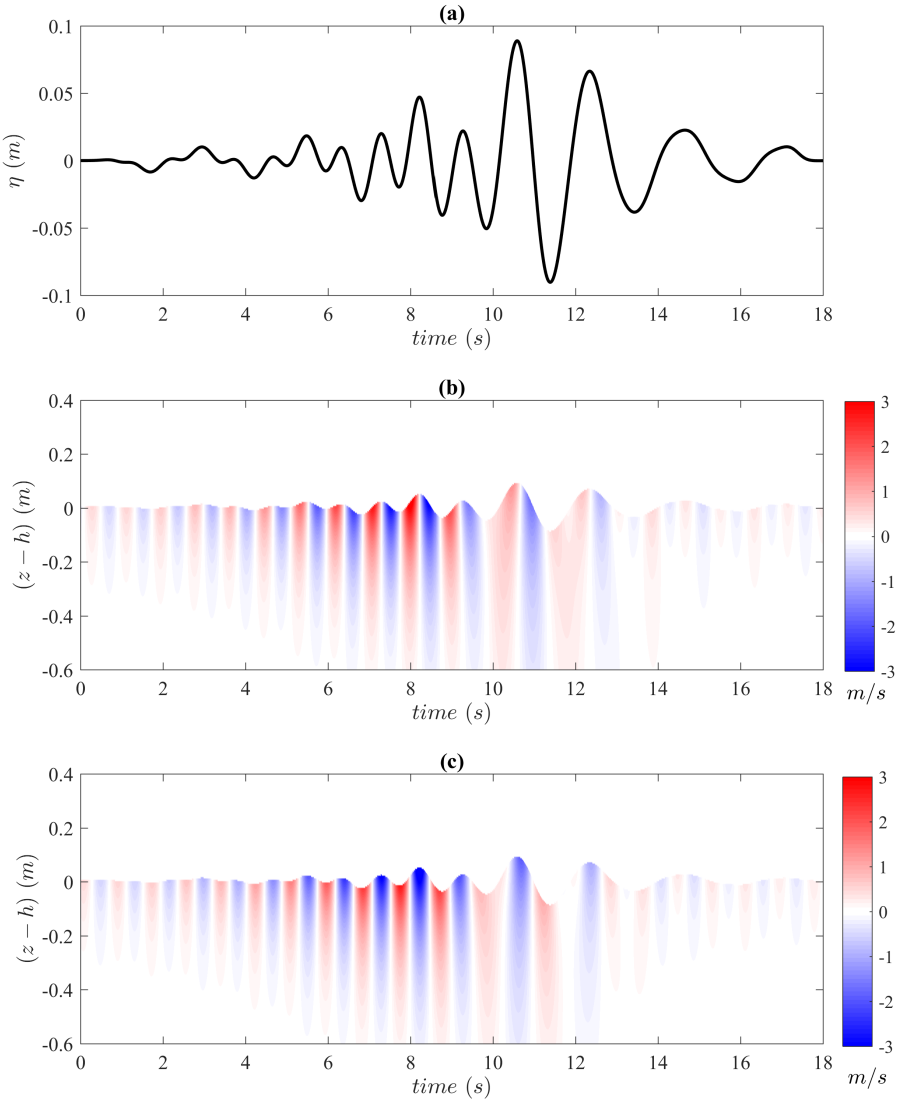

Figure 4.3: (a) An example of surface displacement $\eta(x = 0, t)$ at the wave paddle. The wave packet is set to break 6m away from the paddle, with $f_c = 0.8Hz$ and an non dimensional bandwidth $\delta f / f_c$ of 1. Corresponding components of the velocity profile $\mathbf{u}(x = 0, z, t)$, u and v, in m/s.

was set to 6m for the runs using $f_c = 1.28Hz$ and 12m for the ones where $f_c = 0.88Hz$.

4.4 Numerical Wave Channel

The numerical simulation of the wave channel is directly based on the work of Luc Deike (Deike et al., 2014, 2015, 2016, 2017). Here we use a 32m long tank, of height $h = 2m$, and a water level set to $H = 1m$. The top and bottom walls are free-slip. A wave is initialized on the left-hand size of the domain by imposing velocity and air-water interface (i.e. water surface elevation) boundary conditions for the duration of the considered wave packet.

Waves propagate in the x direction and focus at the pre-determined time t_b and location x_b where breaking occurs, if the slope is large enough. To avoid contamination of the remainder of the wave packet reflecting from the right boundary of the domain, we used a technique developed by Deike et al. (2017) that consists of adding a numerical sponge layer in the end part of the channel, by imposing an empirical friction term to attenuate the velocity. Note that a long, sloped beach is usually used to attenuate the waves in laboratory experiments. Here, the sponge layer starts 24m away from the left-hand-side of the domain, consistent with the dimension of the wave channel working area used in the laboratory measurements of Rapp and Melville (1990) and Drazen et al. (2008).

In the simulations, the air-water density ratio $\alpha = \rho_a/\rho_w$ is set to $1/850$, the air-water dynamic viscosity ratio $\beta = \mu_a/\mu_w = 1.96 \times 10^2$ given by $\mu_a = 1.74 \times 10^7\ kg/(m\ s)$ and $\mu_w = 8.9 \times 10^{-4} kg/(m\ s)$.

The Reynolds number in the water Re is defined as

$$Re = cL/\mu_w, \tag{4.15}$$

where $L = \lambda$ the length scale, c the linear gravity wave phase speed, such that

$$c = \frac{\omega}{k} \approx \sqrt{\frac{g}{k}} \tag{4.16}$$

giving

$$Re = \frac{\sqrt{g\lambda^3}}{\nu_w} \tag{4.17}$$

Where ν_w is the kinematic viscosity of water. Following the approach of Deike et al. (2015), we empirically reduce the water kinematic viscosity to obtain a Reynolds number

of about 40000 while keeping the value of the dynamic viscosity ratio β at its physical value defined earlier. This requirement is driven by computational limitations, translating into spatial resolution constraints. While this number is much smaller than the Reynolds number corresponding to waves propagating in a wave channel (i.e. $Re \approx 10^6 - 10^7$), this value is sufficient to correctly resolves the viscous boundary layer, essential to properly resolve the jet generated at the onset of breaking (Deike et al., 2014, 2015). Additionally, the numerical studies of Deike et al. (2014, 2015, 2016) have demonstrated that such parameterizations lead to results consistent with laboratory studies.

In the simulations L_{max} was set to 11 at the air-water interface, leading to a maximum mesh resolution of $2/2^{11} \approx 1mm$. The maximum grid level in the water and air was set to 9, giving a maximum mesh resolution of approximately 4mm to resolve vortical structures in the air or water.

The domain is seeded with particles to characterize the vertical transport and turbulent mixing along the lines of the Rapp and Melville (1990) surface dye experiments. To this effect, the flow is initially seeded with particles $2mm$ apart, $\pm 3m$ from x_b, at depths ranging from the surface to $10mm$. For the latter case, only particles at depths less than $4mm$ are considered in the analysis. The location of each particle is tracked in space and time, with an update every 0.1 sec.

Figures 4.4 and 4.5 show examples of the evolution in time and space of the surface elevation $\eta(x,t)$ for two different center frequencies f_c, 0.88 and 1.28 Hz. Waves are propagating left to right in the domain, focusing around the breaking time t_b. The wave focusing is evident in both cases, leading to a wave breaking (plunging) around $x_b = 12m$ and $x_b = 6m$ for figures 4.4 and 4.5 respectively. Note that no wave reflection from the right side of the tank is visible, in particular in the lower frequency case, where the wave packet is traveling much faster demonstrating the efficiency of the sponge layer developed by Deike et al. (2017).

Unless stated otherwise, all the quantities presented in the following are normalized by the center radial frequency ω_c, the corresponding wavenumber k_c and phase speed c_c obtained from the linear surface wave dispersion relationship, t_b the time of breaking, and x_b the measured breaking location such that

$$x^* = (x - x_b)\, k_c, \tag{4.18}$$

$$t^* = (t - t_b)\, \omega_c, \tag{4.19}$$

$$z^* = z k_c. \tag{4.20}$$

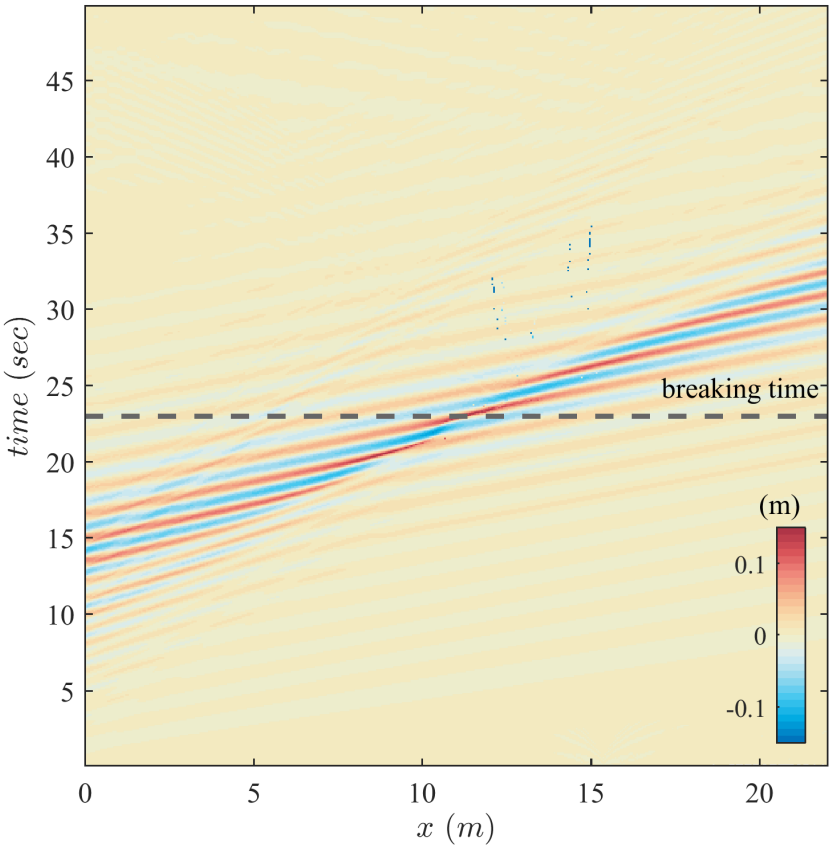

Figure 4.4: Space-time diagram of $\eta(x,t)$ showing the propagation and focusing of the wave packet at the predetermined location x_b and t_b. Here $f_c = 0.88Hz$, $\delta f/f_c = 0.75$, the slope $S = 0.432$.

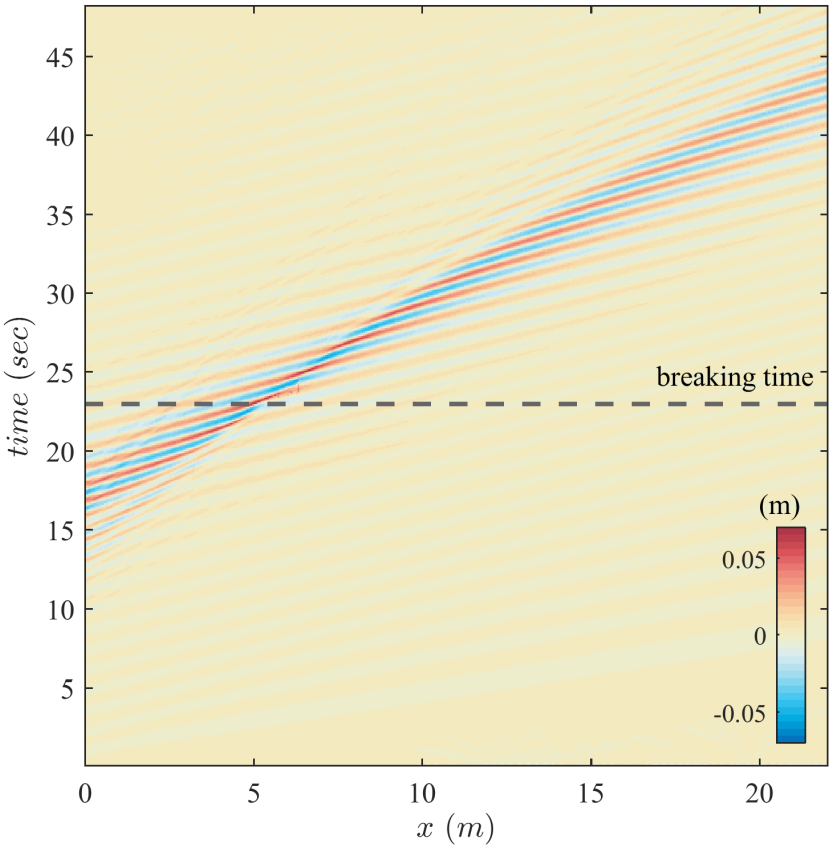

Figure 4.5: Same as figure 4.4 for $f_c = 1.28Hz$, $\delta f/f_c = 0.75$, the slope $S = 0.416$. Note that the wave focusing and subsequent breaking occurs at $x_b \approx 5.5 - 6m$ in this case.

The water velocity vector $\mathbf{u}$ is normalized by the phase speed c_c. The vorticity in both phases Ω is defined as

$$\Omega = \frac{\partial v}{\partial x} - \frac{\partial u}{\partial z}, \tag{4.21}$$

and is normalized by

$$\Omega_o = \frac{\sqrt{g\lambda}}{\lambda}. \tag{4.22}$$

Figure 4.6 shows a representative example of the evolution of a plunging breaker ($f_c = 1.28Hz$, $\delta f/f_c = 0.75$, and $S = 0.416$) generated in the numerical wave tank. The surface elevation $\eta(x,t)$ is shown as a black line, while the blue dots show the location of the particles seeded in the flow. Note that the location of each Lagrangian tracer i is defined as $(x_i^L(t), z_i^L(t))$.

The sequence of images selected around the predicted time and location of breaking is qualitatively similar to the sequence of photos collected in a laboratory wave channel presented in figure 4.2, the laboratory work of Rapp and Melville (1990), Drazen et al. (2008), Drazen and Melville (2009) as well as previously performed numerical simulations of plunging breakers, both DNS (Iafrati, 2009, 2011) and Large Eddy Simulations (Derakhti and Kirby, 2014, 2016). Here we find that once the focused wave becomes steeper, to the point that the forward face of the wave is almost vertical, a jet is formed at the wave crest, then rapidly plunges toward the surface underneath, under the influence of gravity, producing air entrainment and bubbles in the water and the generation of spray aerosols in the air.

Figures 4.7 and 4.8 show the normalized velocity field $(u(x^*, z^*), v(x^*, z^*))/c_c$ for selected values of t^*. The maxima of the horizontal velocity field is found near the crest of the wave, increasing in amplitude as the jet forms, then following a ballistic trajectory (Drazen et al., 2008). The normalized vertical velocity field is negative to the left of the wave crest, and positive on the right side, with a maximum value found shortly before breaking on the forward face of the focused wave. Figures 4.9 and 4.10 show the normalized vorticity Ω/Ω_o for the same value of t^*. During the breaking process, the positive (counterclockwise) vorticity remains located above the crest and the jet, while the vorticity right above the trough is negative (clockwise) and of much smaller amplitude. A separation of the vorticity layer in the air to the left of the crest is evident. Finally, after the jet hits the surface and subsequently overturns, a lot of spatial variability is found in the vorticity field. Note for example the generation of areas of high vorticity, both positive and negative, in the wake of the aerosols generated during the breaking process, traveling away from the location of impact, and visible in the last panel of figure 4.9. We

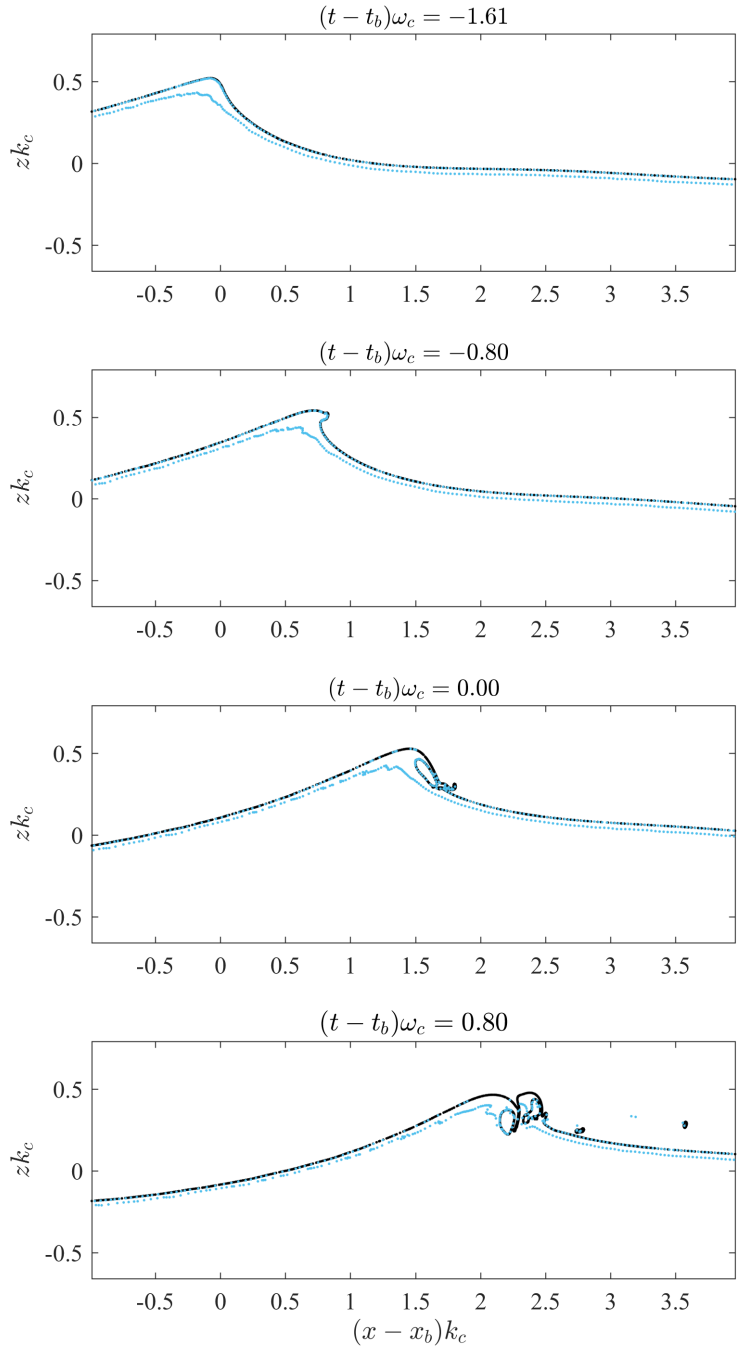

Figure 4.6: Evolution of surface elevation $\eta(x,t)$ (black line) and seeded particles (blue dots) around the time of breaking for $f_c = 1.28Hz$, $\delta f/f_c = 0.75$, and $S = 0.416$. Focusing occurs at $t \approx t_b$.

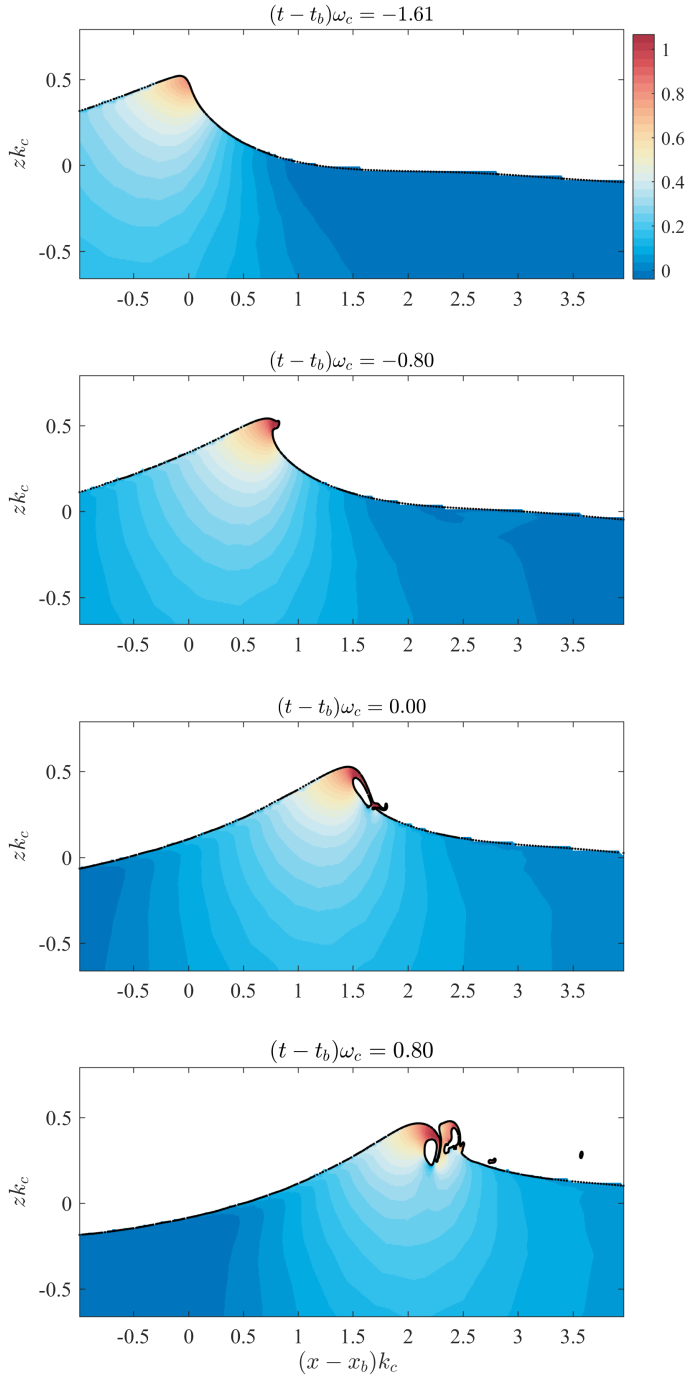

Figure 4.7: Evolution of the normalized horizontal velocity u/c_c around the time of breaking for $f_c = 1.28Hz$, $\delta f/f_c = 0.75$, and $S = 0.416$. Focusing occurs at $t \approx t_b$. Note that only the velocity in the water phase is shown.

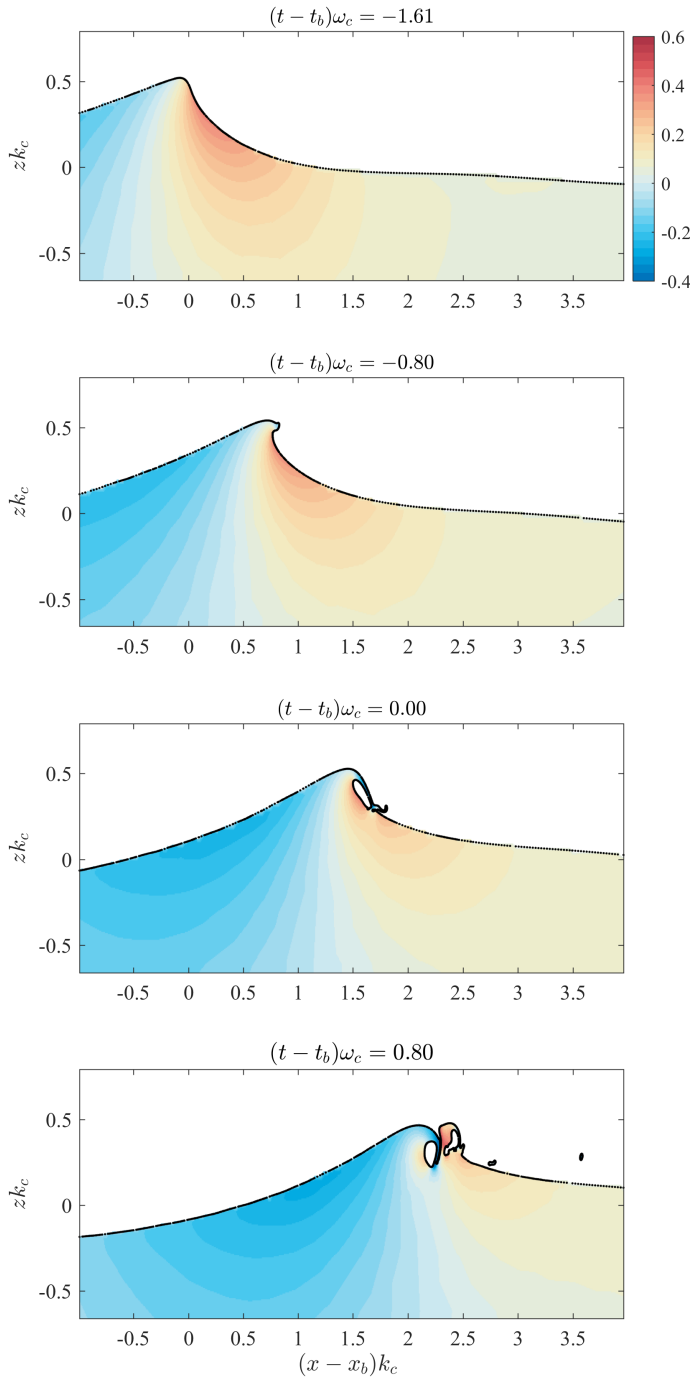

Figure 4.8: Evolution of the normalized vertical velocity v/c_c around the time of breaking for $f_c = 1.28Hz$, $\delta f/f_c = 0.75$, and $S = 0.416$. Focusing occurs at $t \approx t_b$. Note that only the velocity in the water phase is shown.

find the vorticity in the water to be much smaller than that of the air, slightly positive below the crest of the wave prior to the generation of the jet, and then mostly negative up to the point where the jet hits the surface.

4.5 Mixing Properties in the Breaking Region

In Rapp and Melville (1990)'s laboratory experiments, the study of mixing in the breaking region was done by quantifying the rate and spatial extent of the portion of the water initially at the surface. To do so, a dye patch, or rather sheet, was released near the breaking location in such a way that its vertical extent was kept minimal. The evolution of the geometry of the plume was then recorded using flow visualization techniques, in order to characterize the time rate of lengthening, deepening and the increase of area of the mixed region, identified by the dye.

As we are not able to release dye in the present numerical wave tank simulations, that would require, among other things, the parameterization of a diffusion model for the dye, our approach here is to release a large amount of Lagrangian particles, initially at the surface (see details in prior section) and then track their position $(x_i^L(t), z_i^L(t))$ in space and time to identify any behavior or pattern in the group of particles being mixed down after the breaking event.

Here the groups of particles were analyzed to obtain the maximum depth $D(t^*)$, non-dimensionalized using k_c^{-1} as the length scale. We use the depth of the particles $\tilde{z}_i^L$ relative to the free surface $\eta(x^*, t^*)$ defined such that

$$\tilde{z}_i^L(x^*, t^*) = z_i^L(x^*, t^*) - \eta(x^*, t^*). \tag{4.23}$$

Numerical simulations of deep water plunging breaking waves were conducted for two center frequencies f_c, equal to 1.28Hz and 0.88Hz. The frequency bandwidth $\delta f / f_c$ was kept constant in all runs. The slope was ranged from $S = 0.368$ to $S = 0.432$ for $f_c = 0.88Hz$ ($S = 0.368; 0.400, 0.432$) and from $S = 0.390$ to $S = 0.416$ for $f_c = 1.28Hz$ ($S = 0.390; 0.410; 0.432$). No spilling cases were simulated at this time.

Figure 4.11 and 4.11 show the evolution of the plume of particles after a breaking event for two different slopes, $S = 0.432$ and $S = 0.368$ respectively. The flow is initially seeded with particles $2mm$ apart, $\pm 3m$ from x_b, at depth ranging from the surface to a depth of $4mm$, for a total of 9000 tracers, corresponding to the top panel in both figures. The red line corresponds to the vertical extent of the particle plume, conceptually

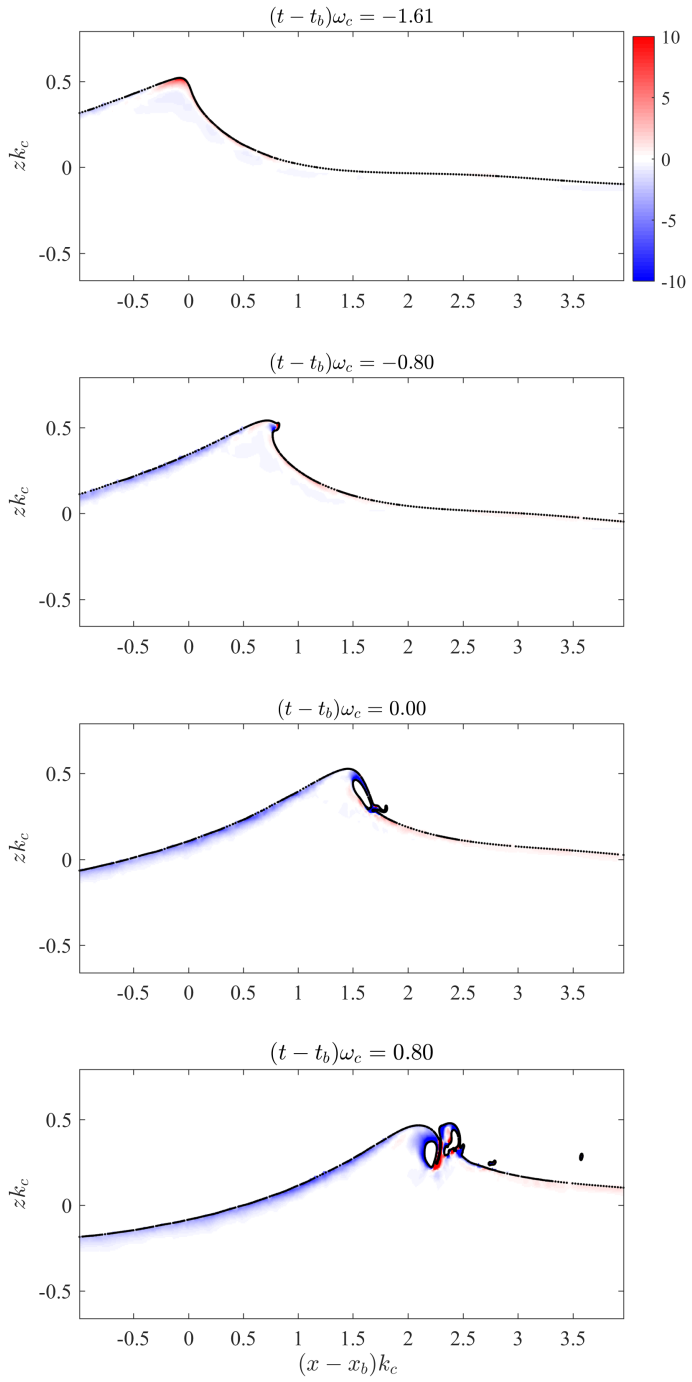

Figure 4.9: Evolution of the normalized vorticity Ω/Ω_o in the water around the time of breaking for $f_c = 1.28Hz$, $\delta f/f_c = 0.75$, and $S = 0.416$. Focusing occurs at $t \approx t_b$.

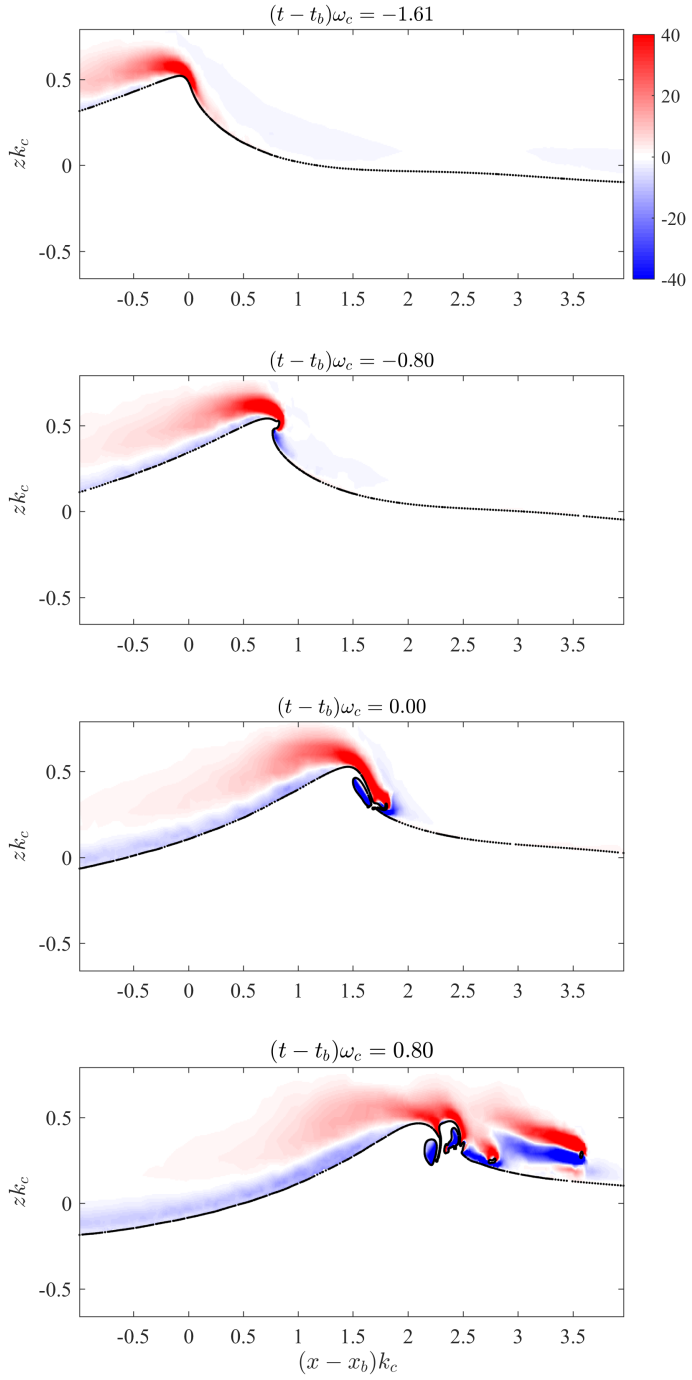

Figure 4.10: Evolution of the normalized vorticity Ω/Ω_o in the air around the time of breaking for $f_c = 1.28Hz$, $\delta f/f_c = 0.75$, and $S = 0.416$. Focusing occurs at $t \approx t_b$. Note the change of colorscale as compared to figure 4.9.

equivalent to the maximum depth of the dye plume imaged in the laboratory experiments of Rapp and Melville (1990). In both figures, we find that the group of particles slowly deepens, much faster in the case of the larger slope, reaching ≈ -0.58 at $t^* = 77.41$ while only getting to a depth ≈ -0.40 for the lower slope, at the same time. Also note that there appears to be significantly more mixing within the plume of particles in the case of largest slope, as opposed to the smaller slope case where the particles remain better organized.

Figure 4.13(a) shows the maximum depth of the particle plume Dk_c as function of non dimensionalized time $t^* = \omega_c(t - t_b)$ for $f_c = 0.88Hz$, $\delta f / f_c = 0.75$, and $S = 0.368$. We find that the depth of the particle plume initially rapidly increases, for a duration equivalent to approximately 2-3 wave periods, reaching $Dk_c \approx -0.3$. The deepening subsequently continues but at a much slower rate, caused by turbulent diffusion in the turbulent flow created after the wave broke (Rapp and Melville, 1990; Drazen and Melville, 2009), approaching $DK_c = -0.46$ for $t^* = 88$.

Following Rapp and Melville (1990), the data are fitted to a power law, defined as

$$Dk_c = \Gamma_1 \left[\omega_c \left(t - t_b\right)\right]^{1/4}, \tag{4.24}$$

based on a self-similarity assumption of the evolution of the particle plume. Figure 4.13(b) shows the same data as presented in 4.13(a), this time plotted in log-scale to highlight the $1/4$ power law behavior of the rate of deepening. A fit of the data is also shown, where $\Gamma_1 = 0.14$. Only data after the original deepening of the particles, approximately after 2 to 3 wave periods, are considered in the computation of the fit.

The rate of deepening of the particle cloud is qualitatively in agreement with the experimental results of Rapp and Melville (1990) though differences are present. While the slow $t^{*\,1/4}$ power law is found in both numerical and experimental results, the initial deepening of the dye (or particle) plume is much faster and stronger in the laboratory experiments. This difference might be related to the type of wave packet used in the generation of the breaking wave, as Rapp and Melville (1990) used a constant **amplitude**, while here a constant **slope** assumption is made. Additionally, the resolution limitation ($1mm$ at the interface) reduces our ability to completely simulate the details of the breaking process and perhaps some of the dynamics occurring at, and shortly after, the impact, effectively decreasing the initial penetration depth. Finally, as stated earlier, using Lagrangian particles is a simple representation of the dye plume evolution, and we therefore do not expect a complete agreement between the two.

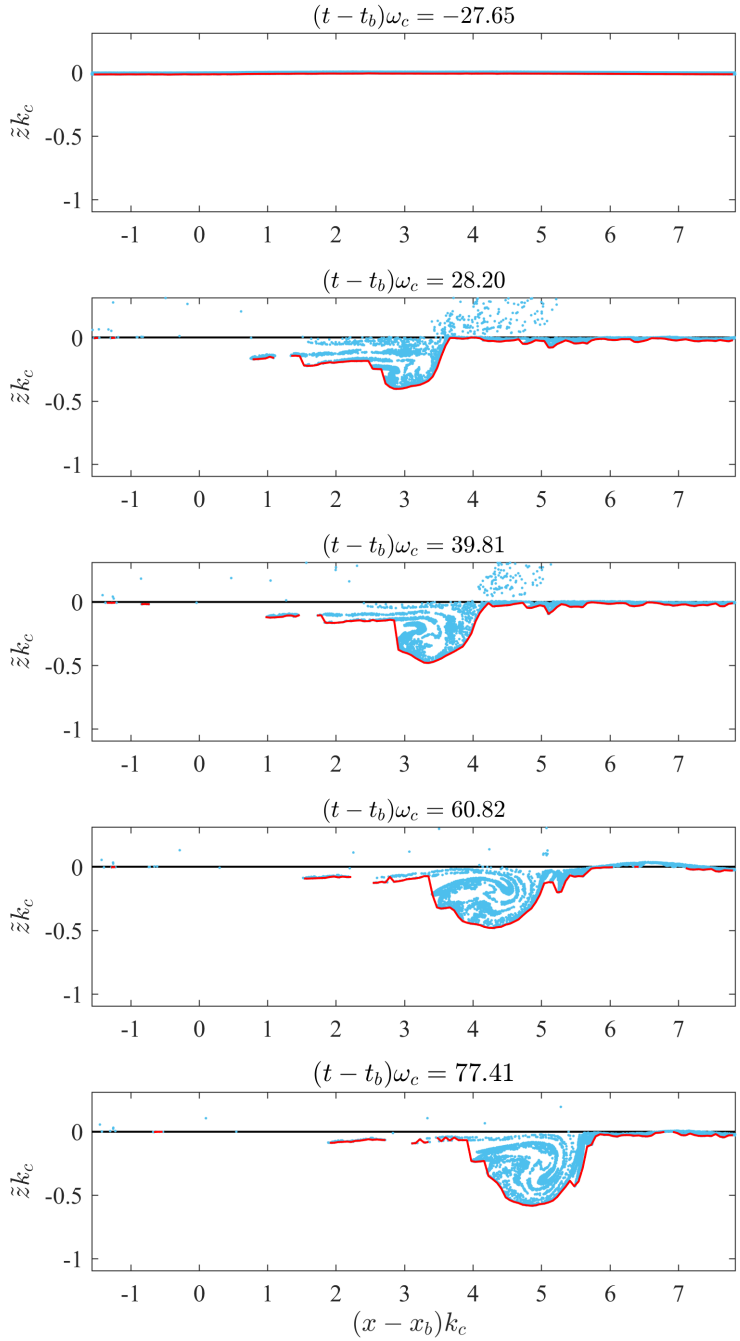

Figure 4.11: Evolution of the location of the Lagrangian particles for different values of t^* starting *before* the breaking event. The particles are initially located at the surface, as shown in the top panel. The red line correspond to the vertical extent of the particle plume. Note the deepening of the particles over time. Here the wave packet was set with $f_c = 0.88Hz$, $\delta f/f_c = 0.75$, and $S = 0.432$. Focusing occurs at $t \approx t_b$.

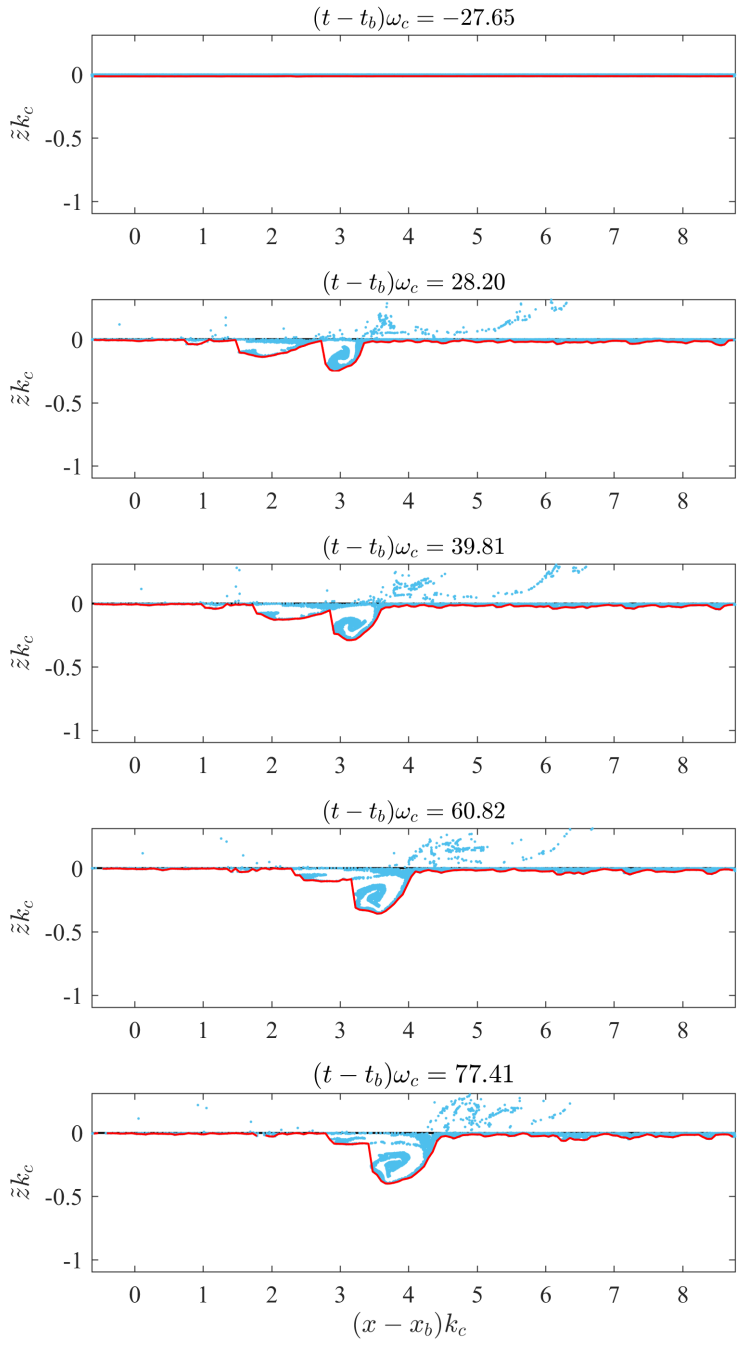

Figure 4.12: Same as figure 4.11 but this time the wave packet parameters were set to $f_c = 0.88Hz$, $\delta f/f_c = 0.75$, and $S = 0.368$. Focusing occurs at $t \approx t_b$.

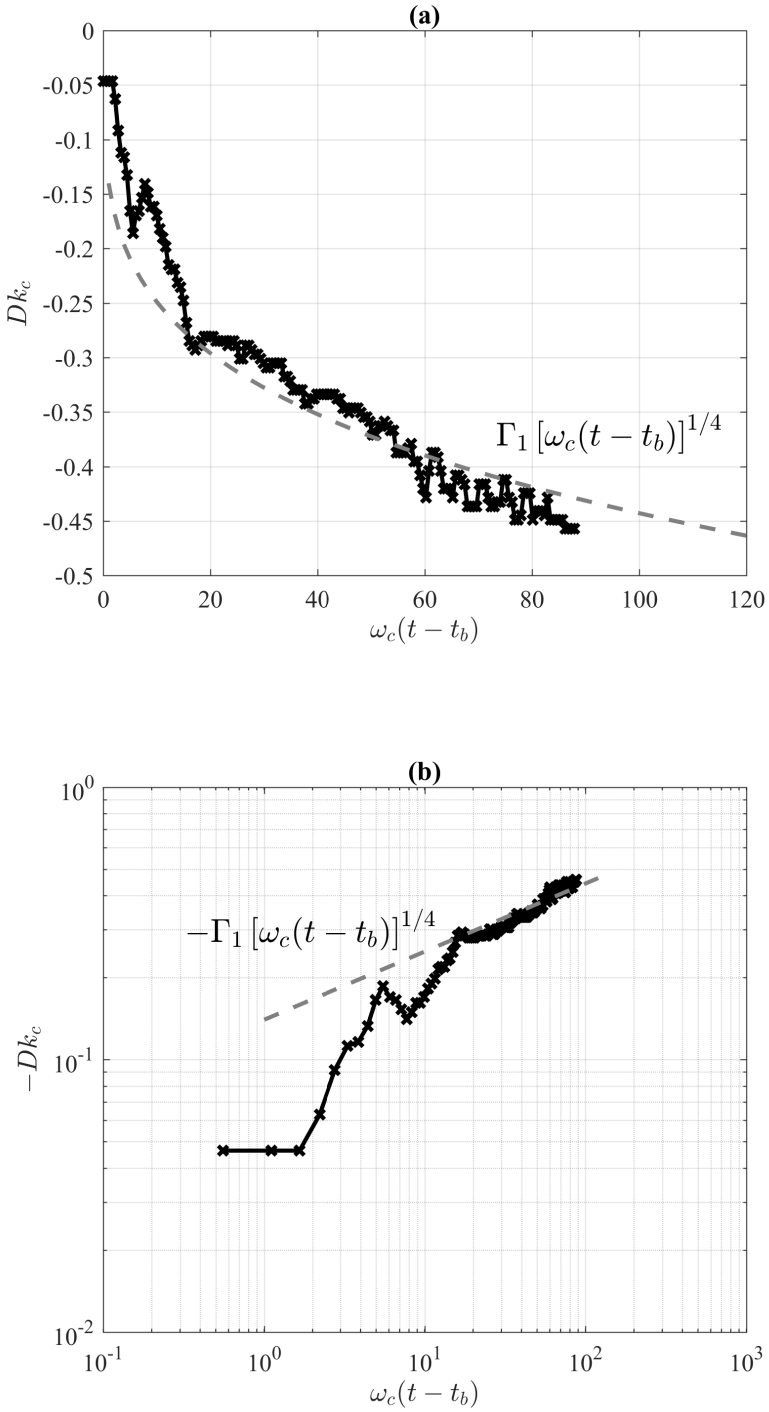

Figure 4.13: Maximum depth of the particle plume Dk_c as function of non dimensionalized time $t^* = \omega_c(t - t_b)$ ($f_c = 0.88Hz$, $\delta f/f_c = 0.75$, and $S = 0.368$). (a) linear scale, and (b) in log-scale to highlight the $1/4$ power law.

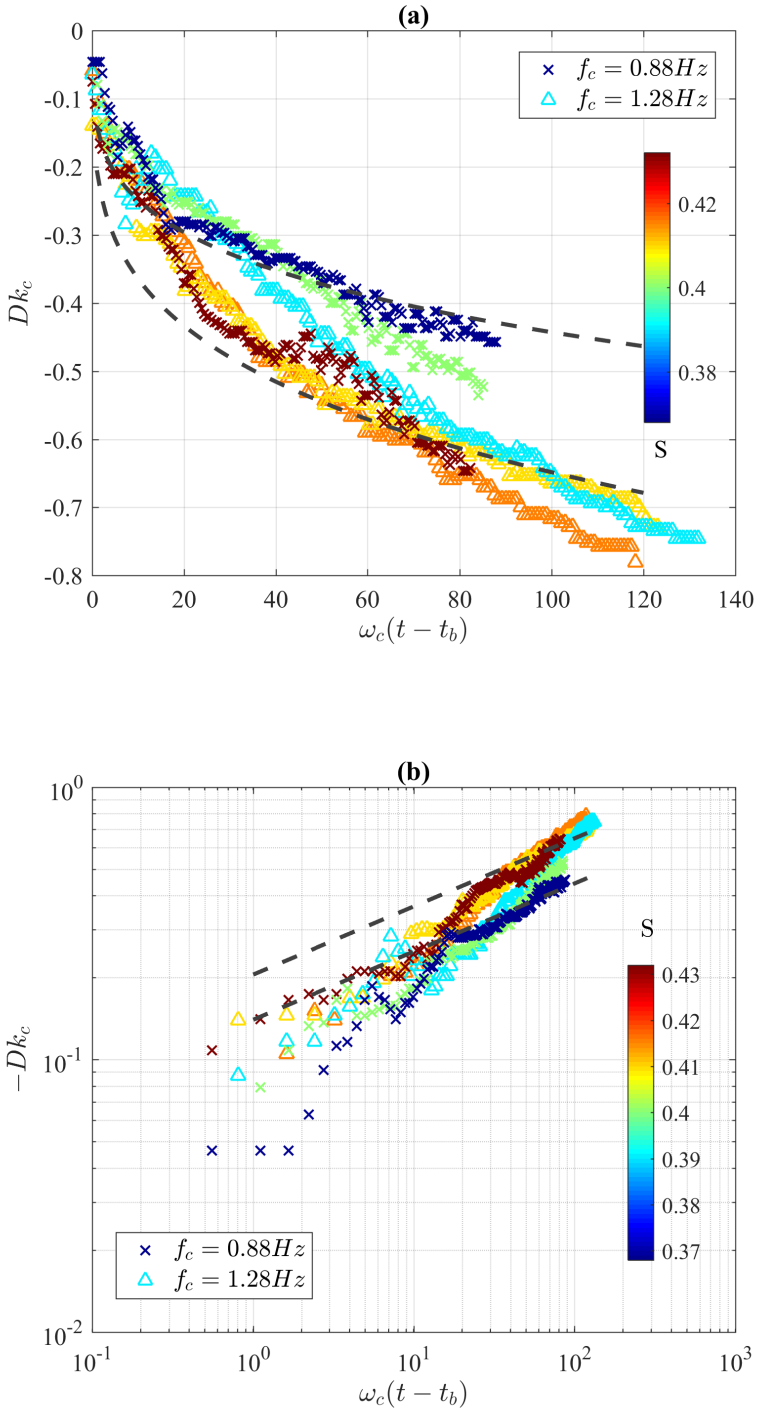

Figure 4.14: Maximum depth of the particle plume Dk_c as function of non dimensionalized time $t^* = \omega_c(t - t_b)$ for two values of fc, 0.88Hz and 1.28Hz and colorcoded for the slope S. (a) linear scale, and (b) in log-scale to highlight the $1/4$ power law.

Figure 4.14 shows the maximum depth of the particle plume Dk_c as a function of non dimensionalized time $t^* = \omega_c(t - t_b)$ for two values of f_c, equal to 0.88Hz and 1.28Hz and colorcoded for the slope S. Two fits are shown, based on equation 4.24, for $\Gamma_1 = 0.14$ and $\Gamma_1 = 0.205$. The rate of deepening of the particle plume generally follows the behavior of the case described in figure 4.13, with an initial rapid deepening then slowing down following a $t^{*\,1/4}$ power law. In a few cases, we find that the rate of deepening increases after a certain amount of time, no longer showing a $t^{*\,1/4}$ power law, varying depending on the runs (generally starting as low as $t^* = 40$), while it is not expected for this rate to decrease over time as the turbulent flow dissipates. This is likely caused by a numerical artifact, perhaps we are not resolving the background flow well enough with the prescribed resolution ($4mm$) combined with the effect of the return flow in the bottom half of the tank, insuring mass conservation. Nevertheless, we find that the maximum depth of the particle plume reaches values of up to -0.65 to -0.75 for the largest slope S, in the portion of data following the $1/4$ slope behavior. This is not as large as the measurements of Rapp and Melville (1990) but still corresponds to one to two heights of the breaking waves. It should also be noted that these simulations are performed assuming fresh water. It is expected that the penetration depth will be slightly reduced ($5 - 15\%$) for sea water as shown in the void fraction laboratory measurements under a breaking wave in Blenkinsopp and Chaplin (2007) and Blenkinsopp and Chaplin (2011).

4.6 Spray Generated by Breaking Waves

In chapter 3, we made the case that while poorly understood, the generation and transport mechanisms that lead to the presence of large sea spray aerosols in the Marine Atmospheric Boundary Layer is and essential component of the interaction between the ocean and the atmosphere.

Laboratory measurements of spray droplets generated from breaking waves, both wind and mechanically generated are very sparse and are generally limited to a smaller range of aerosol diameters (Anguelova et al., 1999). Veron et al. (2012) performed a series of experiments in high wind speed conditions, focusing on the generation of spume droplets, created when water is sheared off a wave crest by the wind. They found that the droplet size distribution followed a -3 power law for droplet diameters ranging from $196\mu m$ to approximately $700\mu m$, and -5 for the larger diameters, up to $\approx 5000\mu m$.

D. Towle under the direction of Professor James Duncan, University of Maryland, in

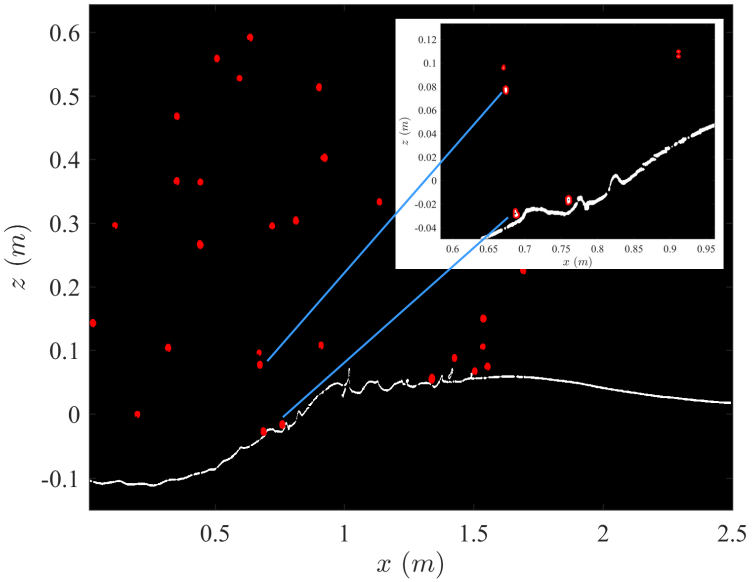

Figure 4.15: An example showing detected droplets used to generate the particle size statistics. The red lines represent the detected contour of the droplets. The insert is the magnified part of the main figure, identified by the blue lines.

2014 conducted an experimental study of droplets produced by mechanically generated plunging breaking waves (Towle, 2014). He found that the droplet diameter distribution followed a -4.68 power law for the less energetic focused breaking wave they studied, up to diameters of $3000\mu m$ and for the more energetic case, two power law scalings: -1.5 for $d < 1250\mu m$, and -8.79 for $d > 1250\mu m$.

Recent 3D numerical simulations of the breaking of a third-order Stokes wave using a VOF solver (Wang et al., 2016) shows a power law scaling of -4.5 for the aerosol size distribution.

In the present study, we used the 2D numerical simulations of deep-water breaking waves described earlier, with a center frequency $f_c = 0.88Hz$ and a bandwidth $\delta f/f_c = 0.75$ and a slope ranging from $S = 0.368$ to $S = 0.432$. Two-dimensional droplets are identified in the output of the simulation by detecting closed contours in the volume fraction $T(x, y, x, t)$ (see equation 4.5) over an area centered on the breaking location ($2m$ length by $1.2m$ height, starting from $z = -0.2m$, below the water surface). Four seconds of numerical data is considered in the analysis, starting approximately 1sec prior to the jet hitting the surface, every 0.1sec. The equivalent diameter of each one of these droplets, i.e. the diameter of a circle with the same area as the detected region, is then quantified using the Matlab standard function *regionprops.m*.

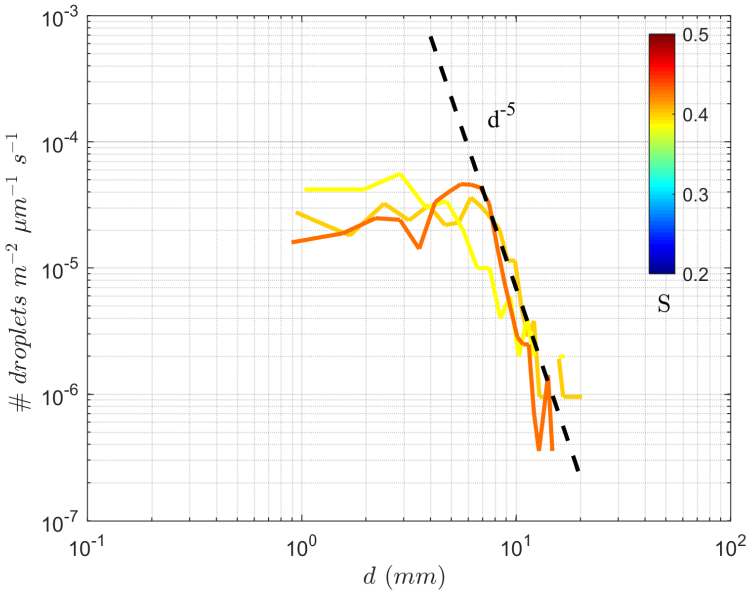

Figure 4.16: Distributions of number of droplets per m^2 of air, per diameter increment and per second for three slopes $S = 0.432, 0.400, 0.368$. Also shown is a -5 power-law scaling for reference

The droplet equivalent diameters are sorted in 30 size bins over the range of measured diameters, ranging from approximately 1 to 20mm. The number of droplets in each diameter bin is then normalized by the measurement area (of air only) and averaged over the 4 seconds of analyzed data, leading to a distribution of number of droplets per m^2 of air, per diameter increment and per second.

These distributions are presented in figure 4.16. We find that they follow a d^{-5} behavior, except for the lowest slope, i.e. the case with the fewest amount of droplets being generated. Here the slope of the distribution is not as steep, closer to a -4 power-law scaling. it is intriguing to find that these droplet size distributions, produced from mechanically generated breaking waves, exhibit similar power-law scaling than what found by Veron et al. (2012) for spume droplets, and Towle (2014). We however have to be cautious in our interpretation of these results as they are based on 2D numerical simulations, and therefore are unable to compute aerosol droplet concentration distributions where volume is needed, as is required for quantitative comparison with these other studies. Additionally, the present resolution (1mm) greatly limits the lower range of diameters we can resolve. Higher resolution, three-dimensional simulations are needed to improve the results and conclusion of this work.

4.7 Section Summary

Numerical simulations of deep-water breaking waves in an idealized wave channel were conducted by solving the full Navier-Stokes equations in a two-phase flow (air and water), in two dimensions using Gerris over a range of frequency f_c and slope S. The flow was seeded with a dense sheet of Lagrangian particles to study the mixing in the breaking region and to quantify the deepening rate of the portion of the water initially at the surface. The rate of deepening of the particle cloud is qualitatively in agreement with the experimental results of Rapp and Melville (1990) though differences are present, likely associated with numerical resolution and/or artifacts. We find that the maximum dimensionless depth of the particle plume, Dk_c, reaches values of up to -0.65 to -0.75 for the largest slope S, in the portion of data that follows the $t^{*\,1/4}$ power-scaling behavior. This is not as large as the measurements of Rapp and Melville (1990) but still corresponds to one to two wave heights of the breaking waves. Note that we showed in Chapter 2 and 3 that the significant wave height H_s could reach up to 5 m in storms off the coast of California. In other parts of the world (i.e. North Sea or in a Tropical Cyclones such as TC Freda), H_s can often get larger than 10m. While the significant wave height is only a representation of the statistical mean wave height, it is anticipated that a fraction of the waves present in the storm will have an amplitude equal to $1.5 - 2 \times H_s$, implying that water initially at the surface could reach depths of up to 20-40 m just through the effects of wave breaking, and producing significant mixing in the process.

To improve the numerical characterization of the mixing under a breaking wave, another approach to consider in future work is to follow the method of Drazen and Melville (2009) where laboratory experiments with the same parameters were reproduced multiple times to allow the decomposition of the measured flow field in mean and turbulent parts.

Size distributions of droplets generated during the breaking process show a surprising good agreement with the power-law scaling found in past laboratory and numerical studies, though the present 2D setup can not lead to any quantitative comparisons: three-dimensional, higher resolution simulations are required to compute the droplet size concentration functions.

CHAPTER 5

Toward Improved Characterization of Air-Sea Interaction Processes in High-Wind Regimes using Unmanned Surface Vehicles

Contents

5.1 Introduction

Hurricanes, otherwise known as tropical cyclones (TC) or typhoons, are among the most destructive natural phenomena impacting the oceans and coastal waters. Tropical cyclone

intensity, characterized by the Saffir-Simpson scale of sustained winds, is a key parameter that ultimately helps define the potential impact of the surface winds, the extent of storm surge, and the depth of upper-ocean mixing. While forecasting the track of tropical cyclones has significantly improved in recent decades, TC intensity forecasts remain uncertain in a context where climate models suggest an increase in the frequency of intense TCs (Bender et al., 2007).

A number of studies have aimed to improve our understanding of tropical cyclone genesis and dynamics (Price, 1981; D'Asaro et al., 2006; Black et al., 2007; D'Asaro et al., 2007; Sanford et al., 2007, 2011a,b; Bell et al., 2012; Mrvaljevic et al., 2013). One of the challenges in this area of air-sea interaction research is the lack of in-situ measurements in close proximity to these intense storms. Past studies have often been limited to using remote sensing products and air-launched instrumentation (Powell et al., 2003; Sanford et al., 2011b). Very few of those measurement campaigns collected a combination of atmospheric, surface dynamics, and oceanographic measurements at the same time and location.

Though a significant number of one-dimensional wave spectra and samples of wave statistics in TCs have been collected over the past couple of decades (Young, 2003, 2006), wave directional spectra remain sparse (Young, 2006) and are often constrained to radar-based airborne wave mapping techniques that better resolve the longer waves (Black et al., 2007; Moon et al., 2003; Walsh et al., 1985). In addition, the sampling of the lower part of the MABL in those intense storms is often only achievable using limited air-launched instrumentation like GPS dropsondes (Powell et al., 2003). Measuring the evolution of the wave directional spectrum in a tropical storm is critical for improving hurricane intensity forecasts, as the Stokes drift of the surface wave field interacting with the vorticity of surface shear currents produces Langmuir circulations (LCs) through the vortex force of the Craik-Leibovich (1976) theory (Craik and Leibovich, 1976). LCs contribute to the mixing of the upper ocean and hence to the enthalpy transfer between the ocean and the atmosphere (Sullivan et al., 2010, 2012) through contributions to entrainment of cooler water from below by "Langmuir turbulence" and shear associated with strong currents in the wake of the storm (D'Asaro et al., 2007; Sanford et al., 2007).

In this chapter, we present oceanographic and atmospheric boundary layer data collected from an instrumented unmanned surface vehicle (USV: Wave Glider, Liquid Robotics) as it passed near the category 3 Tropical Cyclone Freda.

The PacX project, to send Wave Gliders across the Pacific from California to Australia and Asia, was not designed as a tropical cyclone science program, but the serendipitous

availability of the rare data that was gathered, while limited, supports recent hurricane modeling results and opens a window to the development of improved methods of measuring SOLA processes in tropical cyclones. Evolution of the wind, the directional wave field and estimates of the Stokes drift profile are presented and discussed. In section 2 the Wave Glider and its instrumentation are described. In section 3 we briefly describe TC Freda. In section 4 we present the measurements of the SOLA response to Freda. In section 5 we present evidence of the ocean's biophysical response to the TC, and in section 6 we summarize and discuss our findings.

5.2 The Instrumented Wave Glider

The Liquid Robotics (LR, Sunnyvale, CA) Wave Glider is a novel ocean-wave-propelled autonomous surface vehicle (ASV) with a two-body design. The lower part, called the "glider" is tethered to the surface "float" section of the vehicle by an approximately seven-meter long umbilical cable. The fins installed on the glider convert the orbital motion of the wave into a horizontal force (much the same way as personal swim fins do) that tows the instrumented surface float. Though the Wave Glider's propulsion system is purely mechanical, there are two solar panels mounted on the float to supply power for the navigation and communication systems and on-board instrumentation.

Wave gliders are controlled and navigated using an Iridium satellite link back to shore. Waypoints are sent to the vehicle using the Wave Glider Management System (WGMS), proprietary Liquid Robotics control software. Details about the vehicle design and performance are provided in Table 5.1.

5.2.1 PacX experiment

In November of 2011, Liquid Robotics launched the PacX experiment, sending four Wave gliders across the Pacific Ocean to demonstrate the endurance and reliability of their vehicles. The four Wave Gliders left from San Francisco, CA, and first transited to Hawaii. From there, two vehicles headed to Australia and two to Japan. One of the two Wave Gliders heading to Australia, WG Benjamin, named in honor of the early American scientist and Gulf Stream pioneer, Benjamin Franklin, came in close proximity to the category 3 Tropical Cyclone, Freda.

Dimensions	Float (length x width): 208 cm x 60 cm Underwater Glider, at 7 m depth (height x length): 40 cm x 191 cm Wings: 107 cm wide
Weight (dry) Buoyancy (in water)	Mass: 90 kg Displacement: 150 kg
Endurance	Up to 1 year (variable)
Speed in water	0.4-2 kts (variable)
Depth rating	Continuous wash and salt spray Brief submergence to 2 m
Propulsion	Mechanical conversion of wave energy into forward propulsion
placeBattery	665 Watt-hours - Lithium-ion rechargeable
Solar Power	80W (peak) for battery charging, onboard electronics & payloads
Command & Control Power	1.5W continuous
Available Payload Power	10A (max) continuous at 13.2V
Communication	Iridium and 2.4 GHz
Navigation Accuracy	3 m radius CEP50
Station keeping	40 m radius CEP90 in WMO sea state 3 (with current <0.5 kts)

Table 5.1: Liquid Robotics Wave Glider specifications

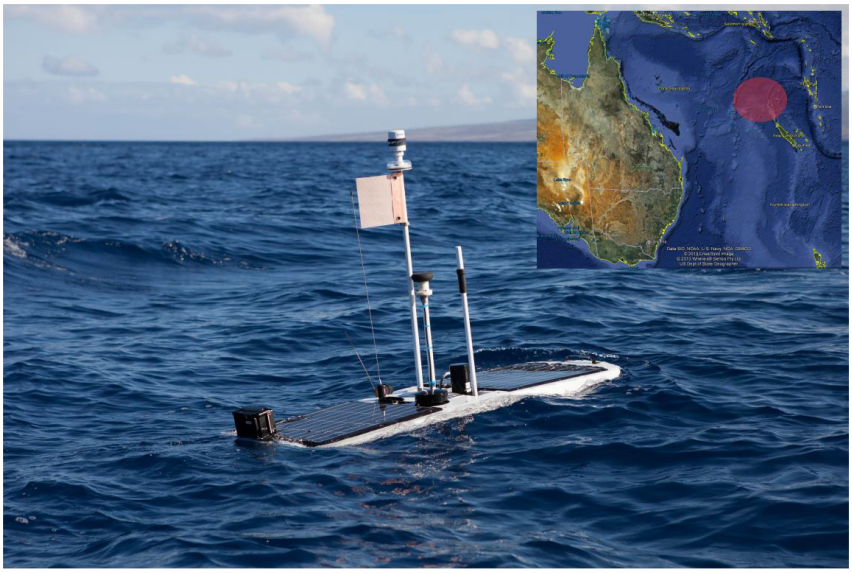

Figure 5.1: Wave Glider "Benjamin" during engineering tests off the island of Hawaii, prior to the PacX deployment. The insert shows the geographical area where the glider encountered Tropical Cyclone Freda, on December 31 2012, north-west of New Caledonia.

5.2.2 Instrumentation

Liquid Robotics fitted all four wave gliders with a suite of atmospheric and oceanographic instruments. Figure 5.1 shows a picture of the instrumented glider during engineering tests off the west coast of the of Hawaii prior to the start of the PacX project. An Airmar (Milford, NH) PB200 sensor was installed to measure air temperature, barometric pressure, wind speed, wind gust speed, and wind direction one meter above the deck of the Wave Glider. Data were sampled at 1 Hz then averaged over a 10 min window before being transmitted back to shore through Iridium communications.

The wave field was characterized using a Datawell (Haarlem, The Netherlands) MOSE G-1000 wave sensor installed on the glider float. This sensor produces three-component displacements in a north–east–vertical coordinate frame using a high-accuracy GPS receiver-based system that measures the horizontal and vertical buoy velocities based on the Doppler shift in received GPS signals. These velocities are then integrated internally in the unit to produce north–east–vertical displacement time series. The standard Datawell output products (bulk wave parameters, frequency spectra) were streamed back to shore while the continuous, 2 Hz time series were logged internally and recovered once WG Benjamin reached its final destination in Australia. All spectra considered in the analysis reported here were reprocessed using the raw 2-Hz data stream to account for brief loss

of GPS signal during heavy seas that may have been caused by occasional submergence of the antenna under breaking waves. As described later in the text, since the Wave Glider is not optimally designed as a wave buoy, the wave measuring Wave Glider system was tested against a separate Datawell directional wave buoy.

A Sea-Bird Electronics (Bellevue, WA) water conductivity, temperature, depth (CTD), and dissolved oxygen sensor was installed at the base of the float. The GPCTD ("Glider Payload CTD") is specifically designed for use on autonomous platforms. It is a self-contained CTD equipped with onboard memory and storage, and integrated pump with low power consumption and small form factor. A flow-controlled dissolved oxygen (DO) sensor was added directly in line with the T and C sensors. A collocated pressure sensor provides depth information. The GPCTD is designed to minimize power consumption. During the PacX experiment, the instrument was set to burst sample at ten-second intervals over 70 seconds every ten minutes. A Turner Designs (Sunnyvale, CA) C3 fluorometer designed to measure chlorophyll-a *in-vivo* fluorescence (460nm excitation and 696nm emission wavenumber, Raw Fluorescence Units RFU), turbidity (850nm excitation and 850nm emission, Nephelometric Turbidity Units NTU), and crude oil material (325nm excitation and 410-600 nm emission) was also installed below the glider float. The sampling interval was set to 2 min. The sensor was calibrated before and after the PacX experiment following the manufacturer's recommendations.

5.2.3 Remote sensing products

In addition to the in-situ measurements, remote sensing products were also available in the present study. We used the Multiplatform Tropical Cyclone Surface Wind Analysis (MTCSWA) data set, an operational product available through the NOAA National Environmental Satellite Data and Information Service (NESDIS) and the Regional and Mesoscale Meteorology Branch (RAMMB) at Colorado State University, Fort Collins, CO. Global tropical cyclone surface and flight level wind analyses are produced every 6 h, through objective mapping of remotely sensed winds from satellites (Knaff et al., 2011).

5.2.4 Numerical model

Numerical products (significant wave height, surface winds) publicly available from the combined Joint Typhoon Warning Center WaveWatch III (JTWC/W3) model were also used in the present study. The model uses a modified NOGAPS wind field forecast, using

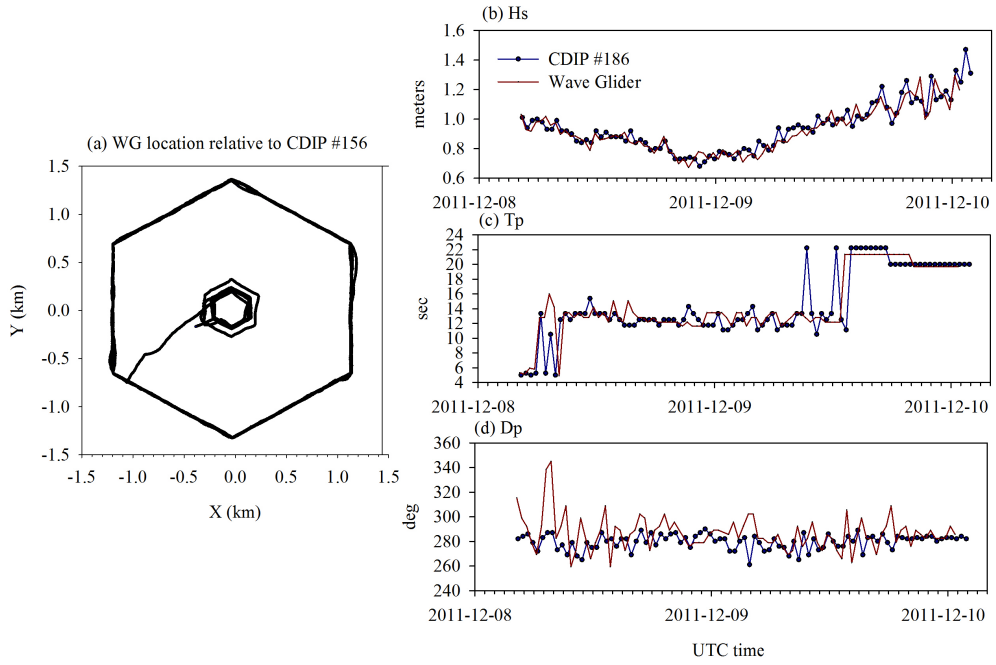

Figure 5.2: (a) Wave Glider position relative to CDIP buoy #156 from 04:00 UTC December 8, 2011, to 02:00 UTC December 10, 2011. The right panels show a comparison of bulk parameters measured by the wave glider and the wave buoy for the same period of time: (a) significant wave height H_s, (b) peak period T_p, and (c) peak direction D_p (coming from, true north).

a JTWC estimate of the storm (radius of maximum winds, and radius of the outermost closed isobar to characterize the extent of the TC circulation), which is then used as input to WaveWatch III to improve wave height forecasts (Sampson et al., 2010, 2013).

5.3 Directional Wave Measurements from a Wave glider

While the Wave Glider is equipped with a Datawell directional wave sensor, the Wave Glider platform is not optimized for wave measurement as is the Datawell family of wave buoys, so a direct intercomparison of wave measurements from the two platforms was conducted.

A short deployment of Wave Glider Benjamin to evaluate its performance as a directional wave sensor was conducted prior to the start of the PacX project, from 04:00 UTC, December 8, 2011, to 02:00 UTC, December 10, 2011, in close proximity to a Mark II Datawell directional wave buoy (CDIP #156) located in Monterey Bay, CA. Figure 5.2(a) shows the glider track, relative to the buoy location. Two polygonal patterns

centered on the buoy location were used; a larger one, with sides of approximately 1.3km and a smaller one with sides of approximately 300 to 400m in length. The Datawell buoy is sampled at 1.28Hz, with a low-frequency cutoff at 0.033Hz while the Wave Glider DWR-G is sampled at 2Hz with a cutoff at 0.01Hz. Horizontal (x,y) and vertical (z) displacements of the buoy and Wave Glider were analyzed to compute bulk wave parameters shown in Figure 5.2(b-d). For each 30-min record, auto-, co-, and quadrature spectra were computed using 256-sec FFT windows with 50% overlap. Significant wave height H_s was computed as $H_s = 4 * \left\langle \eta^2 \right\rangle$, where $\eta(t)$ is the vertical displacement and $\langle \bullet \rangle$ is the time average; the peak period T_p as the most energetic frequency in a given wave spectrum, and D_p the corresponding peak direction. Overall, the bulk parameters estimated from the wave glider and the Datawell directional wave buoy are in very good agreement. In addition, standard methods are used to compute frequency-dependent mean wave direction $\bar{\theta}(f)$ and directional spread $\sigma_\theta(f)$, based on the first- and second-order Fourier moments of the directional distribution of wave energy $S(\theta)$, expressed in terms of auto- (E_{xx}, E_{yy}, E_{zz}), co- (C_{xy}) and quadrature (Q_{xz}, Q_{yz}) spectra (Herbers et al., 2012; Long, 1980).

In this study, the mean direction $\overline{\theta}$ and directional spread σ_θ were computed using the first-order moments a_1 and b_1 of the directional distribution:

$$\tan(\bar{\theta}) = \frac{b_1}{a_1} \tag{5.1}$$

and

$$\sigma_\theta = \sqrt{2\left(1 - \sqrt{a_1^2 + b_1^2}\right)}, \tag{5.2}$$

$$\text{where} \begin{pmatrix} a_1 \\ b_1 \\ a_2 \\ b_2 \end{pmatrix} = \begin{bmatrix} Q_{xx} \Big/ \sqrt{\left(E_{xx} + E_{yy}\right) E_{zz}} \\ Q_{yz} \Big/ \sqrt{\left(E_{xx} + E_{yy}\right) E_{zz}} \\ \left(E_{xx} - E_{yy}\right) \Big/ \left(E_{xx} + E_{yy}\right) \\ 2C_{xy} \Big/ \left(E_{xx} + E_{yy}\right) \end{bmatrix}$$

A representative sample from the Wave Glider (dark red) and Datawell directional wave buoy (dark blue) is shown in figure 5.3. The top panel (a) shows the wave frequency spectrum, (b) the mean wave direction and (c) the directional spread. The wave field is dominated by swell coming from the west, and wind waves were also coming from the west while a higher frequency component coming from the east is also observed. The agreement in wave spectral estimates is excellent for frequencies ranging

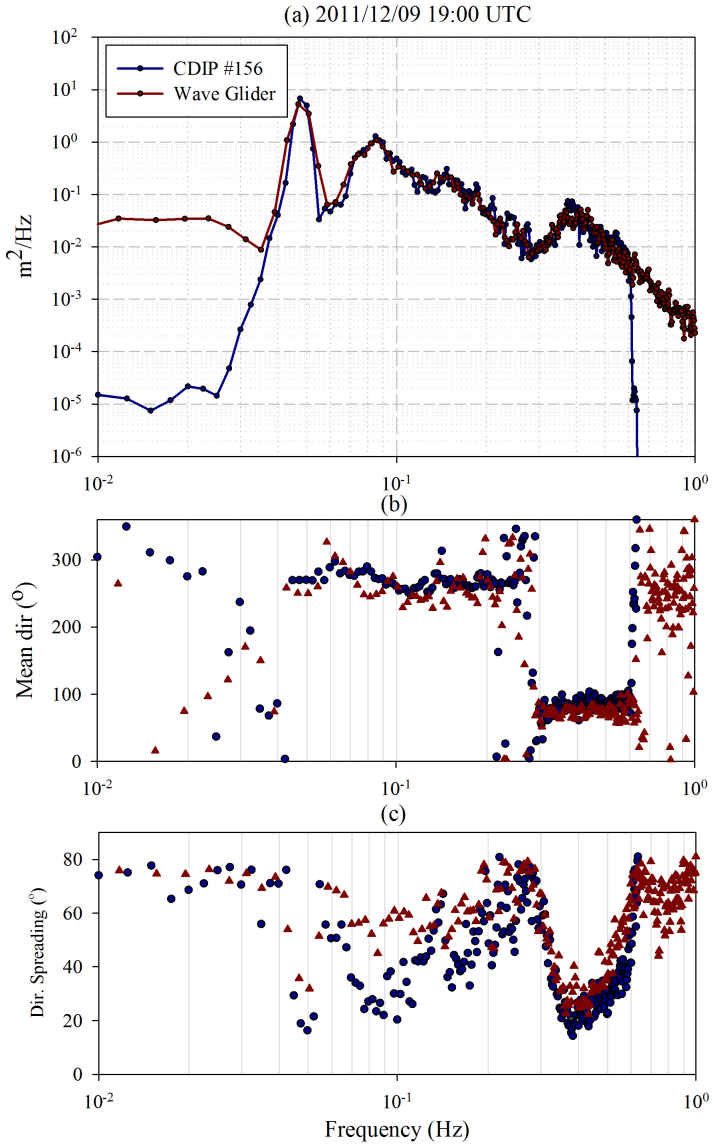

Figure 5.3: Comparison of (a) wave frequency spectra computed from 30min of data collected at 19:00 UTC on December 9, 2011, (b) frequency-dependent mean direction $\bar{\theta}(f)$ and (c) directional spread $\sigma_\theta(f)$.

from 0.033-0.5Hz, the spectral range of the Datawell directional buoy sensor [1]. The mean wave directions computed from the Wave Glider measurements are in good agreement with those of the Datawell buoy, though noisier, especially at lower frequencies. The directional spread estimated from the Wave Glider is larger for the lower frequencies.

From these comparisons, it appears that the quality of the wave directional data measured from the Wave Glider is comparable to that from the standard Datawell directional wave buoy, with the exception of signal-to-noise ratios and directional spreading at lower frequencies. It is likely that these differences at lower frequencies are due to the differences between the tether design optimized for wave measurements by the buoy, and the constraints of the tether on the Wave Glider, which is optimized for propulsion. Notwithstanding these low frequency differences, the measurements demonstrate that the Wave Glider is a useful directional wave measurement platform.

5.4 Tropical Cyclone Freda

Freda became a tropical depression on December 26 2012, forming approximately 295 km northeast of the Solomon Islands in the Western Pacific. The system quickly became a tropical cyclone on December 29 2012, tracking along the northwestern edge of a subtropical atmospheric ridge in a southwesterly direction. It continued intensifying and reached category 3 intensity on December 30^{th} shortly after crossing 161°E, with winds reaching up to 55 $m\,s^{-1}$, and a measured pressure of 975 mbar. The cyclone later weakened due to strong wind shear, was downgraded to a tropical storm on January 1 2013, and then just a low pressure area on January 2 2013 before it struck New Caledonia.

5.5 Ocean response to TC Freda

Figure 5.4 shows Freda's track and intensity (in $m\,s^{-1}$) from December 27 2012 UTC through January 3 2013 UTC. Also shown is the WG Benjamin track, getting as close as 46 km from the center of the eye on December 31 2012 at 12:00 UTC. The storm quickly weakened once it passed south of the Wave Glider. Also note that WG Benjamin was set to be on a constant westerly heading during the storm. The shape of the glider track once it reached the wake of the TC implies very strong westerly then northward surface currents that swept the glider into the wake of the storm.

[1] Though the spectral range of the CDIP buoy measurements extents to 0.64Hz, we find that the obtained

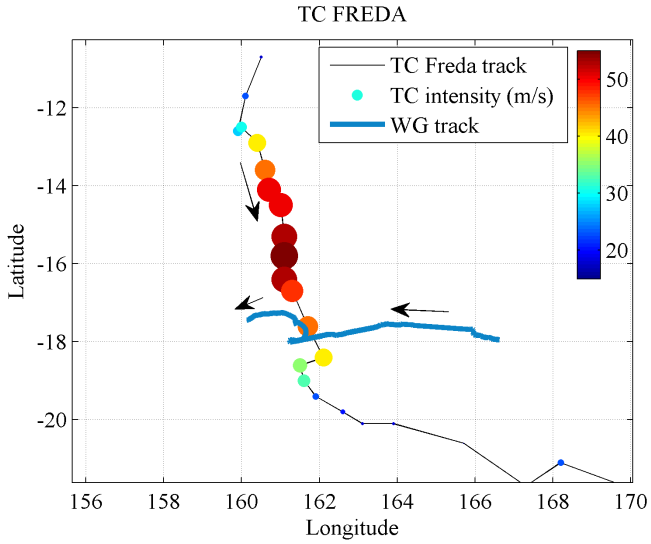

Figure 5.4: The track and intensity (peak winds, color coded m/s) of Tropical Cyclone Freda (black line) and track of the wave glider âĂIJBenjaminâĂİ (blue), from December 27 2012 UTC through January 3 2013 UTC. Note that the diameter of the circles is proportional to the storm intensity.

The relative distance between the WG and the center of the storm is shown in figure 5.5(a). It was able to continuously collect data in three quadrants of the TC. Figure 5.5(b) and (c) shows the eastward and northward (respectively) glider (blue) and surface current (red) velocity components. Unfortunately, the surface velocity sensor used for navigation purposes was turned off from December 31 2012 at 10:30 UTC till January 1 2013 at 19:15 UTC to reduce payload power consumption. During the same period of time, once the WG reached the wake of the TC in quadrant C, platform speed-over-ground (GPS SOG) of up to 1.5 $m\,s^{-1}$ was measured, moving towards the east, in the direction opposite to its navigational setting, implying the existence of opposing near-surface currents of even greater amplitude.

Figure 5.6 shows the evolution of the main parameters of the marine atmospheric boundary layer (MABL) and surface conditions from December 25 2012 through January 1 2013 as the WG passed near the eye of the TC. Each data point represents a 10-min average. Figure 5.6(a) shows the barometric pressure. As expected, the lowest value was recorded near the center of the TC, reaching almost 975 mbar. Figure 5.6(b) shows the significant wave height, H_s, measured from the Datawell sensor and the estimate from the JTWC/W3 numerical forecast at the WG location. H_s is defined as $H_s = 4 * \langle \eta^2 \rangle$, where $\eta(t)$ is the surface displacement and $\langle \bullet \rangle$ denotes the 10-minute average. The significant

spectral density start rolling off rapidly at 0.5Hz, as shown in figure 5.3.

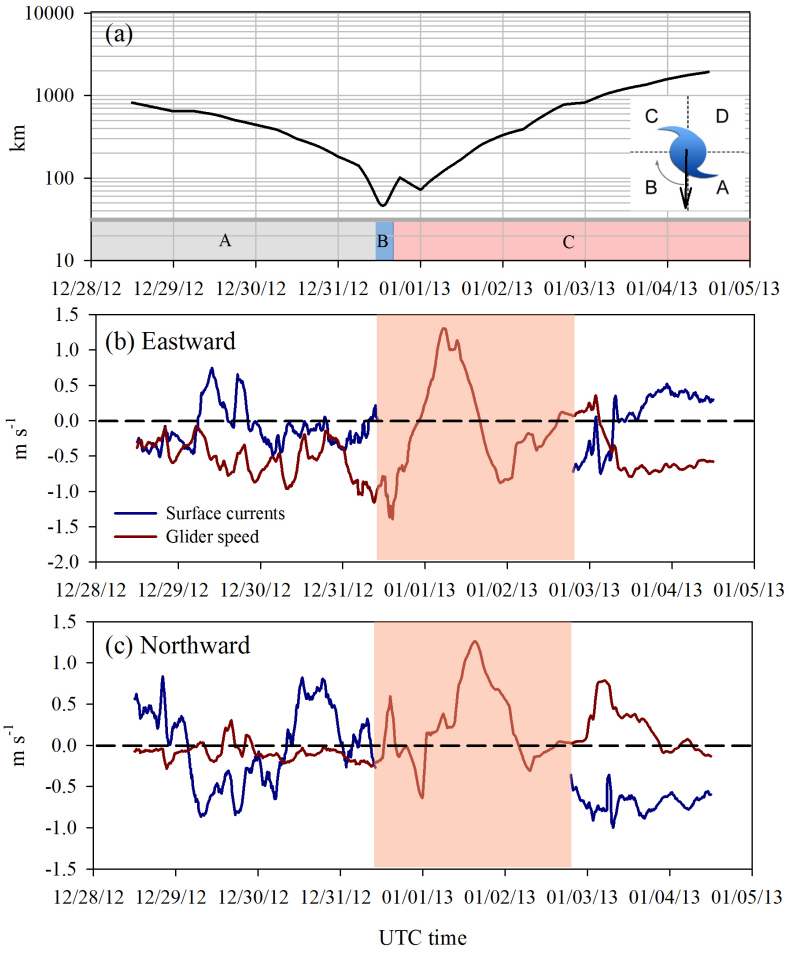

Figure 5.5: (a) Distance between the glider and eye of Tropical Cyclone Freda, as estimated by the Joint Typhoon Warning Center (JTWC), as a function of time. Also highlighted are the quadrant locations of the Wave Glider, relative to TC Freda as defined in the insert. Panels (b) and (c) show the eastward and northward measured surface currents (blue) and Wave Glider GPS Speed-Over-Ground (GPS SOG, red). The surface velocity sensor was unfortunately turned off from December 31 2012 at 10:30 UTC until January 1 2013 at 19:15 UTC to reduce power consumption.

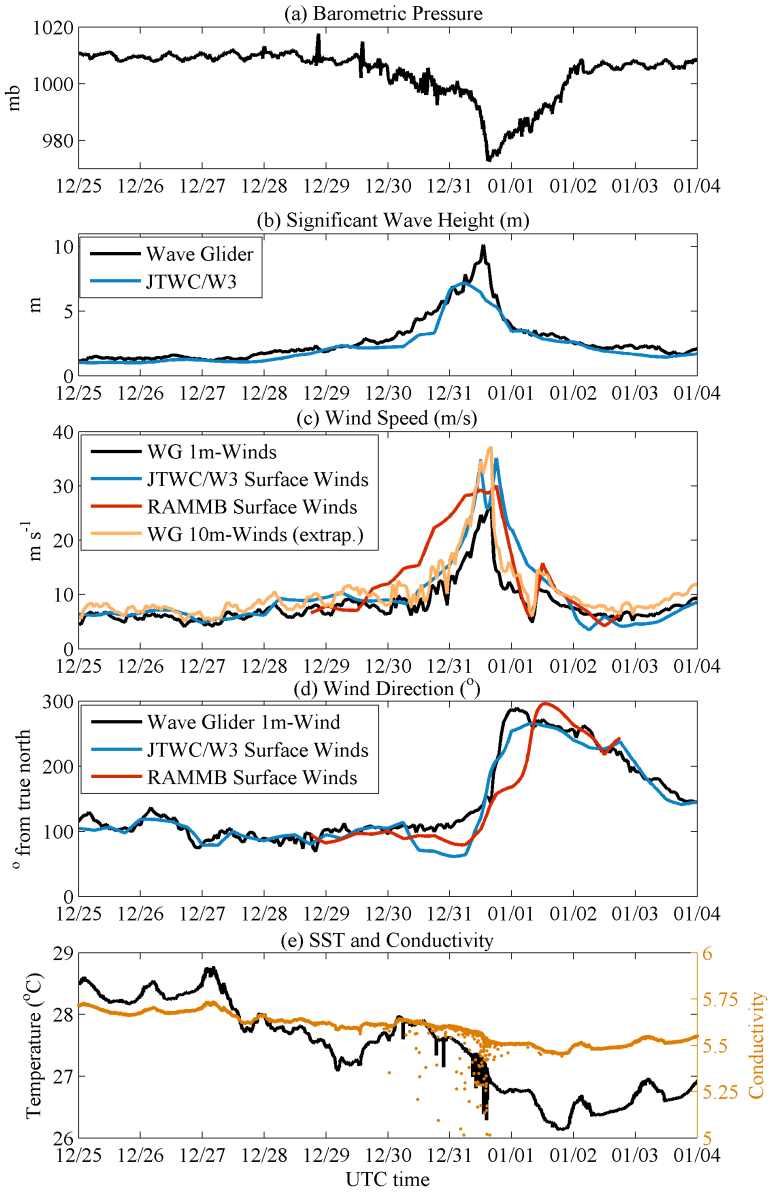

Figure 5.6: Environmental conditions measured by the Wave Glider during TC Freda. (a) Barometric pressure, (b) significant wave height, (c) wind speed in m/s(black: WG U_1 measured at 1m height; blue: surface winds from JTWC/W3 product; red: Regional and Mesoscale Meteorology Branch (RAMMB, Colorado State University), reanalyzed surface winds, and orange: WG U_{10} estimated from U_1), (d) wind direction (coming from true north) and (e) sea surface temperature and conductivity. Noise in conductivity measurements in high wind and wave conditions may be due to near-surface bubble clouds (c.f. Lamarre and Melville, 1991).

wave height rapidly increased as the WG got closer to the eye of the TC, reaching 9.9 m on December 31 2013 at 14:00 UTC. Figure 5.6(c) shows the wind speed measured by the glider at 1 m above the water surface, the spatially interpolated wind products from JTWC/W3 and MTCSWA, and the wind speed U_{10} at 10-m height extrapolated from the WG sonic anemometer at 1 m, computed iteratively using TOGA COARE 3.0 (Fairall et al., 2003) assuming a constant flux layer with a logarithmic wind profile:

$$U_{10} = \frac{u_{*a}}{\kappa} \ln\left(\frac{10}{z_o}\right), \tag{5.3}$$

where u_{*a} is the friction velocity in the air and z_o the roughness length as described in Fairall et al. (2003):

$$z_o = \frac{\alpha u_{*a}^2}{g} + \frac{0.11\nu}{u_*}, \tag{5.4}$$

where ν is the kinematic viscosity and α is Charnock's parameter (Charnock et al., 1955).

Figure 5.6(d) shows the corresponding wind (from) direction relative to true north. Average wind speed quickly increased to 36.5 $m\,s^{-1}$ near the center of the TC, on December 31 2012 at 14:00 UTC. The wind direction shifted from 100° to 280° over the course of 24 hr starting on December 31 2012 as the WG passed through three quadrants of the TC. The wind direction from JTWC/W3 and MTCSWA products are in relatively good agreement with the measured wind direction, while the wind speed from JTWC/W3 product is in good agreement up to the peak of the storm, then diverges significantly. The MTCSWA surface wind product is in poor agreement with the in-situ measurement up to January 1 2013, when it starts to improve significantly. The discrepancy is likely caused by inaccuracies in the TC intensity forecast due to limitations of the JTWC and MTCSWA algorithm (Knaff et al., 2013). We also found that the JTWC/W3 wave product did a poor job reproducing the significant wave height along the track of the wave glider. Figure 5.6(e) shows sea surface temperature (SST) and conductivity measured from the GPCTD mounted at the base of the float. Both SST and conductivity decreased significantly once the glider reached the wake of the TC as reported in previous studies (D'Asaro et al., 2007; Mrvaljevic et al., 2013).

Figure 5.7 shows an example time series of sea surface displacement collected on December 31 2012 around 15:40 UTC. The horizontal velocity in the mean wave direction for that period of time (coming from 150°, relative to true north) is shown as color-coded dots. At that time, the significant wave height H_s = 7.5 m, and the wind speed U_{10} = 36.5 m s^{-1}. A couple of extreme waves, sometimes called "rogue" waves,

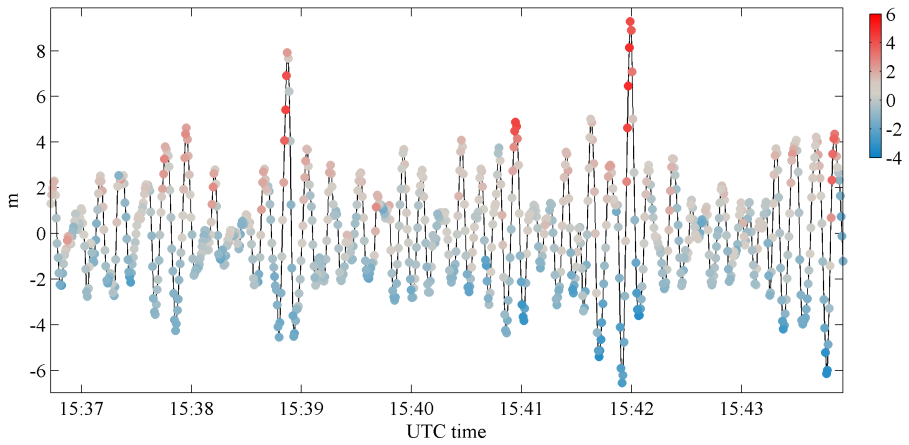

Figure 5.7: Example time series of sea surface displacement measured by the wave glider on December 31 2013 around 15:40 UTC. The measured glider horizontal velocity in the mean wave direction is shown as color-coded dots (in m/s). Significant wave height H_s was equal to 7.5m and wind speed U_{10} was equal to 36.5 m/s at the time of measurement. Note that the largest wave, at 15:42, has a height exceeding $2H_s$.

were measured by the WG, the largest one appeared at 15:42 UTC. Peak-to-peak height was 15.83 m, with a maximum WG horizontal velocity of $4.8m\ s^{-1}$.

The spectrogram of the sea surface displacement is shown in Figure 5.8. The spectra were computed using 256-sec FFT windows with 50% overlap over a 30 min record. Low frequency swell (20-25 sec. period) appeared on December 26 2012 while the TC was still a significant distance from the WG and its period slowly decreased as the TC got closer. On December 30 2012, wind waves became dominant as the wind quickly increased, ultimately reaching speeds close to 27 $m\ s^{-1}$ (at 1m above the surface, equivalent to 36.5 $m\ s^{-1}$ at 10 m) at the peak of the storm. The evolution of the wave frequency spectrum is shown in Figure 5.9. Spectra are color coded for wind speed at 1m height. The evolution of the spectral shape as the wind increases is consistent with the measurements by Donelan et al. (1985) and Young (2006). While a low frequency swell peak is present at the lowest wind speed, where the measurements were collected at a significant distance from the TC, the wave spectrum quickly becomes unimodal as the wind increased and the glider got closer to the center of the TC.

For each 30-minute record, the directional wave spectrum $S_{f\theta}$ is computed using the WAFO MATLAB library (WAFO-Group, 2000) using the horizontal (north, west) and vertical displacement of the glider float. Figure 5.10 presents the evolution of the directional wave field as the TC passed near the WG. The relative storm location is quali-

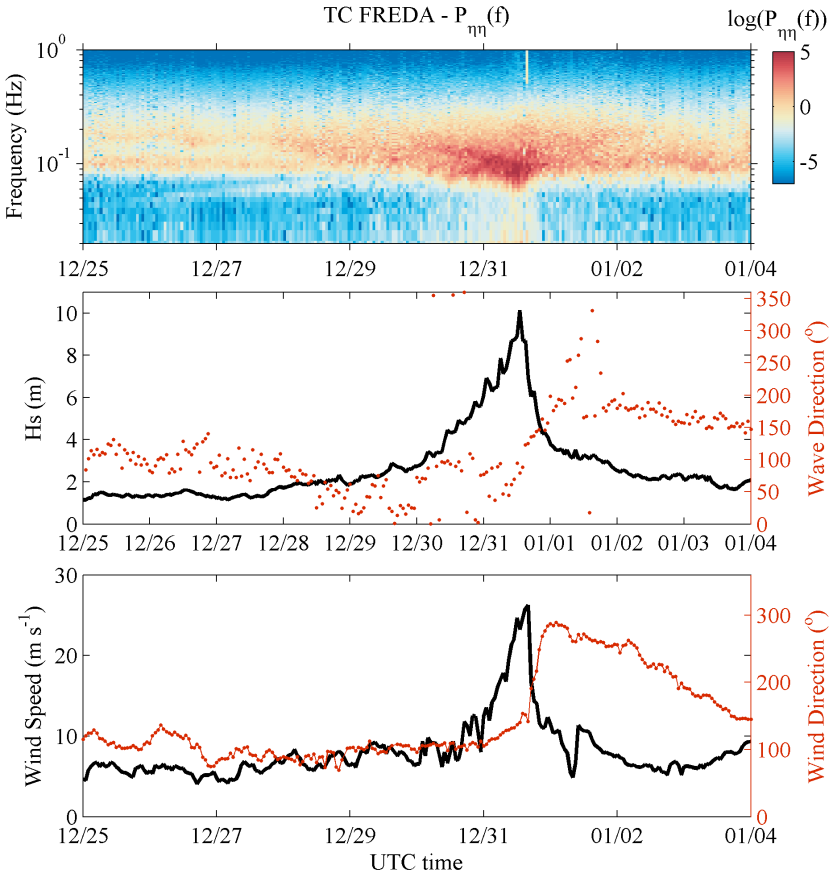

Figure 5.8: (top panel) Spectrogram of the sea surface displacement. The horizontal axis is the time in days. The spectra were computed using 256-sec FFT windows with 50% overlap over 30min windows. (middle panel) Significant wave height H_s (black) and wave direction (red, coming from, relative to true north) and (lower panel) wind speed measured at 1m height from the Wave Glider (black) and corresponding wind direction (red, coming from, relative to true north).

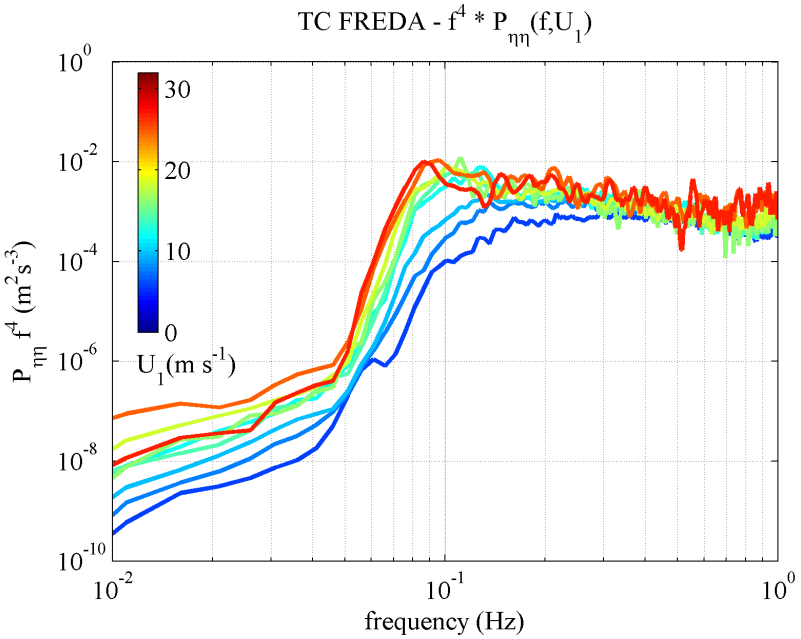

Figure 5.9: Evolution of the weighted (f^4) wave frequency spectrum as a function of wind speed U_1 (color coded, m/s) from 1200 UTC December 29, 2012, through 1200 UTC December 31, 2012. Beyond the peak frequency, f_p, where significant peak enhancement is present, the high frequency tail of the spectra are approximately proportional to f^4. Also note the low frequency swell peak in the low wind case at f = 0.06Hz.

tatively depicted by a hurricane symbol. The red arrow represents the wind vector, while the directional wave information is defined as coming from. The first sign of the approaching storm occurs on December 30 2012, in the form of a northerly swell, while the high frequency part of the spectrum is dominated by westerly wind waves. As the TC got closer to the WG, on December 31 2012 at 09:00, the energy associated with the swell and wind waves increased, with 1m winds reaching close to 19.5 $m\ s^{-1}$, still showing a sharp bimodal distribution of wave energy. A few hours later, as the TC gets even closer to the WG and the wind increased (1m wind U_1= 24.7 $m\ s^{-1}$), the swell and wind wave energy start converging into a single, broader, energy peak, effectively transitioning from a bimodal to a unimodal spectrum. The directional spread of energy at the peak frequency is significant, driven by the rapid change in wind direction as the glider passed through the right (west) side of the TC, relative to the direction of TC propagation. A few hours later, at 16:00 UTC, when the WG was located directly to the right (west) of the eye of the TC, the spectrum was dominated by wind-generated waves, coming from the south-east. Wind speed rapidly decreased once the glider reached the TC wake, with the 1m wind speed, U_1, of only 11.6 $m\ s^{-1}$ at 20:00 UTC on December 31 2012, coming from the south-west. Note that the wind and peak wave directions are not perfectly aligned, as the wave field does not have time to reach wind-wave equilibrium in such a rapidly varying environment.

Spatial variability of the wind speed and significant wave height is depicted in figure 5.11, where the measurement location used is the relative distance (km) in an earth coordinate frame between the WG and the eye of the TC. The mean direction of propagation of Freda is shown as a black arrow. Note the rapid increase in wind and wave conditions as the storm passed to the east of the WG and the sharp change of wind direction as the WG encounters the wake of the TC.

The Craik-Leibovich II (CLII) theory of Langmuir circulation, or "Langmuir turbulence" introduces a vortex force which is the vector product of the Stokes drift of the wave field and the vorticity of the Eulerian current,$F_{\mathrm{v}} = u_s \times \omega$. Early modelling of the effects of the vortex force on the upper ocean used monochromatic wave fields to evaluate the Stokes drift, but recent modelling has used a full directional spectrum (Sullivan et al., 2012) based on Kenyon (1969) spectral description of $\bar{u}_s$ as a function of depth. As only directional wave frequency spectra were available in this study, we estimated u_s using its leading–order expression derived in Webb and Fox-Kemper (2011):

$$u_s = \frac{16\pi^3}{g} \int_0^\infty \int_{-\pi}^{\pi} (\cos\theta, \sin\theta, 0) f^3 S_{f\theta}(f,\theta) e^{\frac{8\pi^2 f^2}{g} z} d\theta df. \tag{5.5}$$

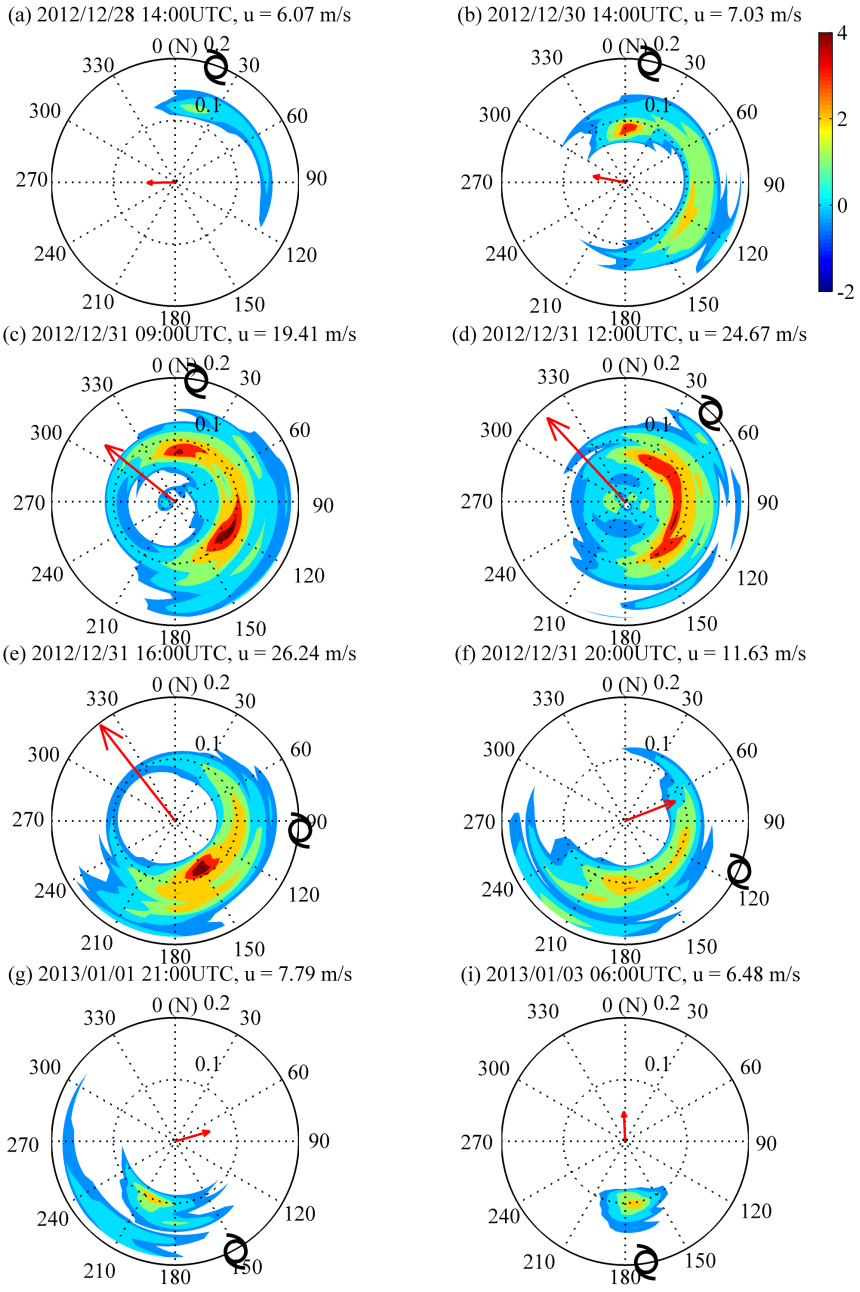

Figure 5.10: Evolution of the wave directional spectrum as TC Freda passed near Wave Glider Benjamin. The relative location of the storm is depicted by a TC symbol. Wave direction is defined as "coming from", the wind vector (red arrow) is measured 1 meter above the Wave Glider float.

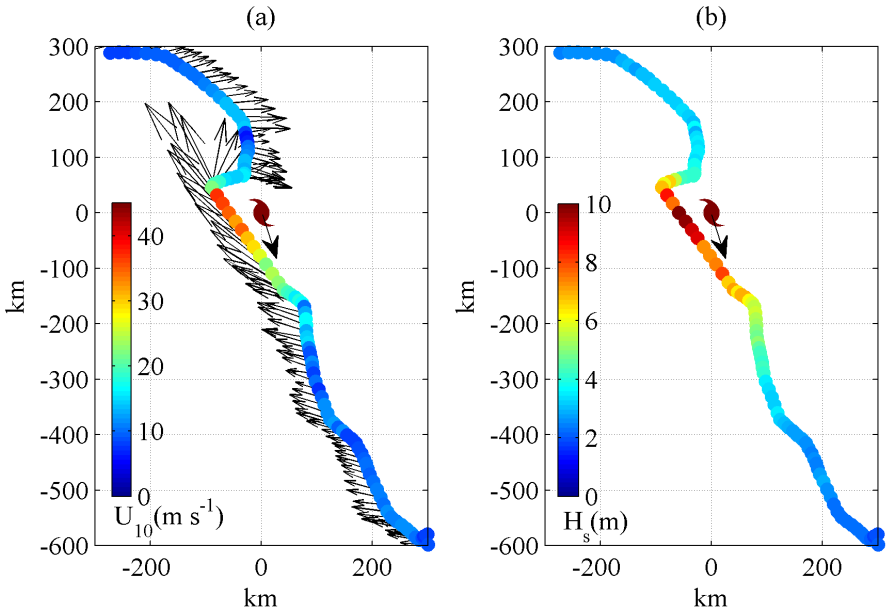

Figure 5.11: (a) Wind speed U_{10} color coded and also shown as vectors along the TC track, and (b) significant wave height H_s as a function of relative distance from the eye of TC Freda. X-axis and Y-axis are oriented in the East and North directions, respectively. Also shown is the storm mean direction of propagation (black arrow). Both variables are represented as color coded dots for each record.

Here $S_{f\theta}$ is the directional wave frequency spectrum, z is the depth, and f the frequency in Hz. Stokes velocity and wind amplitudes and directions are shown in Figure 5.12 (a) and (b). The alignment between Stokes drift velocity and the surface wind is remarkable, reaching at most a 35° offset once the glider is located in the wake of the TC at $t - t_m$ = 10 h, where t_m is the time when measured winds first reached TC force, on December 31 2012 at 1200 UTC (U_{10}= 34.5 $m\ s^{-1}$).

Figure 5.12(c) shows the evolution of the surface turbulent Langmuir number La_t (McWilliams et al. 1997), defined as

$$La_t = \sqrt{\frac{u_{*w}(t)}{|u_s(z=0,t)|}}, \tag{5.6}$$

where $u_{*w}(t)$ is the friction velocity in the water, $u_{*w}(t) = \sqrt{|\tau|/\rho_w}$, ρ_w is the water density, $\tau$the surface stress,$u_s(0,t)$ is the surface Stokes drift velocity calculated from (5.5). Low values of La_t, below 0.4 in the case of aligned wind and Stokes drift vector, are often associated with the generation of Langmuir circulations. In recent work from Harcourt and D'Asaro (2008) the Langmuir number La_{tsl} is defined as $La_{tsl} = \sqrt{u_{*w}/(\langle u_s\rangle_{sl} - u_{sref})}$, based on a near-surface average value of the Stokes drift, $\langle u_s\rangle_{sl}$, and a reference value, u_{sref} at depth (though still in the mixed layer) to account for vortex force production. The definition of the Langmuir number (equation 5.6) was chosen for its simplicity and to provide direct comparison with the numerical simulations of Sullivan et al. (2012). We find the lowest value of La_t in front of the storm at t = -20 hr and later at t=20 hr, qualitatively consistent with the LES modelling of Sullivan et al. (2012).

The representative vertical penetration of the Stokes drift, the Stokes depth scale (figure 5.12(d)), is defined by Sullivan et al. (2012) as:

$$D_s = 4\pi \int_{z_s}^{0} \frac{u_s(z,t)\cdot u_s(0,t)}{|u_s(0,t)|^2} dz, \tag{5.7}$$

where z_s is chosen as the depth where the integrand remains positive.

The Stokes depth scale rapidly increased from 35-45 m to up to 126 m over a 40 hr period as the storm approached the WG, reaching its maximum at t=4 hr, then sharply decreased to pre-storm levels in only 15 hrs. Though we do not find a peak in the Stokes depth scale ahead of the storm as shown in Sullivan et al. (2012), we do observe a rapid decrease of D_s once the glider reached the rear of the storm, consistent with the analysis of the Sullivan et al. model TC.

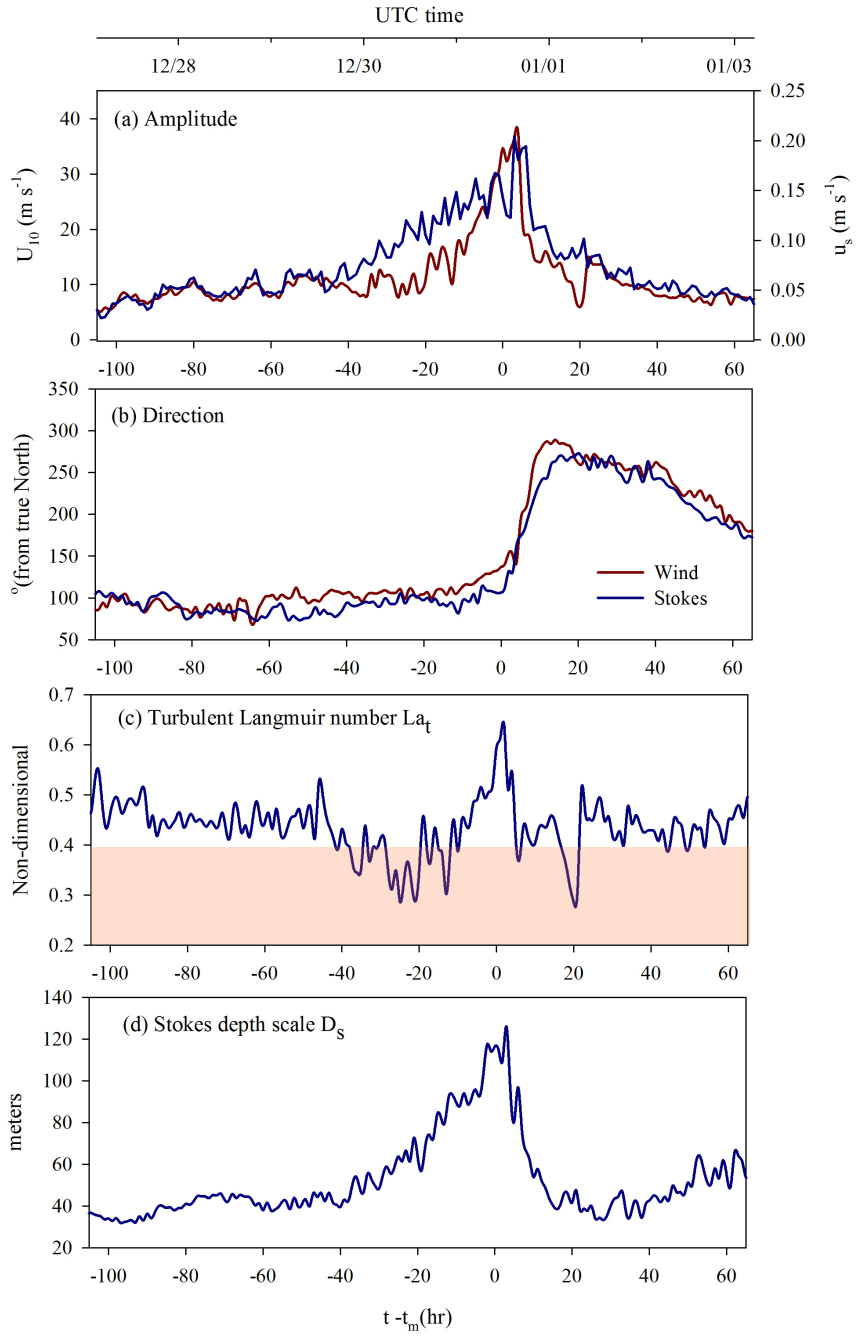

Figure 5.12: (a) Amplitude of the surface Stokes drift velocity (blue) and U_{10}(red) as the WG passed near TC Freda, and corresponding directions (b). (c) Evolution of the turbulent Langmuir number, La_t, with the colored area corresponding to $La_t < 0.4$. (d) Stokes depth scale , D_s, for the same period of time.

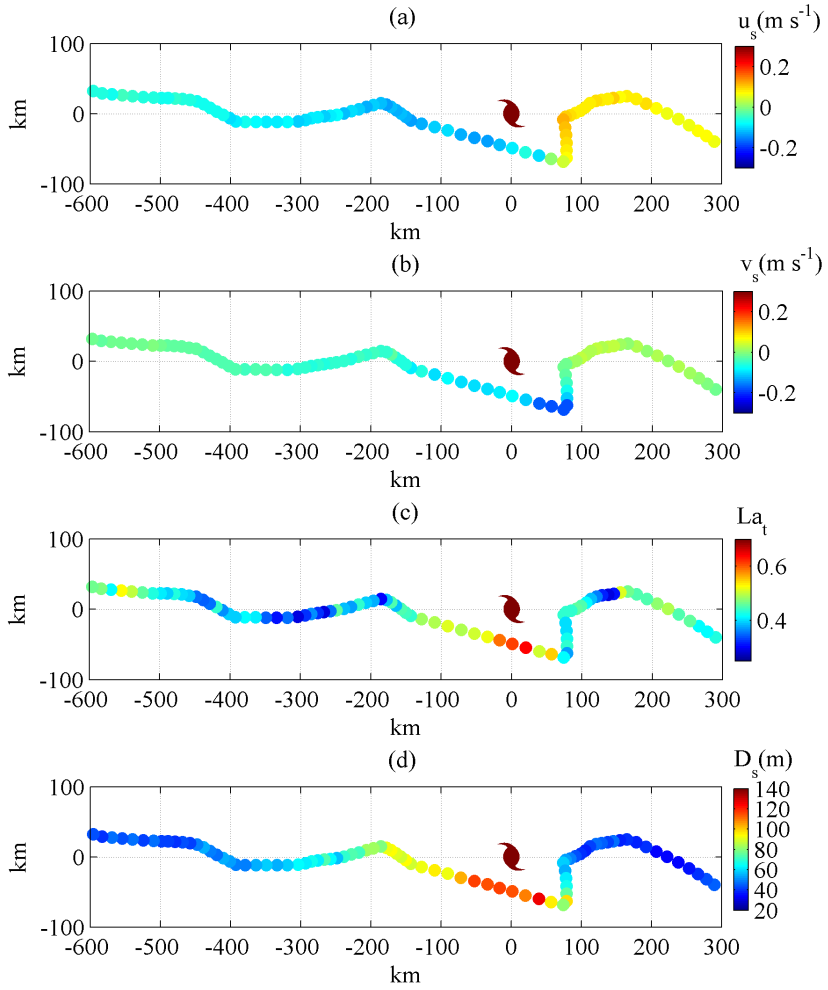

Figure 5.13: Along-track and cross-track storm direction components of the Stokes drift velocity u_s (a) and v_s (b), respectively, calculated at the water surface, z=0, from the measured directional wave spectra. (c) The non-dimensional turbulent Langmuir number,La_t, and (d) the Stokes depth scale , D_s , (m) as a function of distance from the eye of TC Freda.

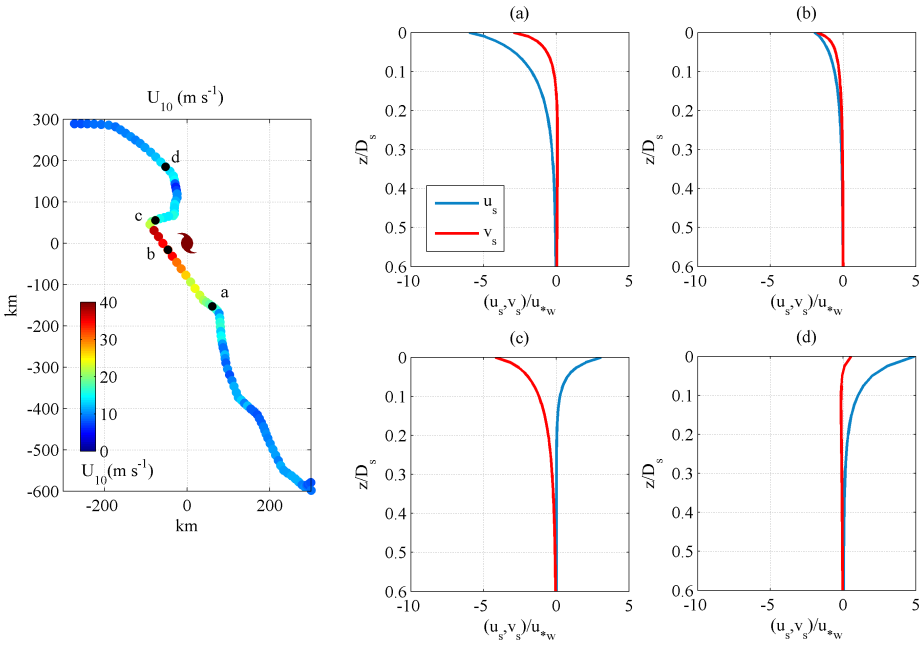

Figure 5.14: Vertical profiles of Stokes drift velocity components (along-track and cross-track storm direction components u_s (blue) and v_s (red)) normalized by the local friction velocity in the water, u_{*w} , at various locations (a-d) with respect to the eye of the storm, as shown in the left panel. The depth is scaled by D_s, the Stokes depth scale.

Figure 5.13 presents the same set of variables (u_s, La_t, D_s), this time as a function of position relative to the storm. The axes have been rotated from an earth-coordinate reference frame, to a TC-coordinate reference frame, where the TC is propagating to the left side of the figure. The (u_s, v_s) vector is rotated in the new reference frame as well for comparison with numerical estimates from Sullivan et al. (2012). The along-track storm direction component of the Stokes drift, u_s, is mostly negative in front of the storm, with values reaching up to -0.2 $m\,s^{-1}$ then sharply changing sign once the TC wake is reached. The cross-track storm component of the Stokes drift, v_s, remains low or close to zero in front of the storm, then reaches a minimum, with a value around -0.2 $m\,s^{-1}$, at Y=-50 km, and X=70 km. This asymmetry is explained by the fact that the wind field is less asymmetric than the distribution of the wave field (Young, 2003). The spatial distributions of the turbulent Langmuir number,La_t, and Stokes depth scale, D_s, are presented in figures 5.13(c) and (d). Larger values are found to the right (negative Y) side of the TC.

Four profiles of the Stokes velocity at various times and locations with respect to the center of the TC are shown in figure 5.14. The velocity profiles, in a TC-coordinate frame,

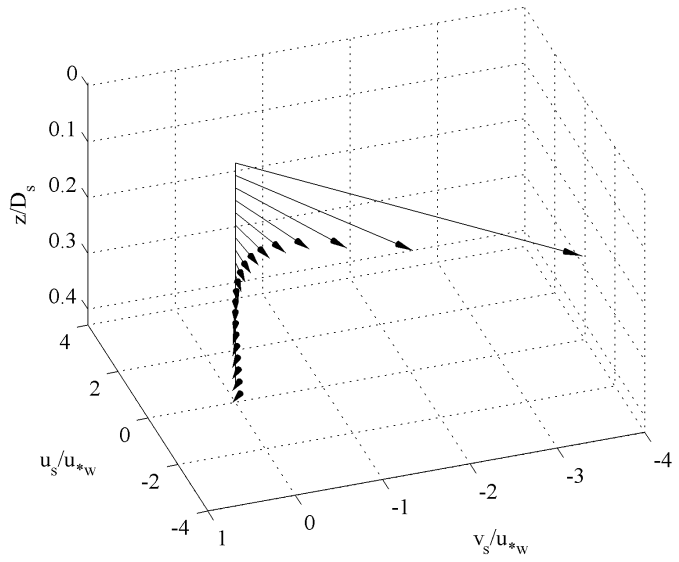

Figure 5.15: Example of a vertical profile of Stokes drift velocity normalized by the local friction velocity in the water on December 31 2012 at 02:00 UTC. The depth is scaled by D_s, the Stokes depth scale.

have been normalized by the local friction velocity in the water, and the depth z is scaled by the Stokes depth scale D_s. Recall that the vertical profile of Stokes drift spirals with depth (see figure 5.15), as it is composed of a mix of swell and wind-wave components each with an e^{kz} vertical dependence that propagated in rapidly changing directions as the TC passed near the WG. It is therefore of interest to characterize the depth dependence of the wind-Stokes-drift alignment (the included angle between them) as it is directly related to the generation of Langmuir turbulence. Van Roekel et al. (2012) showed that Langmuir turbulence generation is minimal for an included angle of 180° and the mixing associated with Langmuir circulation is reduced once the included angle reaches 90°.

Figure 5.16 shows the variation of the wind-Stokes-drift included angle as a function of time, for four selected depths, z = 0, 10, 40, and 80 m along with the magnitude of the wind speed U_{10} in (a) and the evolution of the normalized Stokes drift profile $(u_s, v_s)/u_{*w}$ as a function of non-dimensional depth z/D_s for the same period of time (Figure 5.16(c) and (d) respectively). The alignment is generally better at the surface as shorter locally wind-driven waves rapidly respond to the change in wind direction much faster than it takes for the lower frequency components of the wave field. Around t=-70 hr, as the swell approaches the WG, the misalignment at larger depth (therefore lower frequency of the wave field) rapidly increases, reaching almost 120° at t=-30hr. As the glider moves closer to the center of the TC, the surface wave spectrum changes from a multi- to uni-modal distribution, reducing the depth dependence of the wind-Stokes-drift alignment. At t=4hr, the time of maximum winds, when the wave spectrum is narrow-banded (wind waves rapidly aligning to surface forcing), the Stokes drift is in resonance with the wind, meaning that the entire water column, up to the Stokes depth scale is oriented in, or close to, the wind direction. This is consistent with the results of Sullivan et al. (2012) and of significance as this implies the generation of strong Langmuir turbulence close to the center of the TC. As the TC propagates away from the wave glider, the wind-Stokes-drift alignment at depth rapidly deteriorates, briefly reaching 110° at t=10hr. The alignment subsequently improves over the following 50 hr, before wind-wave equilibrium is reached at t=60hr.

5.6 Biophysical response

Extreme weather events such as Tropical cyclones are known to influence nutrient supply and phytoplankton dynamics, providing a mechanism through which cold, deeper, nutrient-rich water, essential for phytoplankton growth, is entrained into the mixed layer

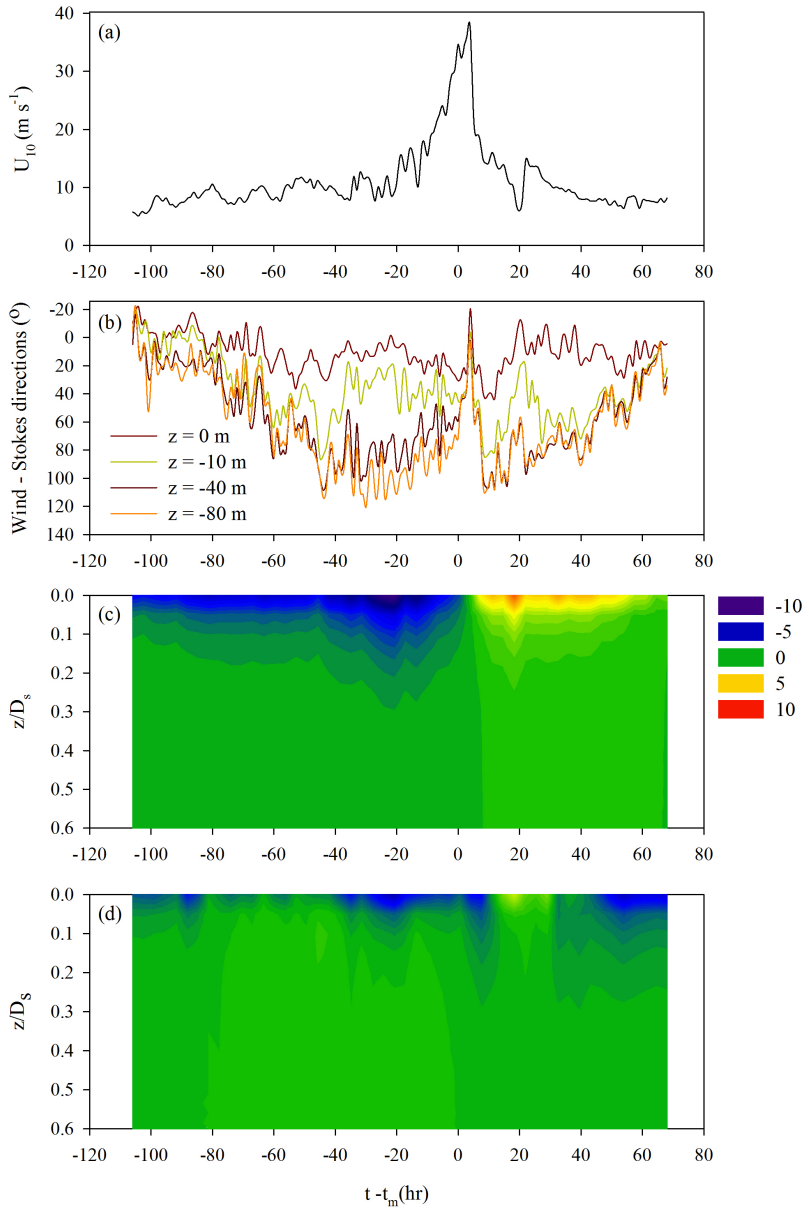

Figure 5.16: (a) The wind speed U_{10} as the WG passed near TC Freda, (b) the difference between the direction of the mean wind and that of the Stokes drift $\mathbf{u}_s(z)$ for $z = 0, 10, 40, 80m$, as a function of time relative to maximum wind. Color coded vertical profiles of Stokes drift (u_s, v_s) normalized by the friction velocity u_{*w} as a function of non-dimensional depth z/D_s are shown in (c) and (d) respectively.

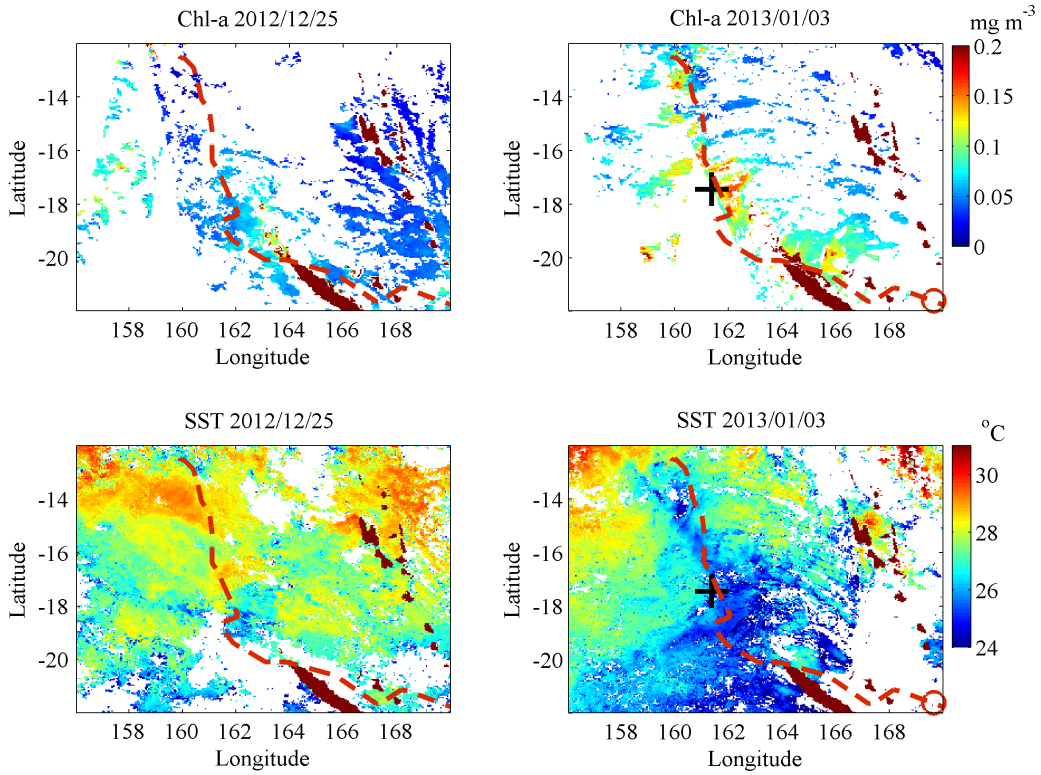

Figure 5.17: (Top panels) Chl-a concentration estimated from MODIS and TERRA level 3 daily products (mg/m^3), before (left) and after (right) TC Freda. The track of the TC is shown as a red dashed line. The average location of the center of the storm and the Wave Glider on January 3 2013 are depicted by a red circle and a black cross, respectively. (Lower panels) corresponding sea surface temperature.

(Babin et al., 2004; Chen et al., 2013; Chung et al., 2012; Hung and Gong, 2011; Hung et al., 2010). Conducting traditional ship-based expeditions to collect in-situ measurements to characterize the biogeochemical ocean response to such extreme events is difficult (Chen et al., 2013), while satellite observations and estimation of ocean biological productivity variables (e.g. Chlorophyll-a) are often limited by cloud coverage, especially in close proximity to large weather systems. This is however where collocated spatio-temporal measurements of the biological and physical processes are most needed, to characterize the mechanisms through which cold nutrient-rich waters are transported to the surface.

Satellite observations of daily chlorophyll concentration and sea surface temperature (SST) from MODIS (Moderate Resolution Imaging Spectroradiometer) collected on December 25^{th} 2012 and January 3^{rd} 2013 (*before* and *after* the tropical cyclone passage)

are shown in figure 5.17. The track of Freda over the area is shown as a dashed red line, while the location of the storm and the WG on January 3 2013 is depicted as a red circle and a black cross, respectively, in the two right panels. Despite the limited field-of-view caused by cloud coverage, especially close to the storm, the TC "cold" wake is clearly visible on January 3^{rd} 2013, and exhibits increased concentration of chlorophyll when compared to the pre-storm levels reaching 0.18 $mg\,m^{-3}$ within the wake of the TC. Surface temperature shows a cooling of up to $4.5^{o}C$ in response to the TC, even several days after the storm passes.

Chlorophyll-a *in-vivo* Fluorescence (RFU) is shown in the upper panel of Figure 5.18. This is not a direct measurement of chl-a concentration, as the fluorescence measurements are affected by a range of processes, including photosynthesis and quenching during day time (Falkowski and Kiefer, 1985). The latter explains the large dips in the chl-a fluorescence values during daytime. We chose the nighttime fluorescence data, the period of the day that is least impacted by these processes (highlighted in black in Fig 16 (a)), as an indicator of the relative evolution of the chl-a concentration as the WG passes near the storm. Also shown are the wind speed U_{10}, significant wave height H_s, and wave glider easterly horizontal velocity in panel (b), SST and surface salinity in panel (c) and dissolved oxygen DO and turbidity in panel (d). The WG easterly horizontal velocity is used as a proxy for the large surface and subsurface currents expected in the wake of the TC (recall from figure 5.5 that the surface current sensor was turned off during the most intense part of the storm). During the studied period, the WG was set to travel toward the west, therefore any positive easterly horizontal velocities imply strong surface currents opposing the WG direction of propagation (i.e. the WG is moving backward). The period of time when the WG was located in the wake of the storm, highlighted in blue in Figure 5.18, was estimated using the available in-situ and satellite products (figure 5.17).

The observed in-situ surface temperature fell by $1.8^{o}C$from December 30 2012 to January 2013, along the track of the WG. The surface salinity drops rapidly starting on December 29 2012, decreasing to approximately 35.05 to 35.15 psu for the following two days before slowly increasing to 35.3 psu on January 4 2013. The decrease in salinity is likely due to intense rain close to the storm. Dissolved oxygen concentration rapidly increased as wind speed rose, caused by the onset of breaking and associated bubble entrainment (Melville, 1996; Wallace and Wirick, 1992) then remained at an elevated level for some time.

The observed nighttime chl-a *in-vivo* fluorescence increased as the TC passed near the WG, starting from 30 RFU on December 28 2012, and reaching 50 to 60 RFU on

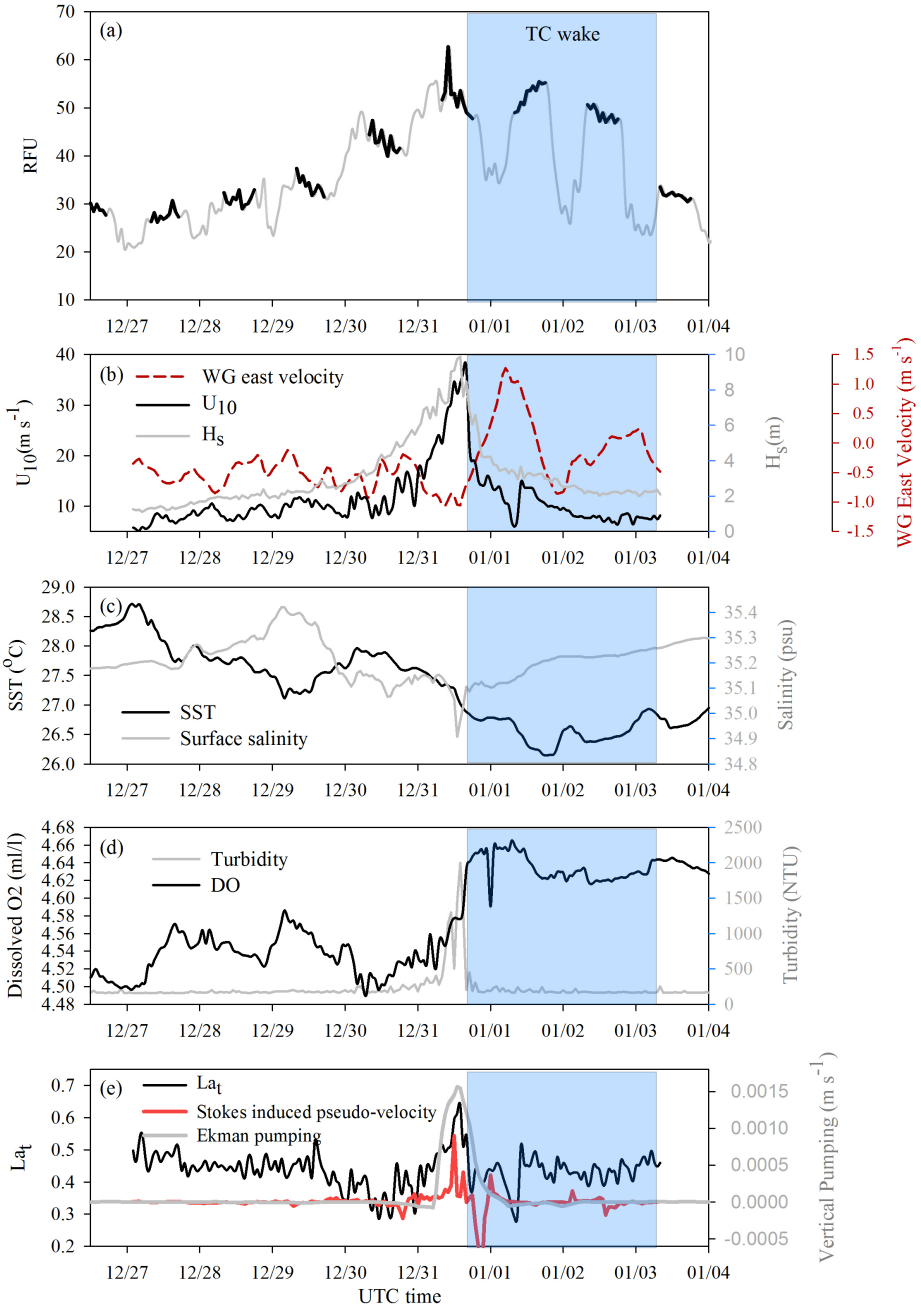

Figure 5.18: Ocean surface conditions measured by the Wave Glider during TC Freda. (a) chlorophyll-a in-vivo fluorescence, the bold black lines represent the night-time portion of the data set; (b) significant wave height (gray), wind speed U_{10} in m/s (black) and horizontal easterly WG velocity in m/s (red) ; (c) surface temperature (SST) and surface salinity; (d) dissolved oxygen (DO) and turbidity; (e) Langmuir number, Stokes induced pseudo-velocity w^{St} and Ekman pumping w_E.

December 31 2013. The observed chl-a remained at this level (or slightly lower) in the TC wake, then rapidly reduced to pre-storm levels once the WG was out of the TC wake. Though we do expect a bias in the chl-a fluorescence caused by bubble contamination in the optical measurements (Omand et al., 2009; Terrill et al., 2001), this would not account for the significant rise of chl-a fluorescence occurring between December 29 2012 and December 31 2012. In addition, the turbidity measurements shown in Figure 5.18 (d) only exhibit a significant increase, also known to be associated with subsurface bubble generation, at the peak of the storm. Note that the apparent constant chl-a *in-vivo* fluorescence in the TC wake from December 31 2012 to January 1 2013, while the SST keeps decreasing suggests that all nutrient-rich water from the euphotic layer was entrained into the mixed layer.

5.7 Section summary and discussion

Atmospheric and oceanographic measurements collected during Tropical Cyclone Freda from an instrumented surface vehicle have been analyzed. The Wave Glider was able to withstand TC (hurricane)-level wind and wave conditions while collecting and transmitting measurements.

The standard surface-ocean-lower-atmosphere (SOLA) measurements of air temperature, winds, SST, and surface currents were measured. In addition, using the motion of the surface flotation for wave field measurements calibrated against a standard wave buoy, the evolution of the directional wave field as the storm passed near the WG was measured and analyzed. It exhibited a transition from a unimodal (swell) to a bimodal distribution (swell + wind waves) in front of the TC, changing to a unimodal distribution close to the eye of the TC and in its wake. The frequency spectrum of the sea surface displacement (i.e. the wave spectrum) shows close to a f^{-4} dependency over a range of frequencies, consistent with past studies (Donelan et al., 1985; Young, 2006).

Stokes drift velocities were estimated from the wave directional spectrum. The Langmuir turbulence number, the Stokes depth scale, and the Stokes drift computed from measurements of the directional wave spectrum across the track of TC Freda show remarkable agreement with recent hurricane marine boundary layer studies that include numerical wind-wave model predictions as input to the LES model of the marine boundary layer (Sullivan et al., 2012). The surface turbulent Langmuir numberLa_t, based on wave measurements, varied from 0.28 to 0.6, with the lower values, below 0.4, found ahead of the storm, and in its wake. We find a spatial distribution of the Stokes drift vec-

tor comparable to that in Sullivan et al. (2012), with a maximum magnitude at the closest point from the eye of the TC, to its right side, mostly driven by v_s, the component orthogonal to the path of the TC. Though we do expect an enhancement of vertical mixing by Langmuir turbulence through the vortex force when the Stokes drift vector is aligned with the current, large misalignments between the wind and Stokes drift vector, at depth in particular, will lead to situations where the vertical gradients of Eulerian velocities and Stokes drift are of opposing signs, effectively reducing the contribution of Langmuir turbulence to vertical mixing. This is of importance, as the depth penetration of the Stokes drift, characterized as the Stokes depth scale, was found to exceed 120m at the time of maximum winds.

Though the deepening of the mixed layer produced by the wake of inertial currents formed behind a tropical cyclone or hurricane (e.g. Price (1981)), remains the dominant dynamical process through which cold, deeper water is entrained into the mixed layer in the wake of TCs and hurricanes, this does not explain the apparent entrainment or upwelling ahead of Freda demonstrated by the chl-a data presented here. It appears that other mechanisms may need to be considered.

Toffoli et al. (2012) suggest wave-orbital-motion-induced turbulence as a possible process to explain the deepening of the mixed layer during tropical cyclones; however, evidence for such turbulence is based on very limited indirect laboratory studies, and as far as we are aware there is no direct field evidence of such turbulence. Recent numerical studies from Sullivan et al. (2012) show the importance of Langmuir turbulence, which is estimated to contribute to up to 20% of the entrainment flux at the base of a marine boundary layer driven by a hurricane. Turbulence generated by wave breaking, a dominant feature of such high wind and wave environments was not taken into account in this study, but is known to contribute significantly (Sullivan et al., 2007) to ocean mixing, through direct injection of turbulence near the surface, which is transported to deeper water by Langmuir circulations. We expect this latter process to be important in tropical cyclones, in particular ahead of the storm, where the Stokes depth scale can reach very large values (up to 120m for TC Freda).

Another mechanism to consider is the Ekman pumping w_E, defined as

$$w_E = \frac{\nabla \times \tau}{\rho_w \mathrm{f}_c} \tag{5.8}$$

where $\nabla \times \tau$ is the wind stress curl, and f_c the Coriolis parameter. Figure 5.18 (e) shows $w_E$calculated from the JTWC/W3 product (gray line) at the WG location. The upwelling

velocity reached 5.5m per hour at the peak of the storm, in an area where the winds were very high (U_{10} >25m/s^{-1}) and their direction was rapidly changing. Also shown is the vertical velocity generated from the spatial divergence of horizontal Stokes drift, introduced by McWilliams et al. (2004) as a pseudo-vertical velocity, w^{St}(red line). This velocity does contribute to the vertical transport near the most intense part of the TC, though to a lesser degree than the Ekman pumping.

Future versions of the SOLA-instrumented Wave Glider should include a current profiler to estimate the Eulerian current shear, which is an important source of mixing in the wake of tropical cyclones, as well as the Stokes shear-production term as a function of depth in the non-equilibrium wind-wave regime.

One of the most important conclusion of this work is that the SOLA measurements, made in close proximity to a category-3 tropical cyclone using the Wave Glider, open the way for more extensive use of this technology in measuring air-sea interaction processes in extreme conditions. There is room for improvement in using more research-grade instrumentation to measure SOLA processes. There is also the opportunity to park a small flotilla of these platforms in "hurricane alley" locations, and, with a 5-7 day hurricane forecast window, be able to send them to cross the hurricane track at various locations.

This work was published in the Journal of Atmospheric and Oceanic Technology (American Meteorological Society) in October 2014:

Lenain, L. and W. Melville, 2014: Autonomous Surface Vehicle Measurements of the Ocean's Response to Tropical Cyclone Freda. J. Atmos. Oceanic Technol., 31, 2169 to 2190, doi: 10.1175/JTECH-D-14-00012.1.

Chapter 6

General Summary

In this thesis, we have presented a series of experiments, both numerical and field observations, focusing on surface wave effects on air-sea interaction processes.

In chapter 2, using an airborne topographic lidar, combined with in-situ atmospheric measurements collected from a research platform, we characterized the directional properties of the wave field across the equilibrium-saturation ranges of wind-generated surface waves and correlates them with the wind forcing. To our knowledge, this is the first study that shows directional characterization of surface waves over such a broad range of wavenumbers and environmental conditions. Our measurements extends the known bimodal distribution well beyond what was reported in previous studies, with an azimuthal separation between the two lobes reaching close to π for the highest wavenumbers we could resolve, up to $k/k_p \approx 100 - 200$. Though more work is needed, in particular to resolve the 180^o ambiguity in the directional spectrum computed from the lidar topographic surface wave maps, these results show that waves propagating in opposing directions can be found at wavenumbers around 10-12 rad/m (10-11 rad/s for linear gravity waves) in waves from one storm system, rather than requiring waves from opposing storms. The existence of such wave systems is believed to be a leading mechanism through which microseismic noise and low frequency acoustic is generated in the ocean (Longuet-Higgins, 1950; Farrell and Munk, 2010; Ardhuin et al., 2015).

The omnidirectional wavenumber spectra show a consistent power law behavior, proportional to $k^{-5/2}$ in the equilibrium range, and k^{-3} in the saturation range. The transition between these two regimes is very well defined and we find good agreement with the model of Phillips (1985) that predicts that the upper limit of the wavenumber in the equilibrium range is, to within a factor of 1-2, proportional to $(u_*^2/g)^{-1}$. The collapse across the equilibrium-saturation ranges of the omnidirectional saturation wavenumber spectra plotted against non-dimensional wavenumber ku_*^2/g is remarkable, as shown in figure 2.11. The same scaling is also very effective in collapsing the bimodal azimuthal separation found in the directional properties of the spectra.

Direct measurements of the transition across the equilibrium and saturation regimes,

over a broad range of environmental conditions, offer an opportunity to test the empirical parameterization of transition wavenumber k_n of Romero and Melville (2010a,b), defined as a function of the zero-up crossing wavenumber, k_u, of the azimuth-integrated non-linear energy fluxes S_{nl} based on Phillips' (1985) equilibrium argument. The upper limit of the equilibrium range is indeed a function of k_u, with a clear dependence on wave age and the non-dimensional atmospheric friction velocity $u_*/\sqrt{gH_s}$. This non-dimensional quantity appears to be better suited in the present data set to capture the evolution of the equilibrium-saturation ranges than is the wave age.

In the third chapter, we focused on the generation of sea-spray aerosols, another surface process influencing the coupling between the ocean and the atmosphere. We analyzed aerosol data collected during an air-sea interaction experiment, the phase-resolved High-Resolution Air-Sea Interaction experiment (HIRES), conducted off the coast of Northern California in June 2010, and the GOTEX2004 experiment, conducted in 2004 in the Gulf of Tehuantepec in Mexico. Detailed measurements of aerosol number concentrations in the Marine Atmospheric Boundary Layer (MABL), at altitudes ranging from as low as 30 m and up to 800 m above mean sea level (AMSL) over a broad range of environmental conditions (significant wave height, H_s, of 2 to 4.5 m, and U_{10} from 10 to 18 m/s) collected from an instrumented research aircraft, were described.

Large aerosol particles ($d > 40\mu m$) were found up to the top of the MABL. This is of importance as the role, generation and transport mechanisms of this range of aerosols are poorly understood (Veron, 2015), but are known to contribute to sensible and latent heat fluxes, and can also offer a means of transport for larger organic carbon compounds from the ocean, including the Dissolved Oxygen Component (DOC) and the Particulate Organic Component (POC)(Quinn et al., 2015).

Despite observational evidence of the importance of surface-wave and wave-breaking related processes in coupling the ocean with the atmosphere, sea-spray source generation functions are traditionally parameterized by the ten-meter (U_{10}) wind speed alone. It is clear that unless the wind and wave field are fully developed, the source function will be a function of both wind and wave parameters. Here we presented the sensitivity to a physically-based non-dimensional parameterization of the aerosol volumetric concentration measured at 30m AMSL during the HIRES2010 and GOTEX2004 experiments. Though limited to one measurement height (30m AMSL), this approach shows promise for including wave effects into models of marine aerosol production.

Our understanding of the physical processes that occur when aerosol particles are created and ejected into the air flow, especially for the the larger particles with $d > 20\mu m$,

is very limited. The scatter in Sea Spray Source Generation function (SSSGF) estimates, especially for larger particles, is significant and has serious implications for modeling global aerosol budgets.

In chapter 4, Numerical simulations of deep-water breaking waves in an idealized wave channel were conducted by solving the full Navier-Stokes equations in a two-phase flow (air and water), in two dimensions using the numerical code Gerris over a range of frequencies, f_c, and slopes, S. The flow was seeded with a dense sheet of Lagrangian particles to study the mixing in the breaking region and to quantify the deepening rate of the portion of the water initially at the surface. The rate of deepening of the particle cloud is qualitatively in agreement with the experimental results of Rapp and Melville (1990) though differences are present, likely associated with numerical resolution and/or artifacts. We find that the water initially at the surface can quickly reach depths equivalent to one to two wave heights of the breaking wave, followed by a slower rate of deepening. Note that we showed in Chapter 2 and 3 that the significant wave height H_s could reach up to 5 m in storms off the coast of California. In other parts of the world (i.e. North Sea or in a Tropical Cyclones such as TC Freda), H_s can often get larger than 10 m. While the significant wave height is only a representation of the statistical mean wave height, it is anticipated that a fraction of the waves will have an amplitude equal to $1.5 - 2 \times H_s$, implying that water initially at the surface could reach depths of up to 20-40 m just through the effects of wave breaking, and producing significant mixing in the process.

We also showed that size distributions of 2D droplets generated during the breaking process in a numerical wave tank show a surprising good agreement with the power-law scaling found in past laboratory and numerical studies, though the present 2D setup can not lead to any quantitative comparisons: three-dimensional, higher resolution simulations are required to compute the droplet size concentration functions, but will be the topic of future research.

In the last chapter, we investigate the use of novel unmanned, autonomous surface vehicles to help elucidate and improve our understanding of the coupling between the ocean and the atmosphere in energetic storms, such as hurricanes and tropical cyclones. On December 31, 2012, an instrumented autonomous surface vehicle (Liquid Robotics Wave Glider, while transiting across the Pacific from Hawaii to Australia as part of the PacX project, came very close (46km) to the center of a category 3 tropical cyclone, TC Freda, experiencing winds of up to 37 m/s and significant wave heights close to 10m. The Wave Glider was instrumented for surface-ocean-lower-atmosphere (SOLA) measurements including atmospheric pressure, surface winds and temperature, sea surface

temperature, salinity, dissolved oxygen, fluorescence (Chlorophyll-a and turbidity), and surface-wave directional spectra.

Using the motion of the surface flotation for wave measurements, the evolution of the directional wave field as the storm passed near the wave glider was measured and analyzed. We found a transition from a unimodal (swell) to a bimodal distribution (swell + wind waves) in front of the Tropical Cyclone, changing to a unimodal distribution close to the eye of the TC and in its wake. The frequency spectrum of the sea surface displacement (i.e. the wave spectrum) shows close to a f^{-4}dependency over a range of frequencies, consistent with past studies (Donelan et al., 1985; Young, 2006).

Stokes drift velocities were estimated from the wave directional spectrum. The Langmuir turbulence number, the Stokes depth scale, and the Stokes drift computed from measurements of the directional wave spectrum across the track of TC Freda show remarkable agreement with hurricane marine boundary layer studies that include numerical wind-wave model predictions as input to the LES model of the marine boundary layer (Sullivan et al., 2012). The surface turbulent Langmuir number La_t, based on wave measurements, varied from 0.28 to 0.6, with the lower values, below 0.4, found ahead of the storm, and in its wake. We find a spatial distribution of the Stokes drift vector comparable to that in Sullivan et al. (2012), with a maximum magnitude at the closest point from the eye of the TC, to its right side, mostly driven by v_s, the component orthogonal to the path of the TC. Though we do expect an enhancement of vertical mixing by Langmuir turbulence through the vortex force when the Stokes drift vector is aligned with the current, large misalignments between the wind and Stokes drift vector, at depth in particular, will lead to situations where the vertical gradients of Eulerian velocities and Stokes drift are of opposing signs, effectively reducing the contribution of Langmuir turbulence to vertical mixing. This is of importance, as the depth penetration of the Stokes drift, characterized as the Stokes depth scale, was found to exceed 120m at the time of maximum winds.

Though the deepening of the mixed layer produced by the wake of inertial currents formed behind a tropical cyclone or hurricane remains the dominant dynamical process through which cold, deeper water is entrained into the mixed layer in the wake of TCs and hurricanes, this does not explain the apparent entrainment or upwelling ahead of Freda demonstrated by the chl-a data presented here. It appears that other mechanisms may need to be considered and are discussed in the chapter.

Overall, we have demonstrated through this series of experimental and numerical studies the value of combining approaches (i.e. laboratory, field and numerical experiments), sensor technology, and measurement platforms (research vessels, aircraft, re-

search platform, unmanned surface vehicles) to improve our understanding of the physics driving air-sea interaction processes. The development of unmanned vehicles, combined with the miniaturization of scientific grade instrumentation, has revolutionized our ability to conduct measurements thought to be beyond the scope of our capabilities not so long ago, such as the SOLA measurements performed at the heart of TC Freda, described in the last chapter. This opens the way for more extensive and regular use of this technology to study and characterize air-sea interaction processes in a broad range of conditions, including energetic storms.

Despite significant progress over the last 50+ years, the air-sea interaction community is still actively working on developing better understanding of the fundamental processes occurring in the coupling between the ocean and the atmosphere, such as the kinematics and dynamics of momentum, heat, moisture, and gas exchange between the atmosphere and ocean as well as the structure of turbulence in the ocean boundary layer. How do breaking waves inject momentum into the upper ocean? How do upper ocean circulations and turbulence affect waves and wave breaking? What are the effects of submesoscale processes in this coupling? What impact do surface waves have on frontal instabilities? How do frontal zones interact with surface wave fields (e.g. Romero et al., 2017, and the enhanced breaking at a frontal boundary shown in figure 1.3)? How should these processes be parameterized in numerical simulations? The list goes on and on.

The need for more laboratory and field measurements is obvious, with broader spatio-temporal coverage, detailed characterization of the MABL and upper ocean mixed layer, using a range of platforms, e.g. research vessels, buoy or platform, or unmanned surface vehicles and at height, from an aircraft (manned or unmanned). These measurements should be collocated with detailed measurements of wave breaking, the surface wave kinematics and dynamics, along with numerical studies to improve our understanding of the physics involved.

One particular topic of interest, that directly builds on this work, is the study of air-sea interaction at frontal boundaries and submesoscale features. It is known that the vertical transport of nutrients in the ocean cannot be accomplished efficiently by the mesoscale and larger-scale flow fields as they usually exhibit very small vertical velocity magnitude. The vertical transport associated with submesoscale variability, where evidence of strong vertical velocities have been found, has therefore a significant impact on ocean biology and physics. The need to better understand the dynamics and thermodynamics of air-sea interaction in both the MABL and the marine boundary layer (MBL) across these features and the contribution of the latter to vertical transport is of significant interest to

the community, especially now that numerical models are becoming technically [1] capable of resolving such phenomena. Of particular interest is the role of the surface wave field in air-sea fluxes and in setting the boundary conditions for both the MBL and MABL, following the work presented in chapter 2, 3 and 4.

In a changing climate, improving our understanding of the coupling between the ocean and the atmosphere, especially in the case of tropical cyclones and hurricanes, has become of societal urgency, as it has been demonstrated during the 2017 Atlantic hurricane season, an unusually active season, both in terms of the large number of storms that made landfall, but also their intensity and destructive power, through winds, rain and flooding. The need to develop better predictive capabilities is obvious, through improved understanding of the physical processes driving the ocean-atmosphere interactions and the intensification processes in hurricanes. In-situ measurements are needed, near or at the ocean surface, along the lines of the instrumented unmanned surface vehicle presented in chapter 5, as well as using airborne systems instrumented with aerosol and atmospheric sensors similar to what was presented in chapter 3.

While our understanding of the physics of the ocean and its relation to the atmosphere above has improved tremendously over the past fifty years, more recently through remote sensing tools (such as the groundbreaking TOPEX/POSEIDON mission that revolutionized our understanding of the global ocean circulation) and in-situ instrumentation technology breakthroughs (e.g. ARGO floats program), more work is needed to resolve some of the remaining fundamental questions found in the fields of air-sea interaction, physical oceanography and atmospheric sciences. It is an exciting time for this area of environmental research, with the recent development of new technological tools, both for the in-situ sampling and the improved numerical capabilities that are now revolutionizing environmental simulations.

[1] Though our understanding of the physical processes and associated parameterization remains a limiting factor.

APPENDIX A

The Gulf Of Tehuentepec Experiment (GOTEX 2004)

The GOTEX experiment was undertaken in February, 2004, in the Gulf of Tehuantepec off the Pacific coast of Mexico, an area known for predictable and repeatable offshore wind jets (known as "Tehuano") during the wintertime. As cold weather systems move south into the Gulf of Mexico, East of the Sierra Madre, an atmospheric pressure difference across the Tehuentepec isthmus creates strong offshore westerly winds flowing through a gap in the mountain range, the Chivela pass (225m AMSL).

The primary goal of GOTEX was to characterize the evolution of the directional wave spectrum, wave breaking and surface kinematics in the fetch limited wave environment generated during Tehuano wind events. An aircraft, the NSF/NCAR C-130Q Hercules, was instrumented with a suite of electro-optical systems that included an earlier version of the NASA ATM lidar (see Romero and Melville, 2010a; Kleiss and Melville, 2010, 2011, for details). Atmospheric momentum flux and surface wave measurements were taken from Romero and Melville (2010a) in the present analysis.

Aerosol measurements were made using a suite of sensors, similar to the CIRPAS Twin Otter setup, installed on wing pylons to provide in-situ sampling of the particles present in the air flow. Among a large suite of atmospheric, cloud physics, and chemistry sensors, a Passive Cavity Aerosol Spectrometer Probe (PMS PCASP-100X) and a forward Scattering Scatterometer Spectrometer Probe (PMS FSSP-100) measured particle size (diameter) from 0.001 to 2.11 μm and 1 to 53.45 μm, respectively, over 30 size bins for each system. The Earth Observing Laboratory Scanning Aerosol Backscatter Lidar (EOL SABL), a compact upward/downward looking aerosol lidar was also installed on the aircraft. This lidar, operating in the IR (1064nm) and Green (532nm) wavelengths was designed to provide qualitative information on the structure of the atmosphere.

Figure A.1(a) shows the SABL lidar profiles (1064nm wavelength) of range-corrected backscatter in units of dB during the return leg of Research Flight 10 (RF10) during the GOTEX2004 experiment on February 27 2004. The corresponding flight track is

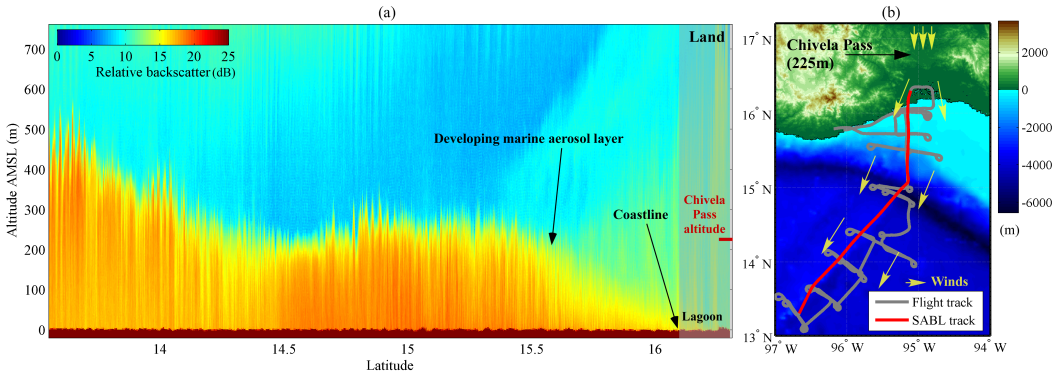

Figure A.1: (a) SABL lidar profiles (1064nm wavelength) of range-corrected backscatter in dB during the return leg of Research Flight 10 (RF10) during the GOTEX2004 experiment on February 27 2004. The corresponding flight track is shown in red in the right plot. (b) Topographic map of the experiment operation area, showing the flight track on February 27 2004 (RF10, gray solid line with the return track featured in red). The yellow arrows conceptually represent the wind direction during a Tehuano event, and the location of the Chivela Pass. Note the developing height of the aerosol boundary layer offshore in the downwind (decreasing latitude) fetch, starting near the surface at the coastline, well below the altitude the Chivela Pass.

shown in red in figure A.1(b). Only the 1064nm is shown, as the 532nm one qualitatively exhibits similar results. The SABL lidar image shows the development of the aerosol boundary layer offshore in the downwind (decreasing latitude) increasing fetch, starting near the surface at the coastline, well below the altitude the Chivela Pass, also shown in the same figure. The height of the aerosol boundary layer rapidly increases from the coastline up to 15.5^o Latitude, reaching close to 300m AMSL, then remains approximately constant up to 14.5^o Latitude, where the height of the aerosol layer starts increasing again, reaching 500m AMSL at $13.5\ ^o$ Latitude. Though low lidar backscatter levels north of $16\ ^o$ Latitude are likely associated with small diameter aerosols generated on land, they remain much less than the backscatter shown offshore in the marine aerosol layer. This is confirmed in figure A.2, where the in-situ aerosol concentration measured from the sensors installed on the C130 wing pylons is shown as a function of latitude and AMSL height for four aerosol sizes: 0.11 μm, 3 μm, 9.7 μm and 20.2 μm. The development of the aerosol boundary layer is evident, especially for the particles of diameter 3-10 μm, with increasing height downwind (decreasing latitude), consistent with the SABL qualitative picture. The smaller diameter particles (0.11 μm) do not show the same spatial pattern, likely driven by aerosol from land or a non-local source, especially at height. Low concentrations of larger diameter aerosols are present, mostly limited to

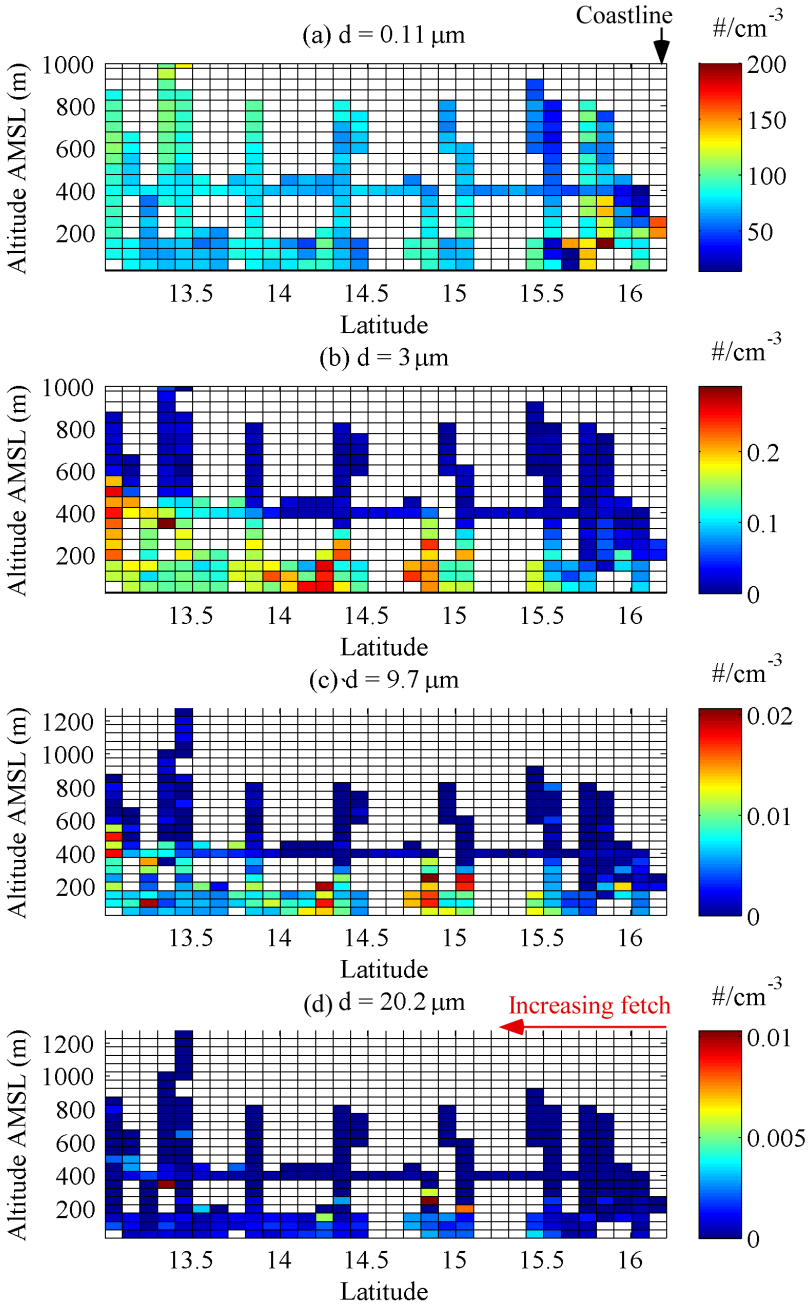

Figure A.2: Aerosol concentration measured during the 30m AMSL portions of RF10 on February 27 2004, for four aerosol diameters: (a) 0.11 μm, (b) 3 μm, (c) 9.7 μm and (d) 20.2 μm.

the lowest part of the aerosol boundary layer.

Bibliography

Agbaglah, G., and Coauthors, 2011: Parallel simulation of multiphase flows using octree adaptivity and the volume-of-fluid method. *Comptes Rendus Mécanique*, **339 (2-3)**, 194–207. (Cited on pages 6, 91 and 92.)

Allaire, G., S. Clerc, and S. Kokh, 2002: A five-equation model for the simulation of interfaces between compressible fluids. *Journal of Computational Physics*, **181 (2)**, 577–616. (Cited on page 90.)

Altomare, C., A. J. Crespo, J. M. Domínguez, M. Gómez-Gesteira, T. Suzuki, and T. Verwaest, 2015: Applicability of smoothed particle hydrodynamics for estimation of sea wave impact on coastal structures. *Coastal Engineering*, **96**, 1–12. (Cited on page 90.)

Andreas, E. L., 1995: The temperature of evaporating sea spray droplets. *Journal of the atmospheric sciences*, **52 (7)**, 852–862. (Cited on page 74.)

Anguelova, M., R. P. Barber Jr, and J. Wu, 1999: Spume drops produced by the wind tearing of wave crests. *Journal of physical oceanography*, **29 (6)**, 1156–1165. (Cited on page 114.)

Ardhuin, F., L. Gualtieri, and E. Stutzmann, 2015: How ocean waves rock the earth: Two mechanisms explain microseisms with periods 3 to 300 s. *Geophysical Research Letters*, **42 (3)**, 765–772. (Cited on pages v, 39, 59 and 153.)

Babin, S. M., J. A. Carton, T. D. Dickey, and J. D. Wiggert, 2004: Satellite evidence of hurricane-induced phytoplankton blooms in an oceanic desert. *Journal of Geophysical Research-Oceans*, **109 (C3)**, doi:ArtnC03043Doi10.1029/2003jc001938, URL <GotoISI>://WOS:000220623300001. (Cited on page 146.)

Bagué, A., D. Fuster, S. Popinet, R. Scardovelli, and S. Zaleski, 2010: Instability growth rate of two-phase mixing layers from a linear eigenvalue problem and an initial-value problem. *Physics of Fluids*, **22 (9)**, 092 104. (Cited on page 91.)

Banner, M., I. S. Jones, and J. Trinder, 1989: Wavenumber spectra of short gravity waves. *Journal of Fluid Mechanics*, **198**, 321–344. (Cited on pages 40 and 46.)

Banner, M., and I. Young, 1994: Modeling spectral dissipation in the evolution of wind waves. part i: Assessment of existing model performance. *Journal of physical oceanography*, **24 (7)**, 1550–1571. (Cited on page 28.)

Banner, M. L., 1990: Equilibrium spectra of wind waves. *Journal of physical oceanography*, **20 (7)**, 966–984. (Cited on pages 28, 29 and 40.)

Battjes, J. A., T. J. Zitman, and L. H. Holthuusen, 1987: A reanalysis of the spectra observed in jonswap. *Journal of Physical Oceanography*, **17 (8)**, 1288–1295. (Cited on page 29.)

Bell, M. M., M. T. Montgomery, and K. A. Emanuel, 2012: Air-sea enthalpy and momentum exchange at major hurricane wind speeds observed during cblast. *Journal of the Atmospheric Sciences*, **69 (11)**, 3197–3222, doi:Doi10.1175/Jas-D-11-0276.1, URL <GotoISI>://WOS:000310652500006. (Cited on page 120.)

Bender, M. A., I. Ginis, R. Tuleya, B. Thomas, and T. Marchok, 2007: The operational gfdl coupled hurricane-ocean prediction system and a summary of its performance. *Monthly Weather Review*, **135 (12)**, 3965–3989, doi:Doi10.1175/2007mwr2032.1, URL <GotoISI>://WOS:000251908400004http://journals.ametsoc.org/doi/pdf/10.1175/2007MWR2032.1. (Cited on page 120.)

Bernard-Champmartin, A., and F. De Vuyst, 2014: A low diffusive lagrange-remap scheme for the simulation of violent air–water free-surface flows. *Journal of Computational Physics*, **274**, 19–49. (Cited on page 90.)

Black, P. G., and Coauthors, 2007: Air-sea exchange in hurricanes - synthesis of observations from the coupled boundary layer air-sea transfer experiment. *Bulletin of the American Meteorological Society*, **88 (3)**, 357–374, doi:10.1175/bams-88-3-357, URL <GotoISI>://000245620700012http://journals.ametsoc.org/doi/pdf/10.1175/BAMS-88-3-357. (Cited on page 120.)

Blenkinsopp, C., and J. Chaplin, 2007: Void fraction measurements in breaking waves. *Proceedings of the Royal Society of London A: Mathematical, Physical and Engineering Sciences*, The Royal Society, Vol. 463, 3151–3170. (Cited on page 114.)

Blenkinsopp, C., and J. Chaplin, 2011: Void fraction measurements and scale effects in breaking waves in freshwater and seawater. *Coastal Engineering*, **58 (5)**, 417–428. (Cited on page 114.)

Bréon, F., and N. Henriot, 2006: Spaceborne observations of ocean glint reflectance and modeling of wave slope distributions. *Journal of Geophysical Research: Oceans*, **111 (C6)**, doi:10.1029/2005JC003343, c06005. (Cited on page 57.)

Brown, E. D., J. H. Churnside, R. L. Collins, T. Veenstra, J. J. Wilson, and K. Abnett, 2002: Remote sensing of capelin and other biological features in the north pacific using lidar and video technology. *ICES Journal of Marine Science: Journal du Conseil*, **59 (5)**, 1120–1130. (Cited on page 67.)

Carrera, P., J. Churnside, G. Boyra, V. Marques, C. Scalabrin, and A. Uriarte, 2006: Comparison of airborne lidar with echosounders: a case study in the coastal atlantic waters of southern europe. *ICES Journal of Marine Science: Journal du Conseil*, **63 (9)**, 1736–1750. (Cited on page 67.)

Cavaleri, L., and Coauthors, 2007: Wave modelling–the state of the art. *Progress in oceanography*, **75 (4)**, 603–674. (Cited on page 17.)

Chan, E., and W. Melville, 1988: Deep-water plunging wave pressures on a vertical plane wall. *Proceedings of the Royal Society of London A: Mathematical, Physical and Engineering Sciences*, The Royal Society, Vol. 417, 95–131. (Cited on page 94.)

Charnock, H., J. Francis, and P. Sheppard, 1955: Medium-scale turbulence in the trade winds. *Quarterly Journal of the Royal Meteorological Society*, **81 (350)**, 634–635. (Cited on page 132.)

Chen, K.-S., C.-C. Hung, G.-C. Gong, W.-C. Chou, C.-C. Chung, Y.-Y. Shih, and C.-C. Wang, 2013: Enhanced poc export in the oligotrophic northwest pacific ocean after extreme weather events. *Geophysical Research Letters*, **40 (21)**, 2013GL058 300, doi:10.1002/2013GL058300, URL http://dx.doi.org/10.1002/2013GL058300. (Cited on page 146.)

Chung, C. C., G. C. Gong, and C. C. Hung, 2012: Effect of typhoon morakot on microphytoplankton population dynamics in the subtropical northwest pacific. *Marine Ecology Progress Series*, **448**, 39–49, doi:Doi10.3354/Meps09490, URL <GotoISI>://WOS:000300661800004. (Cited on page 146.)

Churnside, J. H., V. V. Tatarskii, and J. J. Wilson, 1998: Oceanographic lidar attenuation coefficients and signal fluctuations measured from a ship in the southern california bight. *Applied optics*, **37 (15)**, 3105–3112. (Cited on page 67.)

Churnside, J. H., J. J. Wilson, and V. V. Tatarskii, 2001: Airborne lidar for fisheries applications. *Optical Engineering*, **40 (3)**, 406–414. (Cited on page 67.)

Colagrossi, A., C. Lugni, and M. Brocchini, 2010: A study of violent sloshing wave impacts using an improved sph method. *Journal of hydraulic research*, **48 (S1)**, 94–104. (Cited on page 90.)

Cox, C., and W. Munk, 1954: Measurement of the roughness of the sea surface from photographs of the sunâĂŹs glitter. *JOSA*, **44 (11)**, 838–850. (Cited on pages 30, 56 and 57.)

Craik, A. D. D., and S. Leibovich, 1976: Rational model for langmuir circulations. *Journal of Fluid Mechanics*, **73 (Feb10)**, 401–426, doi:Doi10.1017/S0022112076001420. (Cited on pages 19 and 120.)

Crespo, A. J., and Coauthors, 2015: Dualsphysics: Open-source parallel cfd solver based on smoothed particle hydrodynamics (sph). *Computer Physics Communications*, **187**, 204–216. (Cited on page 89.)

Cunningham, E., 1910: On the velocity of steady fall of spherical particles through fluid medium. *Proceedings of the Royal Society of London. Series A, Containing Papers of a Mathematical and Physical Character*, **83 (563)**, 357–365. (Cited on page 73.)

D'Asaro, E. A., R. Harcourt, E. Terrill, P. P. Niiler, and T. B. Sanford, 2006: The hurricane mixing front. *Bulletin of the American Meteorological Society*, **87 (11)**, 1492–1492, URL <GotoISI>://WOS:000242231600010. (Cited on page 120.)

D'Asaro, E. A., T. B. Sanford, P. P. Niiler, and E. J. Terrill, 2007: Cold wake of hurricane frances. *Geophysical Research Letters*, **34 (15)**, L15 609, doi:10.1029/2007GL030 160, doi:ArtnL15609Doi10.1029/2007gl030160, URL <GotoISI>://WOS:000248872100004http://onlinelibrary.wiley.com/store/10.1029/2007GL030160/asset/grl23233.pdf?v=1&t=hjq6nr5x&s=600b74414e8078ffa98bd8b82d0f2edc5414a1ed. (Cited on pages 120 and 132.)

de Leeuw, G., E. L. Andreas, M. D. Anguelova, C. Fairall, E. R. Lewis, C. O'Dowd, M. Schulz, and S. E. Schwartz, 2011: Production flux of sea spray aerosol. *Reviews of Geophysics*, **49 (2)**. (Cited on pages 62 and 83.)

Deane, G. B., and M. D. Stokes, 2002: Scale dependence of bubble creation mechanisms in breaking waves. *Nature*, **418 (6900)**, 839–844. (Cited on page 94.)

Deike, L., D. Fuster, M. Berhanu, and E. Falcon, 2014: Direct numerical simulations of capillary wave turbulence. *Phys. Rev. Lett.*, **112 (234501)**, 5. (Cited on pages 91, 98 and 99.)

Deike, L., W. K. Melville, and S. Popinet, 2016: Air entrainment and bubble statistics in breaking waves. *Journal of Fluid Mechanics*, **801**, 91–129. (Cited on pages 44, 91, 98 and 99.)

Deike, L., N. Pizzo, and W. K. Melville, 2017: Lagrangian transport by breaking surface waves. *Journal of Fluid Mechanics*, **SUBMITTED**. (Cited on pages 98 and 99.)

Deike, L., S. Popinet, and W. K. Melville, 2015: Capillary effects on wave breaking. *Journal of Fluid Mechanics*, **769**, 541–569. (Cited on pages 91, 98 and 99.)

Derakhti, M., and J. T. Kirby, 2014: Bubble entrainment and liquid–bubble interaction under unsteady breaking waves. *Journal of Fluid Mechanics*, **761**, 464–506. (Cited on page 102.)

Derakhti, M., and J. T. Kirby, 2016: Breaking-onset, energy and momentum flux in unsteady focused wave packets. *Journal of Fluid Mechanics*, **790**, 553–581. (Cited on page 102.)

Després, B., and F. Lagoutière, 2001: Contact discontinuity capturing schemes for linear advection and compressible gas dynamics. *Journal of Scientific Computing*, **16 (4)**, 479–524. (Cited on page 90.)

Dommermuth, D. G., D. K. Yue, W. Lin, R. Rapp, E. Chan, and W. Melville, 1988: Deep-water plunging breakers: a comparison between potential theory and experiments. *Journal of Fluid Mechanics*, **189**, 423–442. (Cited on page 94.)

Donelan, M. A., J. Hamilton, and W. Hui, 1985: Directional spectra of wind-generated waves. *Philosophical Transactions of the Royal Society of London A: Mathematical, Physical and Engineering Sciences*, **315 (1534)**, 509–562. (Cited on pages vii, 29, 56, 133, 149 and 156.)

Drazen, D. A., and W. K. Melville, 2009: Turbulence and mixing in unsteady breaking surface waves. *Journal of Fluid Mechanics*, **628**, 85–119. (Cited on pages 24, 91, 94, 102, 109 and 117.)

Drazen, D. A., W. K. Melville, and L. Lenain, 2008: Inertial scaling of dissipation in unsteady breaking waves. *Journal of Fluid Mechanics*, **611**, 307–332. (Cited on pages 44, 63, 91, 94, 96, 98 and 102.)

Duncan, J., 1981: An experimental investigation of breaking waves produced by a towed hydrofoil. *Proceedings of the Royal Society of London. A. Mathematical and Physical Sciences*, **377 (1770)**, 331–348. (Cited on page 74.)

Dysthe, K. B., K. Trulsen, H. E. Krogstad, and H. Socquet-Juglard, 2003: Evolution of a narrow-band spectrum of random surface gravity waves. *Journal of Fluid Mechanics*, **478**, 1–10. (Cited on pages 28 and 59.)

Edson, J., and Coauthors, 2007: The coupled boundary layers and air–sea transfer experiment in low winds. *Bulletin of the American Meteorological Society*, **88 (3)**, 341–356. (Cited on pages 1 and 14.)

Edson, J. B., A. A. Hinton, K. E. Prada, J. E. Hare, and C. W. Fairall, 1998: Direct covariance flux estimates from mobile platforms at sea. *Journal of Atmospheric and Oceanic Technology*, **15 (2)**, 547–562. (Cited on page 22.)

Elfouhaily, T., B. Chapron, K. Katsaros, and D. Vandemark, 1997: A unified directional spectrum for long and short wind-driven waves. *Journal of Geophysical Research: Oceans*, **102 (C7)**, 15 781–15 796. (Cited on page 46.)

Emerson, S., and J. Hedges, 2008: *Chemical oceanography and the marine carbon cycle*. Cambridge University Press. (Cited on page 14.)

Fairall, C., M. Banner, W. Peirson, W. Asher, and R. Morison, 2009: Investigation of the physical scaling of sea spray spume droplet production. *Journal of Geophysical Research: Oceans (1978–2012)*, **114 (C10)**. (Cited on pages 5, 62, 70 and 73.)

Fairall, C., E. F. Bradley, J. Hare, A. Grachev, and J. Edson, 2003: Bulk parameterization of air-sea fluxes: Updates and verification for the coare algorithm. *Journal of climate*, **16 (4)**, 571–591. (Cited on pages 19, 73 and 132.)

Fairall, C., J. Kepert, and G. Holland, 1994: The effect of sea spray on surface energy transports over the ocean. *Global Atmos. Ocean Syst*, **2 (2-3)**, 121–142. (Cited on page 62.)

Fairall, C. W., E. F. Bradley, D. P. Rogers, J. B. Edson, and G. S. Young, 1996: Bulk parameterization of air-sea fluxes for tropical ocean-global atmosphere coupled-ocean atmosphere response experiment. *Journal of Geophysical Research: Oceans*, **101 (C2)**, 3747–3764. (Cited on page 19.)

Falkowski, P., and D. A. Kiefer, 1985: Chlorophyll-a fluorescence in phytoplankton - relationship to photosynthesis and biomass. *Journal of Plankton Research*, **7 (5)**, 715–731, doi:DOI10.1093/plankt/7.5.715, URL <GotoISI>://WOS:A1985ARV9600011. (Cited on page 147.)

Farrell, W. E., and W. Munk, 2010: Booms and busts in the deep. *Journal of Physical Oceanography*, **40 (9)**, 2159–2169, doi:10.1175/2010JPO4440.1. (Cited on pages v, 59 and 153.)

Forristall, G. Z., 1981: Measurements of a saturated range in ocean wave spectra. *Journal of Geophysical Research: Oceans*, **86 (C9)**, 8075–8084. (Cited on page 29.)

Forster, P., and Coauthors, 2007: Changes in atmospheric constituents and in radiative forcing. chapter 2. *Climate Change 2007. The Physical Science Basis*. (Cited on page 14.)

Fuster, D., G. Agbaglah, C. Josserand, S. Popinet, and S. Zaleski, 2009: Numerical simulation of droplets, bubbles and waves: state of the art. *Fluid dynamics research*, **41 (6)**, 065 001. (Cited on page 91.)

Fuster, D., J.-P. Matas, S. Marty, S. Popinet, J. Hoepffner, A. Cartellier, and S. Zaleski, 2013: Instability regimes in the primary breakup region of planar coflowing sheets. *Journal of Fluid Mechanics*, **736**, 150–176. (Cited on page 91.)

Grare, L., L. Lenain, and W. K. Melville, 2013: Wave-coherent airflow and critical layers over ocean waves. *Journal of Physical Oceanography*, **43 (10)**, 2156–2172. (Cited on page 63.)

Grare, L., L. Lenain, and W. K. Melville, 2016: The influence of wind direction on campbell scientific csat3 and gill r3-50 sonic anemometer measurements. *Journal of Atmospheric and Oceanic Technology*, **33 (11)**, 2477–2497. (Cited on page 31.)

Hanley, K. E., S. E. Belcher, and P. P. Sullivan, 2010: A global climatology of wind-wave interaction. *Journal of Physical Oceanography*, **40 (6)**, 1263–1282. (Cited on pages 51 and 62.)

Harcourt, R. R., and E. A. D'Asaro, 2008: Large-eddy simulation of langmuir turbulence in pure wind seas. *Journal of Physical Oceanography*, **38 (7)**, 1542–1562. (Cited on page 139.)

Hasselmann, K., 1962: On the non-linear energy transfer in a gravity-wave spectrum part 1. general theory. *Journal of Fluid Mechanics*, **12 (04)**, 481–500. (Cited on page 16.)

Herbers, T. H. C., P. F. Jessen, T. T. Janssen, D. B. Colbert, and J. H. MacMahan, 2012: Observing ocean surface waves with gps-tracked buoys. *Journal of Atmospheric and Oceanic Technology*, **29 (7)**, 944–959, doi:Doi10.1175/Jtech-D-11-00128.1, URL <GotoISI>://WOS:000306717400006http://journals.ametsoc.org/doi/pdf/10.1175/JTECH-D-11-00128.1. (Cited on page 126.)

Hung, C. C., and G. C. Gong, 2011: Biogeochemical responses in the southern east china sea after typhoons. *Oceanography*, **24 (4)**, 42–51, URL <GotoISI>://WOS:000298444700010. (Cited on page 146.)

Hung, C. C., and Coauthors, 2010: The effect of typhoon on particulate organic carbon flux in the southern east china sea. *Biogeosciences*, **7 (10)**, 3007–3018, doi:DOI10.5194/bg-7-3007-2010, URL <GotoISI>://WOS:000283659200003. (Cited on page 146.)

Hwang, P. A., 2005: Wave number spectrum and mean square slope of intermediate-scale ocean surface waves. *Journal of Geophysical Research: Oceans*, **110 (C10)**, doi:10.1029/2005JC003002, c10029. (Cited on page 46.)

Hwang, P. A., D. W. Wang, E. J. Walsh, W. B. Krabill, and R. N. Swift, 2000a: Airborne measurements of the wavenumber spectra of ocean surface waves. part i: Spectral slope and dimensionless spectral coefficient. *Journal of Physical Oceanography*, **30 (11)**, 2753–2767. (Cited on pages 28, 29, 40 and 65.)

Hwang, P. A., D. W. Wang, E. J. Walsh, W. B. Krabill, and R. N. Swift, 2000b: Airborne measurements of the wavenumber spectra of ocean surface waves. part ii: Directional distribution. *Journal of Physical Oceanography*, **30 (11)**, 2768–2787. (Cited on pages 2, 28, 35, 38, 40, 41 and 65.)

Iafrati, A., 2009: Numerical study of the effects of the breaking intensity on wave breaking flows. *Journal of Fluid Mechanics*, **622**, 371–411. (Cited on page 102.)

Iafrati, A., 2011: Energy dissipation mechanisms in wave breaking processes: Spilling and highly aerated plunging breaking events. *Journal of Geophysical Research: Oceans*, **116 (C7)**. (Cited on page 102.)

Jähne, B., and K. S. Riemer, 1990: Two-dimensional wave number spectra of small-scale water surface waves. *Journal of Geophysical Research: Oceans*, **95 (C7)**, 11 531–11 546. (Cited on page 46.)

Janssen, P. A., 1991: Quasi-linear theory of wind-wave generation applied to wave forecasting. *Journal of Physical Oceanography*, **21 (11)**, 1631–1642. (Cited on page 19.)

Jones, I. S., and Y. Toba, 2001: *Wind stress over the ocean*. Cambridge University Press. (Cited on page 22.)

Jones, K. F., and E. L. Andreas, 2012: Sea spray concentrations and the icing of fixed offshore structures. *Quarterly Journal of the Royal Meteorological Society*, **138 (662)**, 131–144. (Cited on page 72.)

Kahma, K. K., and C. J. Calkoen, 1992: Reconciling discrepancies in the observed growth of wind-generated waves. *Journal of Physical Oceanography*, **22 (12)**, 1389–1405. (Cited on page 50.)

Kantha, L., H. U. Lass, and H. Prandke, 2010: A note on stokes production of turbulence kinetic energy in the oceanic mixed layer: observations in the baltic sea. *Ocean Dynamics*, **60 (1)**, 171–180. (Cited on page 20.)

Kenyon, K. E., 1969: Stokes drift for random gravity waves. *Journal of Geophysical Research*, **74 (28)**, 6991, URL <GotoISI>://A1969E961600018. (Cited on pages 20 and 136.)

Kitaigordskii, S., V. Krasitskii, and M. Zaslavskii, 1975: On Phillips' theory of equilibrium range in the spectra of wind-generated gravity waves. *Journal of Physical Oceanography*, **5 (3)**, 410–420. (Cited on pages 28 and 40.)

Kitaigorodskii, S., 1962: Applications of the theory of similarity to the analysis of wind-generated wave motion as a stochastic process. *Izv. Geophys. Ser. Acad. Sci., USSR*, **1**, 105–117. (Cited on page 29.)

Kitaigorodskii, S., 1983: On the theory of the equilibrium range in the spectrum of wind-generated gravity waves. *Journal of Physical Oceanography*, **13 (5)**, 816–827. (Cited on page 29.)

Kleiss, J. M., and W. K. Melville, 2010: Observations of wave breaking kinematics in fetch-limited seas. *Journal of Physical Oceanography*, **40 (12)**, 2575–2604. (Cited on pages 5, 31, 76, 83, 84 and 159.)

Kleiss, J. M., and W. K. Melville, 2011: The analysis of sea surface imagery for whitecap kinematics. *Journal of Atmospheric and Oceanic Technology*, **28 (2)**, 219–243. (Cited on pages 31, 83, 84 and 159.)

Knaff, J. A., M. DeMaria, D. A. Molenar, C. R. Sampson, and M. G. Seybold, 2011: An automated, objective, multiple-satellite-platform tropical cyclone surface wind analysis. *Journal of Applied Meteorology and Climatology*, **50 (10)**, 2149–2166, doi:Doi10.1175/2011jamc2673.1, URL <GotoISI>://WOS:000296264100012http://journals.ametsoc.org/doi/pdf/10.1175/2011JAMC2673.1. (Cited on page 124.)

Knaff, J. A., M. DeMaria, C. R. Sampson, J. E. Peak, J. Cummings, and W. H. Schubert, 2013: Upper oceanic energy response to tropical cyclone passage. *Journal of Climate*, **26 (8)**, 2631–2650, doi:Doi10.1175/Jcli-D-12-00038.1, URL <GotoISI>://WOS:000317954700015http://journals.ametsoc.org/doi/pdf/10.1175/JCLI-D-12-00038.1. (Cited on page 132.)

Kokh, S., and F. Lagoutiere, 2010: An anti-diffusive numerical scheme for the simulation of interfaces between compressible fluids by means of a five-equation model. *Journal of Computational Physics*, **229 (8)**, 2773–2809. (Cited on page 90.)

Komen, G. J., L. Cavaleri, M. Donelan, K. Hasselmann, S. Hasselmann, and P. Janssen, 1996: *Dynamics and modelling of ocean waves*. Cambridge university press. (Cited on pages 16, 17 and 51.)

Krabill, W., R. Thomas, K. Jezek, K. Kuivinen, and S. Manizade, 1995: Greenland ice sheet thickness changes measured by laser altimetry. *Geophysical Research Letters*, **22 (17)**, 2341–2344, doi:10.1029/95GL02069, URL http://dx.doi.org/10.1029/95GL02069. (Cited on page 65.)

Kudryavtsev, V., B. Chapron, and V. Makin, 2014: Impact of wind waves on the air-sea fluxes: A coupled model. *Journal of Geophysical Research: Oceans*, **119 (2)**, 1217–1236. (Cited on page 19.)

Kudryavtsev, V., V. Makin, and B. Chapron, 1999: Coupled sea surface-atmosphere model: 2. spectrum of short wind waves. *Journal of Geophysical Research: Oceans*, **104 (C4)**, 7625–7639. (Cited on page 19.)

Kukulka, T., A. J. Plueddemann, J. H. Trowbridge, and P. P. Sullivan, 2010: Rapid mixed layer deepening by the combination of langmuir and shear instabilities: A case study. *Journal of Physical Oceanography*, **40 (11)**, 2381–2400. (Cited on page 20.)

Lamarre, E., and W. Melville, 1991: Air entrainment and dissipation in breaking waves. *Nature*, **351 (6326)**, 469. (Cited on page 94.)

Leckler, F., F. Ardhuin, C. Peureux, A. Benetazzo, F. Bergamasco, and V. Dulov, 2015: Analysis and interpretation of frequency–wavenumber spectra of young wind waves. *Journal of Physical Oceanography*, **45 (10)**, 2484–2496. (Cited on pages 28 and 35.)

Lenain, L., and W. K. Melville, 2014: Autonomous surface vehicle measurements of the ocean's response to tropical cyclone freda. *Journal of Atmospheric and Oceanic Technology*, **31 (10)**, 2169–2190. (Cited on page 87.)

Lenain, L., and W. K. Melville, 2017a: Evidence of sea-state dependence of aerosol concentration in the marine atmospheric boundary layer. *Journal of Physical Oceanography*, **47 (1)**, 69–84. (Cited on page 87.)

Lenain, L., and W. K. Melville, 2017b: Measurements of the directional spectrum across the equilibrium saturation ranges of wind-generated surface waves. *Journal of Physical Oceanography*, **47 (8)**, 2123–2138. (Cited on page 60.)

Lewis, E. R., and S. E. Schwartz, 2004: *Sea salt aerosol production: mechanisms, methods, measurements, and models-A critical review*. American Geophysical Union. (Cited on pages 62 and 72.)

Loewen, M., and W. Melville, 1994: An experimental investigation of the collective oscillations of bubble plumes entrained by breaking waves. *The Journal of the Acoustical Society of America*, **95 (3)**, 1329–1343. (Cited on page 94.)

Long, C. E., and D. T. Resio, 2007: Wind wave spectral observations in Currituck sound, North Carolina. *Journal of Geophysical Research: Oceans*, **112 (C5)**, doi:10.1029/2006JC003835, c05001. (Cited on page 35.)

Long, R. B., 1980: The statistical evaluation of directional spectrum estimates derived from pitch-roll buoy data. *Journal of Physical Oceanography*, **10 (6)**, 944–952, doi:Doi10.1175/1520-0485(1980)010<0944:Tseods>2.0.Co;2, URL <GotoISI>://WOS:A1980KC33100010. (Cited on page 126.)

Longuet-Higgins, M., 1974: Breaking waves in deep or shallow water. *Proc. 10th Conf. on Naval Hydrodynamics*, Vol. 597. (Cited on page 94.)

Longuet-Higgins, M. S., 1950: A theory of the origin of microseisms. *Philosophical Transactions of the Royal Society of London A: Mathematical, Physical and Engineering Sciences*, **243 (857)**, 1–35. (Cited on pages v, 39, 59 and 153.)

Mårtensson, E., E. Nilsson, G. de Leeuw, L. Cohen, and H.-C. Hansson, 2003: Laboratory simulations and parameterization of the primary marine aerosol production. *Journal of Geophysical Research: Atmospheres*, **108 (D9)**. (Cited on page 62.)

McLean, J., Y. Ma, D. Martin, P. Saffman, and H. Yuen, 1981: Three-dimensional instability of finite-amplitude water waves. *Physical Review Letters*, **46 (13)**, 817. (Cited on page 59.)

McWilliams, J. C., J. M. Restrepo, and E. M. Lane, 2004: An asymptotic theory for the interaction of waves and currents in coastal waters. *Journal of Fluid Mechanics*, **511**, 135–178, doi:Doi10.1017/S0022112004009358, URL <GotoISI>://WOS:000223289000008. (Cited on page 151.)

McWilliams, J. C., P. P. Sullivan, and C. H. Moeng, 1997: Langmuir turbulence in the ocean. *Journal of Fluid Mechanics*, **334**, 1–30, doi:Doi10.1017/S0022112096004375. (Cited on page 20.)

Melville, W., 1982: The instability and breaking of deep-water waves. *Journal of Fluid Mechanics*, **115**, 165–185. (Cited on page 59.)

Melville, W., and R. J. Rapp, 1985: Momentum flux in breaking waves. *Nature*, **317 (6037)**, 514–516. (Cited on page 94.)

Melville, W. K., 1996: The role of surface-wave breaking in air-sea interaction. *Annual Review of Fluid Mechanics*, **28**, 279, doi:DOI10.1146/annurev.fl.28.010196.001431, URL <GotoISI>://WOS:A1996TR81500009. (Cited on page 147.)

Melville, W. K., L. Lenain, D. R. Cayan, M. Kahru, J. P. Kleissl, P. Linden, and N. M. Statom, 2016: The modular aerial sensing system. *Journal of Atmospheric and Oceanic Technology*, **33 (6)**, 1169–1184. (Cited on pages 28, 29, 30 and 31.)

Melville, W. K., and P. Matusov, 2002: Distribution of breaking waves at the ocean surface. *Nature*, **417 (6884)**, 58–63. (Cited on page 31.)

Miles, J. W., 1957: On the generation of surface waves by shear flows. *J. Fluid Mech.*, **3 (2)**, 185–204. (Cited on page 16.)

Monaghan, J., 2012: Smoothed particle hydrodynamics and its diverse applications. *Annual Review of Fluid Mechanics*, **44**, 323–346. (Cited on page 90.)

Monahan, E. C., D. E. Spiel, and K. L. Davidson, 1986: A model of marine aerosol generation via whitecaps and wave disruption. *Oceanic whitecaps*, Springer, 167–174. (Cited on page 62.)

Moon, I. J., I. Ginis, T. Hara, H. L. Tolman, C. W. Wright, and E. J. Walsh, 2003: Numerical simulation of sea surface directional wave spectra under hurricane wind forcing. *Journal of Physical Oceanography*, **33 (8)**, 1680–1706, doi:Doi10.1175/2410.1, URL <GotoISI>://WOS:000184753400010http://journals.ametsoc.org/doi/pdf/10.1175/2410.1. (Cited on page 120.)

Mrvaljevic, R. K., and Coauthors, 2013: Observations of the cold wake of typhoon fanapi (2010). *Geophysical Research Letters*, **40 (2)**, 316–321, doi:Doi10.1029/2012gl054282, URL <GotoISI>://WOS:000317829300016. (Cited on pages 120 and 132.)

Mueller, J. A., and F. Veron, 2009: A sea state-dependent spume generation function. *Journal of Physical Oceanography*, **39 (9)**, 2363–2372. (Cited on page 62.)

Norris, S., I. Brooks, B. Moat, M. Yelland, G. de Leeuw, R. Pascal, and B. Brooks, 2013a: Near-surface measurements of sea spray aerosol production over whitecaps in the open ocean. *Ocean Science*, **9 (1)**, 133–145. (Cited on page 62.)

Norris, S. J., I. M. Brooks, and D. J. Salisbury, 2013b: A wave roughness reynolds number parameterization of the sea spray source flux. *Geophysical Research Letters*, **40 (16)**, 4415–4419. (Cited on page 62.)

Obukhov, A., 1971: Turbulence in an atmosphere with a non-uniform temperature. *Boundary-layer meteorology*, **2 (1)**, 7–29. (Cited on page 22.)

Omand, M. M., F. Feddersen, D. B. Clark, P. J. S. Franks, J. J. Leichter, and R. T. Guza, 2009: Influence of bubbles and sand on chlorophyll-a fluorescence measurements in the surfzone. *Limnology and Oceanography-Methods*, **7**, 354–362, URL <GotoISI>://WOS:000267011000004. (Cited on page 149.)

Oost, W., G. Komen, C. Jacobs, and C. Van Oort, 2002: New evidence for a relation between wind stress and wave age from measurements during asgamage. *Boundary-Layer Meteorology*, **103 (3)**, 409–438. (Cited on page 73.)

Ovadnevaite, J., A. Manders, G. De Leeuw, D. Ceburnis, C. Monahan, A.-I. Partanen, H. Korhonen, and C. O'Dowd, 2014: A sea spray aerosol flux parameterization encapsulating wave state. *Atmospheric Chemistry and Physics*, **14 (4)**, 1837–1852. (Cited on page 62.)

Phillips, O., 1960: On the dynamics of unsteady gravity waves of finite amplitude part 1. the elementary interactions. *Journal of Fluid Mechanics*, **9 (02)**, 193–217. (Cited on page 16.)

Phillips, O. M., 1957: On the generation of waves by turbulent wind. *J. Fluid Mech.*, **2 (05)**, 417–445, doi:10.1017/S0022112057000233. (Cited on page 16.)

Phillips, O. M., 1958: The equilibrium range in the spectrum of wind-generated waves. *Journal of Fluid Mechanics*, **4 (04)**, 426–434. (Cited on page 29.)

Phillips, O. M., 1985: Spectral and statistical properties of the equilibrium range in wind-generated gravity waves. *Journal of Fluid Mechanics*, **156**, 505–531. (Cited on pages iii, iv, v, 3, 16, 17, 29, 34, 40, 44, 46, 57, 59, 62, 74 and 153.)

Pizzo, N., and W. K. Melville, 2013: Vortex generation by deep-water breaking waves. *Journal of Fluid Mechanics*, **734**, 198–218. (Cited on page 80.)

Popinet, S., 2003: Gerris: a tree-based adaptive solver for the incompressible euler equations in complex geometries. *Journal of Computational Physics*, **190 (2)**, 572–600. (Cited on pages 91, 92 and 94.)

Popinet, S., 2009: An accurate adaptive solver for surface-tension-driven interfacial flows. *Journal of Computational Physics*, **228 (16)**, 5838–5866. (Cited on pages 91, 92 and 93.)

Powell, M. D., P. J. Vickery, and T. A. Reinhold, 2003: Reduced drag coefficient for high wind speeds in tropical cyclones. *Nature*, **422 (6929)**, 279–283, doi:10.1038/nature01481, URL <GotoISI>://000181637300031. (Cited on page 120.)

Price, J. F., 1981: Upper ocean response to a hurricane. *Journal of Physical Oceanography*, **11 (2)**, 153–175, doi:Doi10.1175/1520-0485(1981)011<0153:Uortah>2.0.Co;2, URL <GotoISI>://WOS:A1981LL14800003. (Cited on page 120.)

Pushkarev, A., D. Resio, and V. Zakharov, 2003: Weak turbulent approach to the wind-generated gravity sea waves. *Physica D: Nonlinear Phenomena*, **184 (1)**, 29–63. (Cited on page 29.)

Quinn, P. K., D. B. Collins, V. H. Grassian, K. A. Prather, and T. S. Bates, 2015: Chemistry and related properties of freshly emitted sea spray aerosol. *Chemical Reviews*. (Cited on pages vi, 87 and 154.)

Rafiee, A., D. Dutykh, and F. Dias, 2015: Numerical simulation of wave impact on a rigid wall using a two–phase compressible sph method. *Procedia IUTAM*, **18**, 123–137. (Cited on page 90.)

Rapp, R. J., and W. Melville, 1990: Laboratory measurements of deep-water breaking waves. *Philosophical Transactions of the Royal Society of London A: Mathematical, Physical and Engineering Sciences*, **331 (1622)**, 735–800. (Cited on pages vi, 24, 59, 91, 94, 96, 98, 99, 102, 106, 109, 114, 117 and 155.)

Reid, J. S., H. H. Jonsson, M. H. Smith, and A. Smirnov, 2001: Evolution of the vertical profile and flux of large sea-salt particles in a coastal zone. *Journal of Geophysical Research: Atmospheres (1984–2012)*, **106 (D11)**, 12 039–12 053. (Cited on page 87.)

Reid, J. S., and Coauthors, 2007: An assessment of the meteorological conditions leading to the noaa wp-3d engine compressor stalls of february 9, 2007, due to sea salt aerosol particle fouling. Tech. rep., DTIC Document. (Cited on page 63.)

Reineman, B. D., L. Lenain, D. Castel, and W. K. Melville, 2009: A portable airborne scanning lidar system for ocean and coastal applications. *Journal of Atmospheric and oceanic technology*, **26 (12)**, 2626–2641. (Cited on pages 28 and 30.)

Resio, D. T., C. E. Long, and C. L. Vincent, 2004: Equilibrium-range constant in wind-generated wave spectra. *Journal of Geophysical Research: Oceans*, **109 (C1)**, doi: 10.1029/2003JC001788, c01018. (Cited on page 29.)

Romero, L., L. Lenain, and W. K. Melville, 2017: Observations of surface wave–current interaction. *Journal of Physical Oceanography*, **47 (3)**, 615–632. (Cited on pages 1, 18 and 157.)

Romero, L., and W. K. Melville, 2010a: Airborne observations of fetch-limited waves in the Gulf of Tehuantepec. *Journal of Physical Oceanography*, **40 (3)**, 441–465. (Cited on pages v, 2, 3, 28, 29, 35, 38, 39, 40, 51, 56, 57, 60, 65, 84, 154 and 159.)

Romero, L., and W. K. Melville, 2010b: Numerical modeling of fetch-limited waves in the Gulf of Tehuantepec. *Journal of Physical Oceanography*, **40 (3)**, 466–486. (Cited on pages v, 28, 29, 34, 60, 65 and 154.)

Romero, L., W. K. Melville, and J. M. Kleiss, 2012: Spectral energy dissipation due to surface wave breaking. *Journal of Physical Oceanography*, **42 (9)**, 1421–1444. (Cited on pages 28, 29, 34, 51, 63, 65 and 80.)

Rouault, M. P., P. G. Mestayer, and R. Schiestel, 1991: A model of evaporating spray droplet dispersion. *Journal of Geophysical Research: Oceans (1978–2012)*, **96 (C4)**, 7181–7200. (Cited on pages 73 and 74.)

Sampson, C. R., P. A. Wittmann, E. A. Serra, H. L. Tolman, J. Schauer, and T. Marchok, 2013: Evaluation of wave forecasts consistent with tropical cyclone warning center wind forecasts. *Weather and Forecasting*, **28 (1)**, 287–294, doi:Doi10.1175/Waf-D-12-00060.1, URL <GotoISI>://WOS:000315540800016http://journals.ametsoc.org/doi/pdf/10.1175/WAF-D-12-00060.1. (Cited on page 125.)

Sampson, C. R., P. A. Wittmann, and H. L. Tolman, 2010: Consistent tropical cyclone wind and wave forecasts for the us navy. *Weather and Forecasting*, **25 (4)**, 1293–1306, doi:Doi10.1175/2010waf2222376.1, URL <GotoISI>://WOS:000280731800018http://journals.ametsoc.org/doi/pdf/10.1175/2010WAF2222376.1. (Cited on page 125.)

Sanford, T. B., K. A. Kelly, and D. M. Farmer, 2011a: Sensing the ocean. *Physics Today*, **64 (2)**, 24–28, doi:Doi10.1063/1.3554313, URL <GotoISI>://WOS:000287225100013http://www.physicstoday.org/resource/1/phtoad/v64/i2/p24_s1. (Cited on page 120.)

Sanford, T. B., J. F. Price, and J. B. Girton, 2011b: Upper-ocean response to hurricane frances (2004) observed by profiling em-apex floats. *Journal of Physical Oceanography*, **41 (6)**, 1041–1056, doi:Doi10.1175/2010jpo4313.1, URL <GotoISI>://WOS:000292405500001http://journals.ametsoc.org/doi/pdf/10.1175/2010JPO4313.1. (Cited on page 120.)

Sanford, T. B., J. F. Price, J. B. Girton, and D. C. Webb, 2007: Highly resolved observations and simulations of the ocean response to a hurricane. *Geophysical Research Letters*, **34 (13)**, L13 604, doi:10.1029/2007GL029 679, doi:10.1029/2007gl029679, URL <GotoISI>://000247880400001. (Cited on page 120.)

Shao, J., H. Li, G. Liu, and M. Liu, 2012: An improved sph method for modeling liquid sloshing dynamics. *Computers & Structures*, **100**, 18–26. (Cited on page 90.)

Shpund, J., M. Pinsky, and A. Khain, 2011: Microphysical structure of the marine boundary layer under strong wind and spray formation as seen from simulations using a 2d explicit microphysical model. part i: The impact of large eddies. *Journal of the Atmospheric Sciences*, **68 (10)**, 2366–2384. (Cited on page 62.)

Shpund, J., J. Zhang, M. Pinsky, and A. Khain, 2012: Microphysical structure of the marine boundary layer under strong wind and spray formation as seen from simulations using a 2d explicit microphysical model. part ii: The role of sea spray. *Journal of the Atmospheric Sciences*, **69 (12)**, 3501–3514. (Cited on page 62.)

Shpund, J., J. Zhang, M. Pinsky, and A. Khain, 2014: Microphysical structure of the marine boundary layer under strong wind and sea spray formation as seen from a 2d explicit microphysical model. part iii: Parameterization of height-dependent droplet size distribution. *Journal of the Atmospheric Sciences*, **71 (6)**, 1914–1934. (Cited on page 62.)

Skyllingstad, E. D., W. Smyth, and G. Crawford, 2000: Resonant wind-driven mixing in the ocean boundary layer. *Journal of physical oceanography*, **30 (8)**, 1866–1890. (Cited on page 20.)

Smith, M., P. Park, and I. Consterdine, 1993: Marine aerosol concentrations and estimated fluxes over the sea. *Quarterly Journal of the Royal Meteorological Society*, **119 (512)**, 809–824. (Cited on page 62.)

Socquet-Juglard, H., K. Dysthe, K. Trulsen, H. E. Krogstad, and J. Liu, 2005: Probability distributions of surface gravity waves during spectral changes. *Journal of Fluid Mechanics*, **542**, 195–216. (Cited on page 59.)

Su, M.-Y., M. Bergin, P. Marler, and R. Myrick, 1982: Experiments on non-linear instabilities and evolution of steep gravity-wave trains. *Journal of Fluid Mechanics*, **124 (1)**, 45. (Cited on page 59.)

Sullivan, P. P., J. C. Mc Williams, and T. Hristov, 2010: Large eddy simulation of high wind marine boundary layers above a spectrum of resolved moving waves. *19th Symposium on Boundary Layers and Turbulence*, Keystone, CO, Amer. Meteor. Soc. (Cited on page 120.)

Sullivan, P. P., and J. C. McWilliams, 2010: Dynamics of winds and currents coupled to surface waves. *Annual Review of Fluid Mechanics*, **42**, 19–42. (Cited on page 20.)

Sullivan, P. P., J. C. McWilliams, and W. K. Melville, 2007: Surface gravity wave effects in the oceanic boundary layer: large-eddy simulation with vortex force and stochastic breakers. *Journal of Fluid Mechanics*, **593**, 405–452, doi:10.1017/s002211200700897x, URL <GotoISI>://000251840100017. (Cited on pages 20 and 150.)

Sullivan, P. P., L. Romero, J. C. McWilliams, and W. K. Melville, 2012: Transient evolution of langmuir turbulence in ocean boundary layers driven by hurricane winds and waves. *Journal of Physical Oceanography*, **42 (11)**, 1959–1980, doi:Doi10.1175/Jpo-D-12-025.1, URL <GotoISI>://WOS:000311174300013http://journals.ametsoc.org/doi/pdf/10.1175/JPO-D-12-025.1. (Cited on pages vii, viii, 21, 25, 120, 136, 139, 142, 144, 149, 150 and 156.)

Sutherland, P., and W. K. Melville, 2013: Field measurements and scaling of ocean surface wave-breaking statistics. *Geophysical Research Letters*, **40 (12)**, 3074–3079, doi:10.1002/grl.50584, URL http://dx.doi.org/10.1002/grl.50584. (Cited on pages 5, 31, 44, 63, 76, 80 and 81.)

Taylor, P. K., and M. J. Yelland, 2001: The dependence of sea surface roughness on the height and steepness of the waves. *Journal of physical oceanography*, **31 (2)**, 572–590. (Cited on page 19.)

Terrill, E., and W. K. Melville, 1997: Sound-speed measurements in the surface-wave layer. *The Journal of the Acoustical Society of America*, **102 (5)**, 2607–2625. (Cited on page 82.)

Terrill, E. J., W. K. Melville, and D. Stramski, 2001: Bubble entrainment by breaking waves and their influence on optical scattering in the upper ocean. *Journal of Geophysical Research-Oceans*, **106 (C8)**, 16 815–16 823, doi:Doi10.1029/2000jc000496, URL <GotoISI>://WOS:000170326000015. (Cited on page 149.)

Toba, Y., 1973: Local balance in the air-sea boundary processes. *Journal of the Oceanographical Society of Japan*, **29 (5)**, 209–220. (Cited on pages 29 and 56.)

Toffoli, A., A. Babanin, M. Donelan, B. Haus, and D. Jeong, 2011: Estimating sea spray volume with a laser altimeter. *Journal of Atmospheric and Oceanic Technology*, **28 (9)**, 1177–1183. (Cited on page 67.)

Toffoli, A., J. McConochie, M. Ghantous, L. Loffredo, and A. V. Babanin, 2012: The effect of wave-induced turbulence on the ocean mixed layer during tropical cyclones: Field observations on the australian north-west shelf. *Journal of Geophysical Research-Oceans*, **117**, doi:ArtnC00j24Doi10.1029/2011jc007780, URL <GotoISI>://WOS:000306703400001. (Cited on page 150.)

Towle, D. M., 2014: Spray droplet generation by breaking water waves. *Master thesis, University of Maryland*. (Cited on pages vii, 24, 91, 115 and 116.)

Tracy, B. A., and D. T. Resio, 1982: Theory and calculation of the nonlinear energy transfer between sea waves in deep water. Tech. rep., WIS Technical Report 11, US Army Engineer Waterways Experiment Station, Vicksburg, MS, USA. (Cited on page 34.)

Tryggvason, G., R. Scardovelli, and S. Zaleski, 2011: *Direct numerical simulations of gas–liquid multiphase flows*. Cambridge University Press. (Cited on page 93.)

Van Roekel, L. P., B. Fox-Kemper, P. P. Sullivan, P. E. Hamlington, and S. R. Haney, 2012: The form and orientation of langmuir cells for misaligned winds and waves. *Journal of Geophysical Research-Oceans*, **117**,

C05 001, doi:10.1029/2011JC007 516, doi:ArtnC05001Doi10.1029/2011jc007516, URL <GotoISI>://WOS:000303669900004http://onlinelibrary.wiley.com/store/10.1029/2011JC007516/asset/jgrc12316.pdf?v=1&t=hkfp19rx&s=e5739b23619be6c9bcba6977970788b82cdac852. (Cited on page 144.)

van Vledder, G. P., 2006: The wrt method for the computation of non-linear four-wave interactions in discrete spectral wave models. *Coastal Engineering*, **53 (2)**, 223–242. (Cited on pages 34 and 51.)

Veron, F., 2015: Ocean spray. *Annual Review of Fluid Mechanics*, **47 (1)**, 507–538, doi:10.1146/annurev-fluid-010814-014651, URL http://dx.doi.org/10.1146/annurev-fluid-010814-014651, http://dx.doi.org/10.1146/annurev-fluid-010814-014651. (Cited on pages vi, 5, 62, 70, 74, 83, 87 and 154.)

Veron, F., C. Hopkins, E. Harrison, and J. Mueller, 2012: Sea spray spume droplet production in high wind speeds. *Geophysical Research Letters*, **39 (16)**. (Cited on pages vii, 24, 62, 91, 114 and 116.)

WAFO-Group, 2000: Wafo - a matlab toolbox for analysis of random waves and loads - a tutorial. Department of Mathematical Statistics, Centre for Mathematical Sciences, Lund University, Lund, Sweden, available online at http://www.maths.lth.se/matstat/wafo/. (Cited on page 133.)

Wallace, D. W. R., and C. D. Wirick, 1992: Large air sea gas fluxes associated with breaking waves. *Nature*, **356 (6371)**, 694–696, doi:Doi10.1038/356694a0, URL <GotoISI>://WOS:A1992HQ14600053. (Cited on page 147.)

Walsh, E., D. Hancock III, D. Hines, R. Swift, and J. Scott, 1985: Directional wave spectra measured with the surface contour radar. *Journal of physical oceanography*, **15 (5)**, 566–592. (Cited on pages 34 and 120.)

Wang, Z., J. Yang, and F. Stern, 2016: High-fidelity simulations of bubble, droplet and spray formation in breaking waves. *Journal of Fluid Mechanics*, **792**, 307–327. (Cited on pages vii, 91 and 115.)

Webb, A., and B. Fox-Kemper, 2011: Wave spectral moments and stokes drift estimation. *Ocean Modelling*, **40 (3-4)**, 273–288, doi:DOI10.1016/j.ocemod.2011.08.007, URL <GotoISI>://WOS:000297879700006http://ac.els-cdn.com/S1463500311001454/1-s2.0-S1463500311001454-main.

pdf?_tid=5526f82a-fece-11e2-92ea-00000aab0f26&acdnat=1375817472_8a7ae2c2492fb6cf94e2f1bb7607cd0b. (Cited on page 136.)

Webb, D., 1978: Non-linear transfers between sea waves. *Deep Sea Research*, **25 (3)**, 279–298. (Cited on page 34.)

Wyngaard, J., and O. Coté, 1971: The budgets of turbulent kinetic energy and temperature variance in the atmospheric surface layer. *Journal of the Atmospheric Sciences*, **28 (2)**, 190–201. (Cited on page 22.)

Young, I., 2010: The form of the asymptotic depth-limited wind-wave spectrum: Part III Directional spreading. *Coastal Engineering*, **57 (1)**, 30–40. (Cited on page 35.)

Young, I. R., 2003: A review of the sea state generated by hurricanes. *Marine Structures*, **16 (3)**, 201–218, doi:PiiS0951-8339(02)00054-0Doi10.1016/S0951-8339(02)00054-0, URL <GotoISI>://WOS:000181740400002http://ac.els-cdn.com/S0951833902000540/1-s2.0-S0951833902000540-main.pdf?_tid=ae930e6a-0e70-11e3-ace4-00000aab0f6b&acdnat=1377536468_c772e249fc68c9ceecf49b5ba449564f. (Cited on pages 120 and 142.)

Young, I. R., 2006: Directional spectra of hurricane wind waves. *Journal of Geophysical Research-Oceans*, **111 (C8)**, C08 020, doi:10.1029/2006JC003 540, doi:10.1029/2006jc003540, URL <GotoISI>://000240335100001. (Cited on pages vii, 120, 133, 149 and 156.)

Yurovskaya, M., V. Dulov, B. Chapron, and V. Kudryavtsev, 2013: Directional short wind wave spectra derived from the sea surface photography. *Journal of Geophysical Research: Oceans*, **118 (9)**, 4380–4394. (Cited on pages 28 and 46.)

Zakharov, V., and N. Filonenko, 1967: Energy spectrum for stochastic oscillations of the surface of a liquid. *Soviet Physics Doklady*, Vol. 11, 881. (Cited on page 29.)

Zappa, C. J., M. L. Banner, H. Schultz, A. Corrada-Emmanuel, L. B. Wolff, and J. Yalcin, 2008: Retrieval of short ocean wave slope using polarimetric imaging. *Measurement Science and Technology*, **19 (5)**, 055 503. (Cited on page 28.)

Zhao, D., and Y. Toba, 2001: Dependence of whitecap coverage on wind and wind-wave properties. *Journal of oceanography*, **57 (5)**, 603–616. (Cited on page 62.)

Zhao, D., Y. Toba, K.-i. Sugioka, and S. Komori, 2006: New sea spray generation function for spume droplets. *Journal of Geophysical Research: Oceans (1978–2012)*, **111 (C2)**. (Cited on page 62.)

université PARIS-SACLAY
ÉCOLE DOCTORALE
INTERFACES
Approches Interdisciplinaires : Fondements, Applications et Innovation

Titre : Études expérimentales et numériques de la dynamique des vagues et leurs implications pour les échanges océan - atmosphère

Mots clefs : Deferlement, interaction ocean-atmosphere, hydrodynamique, ocean, aerosol, Gerris

Résumé : Au cours des dernières décennies, les communautés de recherches océanographiques et atmosphérique ont démontrées que pour améliorer notre compréhension du couplage entre l'atmosphère et l'océan, et le paramétrage du flux de masse entre l'océan et l'atmosphère (gaz, aérosols, par exemple) , de moment (pour la génération de vagues et de courants marins) et d'énergie (flux de chaleur et énergie cinétique pour les courants et le processus de mélange près de la surface) dans les modèles couplés océan-atmosphère, les vagues doivent être prises en compte. La physique du couplage dépend de la cinématique et de la dynamique du champ de vagues, y compris les processus de génération de vagues liées au vent, les interactions non-linéaires, ondes-ondes et la dissipation des vagues, cette dernière étant normalement considérée comme dominée par le déferlement. Nous présentons ici une série d'études expérimentales et numériques, démontrant l'importance du champ de vagues sur les interactions océan - atmosphère.

Title : Experimental and Numerical Studies of the Kinematics and Dynamics of Surface Waves and the Implications to Ocean-Atmosphere Interaction Processes

Keywords : Ocean-Atmosphere interaction, waves, aerosol, sea spray

Abstract : Over the last several decades there has been growing recognition from both the traditional oceanographic and atmospheric science communities that to better understand the coupling between the atmosphere and the ocean, and reflect that understanding in improved air-sea fluxes of mass (e.g. gases, aerosols), momentum (e.g. generation of waves and currents) and energy (e.g. heat and kinetic energy for currents and mixing) in coupled ocean-atmosphere models, surface-wave processes must be taken into account. The underlying physics of the coupling depends on the kinematics and dynamics of the wave field, including processes of wind-wave growth, nonlinear wave-wave interactions, wave-current interactions and wave dissipation, with the last normally considered dominated by wave breaking. Here we present a series of experiments, both numerical and field observations, focusing on surface wave effects on air-sea interaction processes.

Université Paris-Saclay
Espace Technologique / Immeuble Discovery
Route de l'Orme aux Merisiers RD 128 / 91190 Saint-Aubin, France